TECHNISCHE UNIVERSITÄT DRESDEN

Fakultät Elektrotechnik und Informationstechnik · Institut für Automatisierungstechnik

A Contribution to Validation and Testing of Non-Compliant Docking Contact Dynamics of Small and Rigid Satellites Using Hardware-In-The-Loop Simulation

Ein Beitrag zu Validierung und Test von nicht elastischer Andock-Kontaktdynamik von kleinen und starren Satelliten mittels Hardware-in-the-Loop Simulation

M.Sc.

Karim Bondoky

Von der Fakultät Elektrotechnik und Informationstechnik
der Technischen Universität Dresden

zur Erlangung des akademischen Grades

Doktoringenieur

(Dr.-Ing.)

genehmigte Dissertation

—— * ——

Vorsitzender:	Prof. Dr.-Ing. habil. Dipl.-Math. Klaus Röbenack
Gutachter:	Prof. Dr. techn. Klaus Janschek
	Prof. Dr.-Ing. Stefanos Fasoulas
Tag der Einreichung:	02.09.2020
Tag der Verteidigung:	26.10.2020

—— ✻ ——

I dedicate this dissertation to my parents, Nahed and Nashaat, for their non-stopping love, help and support.

—— ✻ ——

Acknowledgements

I would like to express my special gratitude to my supervisor Prof. Dr. techn. Klaus Janschek for the constant assistance and support that he has been providing from the beginning of my doctorate. It is sincerely appreciated that his great practical advice has made it possible to put a realistic framework and goals for the research project, which paved the way for me to successfully complete the project and the dissertation.

I would like to thank Prof. Dr.-Ing. Stefanos Fasoulas for agreeing to be the second reviewer. I truly appreciate your valuable thorough detailed review, which helped to improve the dissertation a lot. Thank you very much.

I would like to express my deepest gratitude to my supervisors at Airbus DS GmbH in Friedrichshafen, Germany. I am truthfully thankful for the enormous efforts of Dr. Andreas Rathke throughout the years, starting by the initiating the doctoral research project in collaboration with TU Dresden, organizing the required funding for the whole doctoral years duration, his collaboration in reviewing the scientific publications, his valuable personal advice about the different career paths and much more.

I would like to offer my special thanks to Sebastian Schwarz for the valuable assistance that he has provided from the beginning, since my master's thesis, till the end of the doctorate. He has been always supportive with practical-creative ideas that allowed the research project and the testbed implementation to move forward and to be realized.

I would like to express my appreciation to Dr. Georg Willich and the *Graduiertenkolleg* of Airbus DS GmbH for the financial support and flexibility throughout the five years of the research and the doctoral project. I would also like to acknowledge the financial support from the the Graduate Academy of TU Dresden, which is supported by means of the Excellence Initiative by the German Federal and State Governments.

I would like to thank my colleagues at the Institute of Automation at TU Dresden, in particular, Matthias Roth, for the good memories, helpful scientific advice and insightful coffee chats. Also thanks to Lukas, Christopher, Chao, Matthias, Martin, Frank for the Campus Colloquium meetings and

discussions. Special thanks to Petra Möge for her support in all the administration work. In addition, I would like to thank Norbert Kindermann for his assistance in the experiment setup, Mario Herhold for his technical support and Dr. Sergey Dyblenko for his assistance with grant applications.

I am grateful for the contribution of my students to the research project and the experiment setup. Special thanks Matthias Kraft, Daniel Wohllebe and Zhou Lei.

I would like to express my wholehearted gratitude to Mark Brislin and Dr. Nadine Siebdrath for the detailed reviewing and proof-reading of the whole dissertation, to Chao Yao for the technical review of chapter 8, and to Friederike Michalik for her help in polishing and reviewing the German abstract. I would not have made it without your help. Thank you.

I owe my deepest heartfelt gratitude and honor to my family for the continuous love and support, in particular my mother Nahed for being there always for me with your kindness, never-ending love, help and prayers, as well as my father Nashaat for being always encouraging, motivating and supportive. I would have never done it without you.

My deepest love to Ramy, Thimar, Asaph and Anna for being a caring heart and comforting place for me. My truthful appreciation to Glory for being a good-listening supportive friend and cousin. My deepest gratitude for your pure love and kindness Misho, Hoda, Hany, Marinette, Sara, Dano.

I am grateful for your love: teta Monda, Shadia, Wafik, Sherin, Heidy, Farah, Sarah as well as Mounir, Nohad, Fady, Yousri, Marise, Magd, Mira, Sherif, Iman, Andrew and Mark. Last but not least, to gedo Emil, teta Tuna and Rita, you are truly loved, missed and forever in my heart.

I would like to express my special gratitude to my friends for their support, encouragement, prayers, shared fun memories and laughter during the last five years. Special thanks to Nadine Siebdrath for the continuous help and support throughout the years of my doctorate. Thanks to Debby Scharnowski, Hannah Griffin, Jakob Fiedler, Jeremy Krider, Johanna Zeeh, Joni Schnabel, Lydia Rossner, Martin Schieferdecker, Mary Hanna, Peter Herbert, Ray Pieratt, Rieke Michalik, Shady Khella, Shady Dawood, Sam & Mellie Bode, Ferdi & Stephi Gerstetter, Tobi & Judith Remtisch.

I would like to give thanks to my Lord Jesus Christ, for His grace, favor and for being my main source of love, support and motivation.

A Contribution to Validation and Testing of Non-Compliant Docking Contact Dynamics of Small and Rigid Satellites Using Hardware-In-The-Loop Simulation

Karim Bondoky

Abstract

Spacecraft (S/C) docking is the last and most challenging phase in the contact closure of two separately flying S/C. The design and testing of S/C docking missions using software-multibody simulations need to be complemented by Hardware-In-The-Loop (HIL) simulation using the real docking hardware. The docking software multibody simulation is challenged by the proper modeling of contact forces, whereas the HIL docking simulation is challenged by proper inclusion of the real contact forces. Existing docking HIL simulators ignore back-reaction force modeling due to the large S/C sizes, or use compliance devices to reduce impact, which alters the actual contact force. This dissertation aims to design a docking HIL testbed to verify docking contact dynamics for small and rigid satellites by simulating the real contact forces without artificial compliance.

HIL simulations of docking contact dynamics are challenged mainly by:

I. *HIL simulation quality*: quality of realistic contact dynamics simulation relies fundamentally on the quality of HIL testbed actuation and sensing instrumentation (non-instantaneous, time delays, see Fig. 1)

II. *HIL testbed design*: HIL design optimization requires a justified HIL performance prediction, based on a representative HIL testbed simulation (Fig. 2), where appropriate simulation of contact dynamics is the most difficult and sophisticated task.

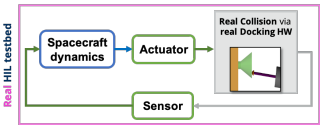

Figure 1: HIL docking testbed block-diagram

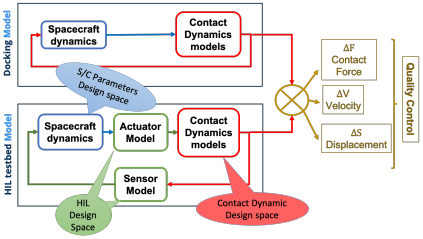

Figure 2: Models with labeled design-spaces

The goal of this dissertation is to carry out a systematic investigation of the technically possible HIL docking contact dynamics simulation performances, in order to define an appropriate approach for testing of docking contact dynamics of small and rigid satellites without compliance and using HIL simulation. In addition, based on the investigations, the software simulation results shall be validated using an experimental HIL setup.

To achieve that, multibody dynamics models of docking S/C were built, after carrying out an extensive contact dynamics research to select the most representative contact model. Furthermore, performance analysis models of the HIL testbed were built. In the dissertation, a detailed parametric analysis was carried out on the available models' design-spaces (e.g., spacecraft, HIL testbed building-blocks and contact dynamics), to study their impacts on the HIL fidelity and errors (see Fig. 1). This was done using a generic HIL design-tool, which was developed within this work. The results were then used to identify the technical requirements of an experimental 1-Degree-of-Freedom (DOF) HIL testbed, which was conceived, designed, implemented and finally utilized to test and validate the selected docking contact dynamics model.

The results of this work showed that the generic multibody-dynamics spacecraft docking model is a practical tool to model, study and analyze docking missions, to identify the properties of successful and failed docking scenarios before it takes place in space.

Likewise, the "Generic HIL Testbed Framework Analysis Tool" is an effective tool for carrying out performance analysis of HIL testbed design, which allows to estimate the testbed's fidelity and predict HIL errors.

Moreover, the results showed that in order to build a 6DOF HIL docking testbed without compliance, it is important to study and analyze the errors's sources in an impact and compensate for them. Otherwise, the required figure-of-merits of the instruments of the HIL testbed would be extremely challenging to be realized.

In addition, the results of the experimental HIL simulation (i.e., real impacts between various specimen) serve as a useful contribution to the advancement of contact dynamics modeling.

Ein Beitrag zu Validierung und Test von nicht elastischer Andock-Kontaktdynamik von kleinen und starren Satelliten mittels Hardware-in-the-Loop Simulation

Karim Bondoky

Kurzfassung

Das Andocken von Satelliten ist die letzte und schwierigste Phase des mechanischen Kontaktschlusses von zwei getrennt fliegenden Raumfahrzeugen. Der Entwurf und das Testen von Satelliten-Andockmissionen unter Verwendung von Software-Mehrkörper-Simulationen müssen durch Hardware-in-the-Loop (HIL) Verifikation unter Verwendung der realen Andockhardware ergänzt werden. Die größte Herausforderung der Andock-Software-Mehrkörper-Simulation ist eine realistische Modellierung der Kontaktkräfte, wogegen die treibende Herausforderung der HIL Andock-Simulation in der korrekten Einbeziehung der realen Kontaktkräfte besteht. Bei bestehenden HIL Andock-Simulatoren wird entweder die Modellierung der Reaktionskräfte aufgrund der großen Raumfahrzeuggrößen ignoriert oder es werden nachgiebige Elemente verwendet, um den Stoß zu reduzieren, wodurch jedoch die tatsächliche Kontaktkraft verändert wird. Ziel dieser Arbeit ist der Entwurf eines HIL Docking Testbeds, um die Andock-Kontaktdynamik für kleine und starre Satelliten zu verifizieren, indem die realen Kontaktkräfte ohne künstliche Nachgiebigkeiten simuliert werden.

HIL Simulationen der Andock-Kontaktdynamik werden hauptsächlich durch folgende Punkte erschwert:

I. *Qualität der HIL-Simulation*: die Qualität einer realistischen Kontaktdynamiksimulation hängt grundlegend von der Qualität der Steuerung und Sensorik des HIL Prüfstands ab (Zeitverzögerungen, siehe Abb. 1).

II. *Entwurf des HIL-Prüfstands*: die Optimierung des HIL Designs erfordert eine belastbare HIL Leistungsvorhersage auf Grundlage einer repräsentativen, modellbasierten HIL Simulation (Abb. 2), wobei die realistische Simulation der Kontaktdynamik am schwierigsten und anspruchsvollsten ist.

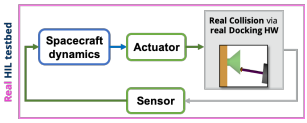

Abbildung 1: HIL Andock-Prüfstands-Blockdiagramm.

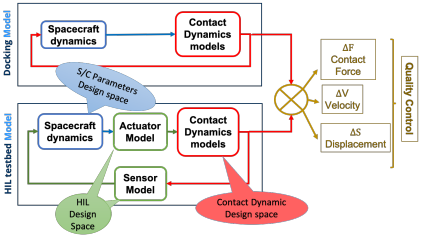

Abbildung 2: Modelle mit beschrifteten Konstruktionsflächen.

Das Ziel dieser Dissertation ist eine systematische Untersuchung der technisch möglichen Leistungen der HIL Simulation der Andock-Kontaktdynamik, um einen geeigneten Ansatz für die Prüfung der Andock-Kontaktdynamik von kleinen und starren Satelliten (ohne jegliche Nachgiebigkeiten) mittels HIL Simulation zu definieren. Darüber hinaus sollen auf der Grundlage der Untersuchungen die Ergebnisse der Softwaresimulation mit einem experimentellen HIL Aufbau validiert werden.

Um dies zu erreichen, wurden Mehrkörper-Dynamikmodelle von andockenden Satelliten eingehend untersucht, um das repräsentativste Kontaktmodell auszuwählen. Darüber hinaus wurden Leistungsanalysemodelle des HIL Prüfstands erstellt. In dieser Dissertation wurde eine detaillierte parametrische Analyse des Entwurfsparameterraumes (z.B. Raumfahrzeuge, HIL Testbed-Bausteine und Kontaktdynamik) durchgeführt, um den Einfluss der Entwurfsfreiheitsgrade auf die Genauigkeit und Fehler der HIL Simulation zu untersuchen (siehe Abb. 1). Dies geschah mit Hilfe eines generischen HIL Design-Tools, das im Rahmen dieser Arbeit entwickelt wurde. Anschließend wurden diese Ergebnisse verwendet, um die technischen Anforderungen für einen experimentellen 1-Degree-of-Freedom (DOF) HIL-Prüfstand abzuleiten, welcher konzipiert, entworfen, implementiert und schließlich verwendet wurde, um das verwendete Andock-Kontakt-Dynamikmodell zu testen und zu validieren.

Die Ergebnisse dieser Arbeit zeigten, dass mit dem generischen Mehrkörper-Dynamikmodell für das Andocken von Raumfahrzeugen ein praktisches Werkzeug zur Verfügung steht, um Andockmissionen zu entwickeln, zu studieren und zu analysieren. Damit können die Eigenschaften von erfolgreichen und fehlschlagenen Andock-Szenarien analysiert werden, bevor sie im Weltraum stattfinden. Gleichermaßen ist das "Generic HIL Testbed

Framework Analysis Tool" ein überaus nützliches Hilfsmittel zur Durchführung von Performance-Analysen des HIL Testbed-Designs, das es ermöglicht, die Genauigkeit des Testbeds einzuschätzen und HIL Fehler vorherzusagen. Darüber hinaus zeigten die Ergebnisse, dass es für den Aufbau eines 6DOF HIL Andock-Testbeds ohne Nachgiebigkeiten wichtig ist, die Fehler hinsichtlich der einzelnen Auswirkungen zu untersuchen, zu analysieren und auszugleichen. Andernfalls wären die technischen Anforderungen an das HIL-Testbed (z.B. Roboter Gütezahl) äußerst anspruchsvoll zu realisieren. Die Ergebnisse der experimentellen HIL Simulation (d.h. reale Auswirkungen zwischen verschiedenen Proben) stellen einen sehr nützlichen Beitrag zur Weiterentwicklung von Kontaktdynamik-Modellen dar.

Contents

List of Figures

List of Tables

List of Abbreviations and Symbols

Abbreviations

aka	Also Known As
CoG	Center of Gravity
COM	Center-Of-Mass
COR	Coefficient of Restitution
CSA	Canadian Space Agency
DDOF	Design-Degrees-Of-Freedom
DLR	German Aerospace Center
DOF	Degrees-Of-Freedom
EOM	Equation-of-Motion
EPOS	European Proximity Operations Simulator
ESA	European Space Agency
HIL	Hardware-in-the-Loop
IBDM	International Berthing and Docking Mechanism
Max.	Maximum
MoI	Moment of Inertia
NASA	National Aeronautics and Space Administration
NRL	United States Naval Research Lab
OOS	On-Orbit Servicing
POT	Proximity Operations Testbed

PSD	Power Spectral Density
S/C	Spacecraft
T.F.	Transfer Function
TUD	Technical University of Dresden
w.r.t.	With Respect To

General Nomenclature

$\mathbf{A}$	Variable Matrix
$\mathbf{a}$	Variable vector
$\mathbf{I_d}$	Constant Identity Matrix
a	Variable scalar

Generic HIL Testbed Framwork Analysis Tool

$\Delta T_{contact}$	Contact Time Duration Error
$\hat{H}$	HIL model
$\hat{I}$	Ideal Docking model
e_v	Velocity error percentage
$e_{A_{int}}$	Modulus absolute integral error
e_{abs}	Max. absolute error
$e_{H_{int}}$	Modulus HIL integral error
e_{Hmax}	Max. HIL error
e_{Imax}	Max. instantaneous error

Contact Dynamics

δ	Penetration depth
$\dot{\delta_f}$	Final Penetration Velocity (velocity after separation)

$\dot{\delta}_i$	Initial Penetration Velocity (initial impact velocity)
$\dot{\delta}$	Penetration Velocity
$\hat{n}$	Surface Normal Vector
λ	Hysteresis Damping Factor
μ_0	friction coefficient during stiction
μ_1	friction coefficient during perfect sliding
ν	Poisson Ratio
c_r	Coefficient of Restitution
E	Young's modulus
E^*	Combined Young's modulus of two bodies
F	Contact Force
F_f	friction force
k	Hertzian Stiffness
R	Radius of curvature
R^*	Combined Radius of two surfaces
v_{rel}	Relative velocity between two bodies
v_S	Stribeck velocity

Reference Frames

$\{C_0\}$	Chaser S/C COM
$\{F_1\}$	Reference Frame of Chaser rigid-cylinder's base
$\{F_2\}$	Reference Frame of docking probe-beam's Base
$\{F_3\}$	Reference Frame of docking probe-tip's Base
$\{F_4\}$	Reference Frame of docking cone's Base

$\{F_5\}$	Reference Frame of docking cone's tip
$\{T_0\}$	Target S/C COM
$\{W\}$	World inertial-fixed frame
c_i	Chaser's simple-shaped rigid-body number i
t_i	Target's simple-shaped rigid-body number i
I	Inertial Reference Frame

Multibody Dynamics Models

$\ddot{x}_i$	acceleration of body i
$\dot{x}_i$	velocity of body i
γ	angle between i and z-axis, in YZ plane
θ_c	Docking cone angle
$\hat{\mathbf{n}}_{\mathbf{tc}}$	Unit vector of normal reaction force from Chaser to Target
$\hat{\mathbf{t}}_{\mathbf{tc}}$	Unit vector of tangential reaction force from Chaser to Target
$\mathbf{\Phi}$	Euler angles
$\mathbf{C_c}$	Contact-point position vector on Chaser's Probe-tip, w.r.t Drogue-base
$\mathbf{C_t}$	Contact-point position vector on Target's drogue, w.r.t Drogue-base
$\mathbf{I}_{b_i}$	Inertia tensor of b_i defined in its own COM
$\mathbf{K}$	Perpendicular displacement vector, from drogue surface to probe-tip base.
$\mathbf{M}_{B_0}$	Mass-matrix of body B_0
$\mathbf{P}$	displacement vector of probe-tip base $\{F_3\}$ w.r.t drogue's base $\{F_4\}$, represented in $\{F_4\}$

$\mathbf{R}_{bw}$	Rotation transformation matrix that transforms from world reference frame (w) to body-fixed frame (b)
${}_b\boldsymbol{\tau}$	External Torque acting on body's COM
${}_b\boldsymbol{\Omega}$	Angular velocity vector defined in body-fixed frame
${}_b\mathbf{F}$	External force acting on body's COM
${}_b\mathbf{V}$	Linear velocity vector defined in body-fixed frame
${}_b\mathbf{Y}$	Velocity vector defined in body-fixed frame
${}_w\mathbf{S}$	Linear position vector defined in inertial world frame
${}_w\mathbf{Z}$	Pose vector defined in inertial world frame
${}_{B_0}(\mathbf{I}_{b_i})$	Inertia tensor of b_i transported in body (B_0)'s COM
c	outer radius of varying-frustum
i	distance from probe-tip base, to drogue's base in YZ plane
I_d	Identity Matrix
j	distance from probe-tip base, to to frustum in YZ plane
k	distance from probe-tip base, to frustum
l	minimum distance to impact
l_c	length of docking cylinder
m_i	mass of body i
m_{B_0}	Mass of body B_0
r_c	radius of docking cylinder
r_p	radius of probe-tip
x_i	displacement of body i

Hardware Models

ω_o	Natural frequency

τ_{del}	Total time-delay
d_o	Damping value in modeled hardware
D_{act}	Total time-delay of actuator's model
D_f	Total time-delay of force-sensor's model
D_{rob}	Total time-delay of robotic hardware's model
f_o	bandwidth frequency
G_{LPS}	2nd order Low-Pass System (LPS) equation
Q	Quantizer used to model resolution of a hardware
R_{act}	Resolution of actuator's model
R_f	Resolution of force-sensor's model
R_{rob}	Resolution of robotic hardware's model
T_c	Time constant

HIL Simulation

η	Noise model
σ^2	Variance
σ_d	Standard deviation
ζ	Fidelity
d	"Docking model"
E_{hd}	*Real HIL* Error
E_{hm}	HIL Contact Error
E_{md}	*Simulated HIL* Error
F_{act}	Max. blocking force of piezoactuator in its datasheet.
F_{test}	Predicted max. force in a scenario.

h	"Real HIL Test"
m	"HIL model"
S_n	Power Spectral Density
$T_{act}(s)$	Transfer-function of controlled actuator system
$T_e(s)$	Transfer-function of eddy-current sensor
$T_f(s)$	Transfer-function of force sensor
X_{act}	Max. stroke of piezoactuator in its datasheet.
X_{test}	Predicted max. extension in a scenario.

Controller Design

d	Damping constant
d_{ls}	Displacement output of laser sensor
e	Control error
$G(jw)$	Frequency response of system under inspection
$G(s)$	Transfer-function of whole plant
$G_1(s)$	Transfer-function of piezoactuator-amplifier only
$G_2(s)$	Transfer-function of piezoactuator and eddy-current sensor
$H(s)$	Controller
K	Gain
$L(s)$	Open-loop transfer-function
L_{max}	Maximum distance detected by laser sensor
L_{min}	Minimum distance detected by laser sensor
m	output-signal of actuator amplifier
$M(s)$	Laplace-transformation of the signal m

r	Reference input
$R(s)$	Laplace-transformation of the signal r
$r_{uu}(\tau)$	auto-correlation of the signal $u(t)$
$r_{uy}(\tau)$	cross-correlation of the signals $y(t)$ and $u(t)$
S_{uu}	Power spectral density
S_{uy}	Cross spectral density
$T(s)$	Closed-loop transfer function
u	Controller output
u	Input-signal of the researched object (Plant).
$U(s)$	Laplace-transformation of the signal u
V_{ls}	Voltage output of laser sensor
V_{max}	Maximum voltage output by laser sensor
V_{min}	Minimum voltage output by laser sensor
w	Filtered feference input
$W(s)$	Laplace-transformation of the signal w
y	Controlled variable (i.e., displacement of actuator measured by eddy-current sensor)
y	Output-signal of the researched object (Plant).
$Y(s)$	Laplace-transformation of the signal y

Chapter 1

Introduction

1.1 Background/Motivation

Spacecraft Docking

Spacecraft (S/C) docking is the joining process of two separately flying S/C. It is the last and most challenging phase in the S/C physical-joining mission, which comes after the S/C rendezvous phase. The goal of docking is to assure that a rigid and robust physical connection between both S/C is established. After firing the last impulse from the active S/C propulsion, the scenario switches from two independently flying S/C to two physically impacting space vehicles. It is in that moment that it is up to the docking mechanism to decide if S/C would successfully dock or not. Therefore, the docking mechanism and the docking phase are significantly critical for any S/C physical-joining mission.

Docking Research

The demands to research S/C docking have been increasing in the recent years because of various space technologies, such as: automated docking [Wertz and Bell, 2003], On-Orbit Servicing (OOS) [Flores-Abad et al., 2014] and the increasing number of small S/C in space. Most of the realized docking in space were between large S/C ($> 1ton$). However, with the increasing number of small ($10kg-1ton$) S/C, the necessity has arisen to research docking for such cases. Another reason is the OOS, which, in particular, is a very hot space technology topic and would be very beneficial for space science and industry, when it is ready to be implemented [Flores-Abad et al., 2014]. OOS is focused on the extension of the lifetime of the in-orbit satellites, which could reduce the overall costs of satellite manufacturing. This would be achieved by refueling the target satellites, changing dead batteries, or fixing hardware problems, etc. In addition, OOS aims at reducing the space debris, which is a very important issue. This would be achieved by carrying out controlled de-orbiting missions of dead satellites. One necessary prerequisite of any of the above mentioned tasks, is to have a successful

docking in order to ensure a rigid and robust physical connection between both docking S/C; the chaser and the target.

Non-Compliant Docking

Many S/C are not designed to be docked to, i.e., they do not have a compliant docking adapter or mechanism that facilitates docking. These S/C should be considered during the research and development of OOS missions, in order to ensure the OOS capability to any arbitrary S/C, even the ones which are not designed to be docked to. To do so, it is required to find generic solutions to dock with any S/C in space, even if it is not designed to undergo docking (i.e., non-compliant). Accordingly, this work is focused on the non-compliant docking analysis of S/C. One generic solution to ensure docking with any arbitrary satellites could be docking to the thruster nozzle of the S/C, e.g., the thruster nozzle of the apogee engine of a geostationary satellite. Taking into consideration the above scenario, a non-compliant probe and drogue (cone shaped) docking mechanism is considered in this work, as seen in Fig. 1.1.

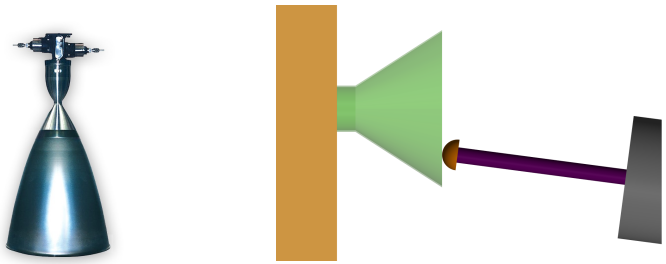

Figure 1.1: Thruster Nozzle could be utilized as a Docking Drogue (in the Probe-Drogue Docking Mechanism) for OOS of arbitrary satellite. Left figure shows apogee thruster nozzle S400-12 by ArianeGroup, [Ariane Group, 2017]. Right figure shows probe and drogue docking mechanism visualization

Docking Testing

To assure successful docking, each docking scenario and its attributes must be taken into consideration, analyzed and tested. Some of these attributes are: S/C physical properties (e.g., mass, material, etc.), relative-velocity between both S/C, relative-pose, etc. Failing to consider these attributes and assuming that the docking mechanism is the only deciding factor, would

probably lead to a failed docking. Real-life missions that faced failed docking attempts (e.g., Soyuz MS-14, Apollo 14) prove that docking is not an intuitive process. Therefore, it is required to model and test each docking scenario (while including as many details of the scenario as possible), before it is realized in space. Accordingly, the design of docking missions needs to be verified by software multibody docking modeling and simulations, which needs to be complemented and validated by an experimental docking testbed, using the real docking hardware. In this way, one would be able to make reliable and justified predictions of the docking scenario.

Various docking testing techniques have been previously implemented to test docking, such as: air-bearing table [Schwartz et al., 2003] and Hardware-in-the-Loop (HIL) simulations (e.g., [Han et al., 2008], [Zebenay et al., 2015]). Both techniques utilize the real docking hardware, which is a requirement within the scope of this work. However, HIL simulation has more advantages, as follows:

- It simulates the gravitational-less space environment and 6 Degrees-Of-Freedom (DOF) S/C motion in space. Unlike the air-bearing table, which is limited to 5 DOF and cannot simulate the non-gravitational environment.

- It is easier to vary the considered docking scenarios and its attributes (such as, mass, inertia, material, etc.), because they can be easily modified in the computer models. In contrast, in the air-bearing table technique, these changes have to be applied in the real-life experiment, i.e., add more masses to the S/C physical model.

Previous HIL testbeds

Existing docking HIL simulation testbeds (e.g., CDSL (NASA)[Hall et al., 2006], STVF (CSA) [Piedboeuf et al., 1999], IBDM Testing (ESA) [Hardt et al., 2011] and EPOS (DLR) ([T. Boge et al., 2010], [Toralf Boge et al., 2012], [Ma et al., 2012]) had limitations, which made them unsuitable for the verification of the docking scenarios under consideration. The shortcomings arose from the use of highly rigid industrial hardware for the generation of the multibody dynamics combined with a damping element that isolated the simulator hardware from the hardware under test. Such setups are satisfactory for the simulation of very large mass S/C as used in human spaceflight, in which the contact dynamics lead to negligible back-reaction on the multibody dynamics. However, for small S/C, the back-reaction of the contact on the relative trajectory is significant and many contact

parameters (in particular, material friction, damping and stiffness) need to be considered in the simulation at high fidelity, in order to represent the true behavior.

Project Overview

According to what is mentioned above and the existing HIL docking testbeds, Airbus Defence and Space GmbH in Friedrichshafen, Germany, in cooperation with Technische Universität Dresden (TUD) decided to conceive, design and implement a novel HIL simulation testbed. The HIL testbed shall be used to validate docking contact dynamics of small and rigid S/C, using the real docking hardware and without any compliant devices. A conceptual design of the HIL testbed is illustrated in Fig. 1.2.

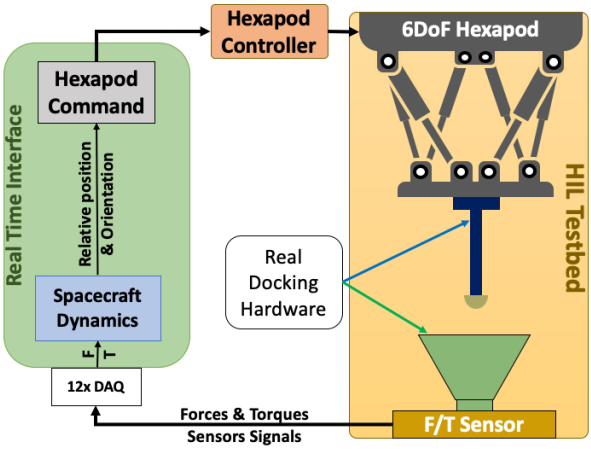

Figure 1.2: Conceptual 6DOF HIL Simulation Testbed

Dissertation Goal

The goal of this dissertation is focused on carrying out a systematic investigation of the technically possible HIL docking contact dynamics simulation performances. This was carried out by exploring the design-spaces (e.g., spacecraft, HIL testbed building-blocks and contact dynamics), using a parametric HIL design-tool for the available design-spaces. Afterwards, the verification of the software simulation results was carried out using an

experimental 1DOF HIL setup.
In addition, a performance analysis of a 6DOF spacecraft docking (as a case study) was carried out, in order to identify the successful and failed docking scenarios properties using software simulations.

1.2 State-of-the-art

In this section, various HIL docking simulation testbeds that have been developed are introduced, along with their advantages, as well as their shortcomings.

Various HIL testbeds were built to simulate the proximity operations dynamics of S/C, e.g., rendezvous, docking and capture. The existing testbeds were built by space agencies, industrial companies and universities.

European Proximity Operations Simulator (EPOS)
EPOS is a huge facility that was developed by the German Aerospace Center (DLR) and the European Space Agency (ESA) at DLR-Oberpfaffenhofen, Germany ([T. Boge et al., 2010], [Toralf Boge et al., 2012], [Ma et al., 2012]). It is considered (in this work) as the state-of-the-art in HIL simulations of proximity operations. EPOS consists of two huge KUKA robotic arms that are capable of moving in 6DOF. Each robotic arm can carry a mock up of each of the S/C and imitate the 6DOF motion of each of the S/C in space while simulating proximity operations, such as: rendezvous, refueling, docking, etc. Moreover, one of the robotic arms can move alongside a long horizontal rail, which allows to simulate rendezvous even when both S/C are far away from each other. However, various problems arose from using huge large-mass high-stiffness robotic arms in this large-scale docking simulation facility. These robotic arms' stiffness, as well as the long delay (32ms) could lead to the destruction of the robotic arms, while simulating the docking and the physical impacts in particular. This forced the engineers working in this facility to utilize an artificial compliance device at the end-effector to avoid any hazardous collision during the simulation, [Zebenay, 2014], [Zebenay et al., 2015]. This compliance device, however, alters the real docking contact forces that needs to be measured and simulated. Moreover, the big high-stiffness robotic arms do not have enough motion resolution and accuracy, which is required to simulate real contact dynamics in the HIL simulation.

Proximity Operations Testbed

Likewise, Proximity Operations Testbed (POT) [Bell et al., 2003] operated by the United States Naval Research Lab (NRL), is a huge facility that used also huge industrial robotic arms, as well as trolleys to simulate the proximity operations. This facility was used to test the NRL's robotic arm system called FREND. The long trolleys gave the robots enough range of motion to simulate proximity operations when they were far from each other. Although detailed information concerning the facility could not be found for public access, the available public information showed that with the given accuracy and resolution of the robotic arms, the HIL simulation of docking contact dynamics for small satellites, would be also quite challenging to be carried out.

Chinese HIL docking facility

Chinese space industry and universities developed a large HIL docking test facility. In their facility, they developed two customized 6DOF parallel robotic systems to simulate the docking contact dynamics [Q. Wang et al., 2017]. Intense investigations were carried out to use their developed parallel robots. However, the test facility was using a rather simple docking mechanism to carry out their tests. The question remains open whether their HIL testbed could test a realistic probe-drogue docking mechanism for small satellites or not.

Other Docking HIL testbeds

Chinese engineers and scientists built a HIL simulation testbed using two huge 6DOF hexapod platforms, in order to simulate docking contact dynamics [Han et al., 2008]. The big-masses hexapods forced them to use compliance devices (like EPOS approach) to overcome any hazardous collision, due to high-stiffness or delay. However, as mentioned earlier, using compliance devices, would alter the real docking contact forces that should be measured.

The European Space Agency (ESA) developed a docking HIL simulation facility to validate the International Berthing and Docking Mechanism (IBDM). In this facility, only one industrial robotic arm was used to simulate the motion of the active S/C carrying one side of the docking mechanism,

while the other side of the docking mechanism was attached to a fixed platform representing the passive S/C [Hardt et al., 2011]. However, in the test, the back reaction force and torques from the passive S/C were not taken into consideration. Such a test could be acceptable for heavy mass satellites where the momentum of the heavy moving S/C is large enough to force docking trajectory to succeed. However, for small or micro S/C, each small physical impact would affect the pose of the S/C. Hence, this test facility also can not be acceptable for the considered system.

1.3 Problem Definition

Spacecraft docking simulation and HIL tests for docking contact dynamics are challenged by the following issues:

1. **Contact Dynamics and Docking Simulation**
   Multibody docking software simulation is mainly concerned with modeling of mulitbody dynamics and contact dynamics. Contact dynamics aspect is the most challenging one, because of the significance of the physical impacts in any docking scenario. Contact forces (generated from physical impacts) during docking affect the reaction motion of each S/C significantly. This is even more crucial in case of non-compliant docking scenarios, because hard physical impacts are expected during docking. Therefore, to model contact dynamics properly, it is important to study and analyze various contact models, in order to select the most representative contact model to be used in the docking simulations.

2. **HIL Simulation Quality**
   In a docking HIL simulation, the robotic hardware motion (which emulates the spacecraft's motion in space during docking) is based on the real contact force measurements resulting from the real docking hardware. Accordingly, the quality of the HIL simulation of docking contact dynamics depends mainly on the quality of the HIL testbed actuation and sensing instruments. The dynamics of each instrument in the HIL testbed (e.g., non-instantaneous, time delays, inaccuracy, etc.) introduce some errors to the HIL simulation. Hence, the fidelity of the HIL simulation is critically dependent on the testbed implementation and its instruments. Therefore, HIL instruments have to be properly selected.

3. **HIL Testbed Design**
   HIL design optimization requires a justified performance analysis on a representative HIL testbed model. A systematic performance analysis allows to define the adequate figure-of-merits of each instrument. Moreover, it would provide insight, if the fidelity of the HIL simulation is satisfactory to the docking contact dynamics problem under consideration. Therefore, a representative HIL testbed model needs to be built, upon which performance analysis is required to be carried out.

4. **HIL Testbed Setup**
   The most suitable instruments for the HIL testbed need to be identified and procured from the market if available, otherwise custom-made instruments are to be designed. Afterwards, the HIL testbed needs to be integrated and set up to test and validate the docking contact dynamics.

1.4 Dissertation Objectives

The objective of this dissertation is to model and analyze multibody (spacecraft) docking contact dynamics problems, in order to define an appropriate HIL simulation approach to validate docking contact dynamics of small and rigid satellites. Moreover, performance analysis of various docking scenarios of a specific S/C is required. In addition, a systematic investigation of a model of the HIL performance model needs to be carried out (after building the HIL model). Accordingly, the figure-of-merits of the required instruments are to be defined, selected and procured. Finally, the HIL testbed is to be set up in order to carry out the HIL simulation.

Therefore, the objectives of this work are summarized as follows:

1. **Non-linear Contact Dynamics Research**
   Docking contact dynamics is one of the most challenging aspects of this work. Hence, detailed research, investigation and analysis of existing non-linear contact dynamics models need to be carried out. Accordingly, the most representative non-linear contact dynamics model shall be selected and utilized in the multibody docking simulation.
2. **Performance Analysis of Spacecraft Docking**, as follows:
   a) Building a multibody dynamics model of the docking spacecraft.

b) Prediction of docking scenario simulation results.

c) Verification of docking using software simulations.

d) Studying and analysis of various docking scenarios of a case-study, to define the properties of the successful and the failed docking scenarios. This would assist engineers to identify the sensitive attributes (and their acceptable range) of the docking spacecraft under consideration.

3. **Generic HIL Testbed Framework Analysis Tool**
   A generic tool for performance analysis and fidelity estimation of any HIL testbed needs to be built. This tool would carry out a systematic investigation of the technically possible HIL docking contact simulation performances. Using this parametric HIL framework design tool, the available design-spaces in the testbed design framework shall be explored. Hence, the figure-of-merits of HIL instruments are identified in accordance with the required design-framework. Based on the results, required HIL instruments are selected and procured (after a market survey is carried out).

4. **HIL Simulation Setup**
   A HIL testbed needs to be designed, assembled and set up using the equipment defined. Afterwards, a proper closed-loop displacement controller shall be designed for the selected actuator. Then, the whole real-time HIL setup requires to be validated.

5. **Testing and Validation of docking contact dynamics using HIL simulation**
   A HIL simulation shall be carried out in order to test and validate docking contact dynamics. In addition, the HIL simulation would prove the validity of the proposed concept of testing and validation of contact dynamics models using 1DOF HIL simulation.

1.5 Scientific Contribution

Seven main contributions are provided in this dissertation:

Contribution 1. Generic HIL Testbed Framework Analysis Tool.

Contribution 2. Critical analysis of non-linear contact dynamics models.

Contribution 3. Investigation and analysis of 1DOF HIL testbed design.

Contribution 4. Generic 6DOF spacecraft docking model.

Contribution 5. Docking performance analysis of a case-study.

Contribution 6. Investigation and analysis of 6DOF HIL testbed design.

Contribution 7. Experimental testing and validation of contact dynamics, using an innovative 1DOF HIL testbed which was uniquely designed and built.

1.6 Dissertation Structure

Chapter 2: presents the adopted methodology in this work and the workflow which was followed to achieve the required objectives.

Chapter 3: (Contribution 1) - presents the detailed description of the "Generic HIL Testbed Framework Analysis Tool", as well as the HIL errors (quality control parameters).

Chapter 4: (Contribution 2) - presents the detailed research and investigation of non-linear contact dynamics models. This analysis and investigation allowed to select the most representative contact dynamics model, which was utilized for the software-multibody modeling of the docking scenario under consideration.

Chapter 5: (Contribution 3) - presents the investigation and analysis of a simplified model of the 1DOF HIL testbed, as well as the parametric study that was carried out on the 1DOF model using the "Generic HIL Testbed Framework Analysis Tool", to identify the key-design-parameters. Based on the results and the analysis of HIL model errors, the required figure-of-merits of an actuator were identified.

Chapter 6: (Contribution 4 & 5) - presents the generic 6DOF docking spacecraft model, as well as the model of the 6DOF HIL docking testbed. In this chapter, it was explained in detail how each of the "Docking Model" and "HIL Model" were built. Afterwards, the results of both models' simulation were studied and analyzed.
In addition, an analysis of a docking case-study was presented, which allowed to identify the properties of the successful and the failed docking scenarios of a considered system. Hence, it showed to be a useful example for the analysis of future docking missions.

Chapter 7: (Contribution 6) - presents an expanded parametric study on the 6DOF HIL docking testbed model, which was carried out using the "Generic HIL Testbed Framework Analysis Tool". The results of this study allowed the identification of the preliminary requirements of a 6DOF docking HIL testbed. More importantly, it demonstrated how such parametric studies should be carried out before building a testbed, in order to assist a system engineer to make justified decisions regarding docking HIL testbed implementation.

Chapter 8: (Contribution 7) - presents the detailed explanation of the HIL testbed implementation, the HIL contact dynamics simulation and the experimental HIL results using the introduced one-of-a-kind 1DOF HIL simulation testbed.

Chapter 9: presents the summary of the results of this work, the main conclusions and the future work.

Chapter 2

Methodology

In this chapter, the methodology and the work-flow which were followed to achieve the objectives of this dissertation (presented in Section 1.4) are introduced.

Firstly, in Section 2.1, the design process that was followed to design a HIL testbed is presented. Secondly, in Section 2.2, it is explained why a 1DOF HIL testbed was required. Thirdly, in Section 2.3, the proposed concept of the contact dynamics validation using a 1DOF HIL testbed is presented. The proposed concept was adopted in this work and it showed that the 1DOF HIL testbed is sufficient for the validation of the contact dynamics. Finally, in Section 2.4, the steps of work (i.e., work-flow) which were followed in this work are presented.

2.1 HIL Testbed Design Process

In order to design a docking HIL simulation testbed, some building-blocks are needed to be ready beforehand. Therefore, the design process of the HIL testbed that was proposed and followed, is presented in the proper sequence as follows:

1. **Docking Simulation**
   Firstly, it is required to have a software multibody simulation of the docking scenario of the multiple free-flying spacecraft in space (non-gravitational environment). Thus, a "Docking Model" was created, which models the "Real Docking" scenario that takes place in space between two free-flying S/C, namely: Chaser and Target, see Fig. 2.1. The "Real Docking" was simplified into two main subsystems: Spacecraft (S/C) dynamics in space and the physical impacts that takes place between both S/C during docking. Accordingly, the "Docking Model" was focused mainly on two subsystems: *Spacecraft Dynamics* and *Contact Dynamics*. *Spacecraft Dynamics* subsystem models the physical and dynamical properties of both S/C involved in the dock-

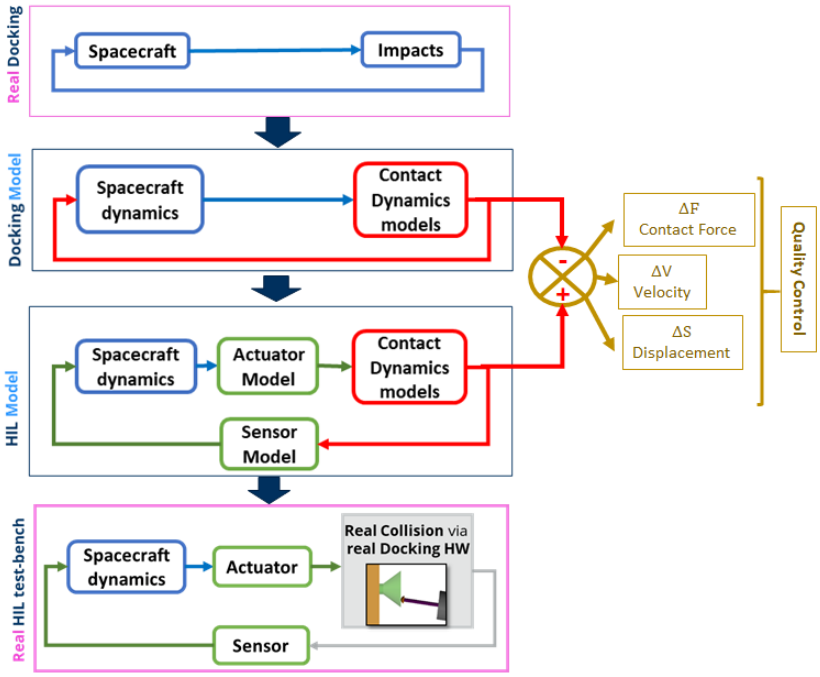

Figure 2.1: HIL Testbed Design Process

ing process. The *Contact Dynamics* subsystem models the physical impact between them.

2. **HIL Model**
   In the second step of HIL testbed design process, a model of the HIL setup was created and was called "HIL Model", where the HIL instruments (e.g., actuator, sensors) were modeled. The objective of the "HIL Model" is to observe and analyze the effects of the HIL instruments dynamics (e.g., total-delays, accuracy) on the HIL simulation and its fidelity. This was done by comparing the results of the "HIL Model" to the "Docking Model" and estimating the relative errors and HIL system's fidelity.

3. **HIL Performance Analysis**
   Third step, a systematic investigation and analysis of the the simulation approach including performance budgeting was carried out, in order to get insight about the key-design-parameters in the HIL design (key-parameter is a parameter in a design-space which has a high sensitivity to the metrics under evaluation). To achieve this, a "Generic HIL Testbed Framework Analysis Tool" was built. It is a parametric study tool which systematically investigates the parameters in the available design-spaces, in order to identify the key-parameters in the HIL testbed design.

4. **Figure-of-Merits Definition**
   Fourth step, based on the results from the "Generic HIL Testbed Framework Analysis Tool" an appropriate HIL testbed design was defined. Accordingly, the required figure-of-merits of the needed hardware were also identified in accordance to the HIL testbed design-requirements.

5. **HIL Setup and Simulation**
   Fifth step, based on the results from the previous step, a "Real HIL testbed" was implemented and adapted (in terms of control capabilities) to the HIL design-requirements. Afterwards, a system stability analysis was carried out and accordingly the docking contact dynamics HIL simulation was carried out and tested.

2.2 1DOF HIL testbed

Before building a complete 6DOF HIL docking simulation testbed, a 1DOF HIL testbed was designed and built, see Fig. 2.2. The design-process defined above is valid for any of the testbeds: 6DOF or 1DOF. The 1DOF HIL testbed is an attractive option as a simpler lower-cost precursor to a 6DOF HIL simulator. It allowed to demonstrate the feasibility and principle performance of the HIL simulation. Most importantly, the 1DOF HIL testbed showed to be sufficient to test and validate the contact dynamics models implemented in the docking simulations, based on the proposed validation concept, which is explained next in Section 2.3.

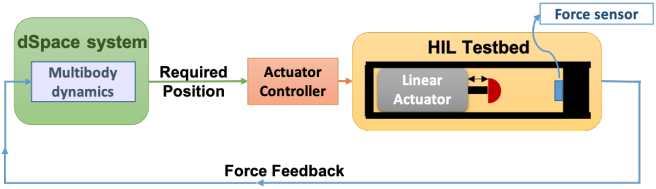

Figure 2.2: 1DOF HIL Concept

2.3 Contact Dynamics Validation Concept

One way to validate the contact dynamics model utilized in the docking simulation was to compare the errors of the *Real HIL* system and the *Simulated HIL* system, in order to investigate whether they were close to each other, see Fig. 2.3. The *Real HIL* and the *Simulated HIL* system are described below.

The *Simulated HIL* system (depicted in Fig. 2.3) predicted the HIL testbed fidelity and errors, by calculating how identical was the modeled HIL testbed "HIL Model" to the modeled ideal docking scenario "Docking Model". The errors in the *Simulated HIL* arose only due to the modeled hardware dynamics (i.e., total-delay, resolution), because these are the only differences between both models. In other words, both "HIL Model" and "Docking Model" had identical *"spacecraft dynamics"* and *"contact dynamics model"* implemented in their systems, while the only difference was the models of the HIL instruments (*"actuator model"*, *"sensor model"*).

On the other hand, the errors and fidelity of the *Real HIL* system were calculated by comparing the "Real HIL testbed" to the modeled ideal docking scenario "Docking Model" (i.e., to identify how identical was the "Real HIL testbed" (real physical testbed) simulation to the modeled ideal docking scenario "Docking Model"), see Fig. 2.3. The errors here arose due to two sources: the dynamics of the real HIL hardware (actuator, sensor) and the accuracy of the contact model utilized in the "Docking Model" (which was the same utilized in the *Simulated HIL*).

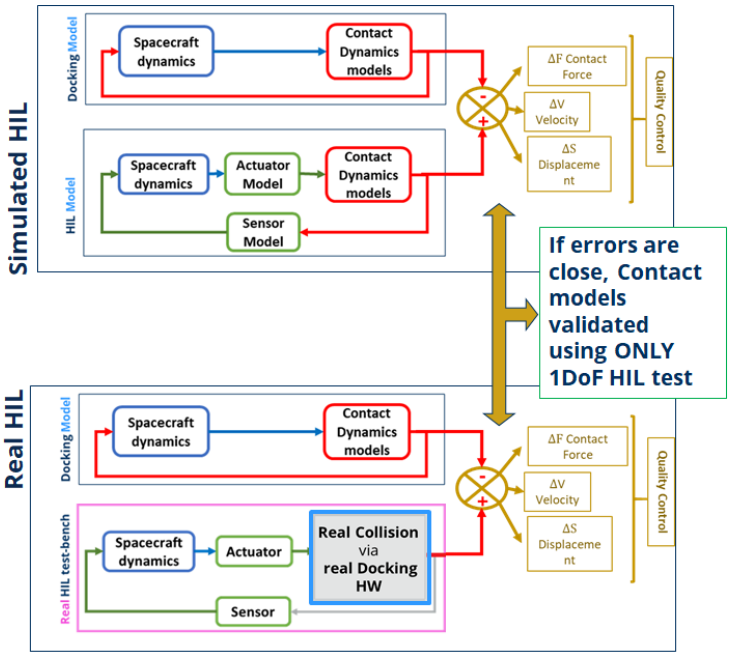

Figure 2.3: Contact Dynamics Validation Concept

It was assumed that the accuracy of the hardware models (*"actuator model"*, *"force sensor model"*) of the real physical hardware (*"actuator"*,

"force sensor") are almost identical. Therefore, the only differences (errors) between the two systems (*Simulated HIL* and *Real HIL*) were the contact dynamics model and the real-physical contact. Based on that, it was concluded that the contact dynamics model is validated, if the results (errors estimations) of the *Real HIL* system are close enough to the *Simulated HIL* system.

2.4 Work-Flow

Based on the description of the methodology and design-process, the following work-flow was followed in this work to achieve the required objectives. The work-flow was divided into four steps, with each step having goals that match the objectives (refer to Section 1.4). Each step was a building block for the following step, in order to finally achieve all the objectives in this work. All these steps used (partially or totally) the parametric study tool (i.e., "Generic HIL Testbed Framework Analysis Tool").

Therefore, the **Main Step** was building the "Generic HIL Testbed Framework Analysis Tool" (presented in Chapter 3). Accordingly, the following four steps were as follows:

1. **First Step**: Analysis and Performance Evaluation of Contact Dynamic Models. (Chapter 4)
   Goal: Find most representative contact dynamics model for the docking system under consideration.

2. **Second Step**: Investigation and Analysis of 1DOF HIL System. (Chapter 5)
   Goals:
   a) Find key-design-parameters of 1DOF HIL model.
   b) Identification of actuator's figure-of-merits.

3. **Third Step**: Investigation and analysis of 6DOF HIL System. (Chapters 6 and 7)
   Goals:
   a) Performance analysis of the docking S/C to define the properties of the successful and the failed docking scenarios.
   b) Find key-design-parameters of 6DOF HIL model.

c) Identify preliminary requirements of a 6DOF HIL testbed for docking simulation (Chapter 7).

4. **Fourth Step**: Experimental 1DOF HIL Simulation Testbed. (Chapter 8)
   Goals:
   a) Proof of proposed contact dynamics validation concept.
   b) Testing and validation of contact dynamics model.

Chapter 3

Generic HIL Testbed Framework Analysis Tool

In this work, a generic HIL-testbed design-framework analysis tool was built, in order to carry out the following: a) performance analysis of docking HIL testbed performance model, b) HIL errors estimation, and c) prediction of systems fidelity and reliability. In addition, this tool facilitates the general mapping from docking scenario parameters to the HIL simulator requirements. Moreover, this generic tool was used for the analysis of docking scenarios for a defined two spacecraft system, allowing the prediction and the identification of the successful and failed docking scenarios and their properties (as shown in the case-study in Section 6.5.1).

Using such a tool would enable a system engineer to make justified decisions, whether a docking testbed is required to be built or not, according to the design requirements of each case. This tool was built in a generic way, so that it can be adapted for any HIL testbed and scenario.

This tool carries out a systematic investigation of all technically possible HIL simulation performances by exploring the available design-spaces. The detailed description of the methodology is presented in Section 3.2.

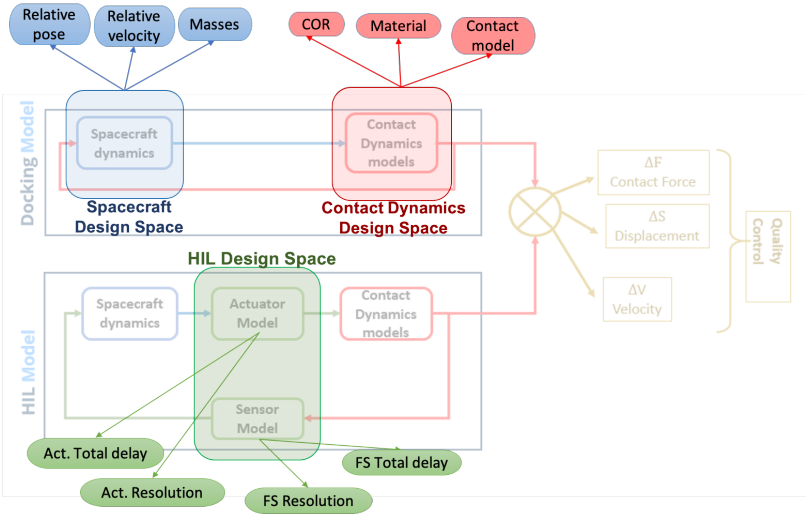

Figure 3.1: Design Spaces

3.1 Tool Objectives

The goals of this tool are the following:

- Find key-design-parameters of each design-space.
- Find the appropriate framework of the HIL design.
- Carry out performance analysis of potential HIL testbed.
- Facilitate general mapping from docking scenario parameters to the HIL testbed design requirements.
- Analyze and identify the successful and failed docking scenarios and their properties.

3.2 Methodology

In order for this tool to carry out a systematic investigation of all the technically possible HIL docking simulation performances, it explored all the available design-spaces modeled in the system, as well as all the parameters

available in each design-space. Meaning, it went through all the range of the identified values of each parameter and repeated the whole simulation every time with a new value from the defined range. In each simulation, the estimated HIL errors between the HIL Model and the Docking Model were calculated.

Three different design-spaces were defined in this tool, namely: Spacecraft, HIL Instruments and Contact Dynamics, see Fig. 3.1. Each design-space had its own parameters, such that the user was allowed to modify their values according to the considered scenario. More importantly, the user was allowed to define the range of each of the key-parameters.

The three design-spaces and their parameters that were defined, are as follows (also see Fig. 3.1 and Fig. 3.2):

1. Spacecraft design-space: it is concerned with the physical and dynamical properties (masses, dimensions, pose (i.e., position and orientation), velocity, etc.) of each of the considered spacecraft. In the considered system, the following parameters could be varied for the docking analysis, as well as the HIL framework analysis: S/C masses, relative velocity and relative pose (i.e., position and orientation).

2. HIL instruments design-space: it is concerned with the properties of the modeled HIL instruments of the system. In the considered system, two instruments were modeled: robotic hardware (e.g., actuator) and sensor (e.g., force or force/torque). Two main parameters were defined for each modeled instrument: total-delay and resolution.

3. Contact dynamics design-space: it is concerned with the contact dynamic modeling. In the considered system, three main parameters were examined in the docking analysis and the HIL framework analysis, which are: material of the impacting bodies, contact model and Coefficient-of-Restitution (COR).

After carrying out systematic investigation of the available design-spaces, the error-percentage and system fidelity of the modeled HIL system in comparison to the modeled ideal system were estimated based on various defined quality-control parameters and errors.

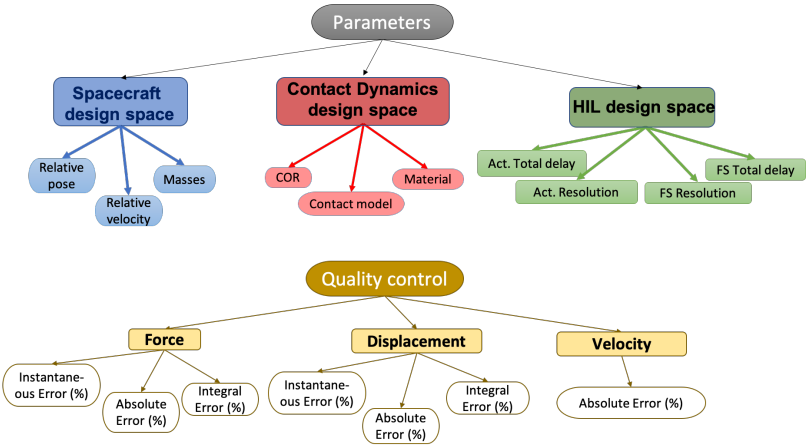

Figure 3.2: HIL Framework Analysis

3.3 Quality Control and Errors

Many errors were defined in this tool, in order to analyze the system under consideration in the most detailed way. The main three aspects considered as quality control factors are: force, displacement and velocity. Some further aspects were considered as well for detailed insight and analysis, which are: energy analysis and contact duration.

3.3.1 Overview

In this section, the HIL errors and their calculation methods are presented. The HIL errors are important factors in the parametric study because they are considered as the quality control factor. HIL errors assist to identify the correct actuator requirements and eventually define the required figure-of-merits.

There are different types of HIL errors that were defined, through which the fidelity of the HIL testbed could be defined with respect to the ideal (no delays) non-linear physical model. The errors are defined as follows:

1. Force error:
    a) Max. instantaneous error $(e_{Imax})^+$

   b) Max. HIL error (e_{Hmax})*
   c) Max. absolute error (e_{abs})*
   d) Modulus HIL integral error ($e_{H_{int}}$)*
   e) Modulus absolute integral error ($e_{A_{int}}$)*$^{+}$

2. Displacement error:
   a) Max. instantaneous error (e_{Imax})$^{+}$
   b) Max. HIL error (e_{Hmax})*
   c) Max. absolute error (e_{abs})*
   d) Modulus HIL integral error ($e_{H_{int}}$)*
   e) Modulus absolute integral error ($e_{A_{int}}$)*$^{+}$

3. Velocity error*$^{+}$

4. Extras:
   a) Energy errors
   b) Contact duration

Some of the defined errors were utilized to analyze the 6DOF HIL docking model (marked with *), others were used for the 1DOF HIL docking system (marked with $^{+}$) or for both. Beside the 6DOF and 1DOF grouping, some errors were mainly useful for the HIL quality analysis, while others were useful for contact dynamics analysis.
Different calculation methods have been utilized in order to take into consideration different error natures. These methods are:

1. Instantaneous error:
   instantaneous difference between the HIL model and the Ideal model.

2. Absolute error:
   difference between peak of each curve independent of time.

3. Integral error:
   difference between the modulus area-under-the-curve of the HIL model and the Ideal model.

3.3.2 Errors Description

For a better understanding, the elements in the error's equations below are depicted in Figure 3.3

1. **Instantaneous errors**

   a) Max. Instantaneous error percentage (e_{Imax}) (1DOF):

   $$e_{Imax} = \frac{e_i(t_m)}{\hat{I}(t_m)} \cdot 100 = \frac{max[e_i(t)]}{\hat{I}(t_m)} \cdot 100 = \frac{max[\hat{H}(t) - \hat{I}(t)]}{\hat{I}(t_m)} \cdot 100 \tag{3.1}$$

   $e_i(t_m)$ is the max. value of instantaneous error during simulation, $\hat{H}$ is the HIL model and $\hat{I}$ is the Ideal docking model. t_m is the time-step at which the max. instantaneous error took place.

   b) Max. HIL error percentage (e_{Hmax}) (6DOF):

   $$e_{Hmax} = \frac{e_i(t_m)}{\hat{I}_{max}} \cdot 100 = \frac{max[\hat{H}(t) - \hat{I}(t)]}{\hat{I}_{max}} \cdot 100 \tag{3.2}$$

   $e_i(t_m)$ is the max. value of the instantaneous error during simulation, $\hat{I}_{max}$ is the peak of the Ideal model and $\hat{H}$ is the HIL model.

2. **Max. absolute errors(e_{abs})** (6DOF):

   $$e_{abs} = \frac{\hat{H}_{max} - \hat{I}_{max}}{\hat{I}_{max}} \cdot 100 \tag{3.3}$$

   e_{abs} is the difference between the peak values of each model (in percentage) with respect to (w.r.t) the Ideal model, $\hat{H}_{max}$ is the peak of the HIL curve and $\hat{I}_{max}$ is the peak of the Ideal curve.

3. **Integral errors**

   a) Modulus absolute integral error ($e_{A_{int}}$) (6DOF):
   It is the difference between the integral (i.e., area under the curve) of the modulus curve of each of the models independently (in percentage) w.r.t. the Ideal model. The error is calculated as

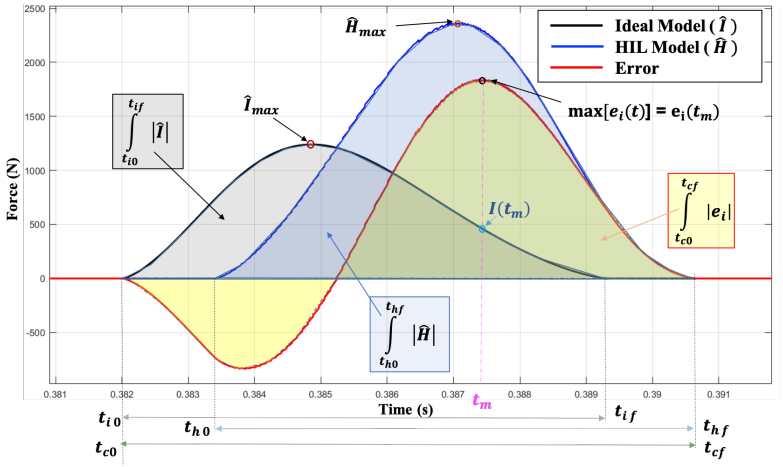

Figure 3.3: HIL Errors Illustration

follows:

$$e_{A_{int}} = \frac{\int_{t_{h0}}^{t_{hf}} |\hat{H}| - \int_{t_{i0}}^{t_{if}} |\hat{I}|}{\int_{t_{i0}}^{t_{if}} |\hat{I}|} \cdot 100 \tag{3.4}$$

t_{i0} is the time at the beginning of contact of the Ideal model and t_{if} is at the end of the contact. t_{h0} and t_{hf} are the time at the beginning and the end of the contact of the HIL model, respectively. (See Fig. 3.3 for illustration)

b) Modulus HIL integral error ($e_{H_{int}}$) (1DOF & 6DOF):
It is the difference between the integral (i.e., area under the curve) of the modulus of the instantaneous-error-curve (in percentage) w.r.t. the Ideal model. . Error is calculated as follows:

$$e_{H_{int}} = \frac{\int_{t_{c0}}^{t_{cf}} |e_i|}{\int_{t_{i0}}^{t_{if}} |\hat{I}|} \cdot 100 \tag{3.5}$$

t_{c0} is the beginning of the combined time range and t_{cf} is at the end of it. t_c (which is used for the integral time-interval) is

the combined range of the contact times of both models (HIL and Ideal), see Fig. 3.3 for illustration. t_{i0} is the time at the beginning of contact of the Ideal model and t_{if} is at the end of the contact.

4. **Velocity error (e_v)** (1DOF & 6DOF)
   The velocity error magnitude is the difference of the velocity-after-impact between the HIL model and the Ideal model, as follows:

   $$e_{v_{mag}} = v_h(t_{hf}) - v_i(t_{if}) \tag{3.6}$$

   Accordingly, the velocity error percentage is the velocity error magnitude in percentage of the Ideal-model velocity-after-impact, as follows:

   $$e_v = \frac{e_{v_{mag}}}{v_i(t_{if})} \cdot 100 \tag{3.7}$$

5. **Energy errors**
   The energy error is the difference in the energy between the HIL model and the Ideal model. This is valid for total-energy-balance, total mechanical-energy and its aspects: kinetic and potential energy.

6. **Contact Time Duration ($\Delta T_{contact}$)**
   This is the difference between the contact duration of the HIL model versus the Ideal model:

   $$\Delta T_{contact} = [t_{hf} - t_{h0}] - [t_{if} - t_{i0}] \tag{3.8}$$

Chapter 4

Contact Dynamics

In this chapter, the contact dynamics research that was carried out within this work is presented. The main goal of this chapter is to select the most representative contact model to be implemented in the docking modeling.

Firstly, in Section 4.1, the background of contact modeling and its application in space technology are introduced. Secondly, in Section 4.2, a brief description of a contact model is presented. Thirdly, in Section 4.3 various contact models, as well as the state-of-the-art considered in this work are presented. Fourthly, in Section 4.4, the investigations and analysis of the various considered contact models are presented. Finally, in Section 4.5, the most representative contact model for this work is selected, based on the results from the investigations and analysis.

4.1 Background

Physical contact (impact) is a phenomena that takes place on a regular basis in our daily lives. Modeling of the physical contact is a topic of continuous research, due to the fact that its applications are quite broad, such as, automotive, robotics, space, multibody dynamics, etc. The availability of powerful computer hardware, as well as reliable software simulations programs has made it possible to perform realistic simulations of different contact scenarios. Many contact models have been introduced for an improved contact modeling, however there is always room for improvement for a more realistic contact modeling and validated results.

Contact Modeling for Space Applications Impact in space applications in particular is quite important. As the properties of the space environment are quite different to that on earth, the need to simulate the multibody interactions with high reliability before realizing them in space is critical. Special Purpose Dexterous Manipulator (SPDM) is a two armed robot on

the International Space Station (ISS), which is designed to handle the replacement of the "On-orbit Replaceable Units" on the ISS. Before SPDM, the astronauts were required to carry this out by themselves, by performing a spacewalk. Such critical tasks carried out by this manipulator in space, require proper tests and validation beforehand, which certainly requires reliable modeling, in particular contact modeling.

In the considered docking application, contact force modeling is required to estimate the force generated, when the two spacecraft undergoing docking come in contact with each other. The more realistic the used contact model is, the more reliable the docking simulations are. Eventually, the goal of the docking simulation is to know if docking will be successful or not and accordingly the design engineer can adapt the spacecraft design, as well as define the properties of the worst case docking-scenario.

Of course, Finite Element Method (FEM) presents a very detailed analysis for impacts. However, it requires large computational efforts. Therefore, contact models have to be incorporated in a (lower time-effort and lower computational-effort) multibody simulation system that uses ODE solvers. This allows the simulation of the different multibody docking scenarios in a relatively faster way.

Historical Background The first relations between impacting bodies have been introduced by Merci in 1639. In 1669, Huygens found that in elastic impacts, normal velocities before and after impact is equal in magnitude, but opposite in direction. Newton extended this kinematic relation in 1686 by deriving experimentally the concept of coefficient-of-restitution, in which he proposed the impact hypothesis considering the loss of the kinetic energy. In 1738, Euler expressed the impact process between two elastic bodies in terms of a mass-less spring, as a continuous process. Then, in 1835 Poisson divided the impact process into two phases: compression and restitution. He proposed that contact in the two different phases can by related by a coefficient-of-restitution. In 1882, Hertz introduced his contact model, which has been the foundation for most of the following work in the field of contact modeling. He described the elastic normal contact as a quasi-static process, where he managed to relate the contact force generated to the normal displacement between the impacting bodies. His resulting approach presents a stiffness coefficient that depends mainly on the geometrical and material properties of the colliding bodies. [Gonthier, 2007]

Elastic vs Dissipative Contact models Most of the contact models mentioned before, including Hertz model, assumed the contact process as an elastic process, i.e., total energy of the system is equal before and after impact. Although, Hertz model is without doubt considered as an achievement in the contact modeling research due to its reliability and simplicity, it is clear that it is neglecting a big factor of what happens in real life during a collision, due to the elasticity assumption. Therefore, other models have been proposed based on Hertz models that included a damping term, which is responsible for the dissipation of energy during impact.

Point Contact Model In this work, mainly point contact models have been considered. Point contact model assumes that the contact occurs only at a mutual point on each body, where they are aligned with normal line-of-action between the two contacting bodies. The point contact model is effective in the case that the two contact surfaces are smooth surfaces (no irregularities), e.g., sphere and flat plane. As the considered application is mainly concerned with a half sphere (probe) and a plane (internal surface of the drogue), the point contact model is utilized in this work. For more complicated applications with irregular body surfaces, other volumetric contact models can be implemented, such as [Gonthier et al., 2004].

In the following sections, the literature review and the state-of-the-art of contact models are presented. These contact models, in particular dissipative models, have been studied, analyzed and compared to Hertz model. Some of the research and analysis in the next sections have been preliminary introduced by my supervised student "Matthias Kraft" [Kraft, 2016].

4.2 Contact Model Description

In a simulation, when two bodies are undergoing contact, various parameters are required for the description of the interaction. Some of these parameters that describe contact are time variant (i.e., change over time during simulation). While other parameters are constant, which describe contact properties, or the physical description of impacting bodies, e.g., material, or masses, or shapes, etc. In this section, some of the most commonly used parameters in the considered contact models are introduced. Namely,

a. Penetration-depth.

b. Relative normal-velocity.

c. Coefficient-Of-Restitution.

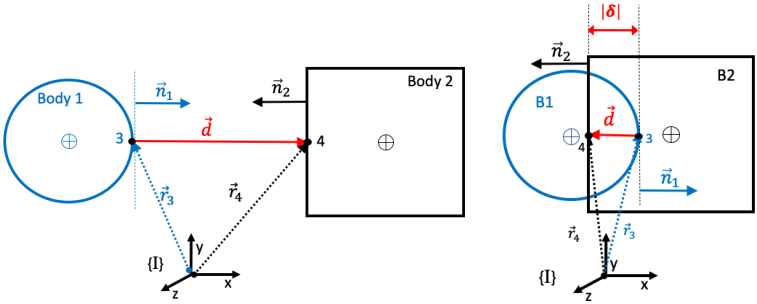

(a) No contact **(b)** During Contact

Figure 4.1: Penetration depth illustration on a sphere and a cube

The possible motion of both rigid-bodies during the impact simulation is dependent on the force calculated based on the contact model. Accordingly, the force calculation is dependent mainly on penetration-depth, as well as penetration-velocity (in case of dissipative contact models).

4.2.1 Penetration-depth (δ)

The penetration-depth (also known as indentation-depth) is an important parameter in all the contact models considered in this work. It is the distance that the two impacting bodies have penetrated (deformed) into each other. It is described as the maximal normal-distance between the two contacting surfaces that lies within the intersecting un-deformed volume. As the contact in rigid multibody simulation is generally described with un-deformed shapes of the bodies, the information of the bodies' deformation and reaction-force is therefore included in the contact model.

The displacement vector $\mathbf{d}$ from which the penetration-depth is computed, is parallel to the normal of the contacting surfaces of both bodies, $\hat{\mathbf{n}}_1$, $\hat{\mathbf{n}}_2$, as depicted in Fig. 4.1. It is described as follows:

$$\mathbf{d} = \mathbf{r}_4 - \mathbf{r}_3 \tag{4.1}$$

such that $\mathbf{r}_3$ and $\mathbf{r}_4$ represents the displacement vectors of the contact points on the sphere and cube's surface, respectively, with respect to the inertial

frame I. Accordingly, the penetration-depth is computed as follows:

$$\delta = \mathbf{n}_2 \cdot \mathbf{d} = \mathbf{n}_2 \cdot (\mathbf{r}_4 - \mathbf{r}_3) \tag{4.2}$$

During contact (when bodies volumes are overlapping), penetration-depth is positive and state of multibody is "in contact". Normally, in force calculation (using the contact model), the absolute value of the penetration-depth is used. Nevertheless, the sign of the penetration-depth is made use of in software models. When the penetration-depth is negative, the contact state is zero (i.e., not in contact). Accordingly, the force is always zero. Once the penetration depth is more than or equal to zero, the contact state turns to one (i.e., in contact) and contact model is activated. Thus, the contact force is calculated.

4.2.2 Penetration Velocity ($\dot{\delta}$)

The relative penetration velocity is described as:

$$\dot{\delta} = \frac{d}{dt}(\delta)$$

4.2.3 Coefficient-of-Restitution (c_r)

Coefficient-Of-Restitution (COR) is a dimensionless variable which provides information about the total energy dissipation in an impact. Newton and Poisson have researched this component differently. On one hand, Newton introduced the COR form, by comparing the relative velocity of the two contacting bodies before impact $\dot{\delta}_i$, to the one after impact $\dot{\delta}_f$. On the other hand, Poisson divided the impact into two phases; compression and restitution and studied the normal forces in each phase. However, Newton's model has been generally accepted and is used as the common way to define the COR, as follows:

$$c_r = -\frac{\dot{\delta}_f}{\dot{\delta}_i} \tag{4.3}$$

COR depends on many boundary conditions, such as, the material pairing, initial impact velocity, geometry of the colliding bodies. Goldsmith [Goldsmith, 1960] has carried out different experiments with different materials, in order to find an approximation for the form of the COR. According to his experiments, he proposed the following form:

$$c_r \approx 1 - \alpha \dot{\delta}_i \tag{4.4}$$

such that α is an empirical material parameter that is obtained from a linear fit of the experimental data for the COR, as a function of impact velocity. Goldsmith states that α is in the range of 0.08 - 0.32 s/m, for materials of steel, bronze, ivory. However, [Herbert and McWhannell, 1977] mentioned in their work, that Eq. 4.4 exhibits considerable errors at lower velocities (< 0.3 m/s). For such velocities, they suggested the following form using a best-fit curve to the experimental results from [Goldsmith, 1960]:

$$c_r \approx 1 - 0.026 \cdot \dot{\delta}_i^{\frac{1}{3}} \tag{4.5}$$

However, neither the validation of such formula, nor the exact formula for the COR for low initial impact velocities (< 0.1 m/s) could be explicitly found. Therefore, the COR is considered as an independent variable within this work, as there was not exact information found for the α of the materials considered. In most of the simulations within this work the COR value was selected to be 0.8, because it was observed that for low impact velocities (< 0.1 m/s) of non-elastics materials, the COR values tends to be higher than 0.8. Therefore, the boundary value (0.8) was selected.

4.3 State-of-the-art

In this section, all the contact models that have been considered and studied in this work are presented. Firstly, the Hertz elastic contact model is presented, then the dissipative linear and non-linear contact models are followed.

Hertz Model Hertz's work on contact mechanics that was written in 1882, was the first published work that focused on contact mechanics [Hertz, 1882]. Hertz stated that the force F generated between two contacting spheres is directly related to the local deformation (indentation) between them. His work laid a foundation for most of the forthcoming contact models, to model the elastic behavior of the contacting bodies. His model is as follows:

$$F = k\delta^n \tag{4.6}$$

where the relative local indentation δ is what was described earlier as the penetration-depth. n is a parameter related to the shapes of the contacting

bodies. Moreover, k is the stiffness parameter that depends on the material and radii of both spheres, as follows:

$$k = \frac{4}{3} \cdot E^* \sqrt{R^*} \tag{4.7}$$

where E^* is the combined Young's modulus and R^* is the combined radius of both spheres. They are both given by:

$$E^* = (\frac{1-\nu_1^2}{E_1} + \frac{1-\nu_2^2}{E_2})^{-1} \tag{4.8}$$

such that ν_1 and E_1 represent the Poisson's ratio and the modulus of elasticity of first body, respectively. The same applies for the second body ν_2 and E_2. Moreover, the combined radius is represented as following:

$$R^* = (\frac{1}{R_1} + \frac{1}{R_2})^{-1} \tag{4.9}$$

such that R_i is the radius of curvature of each body. In case of a flat surface, it would be ∞.

Although Hertz model worked well in a case of quasi-static contact, it did not consider any energy dissipation. In dynamic collisions, energy dissipation plays an important role in the contact process, that is why it needs to be considered in the contact models.

Kelvin-Voigt Model (K&V) Kelvin-Voigt presented a simple contact model (known as spring-dashpot model), which consists of a linear spring model and a linear viscous damping. The stiffness component is based on Hertz stiffness. Additionally, linear damping was added to model energy dissipation. [Goldsmith, 1960], [Hunt and Crossley, 1975]. The model is as follows:

$$F = k\delta + b\dot{\delta} \tag{4.10}$$

where b is the damping coefficient and $\dot{\delta}$ is the instantaneous penetration velocity. Due to the simplicity of the model, it has been utilized in different applications, such as the docking HIL simulation by [Zebenay et al., 2015]. However, this contact model had some drawbacks which were analyzed by Hunt and Crossley [Hunt and Crossley, 1975]. These drawbacks are visualized in Fig. 4.2a and are as follows:

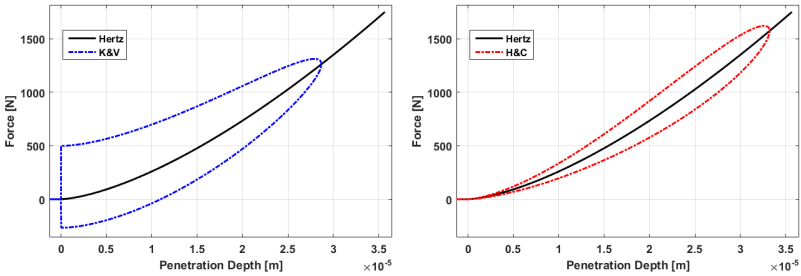

(a) Kelvin-Voigt **(b)** Hunt-Crossley

Figure 4.2: Hysteresis damping (Force vs Penetration-depth) of Hunt-Crossley model overcame the drawbacks of Kelvin-Voigt model

1. The contact force at the beginning of the collision was not equal to zero and appeared as a shock effect. This is mainly due to the linear damping term $b\dot{\delta}$, as it depends mainly on the velocity component.

2. Moreover, at the end of the collision, when the two bodies are separating, there is a negative force that appears, representing a tensile force. This of course does not make sense from the physical point of view, because the bodies can not attract each other during the collision.

Hunt and Crossley Model (H&C) After Hunt and Crossley analyzed the Kelvin-Voigt model and defined its drawbacks, they claimed that the damping term has to be proportional to the power of the spring force (e.g., stiffness coefficient). Therefore, they introduced in 1975 a new model [Hunt and Crossley, 1975], which overcame the previously mentioned drawbacks of the Kelvin-Voigt model, as shown in Fig.4.2. Their new model is basically a combination of Hertz law, combined with a new non-linear damping term. The non-linear damping term introduced by Hunt and Crossley is related to the stiffness coefficient (as well as the penetration depth). Their model is expressed as follows:

$$F = k\delta^n + \lambda\delta^n\dot{\delta} \tag{4.11}$$

such that λ is called a hysteresis damping factor and is expressed as following:

$$\lambda = \frac{3}{2}(1 - c_r)\frac{k}{\dot{\delta}_i} \tag{4.12}$$

where k is the Hertzian stiffness expressed in Eq. 4.7, $\dot{\delta}_i$ is the initial impact velocity and c_r is the coefficient-of-restitution which is introduced in Section 4.2.3.

The Hunt-Crossley model [Hunt and Crossley, 1975] is quite simple, efficient and fast due to the little computational effort required to evaluate the force, the penetration depth and the penetration velocity. Moreover, the model is continuous in its velocities and accelerations, which is useful for the numerical integrator in a multibody simulation. In addition, it can be noticed in the hysteresis loop of Hunt-Crossley model that the compression and restitution phases are not equal, which depicts in a clearer way the physical nature of the collision. Moreover, the contact model indeed overcame the two drawbacks of the Kelvin-Voigt model.

Due to the simplicity of Hunt-Crossley model and how straight forward it is for implementation, many researchers have implemented it in their work, such as [Guess et al., 2010]. Moreover, many researchers have used this model as a basis for expanding their work and creating new models. In the next sections, some of these models are discussed. Consequently, all the next models that are studied in this work, have the same form of Hunt-Crossley model as in Eq. 4.11, while each model introduces a different hysteresis damping factor λ.

Herbert and McWhannel Model (H&M) Herbert and McWhannel [Herbert and McWhannell, 1977] created this model, by combining the Hunt-Crossley model with the equations of motion of the impacting bodies. After analyzing the impact between two bodies and its relation to the surface characteristics function, which is represented by a power series, they proposed a new hysteresis damping coefficient in 1977, as follows:

$$\lambda = \frac{6(1 - c_r)}{(2c_r - 1)^2 + 3} \cdot \frac{k}{\dot{\delta}_i} \tag{4.13}$$

and normal contact force:

$$F = k\delta^n \left[1 + \frac{6(1-c_r)}{(2c_r-1)^2+3} \cdot \frac{\dot{\delta}}{\dot{\delta}_i}\right] \tag{4.14}$$

In comparison to Hunt-Crossley model, it was observed that the hysteresis damping term is relatively higher. Moreover, the area inside their hysteresis loop area is relatively bigger, which means more energy losses, hence lower post impact velocity.

Lee and Wang Model (L&W) In 1983, Lee and Wang proposed a new contact model [Lee and A. C. Wang, 1983], which looks similar to Hunt-Crossley model. While developing their model, they were quite careful to fulfill the condition that the damping force is zero at the very beginning of the contact and at the maximum penetration. Their hysteresis damping coefficient is expressed as follows:

$$\lambda = \frac{3}{4}(1-c_r)\frac{k}{\dot{\delta}_i} \tag{4.15}$$

and when it is implemented in the normal force equation, it is expressed as follows:

$$F = k\delta^n \left[1 + \frac{3}{4}(1-c_r)\frac{\dot{\delta}}{\dot{\delta}_i}\right] \tag{4.16}$$

From their model, it was noticed that the damping coefficient has a relatively lower value than the other studied dissipative models. Therefore, the energy dissipation during a collision (in comparison to previous models) is smaller, which leads to a relatively higher contact force value during the same simulated impact scenario of the other studied models.

Lankrani and Nikravesh Model (L&N) Lankrani and Nikravesh proposed a new contact model in 1990, [H. M. Lankarani and P. E. Nikravesh, 1990] which is also based on Hunt-Crossley model. The contact model has been used frequently in many multibody dynamics with impact simulation. It is one of the famous contact models that has been implemented in different applications. In this model, Lankrani and Nikravesh formed a new expression for the hysteresis damping coefficient based on the work-energy principle. They found a relation between the total energy dissipation and the kinetic energy losses of the impacting bodies. They managed to formulate the total energy dissipation in terms of the coefficient-of-restitution as well as

the initial impact velocity. Finally, they formulated an expression for the hysteresis damping factor as follows:

$$\lambda = \frac{3}{4}(1 - {c_r}^2)\frac{k}{\dot{\delta}_i} \tag{4.17}$$

Consequently, the normal contact force is expressed as:

$$F = k\delta^n \left[1 + \frac{3}{4}(1 - {c_r}^2)\frac{\dot{\delta}}{\dot{\delta}_i}\right] \tag{4.18}$$

This contact model has been very reasonable and it has been implemented by different researchers, e.g., [Pereira et al., 2010], [Wasfy and Noor, 2003]. In general, this model showed good results, especially for general mechanical impacts, where the total energy dissipation is small. According to [Goldsmith, 1960], this model would be valid for coefficient-of-restitution values that are close to unity. However, as it was already mentioned in their original work, the error in the coefficient-of-restitution increases as the projected coefficient-of-restitution decreases. Therefore, Lankarani and Nikravesh updated their model, to account for plastic deformations at high impact velocities, [Hamid M. Lankarani and Parviz E. Nikravesh, 1994].

Gonthier Model (Go) As mentioned earlier, all the previously introduced models are point contact models and based on Hertz model. In 2007, Gonthier proposed a new contact model [Gonthier, 2007], which is based on a modified Winkler elastic foundation with volumetric stiffness. This volumetric model was developed for the contact simulations of robotic tasks with low velocities. In addition, his model is supposed to satisfy the real-time simulation requirements, e.g., small computational effort.
Using the following equation of the relative motion:

$$m\ddot{\delta} + \delta^n(k + \lambda\dot{\delta}) = m\ddot{\delta} + k\delta^n(1 + a\dot{\delta}) = 0 \tag{4.19}$$

one could find a relationship between the coefficient-of-restitution and the damping coefficient. Therefore, Gonthier introduced a dimensionless factor

$$d = ac_r\dot{\delta}_i = \frac{\lambda}{k}c_r\dot{\delta}_i \tag{4.20}$$

By integrating Eq. 4.19 and substituting it in Eq. 4.20, he got:

$$\frac{1+\frac{d}{c_r}}{1-d} = e^{d(1+\frac{1}{c_r})} \tag{4.21}$$

which can be solved numerically. Additionally, he approximated it to the following:

$$d \approx 1 - {c_r}^2 \tag{4.22}$$

accordingly, he expressed his approximated contact model as follows:

$$F = k\delta^n \left[1 + \frac{1-{c_r}^2}{c_r}\frac{\dot{\delta}}{\dot{\delta}_i}\right] \tag{4.23}$$

By analyzing this model, in case of elastic and inelastic collision, the damping coefficient showed to be quite reasonable. From Eq. 4.20, in case of a perfectly inelastic collision ($c_r = 0$) the damping coefficient (λ) is infinite. While in a perfectly elastic collision ($c_r = 1$), the damping coefficient is zero. This observation makes sense physically.

Another comparison is the high and low coefficient-of-restitution's values. For high values of c_r, the compression and restitution phases showed to be symmetrical, meaning that the energy dissipation was almost the same during compression and restitution. For low values of c_r, most of the energy dissipation took place during the compression phase, hence the hysteresis loop was non-symmetric.

Because this is a volumetric contact model, there is a difficulty that arises in finding the volumetric stiffness coefficient value.

Zihing and Qishao Model (Z&Q) In 2006, the Chinese researchers, Zihing and Qishao, published in their own language a new contact model, which aimed to find a relation between coefficient-of-restitution and energy dissipation throughout the contact. Their model is observed to produce realistic results for a great range of coefficient-of-restitution. They proposed the following damping coefficient:

$$\lambda = \frac{3}{4}(1-{c_r}^2)e^{2(1-c_r)}\frac{k}{\dot{\delta}_i} \tag{4.24}$$

Such that the normal contact force equation is expressed as:

$$F = k\delta^n \left[1 + \frac{3}{4}(1 - {c_r}^2)e^{2(1-c_r)}\frac{\dot{\delta}}{\dot{\delta}_i}\right] \tag{4.25}$$

Flores et al. Model (FL) Flores published a more recent point contact model, which is based on Hertz theory, along with a hysteresis damping coefficient for energy dissipation [Flores et al., 2011]. In his work, he separated the energy dissipation due to the contact into, losses during compression and losses during restitution. Hence, he expressed the total energy dissipation using an integral that could be computed only numerically, leading to the following expression:

$$\Delta E = \frac{1}{4}\lambda\big(\dot{\delta_f} + |\dot{\delta_i}|\big)\delta_{max}^{\frac{5}{2}} \tag{4.26}$$

such that δ_{max} is the maximum indentation throughout the whole contact process. $\dot{\delta_i}$ and $\dot{\delta_f}$ are initial impact velocity and velocity at separation, respectively. Using the above information, the energy balance is expressed in combination to the linear momentum balance, yielding the following expression of the hysteresis damping factor:

$$\lambda = \frac{8}{5} \cdot \frac{1 - c_r}{c_r} \cdot \frac{k}{\dot{\delta}_i} \tag{4.27}$$

which leads to the following normal contact force expression:

$$F = k\delta^n \left[1 + \frac{8}{5} \cdot \frac{1 - c_r}{c_r} \cdot \frac{\dot{\delta}}{\dot{\delta}_i}\right] \tag{4.28}$$

Flores contact model is supposed to be mainly valid for situations where elastic and inelastic materials are contacting each other, in which the outcome of his work showed similar results to what was obtained from Gonthier's volumetric model. Moreover, this model is supposed to be valid for impacts of soft materials (high energy losses). Flores showed in his work that the realized coefficient-of-restitution is very close to the projected one, which is a good indication of the model validity. More analysis of this model has been presented by Flores also in [Machado et al., 2012].

4.4 Simulation and Results

As mentioned in the previous sections, the behavior of the non-linear contact model depends on various parameters, such as, the Hertzian stiffness (k) value which depends on the used material, as it is a function of the Young's modulus (E) and the Poisson's ratio (ν). In addition, the contact model behavior depends on the hysteresis damping factor (λ), which depends on the coefficient-of-restitution (c_r), initial impact velocity ($\dot{\delta}_i$) and the Hertzian stiffness (k). Therefore, in this section, a parametric study is presented, which was carried out in order to analyze the dependency of the non-linear contact models on such parameters. Most importantly, this parametric study assisted to select of the most representative non-linear contact model that was implemented in the considered docking system.

In order to carry out this parametric study, a simulation of two rigid bodies impacting each other in 1DOF was modeled, see Fig. 4.3. The simulation was repeated multiple times and each time one of the studied parameters (e.g., contact model, impact velocity, material type and coefficient-of-restitution) was varied. Accordingly, the results were studied and analyzed.

4.4.1 Simulation Model

In order to simulate the impact between two rigid-bodies in 1DOF, a simple mathematical multibody system was modeled, which was implemented and simulated in Simulink®, Matlab®.

The simulation model (Fig. 4.3b) consists of two subsystems: "*multibody dynamics*" and the "*contact model*". "*Multibody dynamics*" subsystem models the physical and dynamic properties of each rigid body and calculates the position and the velocity of each body due to any external forces acting on them. This subsystem provides as outputs the relative-displacement (δ) and the relative-velocity ($\dot{\delta}$) between both bodies to the "*contact model*" subsystem. The "*contact model*" subsystem calculates the magnitude of the continuous force generated when the two rigid bodies are in contact with each other and feeds it back to the *Multibody dynamics* to calculate the position and the velocity in each time-step.

The Equation-Of-Motion (EOM) of each of the rigid bodies in 1DOF are presented in Eq. 4.29. As these are rigid-bodies, the acceleration, velocity and displacement of any reference frame of the rigid-body, are the same as

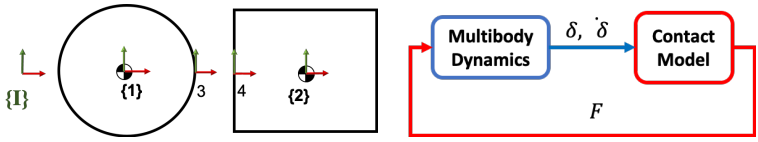

(a) Schematic of two rigid-bodies

(b) Simulink® Model

Figure 4.3: Left figure shows the two rigid impacting bodies (Sphere and Cube). Right figure shows the block-diagram of the model

its Center-Of-Mass (COM). The EOMs are as follows:

$$\ddot{x}_3(t) = \frac{F_3(t)}{m_1}, \qquad \ddot{x}_4(t) = \frac{F_4(t)}{m_2} \tag{4.29}$$

$$\dot{x}_3(t) = \int \ddot{x}_3(t)dt + \dot{x}_3(0), \qquad \dot{x}_4(t) = \int \ddot{x}_4(t)dt + \dot{x}_4(0)$$

$$x_3(t) = \int \dot{x}_3(t)dt + x_3(0), \qquad x_4(t) = \int \dot{x}_4(t)dt + x_4(0)$$

$$\delta = x_3(t) - x_4(t) \tag{4.30}$$

$$\dot{\delta} = \dot{x_3}(t) - \dot{x_4}(t) \tag{4.31}$$

such that m_1 and m_2 are the masses of each rigid-body, respectively. F is the external contact force applied on each body during impact. $\ddot{x}(t)$, $\dot{x}(t)$, $x(t)$ are the acceleration, velocity and displacement of the rigid-body respectively. In addition, δ is the relative-displacement (i.e., penetration-depth) and $\dot{\delta}$ is the relative-velocity (i.e., penetration-velocity).

4.4.2 Simulation Properties

This simulation was carried out using Simulink®, Matlab® 2015b and used ode45 solver with a variable time-step and a maximum time-step of $1\mu s$. The parameters of the simulation were defined as shown in Table 4.1, unless any of these parameters is explicitly mentioned to have a different value. In addition, initial acceleration of both rigid bodies was set to zero. Initial displacements and initial velocities were set based on the required initial impact velocity.

Table 4.1: Contact Models Simulation Parameters

m_1, kg	m_2, kg	$\dot{\delta}_o$, m/s	COR	Material
10	10	0.1	0.8	steel

4.4.3 Results

The results in this section have been published before by the author [Bondoky et al., 2017a]. Therefore, this section is quoted directly from the publication.

4.4.3.1 Impact velocity

" In this test, we vary the initial impact velocity from $10 - 150$ *mm/s for all the nonlinear contact models considered. In Fig. 4.4, we notice that the magnitude of the maximum contact force generated is directly proportional to the impact velocity. However, the differences between the different contact models is relatively small. This difference tends to increase though, as the impact velocity increases, but differences are not big.*
Therefore, for any selected material and according to the velocity range of the test, the magnitude of the initial impact velocity affects the maximum contact force. Whereas the differences observed at the maximum force generated with different nonlinear contact models is not significant.

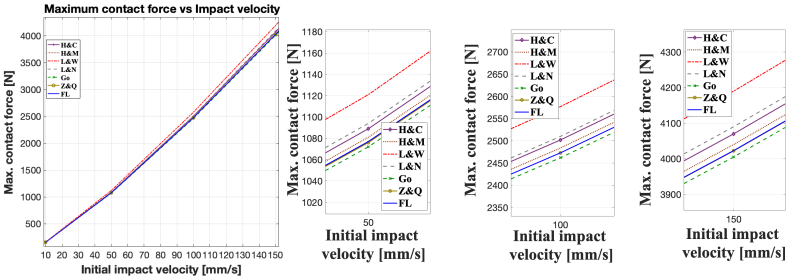

(a) Overview **(b)** $\dot{\delta}_o$=50mm/s **(c)** $\dot{\delta}_o$=100mm/s **(d)** $\dot{\delta}_o$=150mm/s

Figure 4.4: Results of contact models at different impact velocities for steel [Bondoky et al., 2017a]

4.4.3.2 Material

In this test, we vary the material type of the contacting bodies. The material type directly affects the value of the Hertzian stiffness (k) and accordingly, the hysteresis damping value (λ) is also changed. As the geometrical shapes are unchanged, this test measures the change specifically due to the material properties; Young's modulus (E) and Poisson's ratio (ν). In this test, we used only the "Flores" contact model. The properties of the materials chosen are given in Table 4.2.

Table 4.2: Properties of the considered materials

Material	Steel	Aluminum	Polyimide	Rubber
Young's modulus (E_i), [GPa]	200	69	4	0.1
Poisson's ratio (ν_i)	0.3	0.34	0.35	0.5

It is clear that the type of the material affects directly the slope of the elastic Hertzian model, as seen in Fig. 4.5. In particular we observed that the stiffer the material, the steeper the slope of the nonlinear penetration depth versus contact force gets, the stiffer the contact becomes as well and the shorter the contact duration gets. Although the damping depends on the Hertzian stiffness (k), the material type does not affect the damping significantly.

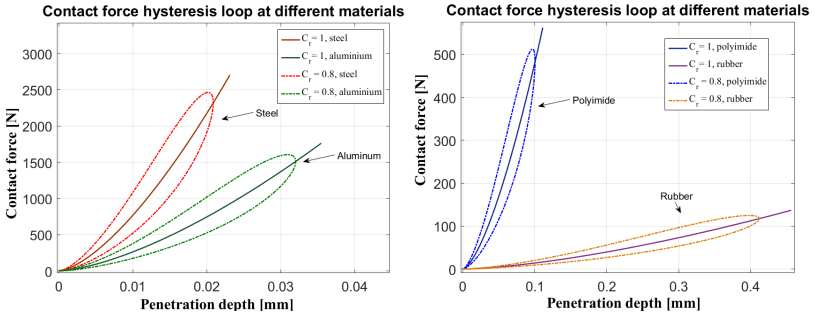

(a) Steel vs aluminum **(b)** Polyimide vs rubber

Figure 4.5: Contact force produced with different material, with "Flores" contact model. [Bondoky et al., 2017a]

4.4.3.3 Coefficient-of-Restitution (COR)

As COR (c_r) is the main parameter in the hysteresis damping (λ) function, it is interesting to observe how the performance of a contact model changes as the COR changes. The input parameter that is given to the contact model is the "projected COR". It defines the microscopic behavior of the contact model. In contrast to this, the "realized COR" is the macroscopic value calculated after the collision is over. In a perfect contact dynamics model, the "realized COR" is equal to the "projected COR", which is the case for all the contact models when the "projected COR" value is 1, i.e., elastic collision.
In this test, the value of the COR has been varied from $50\% - 100\%$ in steps of 10% for the different contact models. The COR variation test shows that the COR value is considered as one of the main parameters that is taken into consideration, for the computation of the hysteresis damping factor. The following points are observed:

(a) Older contact models (H&C, H&M, L&W, L&N) are only good for high projected COR (low energy-loss impacts), but not for the small COR. New contact models (Go, Z&Q, FL) show better results even for the low projected COR and they are closer to the ideal case than the old models. This can be shown clearly in Fig. 4.6a.

(b) The reason for the different behaviors of the models is that each model implements its damping factor (λ) differently. As the newer models have put more emphasis on the damping factor, their damping hysteresis loop became larger (i.e., more energy-loss) compared to the old models. The different shapes of the hysteresis loop can be seen in Fig. 4.6b, where all the contact models are tested at the same COR for the same scenario.

(c) In Fig. 4.6c, we notice that the maximum force of the newer contact models keeps decreasing as long as the COR is decreasing, until it reaches a certain COR and then the maximum force starts to increase again. This behavior is not considered by the old contact models though. An explanation for this is that, as the COR decreases (i.e., the energy dissipation increases), the area of the hysteresis loop gets bigger (due to the higher damping value). In addition, as damping increases, the penetration depth decreases. Because the area of the hysteresis loop corresponds to

the energy loss, this area increases as the COR decreases. At some point, the maximum contact force starts to increase again in order to compensate for the decreasing penetration depth. This can be seen in Fig. 4.6d. "

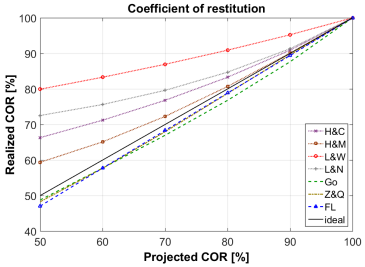

(a) Projected COR vs realized COR for various models

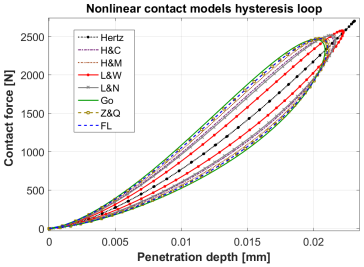

(b) Force hysteresis of various contact models, $c_r = 0.8$.

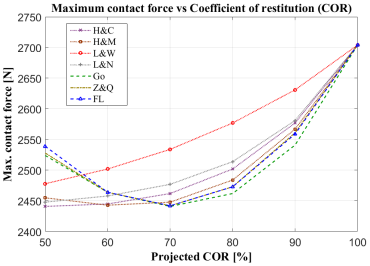

(c) Maximum force of various contact model

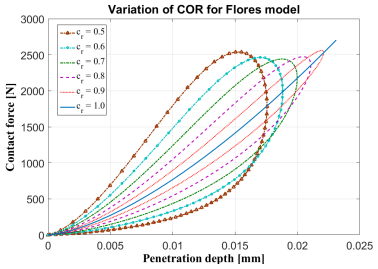

(d) Flores model hysteresis loop at various COR values

Figure 4.6: Coefficient-of-Restitution Analysis [Bondoky et al., 2017a]

4.5 Contact Model Selection

Based on the parametric study results (in Section 4.4), it was observed that the variation of the initial impact velocity, did not significantly affect the differences between the considered contact models results. The same applies for the material type. On the contrary, the COR parameter exhibited the main differences between the considered contact models. Therefore, it was concluded that the contact model is mainly dependent on the COR pa-

rameter, in comparison to the other studied parameters (i.e., initial impact velocity and material type).

Based on the results in Section 4.4.3.3, it was observed that for COR higher than 80%, the three models of Herbert and McWhannel, Zihing and Qishao and Flores et al. are most accurate in comparison to the other studied models, see Fig. 4.6a. However, for COR less than 80%, the models of Flores et al., Gonthier, Zihing and Qishao show better results. For the very low COR values, Gonthier model is the most accurate. Therefore, as the "Flores" contact model showed more accurate results for a large range of different COR values, it was selected to be utilized for the considered docking modeling and analysis.

Chapter 5

1DOF HIL System Model

As mentioned in Section 2.2, a 1DOF HIL testbed is necessary to be designed to test and validate docking contact dynamics of small and rigid satellites without artificial compliance. The 1DOF HIL testbed is considered as a precursor to a 6DOF HIL docking simulator. This chapter prepares for the 1DOF testbed implementation, design and analysis, while the realized testbed is presented in Chapter 8.

In this chapter, an investigation of a simplified model of the 1DOF HIL testbed is presented. Moreover, a simulation of a scenario is presented, in order to show the effect of modeled hardware (in "HIL Model") on the 1DOF model ("Docking Model"). Afterwards, a detailed parametric study and analysis of the modeled design-spaces (i.e., spacecraft, docking hardware and contact dynamics) is presented, which was carried out using the "Generic HIL Testbed Framework Analysis Tool" (presented in Chapter 3). This study assisted to find the key-parameter of the HIL setup (i.e., parameter which affects the HIL errors the most). Based on that, the relative error due to the dynamics of the modeled hardware (actuator and force sensor) was estimated. Accordingly, the required actuator's figure-of-merits were identified. The objectives of this chapter are summarized as follows:

1. Present a 1DOF multibody dynamics model of the docking of small and rigid spacecraft.
2. Present the 1DOF HIL model, as well as the method used to model the HIL equipment (actuator, force sensor).
3. Present a simulation of one scenario to illustrate the errors due to the hardware.
4. Present a detailed parametric study of the available design-spaces and their parameters, in order to identify the key design parameter (most sensitive).
5. Present the required figure-of-merits of the actuator.

Firstly, the concept of modeling and analysis of the 1DOF system is presented in Section 5.1. Secondly, a detailed explanation of how the 1DOF HIL system was modeled is presented in Section 5.2. Thirdly, the results of a simulation of a sample scenario is shown in Section 5.3, in order to demonstrate and explain the HIL errors. Fourthly, in Section 5.4, the analysis and results of the parametric study are presented. Afterwards, the required figure-of-merits of the actuator are defined in Section 5.5. Finally, the chapter is summarized in the conclusion.

5.1 Concept

In order to design and build a HIL testbed for the testing and validation of docking contact dynamics, the following design process was considered. Firstly, a dynamic model of the real life docking scenario was built, then a model of the HIL testbed was built. Afterwards, each model and the effect of HIL equipment on the original dynamic docking simulation were analyzed. Based on that, the dynamic properties and requirements of the HIL equipment were identified. A detailed description of the design process is presented below and illustrated in Fig. 5.1.

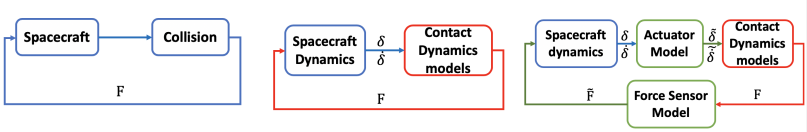

(a) "Real Docking" **(b)** "Docking Model" **(c)** "HIL Model"

Figure 5.1: Simplified block-diagram of each model

Firstly, the "Docking Model" (Fig. 5.1b) was built, which modeled the "Real Docking" scenario (Fig. 5.1a). In the "Real Docking", the whole docking scenario was simplified into two subsystems: "*spacecraft*" for the S/C dynamics and physical properties, as well as "*collision*" for the impacts that occur during docking. Accordingly, in the "Docking Model" block-diagram, the *"spacecraft dynamics"* subsystem modeled the physical and dynamic properties of each spacecraft during the docking process (i.e., it calculates the position and velocity of each spacecraft due to any external forces acting on them). On the other hand, the *"contact dynamics model"* subsystem

modeled the generated force when the two spacecraft are in contact.

Secondly, the "HIL Model" was created as shown in Fig. 5.1c. The goal of the "HIL Model" is to simulate the effect of the dynamics (e.g., time delays, resolution) of HIL equipment in the HIL test and study how they affect the simulation. Accordingly, an actuator and a force sensor were modeled in the "HIL Model".

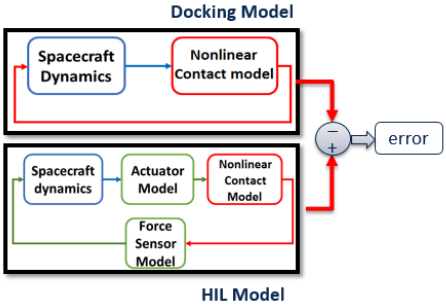

Figure 5.2: Error estimation due to the dynamics of the modeled hardware [Bondoky et al., 2017a]

Afterwards, the HIL errors and fidelity were estimated, when the "HIL Model" and the "Docking Model" were compared to each other (Fig. 5.2). Based on this concept, a parametric study was carried out on the available design-spaces to find the key design parameter in such a setup (the key-parameter is a parameter in a design-space, which has a high sensitivity to the metrics under evaluation). Hence, it affects the HIL errors the most when it is changed. This parametric study can be seen as a sensitivity analysis. In the parametric study, the simulation was repeated several-times, while varying the key-parameter. Accordingly, the required figure-of-merits of the HIL equipment were identified, based on the desired fidelity percentage. Hence, the figure-of-merits of the HIL actuator was selected.

5.2 Modeling

In this section, the modeling of the 1DOF system is described; starting by the "Docking Model", then the "HIL Model".

5.2.1 Docking Model

The "Docking Model" consists of two subsystems: *"spacecraft dynamics"* and *"contact dynamics"*.

5.2.1.1 *Spacecraft dynamics*

"spacecraft dynamics" subsystem is concerned with the physical and dynamic properties of two S/C, that are undergoing impact. The two spacecraft (Chaser and Target) are modeled as two rigid-bodies in 1DOF, in a non gravitational environment, see Fig. 5.3. This subsystem calculates the dynamics (e.g., position, velocity) of each rigid-body due to any external forces acting on them and the dynamics are updated in each time-step of the simulation. The subsystem provides as output the relative-displacement (δ) and relative-velocity ($\dot{\delta}$) between both bodies, to the *"contact dynamics"* subsystem.

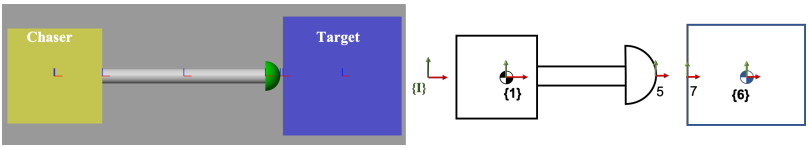

Figure 5.3: Left figure depicts the visualization of the multibody system; right figure shows the multibody model

The Equations-Of-Motion (EOM) of each rigid-body S/C are presented in Eq. 5.1. As these are rigid-bodies, acceleration, velocity and displacement of any reference frame of the rigid-body are the same as the Center-Of-Mass (COM) of the body. The EOMs are as follows

$$\ddot{x}_5(t) = \frac{F_5(t)}{m_1} \quad , \ddot{x}_7(t) = \frac{F_7(t)}{m_6} \tag{5.1}$$

$$\dot{x}_5(t) = \int \ddot{x}_5(t)dt + \dot{x}_5(0) \quad , \dot{x}_7(t) = \int \ddot{x}_7(t)dt + \dot{x}_7(0)$$

$$x_5(t) = \int \dot{x}_5(t)dt + x_5(0) \quad , x_7(t) = \int \dot{x}_7(t)dt + x_7(0)$$

$$\delta = x_5(t) - x_7(t) \tag{5.2}$$

$$\dot{\delta} = \dot{x_5}(t) - \dot{x_7}(t) \tag{5.3}$$

such that m_1 and m_6 are the mass of the chaser and target rigid-body, respectively. F is the external contact force applied on each body during impact. $\ddot{x}_5(t)$, $\dot{x}_5(t)$, $x_5(t)$ are the acceleration, velocity and displacement of chaser rigid-body respectively, while $\ddot{x}_7(t)$, $\dot{x}_7(t)$, $x_7(t)$ are the acceleration, velocity and displacement of target rigid-body respectively. In addition, δ is the relative-displacement (i.e., penetration depth) and $\dot{\delta}$ is the relative-velocity (i.e., penetration-velocity).

In [Bondoky et al., 2017a] and [Bondoky et al., 2017b], an expanded 1DOF model is presented, where the beam of the Chaser is also modeled.

5.2.1.2 *Contact dynamics*

The goal of this subsystem is to calculate the magnitude of the contact force throughout the impact simulation. The detailed description of the Flores non-linear contact model [Flores et al., 2011] and the reason why it was selected to be used in this work have been previously presented in Chapter 4. The Flores contact model equation is as follows:

$$F_N = k\delta^n[1 + \frac{8}{5} \cdot \frac{(1 - c_r)}{c_r} \cdot \frac{\dot{\delta}}{\dot{\delta}_o}] \tag{5.4}$$

such that F_N is the normal contact force, The Hertzian stiffness k takes into consideration the Young's moduli (E_i) and the Poisson's ratios (ν_i) of the bodies. They are both dependent on the type of the material selected. δ is penetration depth n is the power value which is related to the shape of contacting bodies (in the considered model, the contact is assumed to be between a sphere and flat surface, hence $n = 1.5$). $\dot{\delta}_o$ is the initial impact velocity at the very beginning of the impact, while $\dot{\delta}$ is the instantaneous penetration velocity and c_r is the Coefficient-Of-Restitution (COR).

5.2.2 HIL Model

In the "HIL Model" (Fig. 5.1c), two subsystems were added to the "Docking Model", which are the *"actuator model"* and *"force sensor model"*. The goal of the "HIL Model" is to study the effect of the dynamics (i.e., time delays, accuracy) of the hardware used on the system. Afterwards, when the "HIL Model" was compared to the "Docking Model", the relative error due to the dynamics of the used actuator was estimated. Fig. 5.2 depicts the concept of the verification and error estimation. Based on this concept, the required properties of the hardware were studied and defined.

5.2.2.1 *Actuator model*

In order to find the required technical specifications of the actuator, a simplified model of the actuator was built in the "HIL Model". Some of the main actuator's requirements that were needed to be properly identified were: bandwidth frequency (f_o) and motion properties, such as stroke length, velocity, accuracy, etc.

Based on these main requirements (i.e., delay, motion properties), the actuator was modeled as a $2nd$ order Low Pass System (LPS) in order to simulate the delay of the actuator and a quantizer to simulate the positioning resolution of the actuator. The equation of the $2nd$ order LPS is:

$$G_{LPS} = \frac{1}{1 + \frac{2d_o}{\omega_o}s + \frac{s^2}{\omega_o^2}} \tag{5.5}$$

such that the natural frequency is ($\omega_o = \frac{1}{T_c}$) and ($d_o = 0.7$) is the damping value. T_c is the time constant of the actuator, which is the time (in seconds) required by the actuator to reach 63% of its required position. In the 2nd order LPS, the steady state time is reached at around 3.7 times of the time constant, i.e., $T_{ss} \approx 3.7 \cdot T_c$. Accordingly, in order to compensate for any extra delays (e.g., control-bus latency, sensor readout delay), it was assumed that $\tau_{del} = 4 \cdot T_c$. Where τ_{del} is an assumed variable, which represents the total actuator delays, as well as its communication delays. Consequently, the bandwidth frequency is calculated as follows:

$$\omega_o = \frac{1}{T_c} = \frac{4}{\tau_{del}} \tag{5.6}$$

$$f_o = \frac{\omega_o}{2\pi} = \frac{4}{2\pi \cdot \tau_{del}} = \frac{2}{\pi \cdot \tau_{del}} \tag{5.7}$$

In this work, the actuator's total-delay τ_{del} is referred to as D_{act}, while the force sensor's total-delay is referred to as D_f.

5.2.2.2 *Force sensor model*

The force sensor was modeled in the same way as the actuator in section 5.2.2.1. The force sensor model is a 2nd order LPS to model delay, plus quantizer to model resolution of measuring. Based on a market survey, the time constant of the sensor was selected to be small (100 μs) which corresponds to a frequency of 10 kHz, while the accuracy was set to 1 N.

5.3 Simulation and Results (Docking-model vs HIL-model)

In this section, a simulation based analysis of a sample scenario is presented, in order to demonstrate the differences between the "Docking Model" and the "HIL Model".
The simulation ran using a Simulink® model which contained both models (docking and HIL), such that both ran with the same conditions simultaneously. In the results, the relative errors due to the included hardware models and their effect on the simulation were shown. The goal of this section is to explain the effect of hardware dynamics on the docking simulation and show the errors of this scenario.

Firstly, the simulation (and scenario) properties are explained, then the results of the simulation on the quality-control parameters (i.e., displacement, velocity and force) are presented.

5.3.1 Simulation and Sample Scenario Properties

This simulation was carried out using Simulink®, Matlab® 2015b. It ran using ode45 solver with a variable time-step and a maximum time-step of $10\mu s$.

The simulation scenario was an impact between two rigid spacecraft bodies, Chaser (mass m_1 is 30kg) and Target (mass m_6 is 75kg). The required initial impact velocity was 0.1m/s. Accordingly, initial parameters for Chaser are $x_5(0) = 0.35$m, $\dot{x_5}(0) = 0.1$m/s and $\ddot{x_5}(0) = 0\text{m}/s^2$. For Target $x_7(0) = 0.36$m, $\dot{x_7}(0) = 0$m/s, $\ddot{x_7}(0) = 0\text{m}/s^2$.
For the *"contact dynamics"*, the simulation was carried out using contact model "Flores et al." with a COR value of 0.8 and the impact was between a half-sphere of radius 2.5cm (probe-tip) of polyimide and flat surface (target-surface) of aluminum.

For the actuator model a total time-delay (D_{act}) of 1ms with a resolution of 1μm was selected. In addition, for the force-sensor model a total time-delay (D_f) of 0.4ms with a resolution of 1N was selected.

5.3.2 Results of the Sample Scenario

Each graph of Fig. 5.4 contains two models and the error between them. The "Docking Model" is shown in plain black, the "HIL Model" in blue with "o" marker and the error in red with "+" marker. The impact occurs

when the relative displacement between two bodies is more than or equal to zero (i.e., $\delta >= 0$). In Fig. 5.4a, the "Docking Model" starts at time of 0.1 on the x-axis.

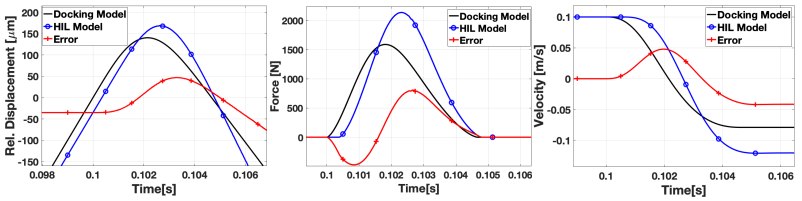

(a) Displacement **(b)** Force. **(c)** Velocity

Figure 5.4: Results of the simulation of a sample scenario (see Section 5.3.1) running simultaneously on "HIL Model" and "Docking Model" in order to present the differences and the HIL errors

In Fig. 5.4b, one observes that the force of the "HIL Model" is slightly delayed relative to the "Docking Model". This is due to the delays presented in HIL equipment models in the "HIL Model". Moreover, maximum impact force of the "HIL Model" shows to be higher than that of the "Docking Model". This is again due to the modeled delays and the resolution implemented in the hardware models of the "HIL Model". The same can be seen in the displacement graph in Fig. 5.4a. In addition, the velocity graph in Fig. 5.4c shows that the velocity-after-impact of the "Docking Model" is -0.08m/s, which means that the realized COR is indeed 0.8, as it was predicted in the contact model (COR = 0.8). However, the velocity-after-impact in the "HIL Model" (-0.12m/s) is much higher than expected in the "Docking Model".

One reasonable way to explain the reason behind these higher peaks (in the force and the penetration-depth) and higher velocity is the modeling of the total delays and the motion capabilities in the hardware models. These resulted in the impact force being applied on the bodies in the "*spacecraft dynamics*" for a longer time in "HIL Model" in comparison to the "Docking Model". Hence, the "*spacecraft dynamics*" subsystem in the "HIL Model" perceived this as follows: a constant force was applied on each body for a longer time (modeled delay-time), accordingly computed accelerations were higher. Therefore, there were higher peaks in force and penetration depth, as well as higher reaction velocity.

5.3.3 HIL Errors

In this section, the calculated HIL errors of the simulated sample scenario is presented in Tab. 5.1.

For the 1DOF HIL modeling, three errors were used here; maximum-instantaneous-error (max. Inst.), modulus HIL-integral-error (i.e., difference between the area under-the-curve) and velocity error. Maximum-instantaneous-error considers the difference between the peak value of the error curve, with respect to "Docking Model". While the HIL-integral-errors considers the difference between the area-under-the-curve of the error curve with respect to the "Docking Model". Lastly, the velocity error in percentage is how much the error (i.e., difference between the final velocity of the "HIL Model" and the "Docking Model") differs from the absolute value of the final velocity of the "Docking Model". The errors definition and explanation have been previously presented in Section 3.3.

Table 5.1: Relative error due to the actuator and force sensor dynamics

Force Error			Displacement Error			Velocity Error	
max. Inst. [N]	max. Inst. [%]	HIL Integral [%]	max. Inst. [μm]	max. Inst. [%]	HIL Integral [%]	$\delta_{f_{error}}$ [m/s]	error [%]
807.34	67.41	45.34	47	45.67	32.63	-0.041	52.52

5.4 Parametric Study

5.4.1 Overview

In this section, the parametric study that was carried out on the different available design-spaces of the 1DOF "Docking Model" and "HIL Model" is presented, see Fig. 3.1. The goal of this study is to carry out a systematic investigation of the available design-spaces in order to find the "key-parameters", which are required to be taken into consideration when designing a HIL testbed. A “key parameter” is a parameter in a design-space which has a high sensitivity to the metrics under evaluation. This study can be seen as a sensitivity analysis. This study assisted to identify the dynamic requirements of the HIL instruments, such that the figure-of-merits of each hardware were identified according to the desired framework. This parametric study was carried out using the "Generic HIL Testbed Frame-

work Analysis Tool" (presented in Chapter 3), which is one of the main contributions of this work.

5.4.2 Objectives and Study Questions

The objectives of this parametric study are formalized in a form of questions, which are then answered through this study. These study questions are as follows:

1. Which is/are the key parameter(s) of the hardware models (in the HIL simulation model) that have a higher effect on the error percentage?
2. Which are the key parameters in the other design-spaces that affect the error percentage?
3. What is the predicted error percentage of the HIL simulation, when the parameters of each design-spaces are varied?

5.4.3 Methodology

In order to find the answer of these study questions, the parametric study has been carried out by systematically changing the parameters of the simulation, repeating the simulation and then analyzing the variation of the error percentages. As the modeled hardware had a higher influence on the results, it was practical to firstly find the key parameters in the HIL design-space. Afterwards, the identified key parameter would be varied against the other design-spaces.

Fidelity Attributes Different attributes were utilized to define quality control. The HIL errors (described in detail in Chapter 3.3) were calculated using the values of these attributes at the "HIL Model", in comparison to the ideal (non-delayed) non-linear physical model (i.e., Docking Model). These attributes are the following:

1. Normal contact force
2. Penetration-depth (normal relative-displacement)
3. Penetration-velocity (normal relative-velocity)

5.4.4 Simulation Properties

The simulation properties of this parametric study were the same as in Section 5.3.1, such that it used the same version of Matlab® and Simulink®.

All the parameters considered in the parametric study have been assigned the same values as noted in Section 5.3.1, unless mentioned otherwise. Meaning, when a design-space (and its parameters) was under investigation, a range of values (for each of its parameters) were defined. Accordingly, the simulation was repeated multiple times and each time a new value from the defined range was assigned to the parameter. Therefore, unless parameters of a certain design-space are explicitly defined, the default simulation parameters are assigned as in Section 5.3.1.

5.4.5 Discussion and Results

5.4.5.1 HIL Design-Space

In the HIL design-space, the following four parameters were part of the "HIL Model". The range of values for these parameters were as follows:

1. Actuator total time-delay (D_{act})
   $[0.4, 0.6, 0.8, 1, 1.2, 1.4]$ (ms)
2. Actuator resolution (R_{act})
   $[0.1, 1, 10]$ (µm)
3. Force-Sensor time-delay (D_f)
   $[0.1, 0.5, 1]$ (ms)
4. Force-Sensor resolution (R_f)
   [0.1,1,10, 100] (N)

These parameters have been selected after doing a wide market survey. In addition, the design-framework of the considered system has been taken into consideration.

Analysis and Results The results of the simulations are shown in the four figures below. In Fig. 5.6, 5.7 and 5.8, one can see that the error percentage remains almost the same when each of the parameters (R_{act}, D_f, R_f) are varied on different ranges. Their behavior showed that they do not have big effect on the error percentage. However, on changing the (D_{act}) in Fig. 5.5, one can see that the error percentage is directly proportional to the actuator total-delay parameter.
Accordingly, the key-parameter was identified to be the actuator total-delay. This answered the first study question.

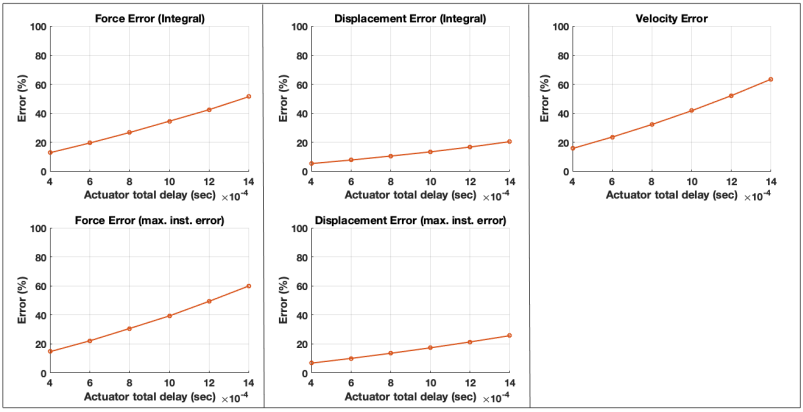

Figure 5.5: Variation of actuator's total-delay (D_{act})

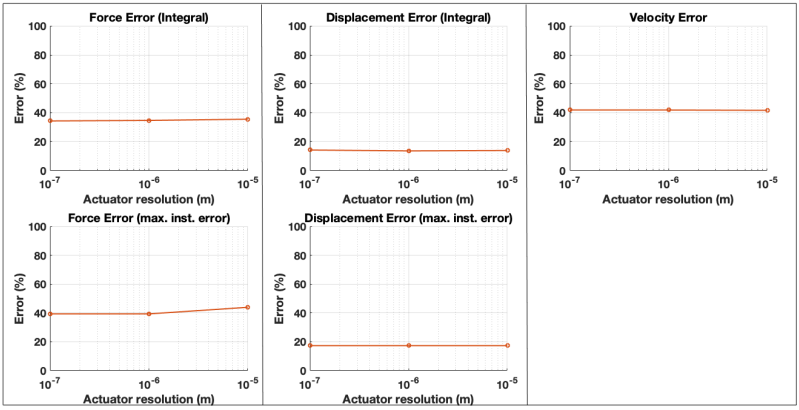

Figure 5.6: Variation of actuator's resolution (R_{act})

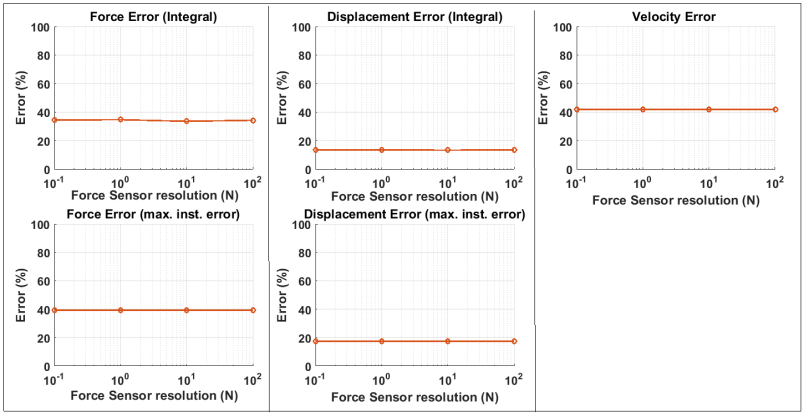

Figure 5.7: Variation of force-sensor's total-delay (D_f)

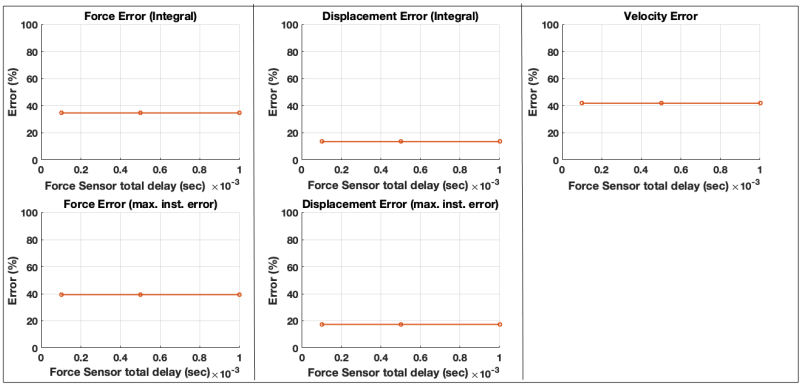

Figure 5.8: Variation of force-sensor's resolution (R_f)

5.4.5.2 Spacecraft Design-Space

The next subsections focus on the second and third study questions.

The parametric study allowed to show the effect of the selected design-space parameters on the predicted HIL simulation and how dependent the error percentage was on them. The results were produced by varying each of the parameters against different values of the HIL design-space key-parameter (actuator total-delay D_{act}).

1. **Masses (kg): [10-10, 35-35, 35-70, 50-50, 50-100, 175-375]**
   The main objective in the investigation of this parameter is to find an answer to the second and third study questions in Section 5.4.2. Furthermore, it investigates whether the ratio between the impacting body masses is an important factor in such impact tests and how the mass ratio affects the predicted HIL simulation errors.

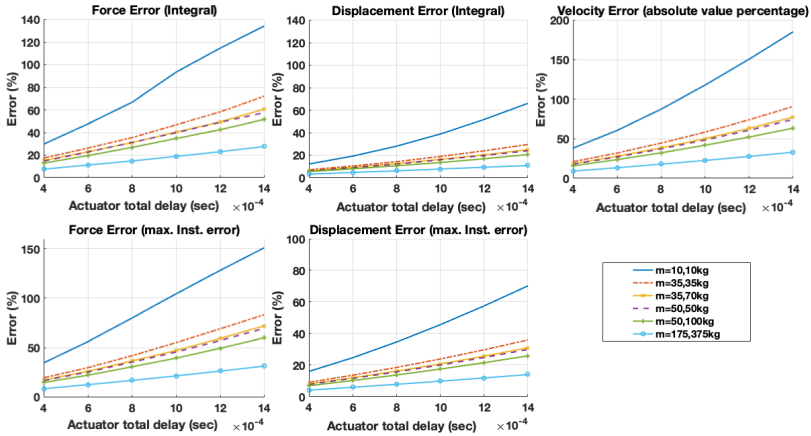

Figure 5.9: Effect of variation of Spacecraft masses and Actuator total-delay (D_{act}) on the predicted HIL simulation errors

Analysis and Results From the results depicted in Fig. 5.9, it is observed that the body-masses ratio is not the main factor to keep an eye on, rather the value of the equivalent-mass of both impacting

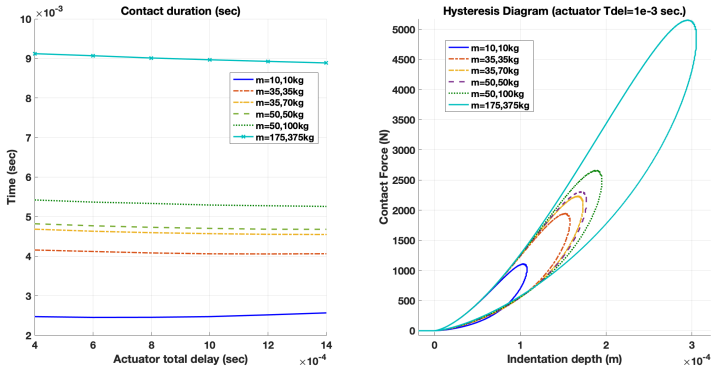

Figure 5.10: Contact duration and force hysteresis of different masses at various Actuator total-delay (D_{act})

bodies. Surprisingly, it was observed that masses are inversely proportional to the HIL error percentage. Meaning, when the masses of both bodies were 10kg, the error percentage showed the highest value always, compared to the other cases. Accordingly, one could conclude that the higher the equivalent masses, the lower the predicted HIL error.

In order to understand this more, the contact-duration of these scenarios were analyzed and the results are depicted in Fig. 5.10. Contact duration is the time that the two impacting bodies are in contact (i.e., touching) with each other.

One observes in Fig. 5.10 that as the equivalent mass becomes smaller, the contact duration becomes shorter and accordingly the HIL errors becomes higher (in Fig. 5.9).
A possible explanation for such phenomenon is that the smaller the equivalent mass, the faster the reaction of the impacting bodies (due to momentum), hence, the shorter contact-duration. Due to the delay caused by the actuator model, the HIL errors increase as the contact duration is shorter. In other words, the shorter the contact duration is, the faster the required actuator's response, to catch up with the motion. A confirmation for this hypothesis is that as the actuator total-delay (D_{act}) increases, the HIL errors also increase, see Fig. 5.9.

As a result, it is concluded that the masses of the impacting bodies

affect the HIL errors. Moreover, it is concluded that the higher the equivalent-masses are, the longer the contact-duration, which leads to the lower HIL error percentage.

2. **Initial Impact Velocity (cm/s): [7.5, 10, 12.5, 15, 17.5, 20]**
   In this test, the initial impact velocity has been varied in order to see how it affects the predicted HIL errors.

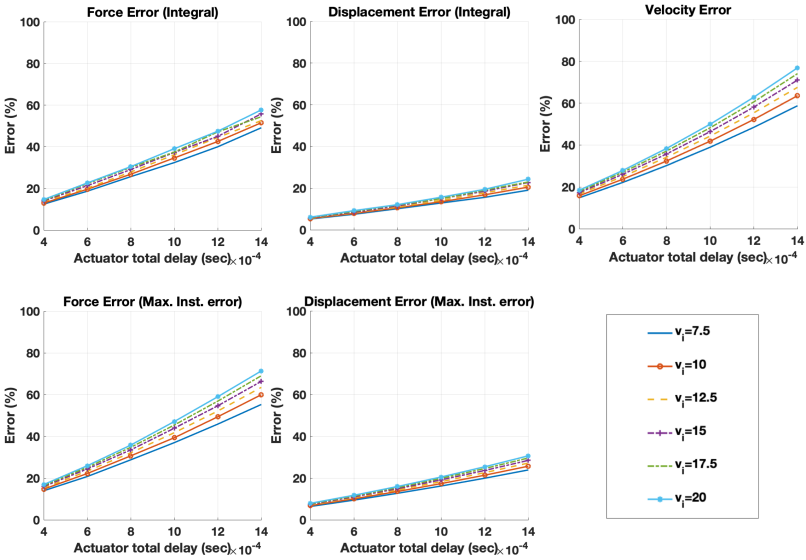

Figure 5.11: Effect of variation of initial impact velocity and Actuator total delay (D_{act}) on the predicted HIL simulation errors

Analysis and Results It is observed from the results depicted in Fig. 5.11 that the HIL errors are directly proportional to the initial impact velocity. Meaning, the higher the initial impact velocity, the higher the predicted HIL simulation errors. However, the difference in errors is not very large, in comparison to other parameters. Figure 5.12 shows the contact duration of each scenario to observe the effect of contact-duration on the HIL errors.

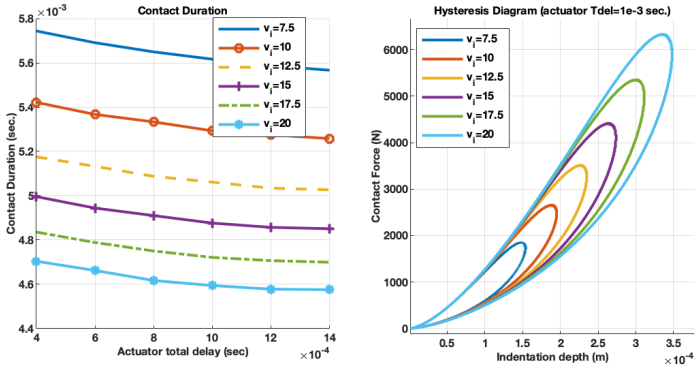

Figure 5.12: Contact duration of different initial velocities at various Actuator total-delay (D_{act})

Accordingly, it is concluded that the initial impact velocity value also affects the HIL errors, but not as significant as other parameters.

5.4.5.3 Contact Dynamics Design-Space

1. **Material** [Aluminum(Alu)-Polyimide(Poly), Alu-Alu, Poly-Poly]
   In this test, the material of the impacting-bodies has been varied (between Alu and Poly) in order to see how this affects the predicted HIL errors.

   Analysis and Results In Fig. 5.13 the HIL errors of the different scenarios are shown. In the Alu-Alu impact scenario, it is observed that the HIL error percentage rises drastically, as the total-delay of the actuator increases. When an impact takes place between Poly-Alu, or Poly-Poly, the HIL errors rising slope is lower than the Alu-Alu scenario.
   In order to analyze this more, Fig. 5.14 depicts the contact-duration, as well as the hysteresis (Impact Force vs Penetration-depth), to understand stiffness and contact duration of each scenario.

   It is observed in Fig. 5.14, that the stiffness of the impact in the Alu-Alu scenario, is much higher than in the other scenarios. In addi-

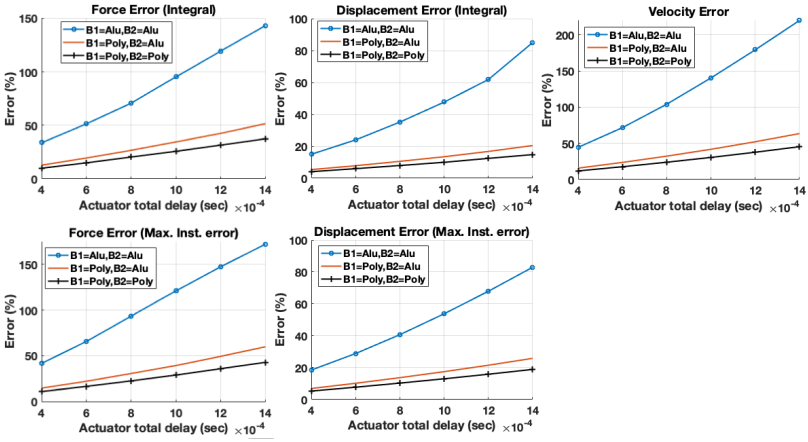

Figure 5.13: Effect of variation of impacting materials and Actuator total delay (D_{act}) on the predicted HIL simulation errors

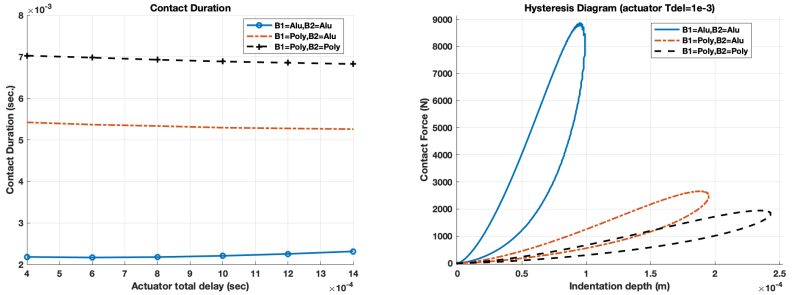

Figure 5.14: Contact duration of impacting materials at various Actuator total-delay (D_{act})

tion, the slope of the HIL errors of the same scenario (Alu-Alu) is also much higher than in the other scenarios, see Fig. 5.13. As a result, it is concluded that the stiffer the material of the impacting bodies, the higher the error percentage of the HIL simulation.
A possible explanation for this phenomenon is that the stiffer the material, the higher the impact force and the shorter the contact duration, hence the higher the impulse. Therefore, due to the delay of the actuator, the error of the HIL simulation tends to be higher for impacts with relatively higher impulses.

Consequently, it is concluded that the material (i.e., a parameter within the contact dynamics design-space) also affects the HIL errors.

5.4.6 Conclusion of Parametric Study

- As expected the delays are driving the simulation errors. Based on the market survey, it was found that the force-sensor delays are in general much smaller than actuator delays, hence the dynamics of the actuator are mainly driving the HIL simulation errors. This is confirmed by the analysis of the HIL design-space parameters' effect on the HIL errors.

  Based on the considered range of values for the total-delays of both hardware models, the actuator time-delay (D_{act}) showed to be the key-parameter of the HIL design-space, as it has the highest effect on the error percentage. **This answers the first study questions.**

- After studying the other design-spaces (S/C, contact dynamics), it is concluded that each of the parameters of each design-spaces affect the HIL simulation errors, but not with the same effect. **This answers the second and third study questions**. Based on this finding, all of these parameters have been varied and tested in the realized HIL testbed.

- The actuator time-delay (D_{act}) is the main key-parameter for the considered HIL design process. It is used to identify figure-of-merits of the required actuator.

5.5 Actuator's Figure-of-Merits Definition

5.5.1 Simulation of various actuator time-delay

In order to define the required figure-of-merits of the actuator, a simulation of the "HIL Model" versus "Docking Model" (exactly like in Section 5.3)

was run multiple times, with various actuator total-delay (i.e., which means various bandwidth frequency), in order to calculate the HIL errors and fidelity. Based on the results and the required fidelity in the HIL testbed framework, the figure-of-merits were identified.

The simulation properties were exactly the same as introduced in section 5.3.1, except that the actuator total-delay was varied with the following values:
Actuator total time-delay (D_{act}) = $[0.4, 0.6, 0.8, 1, 1.2, 1.4]$ (ms)

After running the simulation and comparing the results to the "Docking Model" (as shown in Fig. 5.2), the errors due to the dynamics of the hardware models for the HIL simulator were calculated. The summary of the results are presented in Table 5.2.

Table 5.2: Predicted HIL errors at various actuator's total-delay

Actuator Model	Force Error			Displacement Error			Velocity Error	
D_{act} [ms]	max. Inst. [N]	max. Inst. [%]	HIL Integral [%]	max. Inst. [μm]	max. Inst. [%]	HIL Integral [%]	$\dot{\delta}_{f_{error}}$ [m/s]	error [%]
0.2	162.35	11.36	9.80	8.97	7.18	5.90	-0.008	10.36
0.4	298.11	21.83	17.28	17.11	14.27	11.64	-0.015	19.24
0.6	446.42	34.94	25.91	26.17	23.83	17.90	-0.023	29.14
0.8	617.86	48.57	34.90	36.11	34.43	24.65	-0.032	40.20
1	807.34	67.41	45.34	47.34	45.67	32.63	-0.041	52.52
1.2	997.22	84.60	55.45	59.39	64.12	40.87	-0.052	66.13

5.5.2 Required Figure-of-Merits

One of the main intended uses of the 1DOF HIL simulator is the verification of the "docking contact dynamics validation concept". Therefore, a performance leading to a relative error of up to 60% is acceptable. This is due to the fact that high requirements on the robustness of the docking process will be in place anyway; which in turn relaxes the requirements on the fidelity of the HIL simulation. Consequently, based on the results in Tab. 5.2 and in order to carry out the experiment with a relative-error of approximately 50% to 60%, an actuator is required with a total time-delay in the range of $[1-1.2]$ ms, i.e., a controlled bandwidth frequency (f_o) of $[0.53-0.636]$ kHz.

Based on this analysis, the following requirements are defined for the actuator: minimum force capability of 2.6 kN to be used with a polyimide probe-tip, velocity capability within the range $0.01-0.1$ m/s, minimum stroke length 300 μm, minimum position accuracy 1 μm, minimum acceleration capability 69 m/s^2, position closed-loop controller is required and minimum controlled bandwidth frequency (f_o) required is 0.53 kHz.

5.6 Conclusion

1. In this chapter, a 1DOF docking HIL simulation model has been introduced in detail and studied. Based on simulation results, it is concluded that the dynamics (total-delay, resolution) of the hardware used in the HIL simulation, indeed affect the 1DOF docking system. Accordingly, the HIL errors were calculated and identified.

2. Using the "Generic HIL Testbed Framework Analysis Tool", a detailed parametric study of the available design-spaces and their parameters were carried out, in order to identify the key-parameter (most sensitive). Accordingly, it is concluded that the actuator time-delay is the key-parameter of the HIL design-space and is the main key-parameter for the considered HIL design process. Therefore, it was used to identify figure-of-merits of the required actuator.

3. According to the results of the various actuator's total-delay simulations, the preliminary requirements of the actuator needed for the HIL simulation were defined. These figure-of-merits are a prerequisite for the implementation of the HIL testbed and its realization.

Chapter 6

6DOF HIL System Model

In this chapter, the spacecraft docking model, as well as the Hardware-In-the-Loop (HIL) model are expanded to a 6 Degrees-Of-Freedom (DOF) framework. The 6DOF model is more realistic and more representative to the real life scenario, as it models the dynamics of the free-floating S/C in space. However, the complexity of 6DOF is higher, in terms of mathematical modeling, verification of models and computational effort. The objectives are:

1. Model the 6DOF docking scenario in a generic way, in order to be adaptable for any test-case. The model shall include rigid spacecraft dynamics, docking hardware and contact dynamics.

2. Verify various docking scenarios using the multibody dynamics docking simulation.

3. Identify the properties of the successful and the unsuccessful docking scenarios of the spacecraft under consideration.

4. Build a 6DOF HIL testbed model based on the existing HIL design-frame.

5. Carry out performance analysis on the HIL testbed performance model, to predict and estimate HIL simulation errors and fidelity.

6. Understand the errors of the HIL simulation and identify their sources.

7. Lay the foundation for the 6DOF HIL framework parametric study using the "Generic HIL Testbed Framework Analysis Tool", which carries out a systematic investigation of the available design-spaces, in order to find the HIL testbed key-design-parameters.

Firstly, the concept of the 6DOF system modeling is explained in Section 6.1. Secondly, the modeling method is explained in Section 6.2. Based on that, the detailed explanation of how the 6DOF "Docking Model" was built

is presented in Section 6.3. Likewise, the detailed explanation of how the 6DOF "HIL Model" was built is presented in Section 6.4. In Section 6.5, one can see the models in action, such that in Section 6.5.1, the simulation and the results of a docking case-study are presented and discussed. This case-study allowed to identify the properties of the successful and the unsuccessful docking scenarios. Afterwards, in Section 6.5.2, the simulation and results of the HIL testbed model of a docking scenario are presented, which demonstrated the "HIL Model" in action and allowed to understand where the errors come from. Finally, a summary of the chapter is presented in Section 6.6.

6.1 Concept

HIL Modeling Concept

As mentioned before in Chapter 2, the HIL testbed model is used to study and to analyze how the modeled HIL instruments (and their dynamics) affect the HIL simulation, which is done by comparing the HIL testbed model to the ideal (i.e., without delays) non-linear physical docking spacecraft model.

Following the same naming as in Chapter 2, the ideal physical docking model is called the "Docking Model", the HIL testbed model is called the "HIL Model" and the real HIL simulation testbed is called the "Real HIL testbed".

In the design process introduced in Chapter 2, it was mentioned that it is required to model the "Docking Model" first, then build a model of the HIL testbed and finally define the real HIL testbed requirements. This worked well for the 1DOF system. However, for the 6DOF system, the geometrical and physical properties of the real docking mechanism, as well as the (already defined) HIL testbed design-requirements had be taken into consideration, in order to build the "HIL Model". Therefore, for the 6DOF HIL system modeling, the "Docking Model" was firstly built. Afterwards, the real HIL testbed design frame-work ("Real HIL testbed") was studied. Accordingly, a representative "HIL Model" was built based on the provided information from the "Docking Model" and the "Real HIL testbed", as seen in Fig. 6.1.

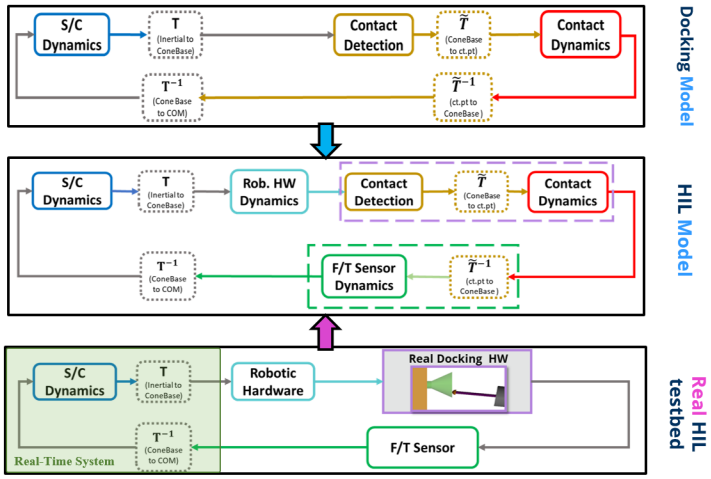

Figure 6.1: Illustration of "HIL Model" design concept, using simplified block-diagrams

6.2 Modeling Methodology

Modeling of spacecraft dynamics in space could be achieved using different methods, e.g., either by utilizing already existing software (e.g., ADAMS, Modelica, etc), or Matlab® toolboxes (e.g., SimMechanics, Aerospace, etc) or by independently building a mathematical multibody dynamics model. The existing multibody software tools and toolboxes make it very easy to construct a multibody model, to simulate and to visualize the desired scenarios, but this comes at the expense of using some black-box tools which have some details that can not be modified or even accessed.

One of the objectives of the docking and HIL testbed models is that they should be adaptable to any S/C docking scenario or HIL testbed that needed to be modeled. Therefore, the models were required to be built in a generic way, such that only a few changes need to be applied to simulate a test-case, but the core concept is generic. Therefore, it was more practical to build an independent mathematical multibody dynamics model and to implement it using Matlab® and Simulink®, in order to have access to all the model properties without any restrictions.

Rigid-body modeling of a spacecraft was adopted in this work for various

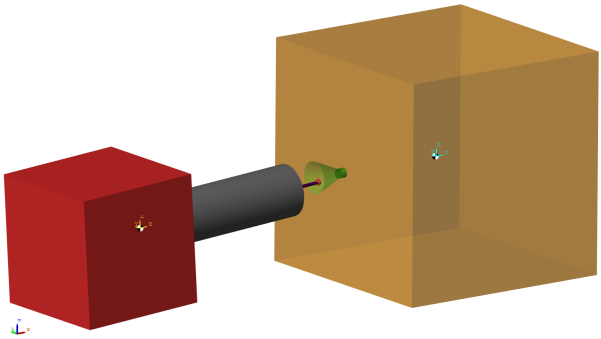

Figure 6.2: 3D Visualization of modeled spacecraft

reasons. First, since HIL simulations run as real-time simulation using a real-time system, the computational effort of the model in-the-loop plays a big role on the performance of the HIL simulation. Modeling spacecraft as flexible bodies, increases the computational effort and time significantly, therefore, it was decided to stick to the rigid-body modeling. Second, by describing the shape of the spacecraft as multiple standard shaped rigid-bodies (as will be explained later in the next section), one would be flexible to quickly model new spacecraft docking scenarios.

6.3 Docking (Physical) Model

The modeling of the spacecraft docking scenario in 6DOF environment was more complicated than the 1DOF model presented before in Chapter 5. In Fig. 6.3, a block-diagram of the concept of the 6DOF "Docking Model" is depicted.

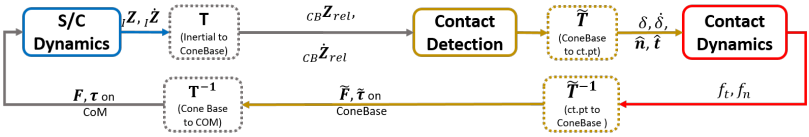

Figure 6.3: Block-diagram of the 6DOF "Docking Model" Concept

The 6DOF "Docking Model" is composed of different subsystems, namely: *S/C Dynamics*, *Contact Detection*, *Contact Dynamics* and *Transformations*. In this chapter, the subsystems are explained in detail. Also, the whole system and the function of each subsystem are briefly explained here, in order to provide an overview of the system.

Model Description

The "*S/C Dynamics*" subsystem is concerned with the 6DOF modeling of the dynamics of each spacecraft in space. Such that the dynamics attributes of each S/C (position, orientation, linear and angular velocity represented in the inertial frame, as well as some attributes in the body-fixed frame, direction-cosine-matrix, etc.) are calculated, based on the external forces and torques acting on the Center-of-Mass (COM) of the S/C. Afterwards, in the next subsystem, ($T_{inertial\ to\ ConeBase}$), the relative motion (pose and velocity) between both S/C is calculated. Moreover, the dynamic attributes are transformed (using homogeneous transformations) in the Drogue-Base frame $\{F_4\}$ (aka ConeBase). Then, the "*Contact Detection*" subsystem comes into action, which is concerned with the following tasks: the detection of contact when it takes place between the two spacecraft (by calculation of minimum normal distance between impacting surfaces), the calculation of the normal and tangential unit-vectors of the reaction forces at the point of impact, as well as the calculation of the normal and tangential velocity between the impacting surfaces. In order to do that, the docking mechanism is geometrically modeled inside this subsystem. Accordingly, the outputs of this subsystem are: penetration-depth, normal and tangential velocity, normal and tangential force unit-vectors. Afterwards, the "*Contact Dynamics*" calculates the magnitude of the impact force using the selected contact model, as well as the friction force model. Then, the force and torque vectors are all calculated in the ConeBase frame. Finally, the forces and torques that act on the COM of each S/C are calculated in the required frames and fed back to the "*Spacecraft Dynamics*" to update the dynamics attributes of each S/C accordingly.

6.3.1 Spacecraft (S/C) Model and Dynamics

In the docking scenario under investigation, two small ($< 1000kg$) and rigid spacecraft are considered, Chaser and Target, as visualized in Fig. 6.4. The docking mechanism utilized is the "probe-drogue" docking mechanism, as it was mentioned before in Section 1.1 why this mechanism was selected.

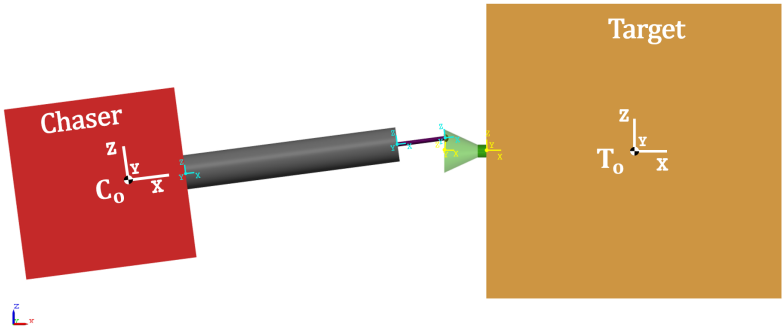

Figure 6.4: Visualization of the docking spacecraft models under consideration

Before initializing the "*Spacecraft Dynamics*" subsystem, the S/C multibody system needs to be defined first. Therefore, in Section 6.3.1.1, the S/C multibody system definition is presented, then in Section 6.3.1.2 the "Spacecraft Dynamics" subsystem is described, finally in Section 6.3.1.3, the implementation of the considered S/C docking scenario is presented.

6.3.1.1 S/C Model

In order to easily model any S/C that needs to be considered and to make it adaptable to any scenarios (i.e., generic modeling), each S/C is defined as a combination of multiple simple-shaped rigid-bodies, which are connected and related to each other. Afterwards, all this information is combined together, out of which one rigid-body S/C is defined, as seen in Fig. 6.5. [Amirouche, 2007] and [Wohllebe, 2017] provided a good foundation for building the model. Modeling the S/C as one rigid-body makes it easier to build simplified S/C models, where the detailed description of bodies are not required, rather only the main properties of the whole body concentrated in its COM. This is very useful for the generic modeling. Moreover, it is required to keep the S/C multibody model as simple as possible, so that the computational effort during simulation would not affect the HIL simulation.
Although each S/C is modeled and is seen as only one rigid-body, modeling each S/C as a combination of multiple rigid-bodies makes it easier (when

the need arises) to upgrade each S/C model to a multibody model. In addition, it can be easily integrated in SimMechanics (toolbox for multibody systems runs on Simulink®), which has been often used within the scope of this project.

The simple-shaped rigid-bodies can be a cube, cuboid, sphere, cylinder, half-sphere or conical frustum. The attributes of each simple-shaped rigid-body are separately defined, as well as the displacements between each rigid-body, based on the S/C under consideration that need to be modeled. The attributes required for each simple-shaped rigid-body are the following:

1. Mass.
2. Geometrical properties (dimensions).
3. Inertia tensor.
4. Displacement w.r.t. to other considered rigid-bodies.
5. Material.

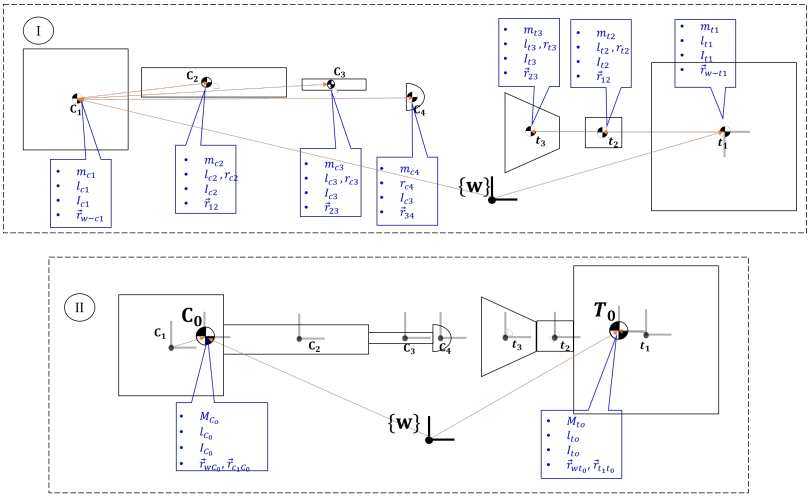

Figure 6.5: Each spacecraft model is made of simple-shaped rigid-bodies.

Each simple-shaped rigid-body is assigned a letter (represents S/C name) and number. For example, "c_3" is Chaser's simplified-body number three

and "t_2" is Target's simplified-body number two. Each S/C has a "mainbody" where most of the mass is concentrated in it and it is assigned the number "1", e.g., "c_1", Chaser's mainbody and "t_1" is Target's mainbody. Based on all the simple-shaped rigid-bodies defined and the attributes assigned for each, a one rigid-body S/C is defined which is assigned a notation of a capital letter and number zero (i.e., Chaser "$\{C_0\}$", Target "$\{T_0\}$").

In order to explain generally, the capital notation B_0 is used to describe the S/C rigid-body and the small notation b_i is used to describe the small-shaped rigid-bodies. Based on that, the following attributes have to be defined for each S/C model:

1. **Total Center-of-Mass** (COM)
   The total COM is calculated based on the mass of each simple-shaped rigid-body and the displacement between each rigid-body COM (b_i) and mainbody COM (b_1). Accordingly, the total COM (B_0) is calculated using the following equation:

$$\mathbf{r}_{COM} = \frac{\sum_{i=1}^{n} m_{b_i}\ \mathbf{r}_{b_1 b_i}}{m_{B_0}} = \mathbf{r}_{b_1 B_0} \tag{6.1}$$

$$m_{B_0} = \sum_{i=1}^{n} m_{b_i} \tag{6.2}$$

   such that $\mathbf{r}_{COM}$ is the displacement from COM of mainbody (b_1) to the calculated total-COM (B_0), n is the number of the simple-shaped bodies for each S/C modeled and m_{B_0} is the total mass of S/C.

2. **Total Inertia Tensor** ($\mathbf{I_{B_0}}$) (defined w.r.t to the total COM)
   The total inertia tensor of the S/C rigid-body is calculated based on the inertia tensor of each simple-shaped rigid-body in the following steps.
   First, the inertia tensor of each simple-shaped rigid-body (I_{b_i}) is defined in its own COM, w.r.t. the mainbody reference frame (b_1) (see [Wohllebe, 2017] for inertia tensors of various simple-bodies considered). Inertia tensor of considered simple-bodies are simple diagonal matrix, as follows:

$$\mathbf{I}_{b_i} = \begin{bmatrix} I_{xx} & 0 & 0 \\ 0 & I_{yy} & 0 \\ 0 & 0 & I_{zz} \end{bmatrix}$$

   Then, using Steiner's theorem (i.e., parallel axis theorem), the inertia

tensor of each body is transformed to the total COM (B_0) of the S/C rigid-body. To transform the inertia tensor using Steiner's theorem, the following equation is used:

$$\mathbf{I}_p = \mathbf{I}_s + m_{b_i}\ \tilde{\mathbf{r}}_{ps}\ \tilde{\mathbf{r}}_{ps}^T \tag{6.3}$$

where I_s is the original inertia tensor, $\mathbf{r}_{ps}$ is the displacement vector from the old to the new reference point and I_p is the transformed inertia tensor. Such that in considered generic notation, it is used as follows:

$$_{B_0}(\mathbf{I}_{b_i}) = \mathbf{I}_{b_i} + m_{b_i}\ \tilde{\mathbf{r}}_{b_i B_0}\ \tilde{\mathbf{r}}_{b_i B_0}^T \tag{6.4}$$

where I_{b_i} is the original inertia tensor in each body's COM, i is the number of the simple-shaped rigid-bodies, $_{B_0}(I_{b_i})$ is the transformed inertia tensor of each body in (B_0) reference frame. $\tilde{\mathbf{r}}_{b_i B_0}$ is the skew-symmetric matrix of $\mathbf{r}_{b_i B_0}$, as follows:

$$\tilde{\mathbf{r}}_{b_i B_0} = \begin{bmatrix} 0 & -r_3 & r_2 \\ r_3 & 0 & -r_1 \\ -r_2 & r_1 & 0 \end{bmatrix},\ \mathbf{r}_{b_i B_0} = [r_1\ r_2\ r_3]^T$$

Afterwards, in order to calculate the total inertia tensor of the S/C rigid-body, the summation of all the inertia tensors of the total number (n) of the simple-shaped rigid-bodies in the total COM is calculated, giving the total inertia tensor of the S/C rigid-body as output.

$$\mathbf{I}_{B_0} = \sum_{i=1}^{n}\ _{B_0}(\mathbf{I}_{b_i}) \tag{6.5}$$

3. **Mass matrix (M_{B_0})**
   As the S/C is modeled as one rigid-body, its mass matrix would consist of a 6x6 matrix, which comprises of the mass and the inertia tensor, as follows:

$$\mathbf{M}_{B_0} = \begin{bmatrix} m_{B_0} I_d & 0_{3\times3} \\ 0_{3\times3} & \mathbf{I}_{B_0} \end{bmatrix}_{6\times6}$$

where m_{B_0} is the total mass, I_d is identity matrix and $\mathbf{I}_{B_0}$ is the inertia tensor.

6.3.1.2 S/C Dynamics

In this section, the equations-of-motion governing the 6DOF motion of each of the considered S/C w.r.t. the inertial-fixed (aka, World) coordinate frame $\{W : X_w, Y_w, Z_w\}$ are described. The model is built based on [Fossen and Fjellstad, 1995], as well as [Ploen et al., 2004], [Zipfel, 2007] and [Witkin and Baraff, 1997].

Assumptions In the model, certain assumptions are made, which simplified the system of equations of each S/C model, as follows:

1. Each S/C is modeled as a rigid-body with defined attributes, namely: a body-fixed reference frame $\{B_0\}$, a total Center-of-Mass (COM), total mass and total inertia tensor.
2. The body-fixed frame coincides with the total COM of the S/C model.
3. The total inertia tensor of each S/C is defined with respect to its own total COM.

General vectors and components To describe the 6DOF motion, the following vectors and components (See Fig. 6.6) are used:

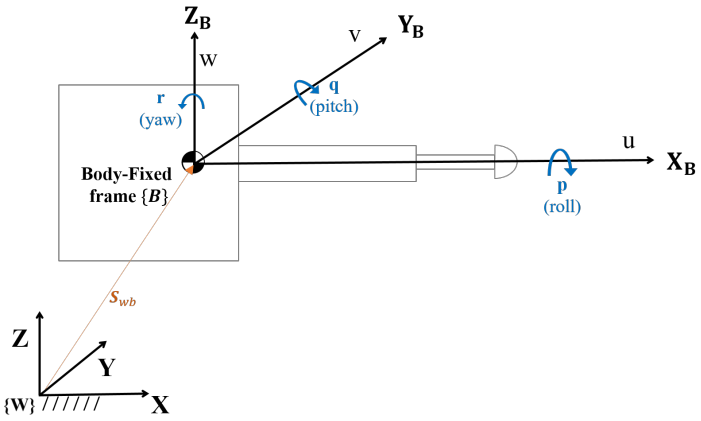

Figure 6.6: Body-fixed and World-fixed (inertial reference) frames

$$
{}_w\mathbf{Z} = [{}_w\mathbf{S}, \mathbf{\Phi}]^T; \quad {}_w\mathbf{S} = [x_w, y_w, z_w]^T; \quad \mathbf{\Phi} = [\phi, \theta, \psi]^T
$$

$$
{}_b\mathbf{Y} = [{}_b\mathbf{V}, {}_b\mathbf{\Omega}]^T; \quad {}_b\mathbf{V} = [u, v, w]^T; \quad {}_b\mathbf{\Omega} = [p, q, r]^T
$$

$$
{}_b\mathbf{F} = [f_x, f_y, f_z]^T; \quad {}_b\boldsymbol{\tau} = [\tau_x, \tau_y, \tau_z]^T
$$

where ${}_w\mathbf{Z}$ is the pose vector in inertial world frame, which is composed of linear position in world-frame (${}_w\mathbf{S}$) and euler orientation ($\mathbf{\Phi}$). ${}_b\mathbf{Y}$ is the body-fixed velocity vector which consists of linear body-fixed velocity (${}_b\mathbf{V}$) and angular body-fixed velocity (${}_b\mathbf{\Omega}$).

Equation-of-Motion (EOM) The EOMs that govern the dynamics of the rigid-body S/C are given as:

1. Translational motion of the rigid-body S/C:

$$
{}_b\mathbf{F} = m({}_b\dot{\mathbf{V}} + {}_b\mathbf{\Omega} \times {}_b\mathbf{V}) \tag{6.6}
$$

   where the external applied force ${}_b\mathbf{F} = [F_{bx}, F_{by}, F_{bz}]'$ acts on the body's COM, m is the constant body-mass, ${}_b\mathbf{V}$ is the body-fixed linear velocity, ${}_b\mathbf{\Omega}$ is the body-fixed angular velocity.

2. Rotational dynamics of the rigid body S/C:

$$
{}_b\boldsymbol{\tau} = \mathbf{I}_B \, {}_b\dot{\mathbf{\Omega}} + {}_b\,\mathbf{\Omega} \times (\mathbf{I}_B \, {}_b\mathbf{\Omega}) \tag{6.7}
$$

   where ${}_b\boldsymbol{\tau}$ is the external applied moment on the S/C COM, $\mathbf{\Omega}$ is the angular velocity, $\mathbf{I}_B$ is the inertia tensor of the S/C represented in its own COM.

Subsystem Initialization In order to initialize the system model for the simulation, the following initial parameters are required for each S/C:

1. initial pose in inertial axes (${}_w\mathbf{Z}$)

$$
{}_w\mathbf{Z}(0)_{[6x1]} = \begin{bmatrix} {}_w\mathbf{S}_{[3x1]} \\ \mathbf{\Phi}_{[3x1]} \end{bmatrix} = \begin{bmatrix} x_w \\ y_w \\ z_w \\ \phi \\ \theta \\ \psi \end{bmatrix} \tag{6.8}
$$

2. initial velocity in body axes (${}_b\mathbf{Y}$):

$$ {}_b\mathbf{Y}(0)_{[6x1]} = \begin{bmatrix} {}_b\mathbf{V}_{[3x1]} \\ {}_b\mathbf{\Omega}_{[3x1]} \end{bmatrix} = \begin{bmatrix} u \\ v \\ w \\ p \\ q \\ r \end{bmatrix} \tag{6.9} $$

3. mass of the body (m)
4. Inertia Tensor ($\mathbf{I}$)

Subsystem Inputs The inputs to the spacecraft dynamics system are:

1. ${}_b\mathbf{F}$: Force acting on COM, in body-fixed frame.
2. ${}_b\boldsymbol{\tau}$: Torque acting on COM, in body-fixed frame.

Subsystem Outputs

1. ${}_w\mathbf{Z}(t)$: the pose in inertial world-frame
2. ${}_b\mathbf{Y}(t)$: the velocity in body fixed-frame.
   It is composed of linear velocity $[u\ v\ w]'$, as well as the body-fixed angular-rates $[p\ q\ r]'$.
3. ${}_w\dot{\mathbf{Z}}(t)$: the velocity in inertial world-frame.
   It is composed of linear velocity (in inertial world frame)$[\dot{x}_w\ \dot{y}_w\ \dot{z}_w]'$, as well as the Euler-angle rates $[\dot{\phi}\ \dot{\theta}\ \dot{\psi}]'$. In order to calculate the Euler-rates from the body-fixed angular rates $[p\ q\ r]'$, the following formula is used:

$$ \begin{bmatrix} \dot{\phi} \\ \dot{\theta} \\ \dot{\psi} \end{bmatrix} = \begin{bmatrix} 1 & \sin\phi\tan\theta & \cos\phi\tan\theta \\ 0 & \cos\phi & -\sin\phi \\ 0 & \frac{\sin\phi}{\cos\theta} & \frac{\cos\phi}{\cos\theta} \end{bmatrix} \begin{bmatrix} p \\ q \\ r \end{bmatrix} \tag{6.10} $$

4. Direction-Cosine Matrix (DCM) ($\mathbf{R}_{wb}$): The Euler 321 sequence is used in the above system. The rotation matrix ($\mathbf{R}_{wb}$) is generated from the 3-2-1 intrinsic Euler angles by multiplying the three matrices generated by rotation about the axis:

$$ \mathbf{R}_{wb} = \mathbf{R}_z(\psi) \cdot \mathbf{R}_y(\theta) \cdot \mathbf{R}_x(\phi) \tag{6.11} $$

where,

$$\mathbf{R}_x(\phi) = \begin{bmatrix} 1 & 0 & 0 \\ 0 & \cos\phi & -\sin\phi \\ 0 & \sin\phi & \cos\phi \end{bmatrix}, \mathbf{R}_y(\theta) = \begin{bmatrix} \cos\theta & 0 & \sin\theta \\ 0 & 1 & 0 \\ -\sin\theta & 0 & \cos\theta \end{bmatrix},$$

$$\mathbf{R}_z(\psi) = \begin{bmatrix} \cos\psi & -\sin\psi & 0 \\ \sin\psi & \cos\theta & 0 \\ 0 & 0 & 1 \end{bmatrix}$$

Accordingly, the $\mathbf{R}_{wb}$ that transforms from the body-fixed frame (b) to world reference frame (w) is shown in Eq. 6.12, which contains the unit vectors of the body-fixed frame described in the world-frame frame. For simplicity, the "cos" is represented with "c", while "sin" is represented with "s", e.g., $c\theta$ is $\cos\theta$:

$$\mathbf{R}_{wb} = \begin{bmatrix} c\psi\ c\theta & c\psi\ s\phi\ s\theta - c\phi\ s\psi & s\phi\ s\psi + c\phi\ c\psi\ s\theta \\ c\theta\ s\psi & c\phi\ c\psi + s\phi\ s\psi\ s\theta & c\phi\ s\psi\ s\theta - c\psi\ s\phi \\ -s\theta & c\theta\ s\phi & c\phi\ c\theta \end{bmatrix} \quad (6.12)$$

The transformation matrix $\mathbf{R}_{bw}$ can be calculated by obtaining the transpose of $\mathbf{R}_{wb}$,

$$\mathbf{R}_{bw} = (\mathbf{R}_{wb})^T \quad (6.13)$$

5. Extra outputs: In addition to the outputs mentioned above, some extra outputs are prepared (in light of generic modeling) so that the model can be easily used with different models or scenarios. These extra outputs are:
   - Acceleration in body-axes (${}_b\dot{\mathbf{V}}$);
   $${}_b\dot{\mathbf{V}} = \frac{{}_b\mathbf{F}}{m} +_b \mathbf{V} \times_b \mathbf{\Omega}$$
   - Angular acceleration in body-axes (${}_b\dot{\mathbf{\Omega}}$);
   $${}_b\dot{\mathbf{\Omega}} =_b \mathbf{I}^{-1}[{}_b\boldsymbol{\tau} - \mathbf{\Omega} \times ({}_b\mathbf{I}\mathbf{\Omega})]$$
   - Body rotational rates in inertial frame (${}_w\mathbf{\Omega}$);
   $${}_w\mathbf{\Omega} = \mathbf{R}_{wb} \times_b \mathbf{\Omega}$$

6.3.1.3 Implementation

In this section, the implementation of the modeling of the S/C under consideration is explained. The geometrical properties of the considered spacecraft

are depicted in Fig. 6.7.

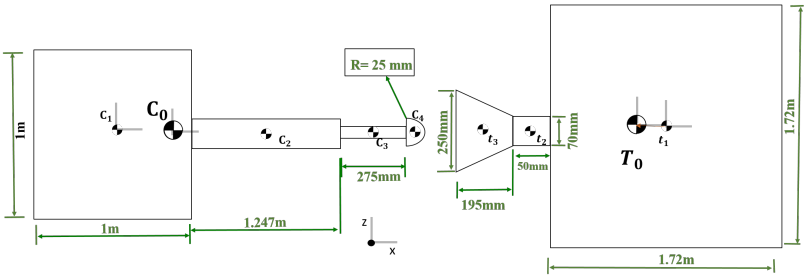

Figure 6.7: Spacecraft geometrical properties illustration (shapes are not to scale)

Chaser Spacecraft The rigid-body model of the "Chaser" spacecraft is defined based on four rigid-bodies. The four rigid-bodies are called, Mainbody, Rigid-cylinder, Probe-beam and Probe-tip, which are defined as: rigid-cube, solid-cylinder, solid-cylinder and half-sphere, respectively. The properties of each body are defined and introduced in Tab. 6.1. Accordingly, the total COM of all bodies is calculated based on Eq. 6.1 and the "total COM" position w.r.t. the Mainbody (c_1) is $[0.1895\ 0\ 0]^T$. Afterwards, using the Steiner theorem, the inertia of the bodies is transformed to the total COM. Consequently, a one rigid-body spacecraft model called "Chaser" is defined, see Tab. 6.2.

Target Spacecraft Likewise, the rigid-body model of the "Target" spacecraft is defined based on three rigid-bodies. The three rigid-bodies are called, Mainbody, Drogue-Cylinder and Drogue-Frustum, which are defined as: rigid cube, hollow-cylinder and hollow-frustum respectively. The Drogue is sometimes referred to as the Docking-Cone. The properties of each body are defined and introduced in Tab. 6.3. Accordingly, the "total COM" of all bodies is calculated and its position w.r.t. the Mainbody (t_1) is $[-0.0123\ 0\ 0]^T$. Afterwards, using the Steiner theorem, the inertia of the bodies is transformed to the total COM. Consequently, a one rigid-body S/C model called "Target" is defined, see Tab. 6.4.

Table 6.1: Physical properties of the rigid bodies, where the rigid Chaser S/C model is defined

Body	**Mass** [kg]	**Displacement** ($r_{c_1-c_i}$) [m]	**Inertia in body's COM** (I_{c_i}) [kg $\cdot m^2$]	**Inertia in total COM** ($_{C_0}[I_{c_i}]$) [kg $\cdot m^2$]
Main-body (c_1)	300	$\begin{bmatrix}0\\0\\0\end{bmatrix}$	$\begin{bmatrix}50 & 0 & 0\\0 & 50 & 0\\0 & 0 & 50\end{bmatrix}$	$\begin{bmatrix}50 & 0 & 0\\0 & 60.77 & 0\\0 & 0 & 60.77\end{bmatrix}$
Rigid Cylinder (c_2)	60	$\begin{bmatrix}1.1235\\0\\0\end{bmatrix}$	$\begin{bmatrix}0.3 & 0 & 0\\0 & 31.25 & 0\\0 & 0 & 31.25\end{bmatrix}$	$\begin{bmatrix}0.3 & 0 & 0\\0 & 83.59 & 0\\0 & 0 & 38.59\end{bmatrix}$
Probe-beam (c_3)	0.366	$\begin{bmatrix}1.8845\\0\\0\end{bmatrix}$	$\begin{bmatrix}0.028 & 0 & 0\\0 & 9.24 & 0\\0 & 0 & 9.24\end{bmatrix} \times 10^{-3}$	$\begin{bmatrix}0.028 \times 10^{-3} & 0 & 0\\0 & 1.06 & 0\\0 & 0 & 1.06\end{bmatrix}$
Probe-tip (c_4)	0.1	$\begin{bmatrix}2.0314\\0\\0\end{bmatrix}$	$\begin{bmatrix}0.25 & 0 & 0\\0 & 0.16 & 0\\0 & 0 & 0.16\end{bmatrix} \times 10^{-4}$	$\begin{bmatrix}0.025 \times 10^{-3} & 0 & 0\\0 & 0.34 & 0\\0 & 0 & 0.34\end{bmatrix}$

Table 6.2: Physical properties of the rigid Chaser S/C

Body	**Mass** [kg]	**total COM** ($r_{c_1-C_0}$) [m]	**Inertia in total COM** (I_{C_0}) [kg $\cdot m^2$]
Chaser Rigid-Body (C_0)	360.466	$[0.1895\ 0\ 0]^T$	$\begin{bmatrix}50.3001 & 0 & 0\\0 & 145.76 & 0\\0 & 0 & 145.76\end{bmatrix}$

Table 6.3: Physical properties of the rigid bodies, where the the rigid Target S/C model is defined

Body	**Mass** [kg]	**Displacement** ($r_{t_1-t_i}$) [m]	**Inertia in body's COM** (I_{t_i}) [kg $\cdot m^2$]	**Inertia in total COM** ($_{T_0}[I_{t_i}]$) [kg $\cdot m^2$]
Main-body (t_1)	759.99	$\begin{bmatrix}0\\0\\0\end{bmatrix}$	$\begin{bmatrix}374.726 & 0 & 0\\0 & 374.726 & 0\\0 & 0 & 374.726\end{bmatrix}$	$\begin{bmatrix}374.726 & 0 & 0\\0 & 374.84 & 0\\0 & 0 & 374.84\end{bmatrix}$
Drogue Cylinder (t_2)	0.77	$\begin{bmatrix}-0.885\\0\\0\end{bmatrix}$	$\begin{bmatrix}1 & 0 & 0\\0 & 0.7 & 0\\0 & 0 & 0.7\end{bmatrix} \times 10^{-3}$	$\begin{bmatrix}1 & 0 & 0\\0 & 587.1 & 0\\0 & 0 & 587.1\end{bmatrix} \times 10^{-3}$
Drogue Frustum (t_3)	9.24	$\begin{bmatrix}-0.949\\0\\0\end{bmatrix}$	$\begin{bmatrix}0.0023 & 0 & 0\\0 & 0.2782 & 0\\0 & 0 & 0.2782\end{bmatrix}$	$\begin{bmatrix}0.0023 & 0 & 0\\0 & 8.3932 & 0\\0 & 0 & 8.3932\end{bmatrix}$

Table 6.4: Physical properties of the rigid Target S/C

Body	**Mass** [kg]	**total COM** ($r_{t_1-T_0}$) [m]	**Inertia in total COM** (I_{T_0}) [kg $\cdot m^2$]
Target Rigid-Body (T_0)	770	[-0.0123 0 0]^T	$\begin{bmatrix}374.729 & 0 & 0\\0 & 383.82 & 0\\0 & 0 & 383.82\end{bmatrix}$

6.3.2 Transformations and Reference Frames

Homogeneous Transformation

In multibody modeling, dynamic attributes of any body are defined with respect to a specific reference frame. Transformation between reference frames is often required, as in this work. For example, the Chaser probe-tip's attributes need to be calculated w.r.t. the world inertial frame $\{W\}$, or w.r.t the Target's drogue-base $\{F_4\}$ when describing the relative-motion between the two spacecraft.

Homogeneous transformation is adopted in this work, in order to transform from one reference frame to another [Schilling, 1996]. It is a compact way to describe the rotation and translation between two different frames in a 4x4 matrix form, as follows:

$$\mathbf{T}_{a-b} = \begin{bmatrix} R_{3\times3} & P_{3\times1} \\ \eta_{1\times3} & \sigma_{1\times1} \end{bmatrix} \tag{6.14}$$

such that $\mathbf{T}_{a-b}$ is the transformation of frame "b" to ref. frame "a", "$\mathbf{R}_{3x3}$" is the rotation matrix that describes the rotation from frame "b" to frame "a", $\mathbf{P}_{3\times1}$ is the translation vector, "$\boldsymbol{\eta}$" is the perspective vector which was always set to zero in this work, as well as the scale vector "σ".

One of the advantages of the homogeneous transformations is the simplicity in transforming from one reference frame to another, by multiplying the transformation matrices by each other in the right order. For example, in order to transform from frame "c" to frame "a", one would first transform from frame "c" to "b", then from frame "b" to "a", (i.e. $\mathbf{T}_{a-c} = \mathbf{T}_{a-b} \cdot \mathbf{T}_{b-c}$). In addition, in order to obtain the inverse transformation (i.e., transformation from frame "a" to frame "c"), one can simply obtain the inverse of the homogeneous matrix, (which is not the same as the inverse of a normal matrix), as follows:

$$\mathbf{T}_{b-a} = \mathbf{T}_{a-b}^{-1} = \begin{bmatrix} \mathbf{R}_{3\times3}^{T} & -\mathbf{R}^{T} \cdot P_{3\times1} \\ {}_{b}\boldsymbol{\eta}_{1\times3} & \sigma_{1\times1} \end{bmatrix} \tag{6.15}$$

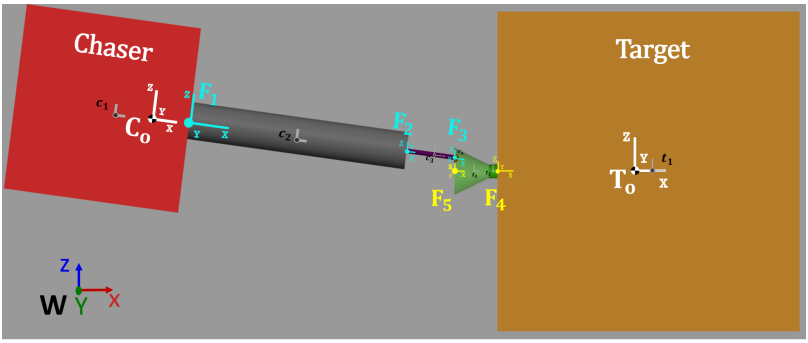

(a) Reference frames defined for the modeled spacecraft

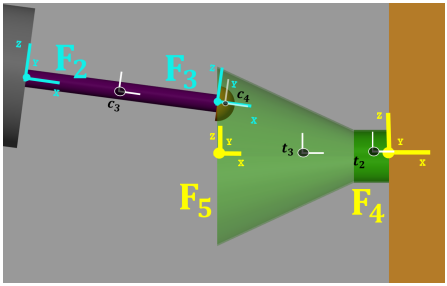

(b) Closer view of the docking mechanism's reference frames

Figure 6.8: Multibody model reference frames

Reference frames

Various reference frames have been defined in the multibody model of the spacecraft, as seen in Fig. 6.8. The reference frames are assigned to specific positions in each S/C model, which are useful for modeling, analysis of the system and future HIL simulations. The description of the reference frames are presented in Table 6.5. In this work, it is required to describe position, velocity, etc. in different reference frames, in order to simplify the model and its analysis.

Table 6.5: Reference frames description of the multibody model of the spacecraft

Reference Frame	Position
$\{W\}$	World frame
$\{C_0\}$	Chaser COM
$\{T_0\}$	Target COM
$\{F_1\}$	Solid Cylinder Base
$\{F_2\}$	Docking Probe-beam Base
$\{F_3\}$	Docking Probe-tip base
$\{F_4\}$	Docking Cone Base
$\{F_5\}$	Docking Cone Tip

Using the transformation diagram in Fig. 6.9, one can visualize the transformations required to transform from one reference frame to another. For example, in order to transform from the drogue-base frame $\{F_4\}$ to the world frame $\{W\}$, (i.e. T_{w-f_4}), one firstly transforms from world frame to Target COM, then from Target COM to drogue-base, (i.e. $T_{w-f_4} = T_{w-t_0} \cdot T_{t_0-f_4}$).

6.3.3 Contact Detection

In this section, the "*Contact Detection*" subsystem is explained, which is mainly concerned with finding whether the 3D geometrically modeled bodies of the docking-hardware are in contact or not.

This subsystem prepares some of the required information for the next subsystem ("*Contact Dynamics*") as follows: whether the bodies are in contact or not, penetration depth, penetration velocity, unit-vectors of (normal

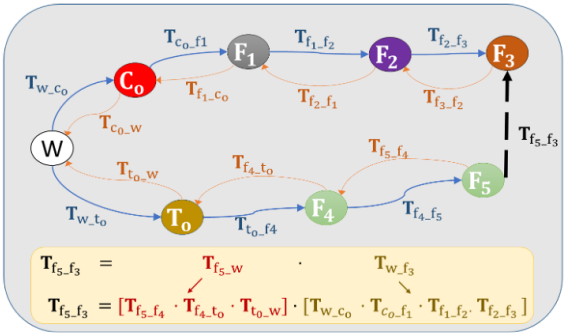

Figure 6.9: Homogeneous Transformation Table

and tangential) reaction forces, tangential relative-velocity (i.e., for friction force calculation), as well as identifying the position of the impact-point on each body (or the closest expected impact point, if bodies are not in contact).

The inputs to this subsystem are: the relative pose and velocity of the probe-beam base $\{F_2\}$ (or Probe-tip base $\{F_3\}$) w.r.t. the drogue-base frame $\{F_4\}$, represented in the drogue-base frame. Moreover, the pose and velocity of the Drogue-Base w.r.t. the world frame (${}_W\{F_4\}$) are required. The outputs are: penetration depth, normal penetration velocity, tangential relative-velocity, contact points position on each body, as well as unit-vectors of normal and tangential forces.

In the following subsections, the method of calculation of the minimum-normal-distance (i.e., penetration-depth) between two bodies, as well as the calculation of the normal and tangential unit-vectors is presented. Afterwards, it is explained how the normal and tangential relative impact-velocities are derived.

6.3.3.1 Minimal Normal Distance Between Bodies

While there are various approaches to find the minimum-normal-distance (or if bodies are in contact or not), the 3D description of the docking hardware has to be provided in all these approaches. Some of these approaches are:

mesh modeling, volumetric equations [Wohllebe, 2017], or vector-analysis approach [Bondoky, 2015]. Mesh modeling approach is accurate, however its computational effort in simulations is quite high, which is not recommended in HIL simulations. Accordingly, the vector-analysis approach was utilized, out of the other approaches, because of its accuracy and simplicity. In Table 6.6 the inputs and outputs for distance calculation are presented.

Table 6.6: Required Inputs and Outputs for calculation of minimal normal distance. See Fig. 6.10 for illustration

Inputs		Outputs	
$\mathbf{P}$	displacement vector of probe-tip base $\{F_3\}$ w.r.t drogue's base $\{F_4\}$, represented in $\{F_4\}$ coordinates	$\mathbf{K}$	Perpendicular displacement from drogue surface to probe-tip base.
l_c	length of docking cylinder	l	minimum distance to impact (i.e., penetration depth)
r_c	radius of docking cylinder	$\hat{\mathbf{n}}_{\mathbf{tc}}$, $\hat{\mathbf{t}}_{\mathbf{tc}}$	Unit vector of normal ($\hat{\mathbf{n}}$) and tangential ($\hat{\mathbf{t}}$) reaction force from Target to Chaser
θ_c	Docking cone angle	$\hat{\mathbf{n}}_{\mathbf{ct}}$, $\hat{\mathbf{t}}_{\mathbf{ct}}$	Unit vector of normal ($\hat{\mathbf{n}}$) and tangential ($\hat{\mathbf{t}}$) reaction force from Chaser to Target
r_p	radius of probe-tip	$\mathbf{C_c}$	contact-point position vector on Chaser's Probe-tip, w.r.t Drogue-base
		$\mathbf{C_t}$	contact-point position vector on Target's Drogue, w.r.t Drogue-base

Assumptions

Firstly, this approach is based on the assumption that impacts take place only inside the drogue, not from outward. Secondly, certain assumptions and time-variant variables have been introduced, in order to simplify the presentation of the approach to the reader (see Fig. 6.10 for illustration), as follows:

- It is assumed that the docking drogue consists of a docking cylinder, a docking-cone and varying-frustum. Varying-frustum is an imaginary frustum, where its base coincides with the docking cone, while its top coincides with the YZ plane that contains the probe-tip base $\{F_3\}$, that is why its length is varying.
- a: length of varying frustum.
- b: distance from rim of varying-frustum to the tip of the docking cylinder in YZ plane.
- c: outer radius of varying-frustum.
- i: distance from probe-tip base, to drogue's base in YZ plane.
- j: distance from probe-tip base, to frustum in YZ plane.
- k: perpendicular distance from frustum surface (in XZ plane) to probe-tip base.
- l: minimum perpendicular distance between frustum surface and probe-tip surface in XZ plane.
- γ: angle between i and z-axis, in YZ plane.
- the drogue is divided into different zones, because it consists of different shapes. These zones (shown in Fig. 6.11) are:
  - Zone A: inside docking cone.
  - Zone B: cylinder-tip.
  - Zone C: inside docking cylinder.

Approach

The idea in this approach is to separately analyze the different planes (plane XZ and plane YZ), in order to calculate the required variables based on the inputs. The condition whether the bodies are in contact or not, is identified based on the sign of the displacement (l), which is the difference between the distance (k) and the radius of the tip (r_p). If it is negative that means the bodies are in contact, otherwise they are separated. Therefore, this acts as the working condition for the contact dynamics subsystem.

In addition, because the drogue is composed of different shapes (frustum and cone), the method of (minimum distance to collision) calculation slightly changes, based on the position of the probe-tip; whether it is inside

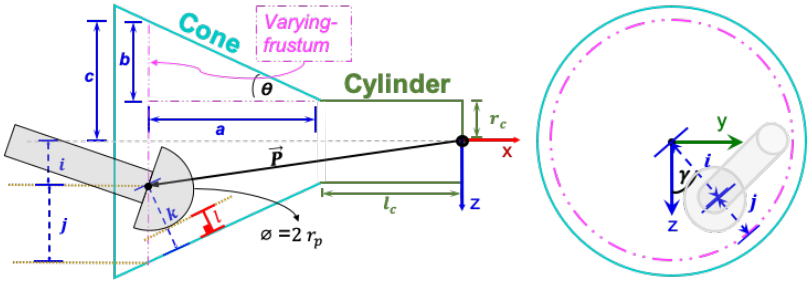

Figure 6.10: Description of Variables used in the contact detection method. Left figure shows XZ-Plane. Right figure shows YZ-Plane.

the frustum, or inside the docking cylinder, etc. Therefore, the drogue is divided into three different zones (as seen in Fig. 6.11). In order to decide in which zone the probe-tip lies, certain conditions are defined w.r.t. the x-axis of $\{F_4\}$ for each zone. By comparing the x-component of the probe-tip displacement vector $({}_{F_4}P_x)$ to each zone's constraint, the zone in consideration is identified. The zones and their conditions are defined as follows:

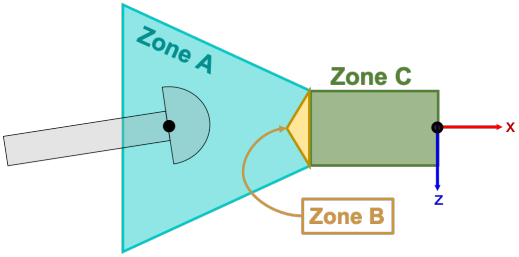

Figure 6.11: The drogue is virtually divided into three different zones.

1. **Zone A**: inside docking cone **(Default Zone)**
   Condition: $(X_{constraint} < \mathbf{P}_x <= (l_c + a))$
   Such that $X_{constraint} = l_c + j\cos\theta\sin\theta$, is the x-position of the intersection point between the constraint-lines of this zone and the z-position of the probe-tip.
   If $\mathbf{P}_x$ (x-component of the probe-tip displacement vector) is bigger

than the constraint defined for zone B and smaller than summation of the length of cylinder and frustum together, then it lies in the docking zone.
Properties:
This is considered to be the default zone, such that all variables stay the same as they were defined.

2. **Zone B**: cylinder-tip.
(This is the transition-zone between docking-cylinder and cone)
Condition: ($l_c < \mathbf{P}_x <= X_{constraint}$)
If the x-component of the probe-tip displacement vector is smaller than the constraints defined and bigger than the length of cylinder, then it lies in this transition zone.
Properties:
This zone looks like a triangle when it is viewed from the XZ plane. In this zone, the actual (or expected) contact point is always the tip of the cylinder. In this zone, the outer radius of the varying-frustum, is non-changing and set to the radius of the cylinder. Accordingly, the distance (j) in YZ plane is updated. As the expected contact point is always the tip of the cylinder, the angle (θ) is always updated in this zone.

3. **Zone C**: inside docking cylinder.
Condition: ($\mathbf{P}_x <= l_c$)
If the x-component of the probe-tip displacement vector is smaller than the length of the cylinder, this means that the probe-tip is inside the docking cylinder.
Properties:
In this zone, the shape is a pure hollow cylinder. Therefore, the variables are updated accordingly. When the probe-tip is in this zone, the following parameters are over-written: angle (θ) is set to zero, the outer radius of the varying frustum stays constant and is set to the same value of the radius of the cylinder, accordingly the distance (j) in the YZ plane is updated.

Algorithm Overview

For a better understanding, an overview of the steps of solutions are introduced (in the sequence of execution) below:

1. Find j

a) find c

b) find i, j

2. Constraints calculation and Zone identification.
3. Calculate k and l
4. Calculate $\hat{\mathbf{n}}_{\mathbf{tc}}$, $\hat{\mathbf{t}}_{\mathbf{tc}}$, $\hat{\mathbf{n}}_{\mathbf{ct}}$and $\hat{\mathbf{t}}_{\mathbf{ct}}$
5. Calculate $\mathbf{K}$, $\mathbf{C_c}$, $\mathbf{C_t}$

Solution

1. Find j:

   a) Plane XZ - Find c:

$$a = P_x - l_c \tag{6.16}$$
$$b = a \tan\theta \tag{6.17}$$
$$c = b + r_c \tag{6.18}$$

   b) Plane XY - Find i, j:

$$i = \sqrt{{P_y}^2 + {P_z}^2} \tag{6.19}$$
$$j = c - i \tag{6.20}$$

2. Constraints calculation and Zone identification:

$$X_{constraint} = l_c + j\cos\theta\sin\theta \tag{6.21}$$

$$Zone(\mathbf{P_x}) = \begin{cases} A & if\ X_{constraint} < \mathbf{P}_x <= (a + l_c) \\ B & if\ l_c < \mathbf{P}_x <= X_{constraint} \\ C & if\ \mathbf{P}_x <= l_c \end{cases}$$

3. Calculate k, l: If the probe-tip lies in the default zone (i.e., Zone A), then no variables need to be overwritten. However, if the probe-tip is in any of the other zones, the following variables need to be overwritten, as in Table 6.7. Accordingly, the variables k and l are also calculated based on the updated variables, if any.

4. Calculate $\hat{\mathbf{n}}_{\mathbf{tc}}$ and $\hat{\mathbf{t}}_{\mathbf{tc}}$:
   To calculate the required unit vectors, the angle gamma γ needs to

Table 6.7: Variables assignment for each zone.

	Zone A	Zone B	Zone C
c	–	$c = r_c$	$c = r_c$
j	–	$j = c - i$	$j = c - i$
θ	–	$\theta = \arctan(\frac{b}{j})$	$\theta = 0$
k	$k = j \cdot \cos\theta$	$k = \frac{j}{\cos\theta}$	$k = j \cdot \cos\theta$
l	$l = k - r_p$	$l = k - r_p$	$l = k - r_p$

be firstly calculated. γ is the angle between the imaginary line i and the z-axis in YZ plane and it is calculated as follows:

$$\gamma = atan2(P_y, P_z) \tag{6.22}$$

Accordingly, the unit vectors of reaction normal and tangential forces from Target to Chaser are as follows:

$$\hat{\mathbf{n}}_{\mathbf{tc}} = \begin{bmatrix} -\sin\theta \\ -\cos\theta\sin\gamma \\ -\cos\theta\cos\gamma \end{bmatrix} \tag{6.23}$$

$$\hat{\mathbf{t}}_{\mathbf{tc}} = \begin{bmatrix} -\cos\theta \\ \sin\theta\sin\gamma \\ \sin\theta\cos\gamma \end{bmatrix} \tag{6.24}$$

In order to find the reaction normal (and tangential) force from the Chaser and Target, the negative vector of the previous unit vectors is simply calculated, as follows:

$$\hat{\mathbf{n}}_{\mathbf{ct}} = -1 \cdot \hat{\mathbf{n}}_{\mathbf{tc}} \tag{6.25}$$

$$\hat{\mathbf{t}}_{\mathbf{ct}} = -1 \cdot \hat{\mathbf{t}}_{\mathbf{tc}} \tag{6.26}$$

5. Calculate $\mathbf{K}$, $\mathbf{C_c}$, $\mathbf{C_t}$:
   As the closest distance vector ($\mathbf{K}$) is always perpendicular to the surface of the drogue, its unit-vector is the same as the Target normal

reaction force ($\hat{\mathbf{n}}_{\mathbf{tc}}$).

$$\hat{\mathbf{k}} = \hat{\mathbf{n}}_{\mathbf{tc}} \tag{6.27}$$

$$\mathbf{K} = k \cdot \hat{\mathbf{k}} \tag{6.28}$$

Based on that, the vector of the actual (or closest) impact point on Target ($\mathbf{C_t}$)and Chaser ($\mathbf{C_c}$) w.r.t. drogue's base ($\{F_4\}$) can be calculated as follows:

$$\mathbf{C_t} = \mathbf{P} - \mathbf{K} \tag{6.29}$$

$$\mathbf{C_c} = \mathbf{P} + r_p \cdot \hat{\mathbf{n}}_{\mathbf{ct}} \tag{6.30}$$

6.3.3.2 Relative Velocity Components

The relative-velocity components, namely: normal relative-velocity (i.e., penetration velocity) and tangential relative-velocity, are required to be calculated for the calculation of the magnitude of the normal contact force and friction force, respectively. Therefore, the relative-velocity ($_{F_4}dV_{43}$) of Chaser's probe-tip-base ($\{F_3\}$) w.r.t. Target's drogue-base ($\{F_4\}$) is projected to the tangential and the normal vector.

$$\mathbf{dV_n} = \hat{\mathbf{n}}_{\mathbf{ct}} \cdot (_{F_4}dV_{43}) \tag{6.31}$$

$$\mathbf{dV_t} = \hat{\mathbf{t}}_{\mathbf{ct}} \cdot (_{F_4}dV_{43}) \tag{6.32}$$

6.3.4 Contact Dynamics

In this subsystem, the magnitude of the normal contact force, as well as the friction force between the two contacting bodies are calculated (Fig. 6.3). The inputs to this subsystem are: the relative displacement between impacting bodies (which would be called "penetration depth" during impact) w.r.t. the drogue base, the relative-velocity, location of the contact point, normal and tangential unit vectors at the contact point. Using these inputs, the magnitude of the impact force and the friction force are calculated. Afterwards, the vector form of the normal impact force and the tangential friction force is calculated, by multiplying the normal unit vector and the tangential unit vector at the impact point between the two bodies by the impact force magnitude and the friction force magnitude, respectively.

6.3.4.1 Contact model

The magnitude of the impact force is calculated using the selected non-linear contact model (i.e., Flores model [Flores et al., 2011]), according to Chapter 4 and in particular Section 4.5. The contact model is implemented exactly as in the 1DOF simulation in Section 5.2.1.2.

6.3.4.2 Friction model

The friction force is calculated using "Tustin friction model". This model combines the standard Coulomb friction model with different phenomena of friction force in one formula. These experimentally discovered phenomena are: viscous friction, static friction and Stribeck velocity [Geenhuizen, 2008]. Since in this simulation, neither fluids nor lubricants are used in the docking scenario, the viscous friction force is neglected. Hence, the Tustin friction model is used as follows:

$$F_f = -sgn(v_{rel}) \cdot F_N \cdot [\mu_1 + (\mu_0 - \mu_1)] \exp^{-\frac{v_{rel}}{v_S}} \tag{6.33}$$

such that F_f is the friction force, sgn is the mathematical sign function, v_{rel} is the relative-velocity between both bodies, F_N is the normal force, v_S is the Stribeck velocity, μ_0 is the friction coefficient during stiction, μ_1 is friction coefficient during perfect sliding.

6.4 HIL Testbed Model

As mentioned in the concept of modeling in Chapter 6.2, the actual HIL testbed has to be taken into consideration during the process of modeling the HIL Testbed. This is required, so that the "HIL Model" would be a reliable representation of the actual HIL testbed. Therefore, in this section the real HIL tested concept and its already existing equipment are described. Afterwards, the HIL testbed modeling method is explained.

6.4.1 Real HIL Testbed Properties

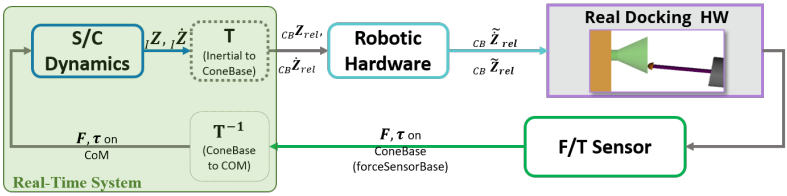

Figure 6.12: Real HIL Testbed Block-diagram

Concept

The concept of the docking HIL testbed proposed by Airbus DS GmbH at Friedrichshafen, Germany (where the testbed will be set up) is that a robotic hardware will be used to realize in real-time the relative motion between the Chaser and the Target throughout the docking simulation. In this test, the probe of the real docking hardware will be mounted on the robotic hardware (see Fig. 1.2), whereas the docking-drogue (aka docking-cone) will be mounted on a 6DOF forces/torques sensor table. This 6DOF sensor table will measure the real forces and torques, due to the real impact between the real docking hardware.

As seen in the block-diagram of the real HIL testbed in Fig. 6.12, the measured forces and torques are fed back into the S/C dynamic models (running on the real-time system), where the new pose and velocity of each S/C is calculated, due to the applied forces and torques. Accordingly, the relative dynamics (pose and velocity of Chaser's probe w.r.t Target's drogue) are sent to the robotic hardware to emulate the motion.

Existing Equipment

A 6DOF force/torque sensor table is already existing at the Airbus DS GmbH facility, which is taken into consideration for the modeling of the HIL testbed. Although the required robotic hardware that will simulate and realize the relative motion is not finally defined yet, a 6DOF hexapod robotic platform is a strong candidate for such an experiment, based on previous studies for this HIL docking testbed [Bondoky, 2015]. Another robotic hardware candidate is a 6DOF robotic manipulator. However, hexapod is more likely to be chosen, due to the foreseen need of fast reaction, high blocking-force capabilities and workspace requirements.

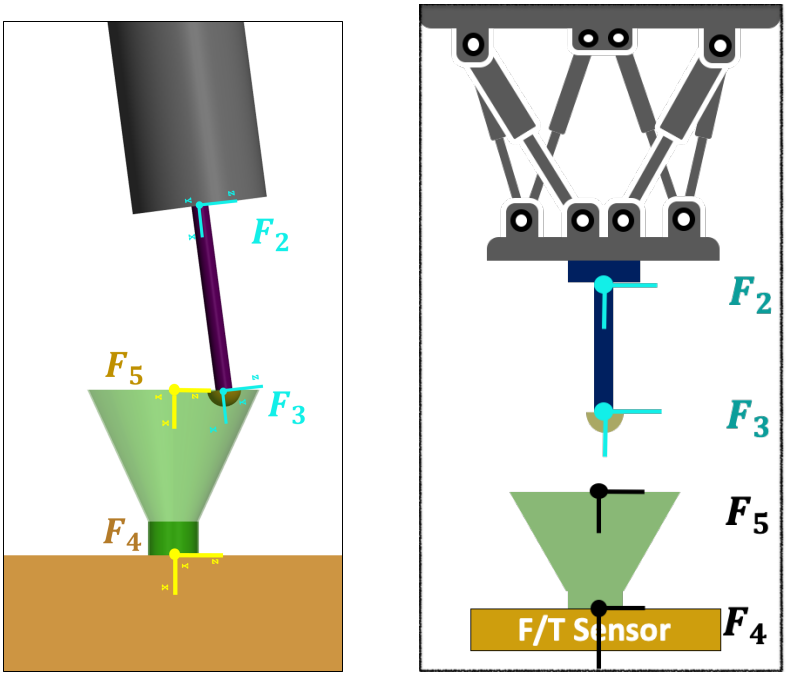

Figure 6.13: (Left) Assigned reference frames in the "Docking Model" versus (the conceptual HIL Testbed Visualization and reference frames (Right)

Real HIL Testbed Description

A visualization of the HIL testbed is depicted in Fig. 1.2 and 6.13. For consistent modeling, the references frames assigned in Fig. 6.13, matches the reference frames that are assigned in the "Docking Model", in the previous section (see Fig. 6.8).

6.4.2 HIL Testbed Model

Based on the HIL modeling concept (see Fig. 6.1) and the description of the real HIL testbed in the previous Section 6.4.1, the model of the HIL testbed is built.

The goal of the HIL testbed model is to predict the performance of the HIL simulation and to estimate the HIL errors (compared to the "Docking Model"), mainly arising from the dynamics and the delays introduced by the HIL equipment. Therefore, the main addition in the "HIL Testbed Model" to the "Docking Model" (like in the 1DOF system in Chapter 5), is the modeling of the HIL equipment, see Fig. 6.14.

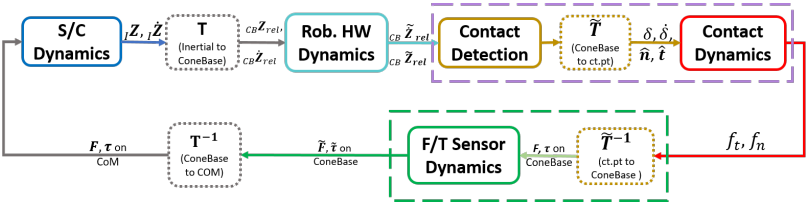

Figure 6.14: HIL Testbed Model Block-diagram

The concept of this modeling promotes it to be implemented in industry. This HIL modeling concept allows the analysis of the docking testbed performance under consideration before building it, which would save efforts and costs. Accordingly, the system engineer could make a justified decision, whether a docking HIL testbed needs to built or not, based on the design requirement.

In the next subsections, the modeling of the HIL equipment (the 6DOF robotic hardware and the 6DOF Force/Torque Sensor) is explained.

6.4.2.1 Robotic Hardware Model

Following the same concept of the 1DOF "HIL Model", the dynamics of the generic robotic hardware is modeled in terms of the total-delay time and

the resolution. In comparison to the 1DOF model, the robotic hardware of the 6DOF model is composed of six components: three for linear motion (S) and three for angular motion (Φ).
Accordingly, each component is modeled as 2nd order Low-Pass System (LPS) to model the total-delay of the hardware (G_{LPS}), as well as a "quantizer" (Q) to model the resolution (of positioning) of the hardware, as depicted in Fig. 6.15
Zero cross-coupling between the DOFs is assumed here. If cross-coupling is not negligible, it could be supplemented by defining a (6x6) transfer function matrix.

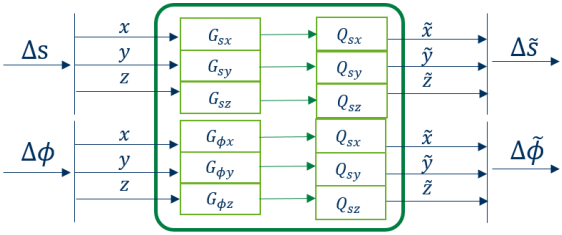

Figure 6.15: Hardware model in the HIL Testbed model

The equation of the 2nd order LPS is exactly the same as Eq. 5.5 in 1DOF modeling.

6.4.2.2 Force/Torque Sensor Model

The 6DOF force/torque sensor is modeled in the same way as the generic 6DOF robotic hardware. It consists of six components as well, i.e., $[f_x, f_y, f_z, \tau_x, \tau_y, \tau_z]^T$. A 2nd order LPS is used for each component to model the total-delay, as well as a quantizer for each component to model the resolution of the sensor. Like the generic robotic hardware model, it is assumed that there is no cross-coupling between axes. If it is needed, it could be modeled by a (6x6) transfer function matrix.

6.5 Simulation and Results

6.5.1 Docking Model Simulation (Case-Study)

In this section, a case-study of a docking mission is presented, where two S/C (Chaser and Target) were required to be modeled to simulate various docking scenarios and to identify the properties of the successful and failed docking scenarios, as well as the key-parameters that affect the docking. This case-study has already been published in [Bondoky et al., 2018], therefore most of this section was mainly taken from this publication and shortened for easier understanding.

The results of this case-study was generated (prior to the finalizing of the "Docking Model") using a SimMechanics-based "Docking Model", which has the same concept, functionality, design and results of the finalized "Docking Model presented in Section 6.3.

By understanding this section, one should be familiar with the capabilities of the "Docking Model" presented above and its applications in real-life problems.

The goals of this case-study are:

- Introduce the key-parameters that affect a docking scenario.
- Simulate different docking scenarios, by varying the key-parameters systematically.
- Identify the boundary (worst-case) successful docking scenario of the proposed spacecraft model.
- Simulate and analyze the worst-case docking scenario.

6.5.1.1 Simulation Properties

A) ***Spacecraft***:
The geometrical properties of the spacecraft were the same as the presented ones in Fig. 6.7, except that the length of the docking-cylinder was $30mm$ and the names of the reference frames were varied. For illustration, a figure of the S/C models of this case-study models are presented in Fig. 6.16. Moreover, the physical properties of each S/C are summarized in Table 6.8.

B) ***Contact Dynamics***
To assign the values of the parameters of the contact model equation

Table 6.8: Physical parameters of simulated spacecraft. Table from [Bondoky et al., 2018]

Chaser		**Target**	
Mass, kg	360	**Mass**, kg	770
CoG (in "Ch-P" frame), [m]	$[-1.833\ 0\ 0]^T$	**CoG** (in "Ta-D" frame), [m]	$[0.847\ 0\ 0]^T$
MoI (in CoG)	[kg·m^2]	**MoI** (in CoG)	[kg·m^2]
I_{xx}	50.341	Ixx	374.734
I_{yy}	122.433	Iyy	385.391
I_{zz}	122.433	Izz	385.391
Probe-tip Material	Polyimide	Drogue Material	Aluminum

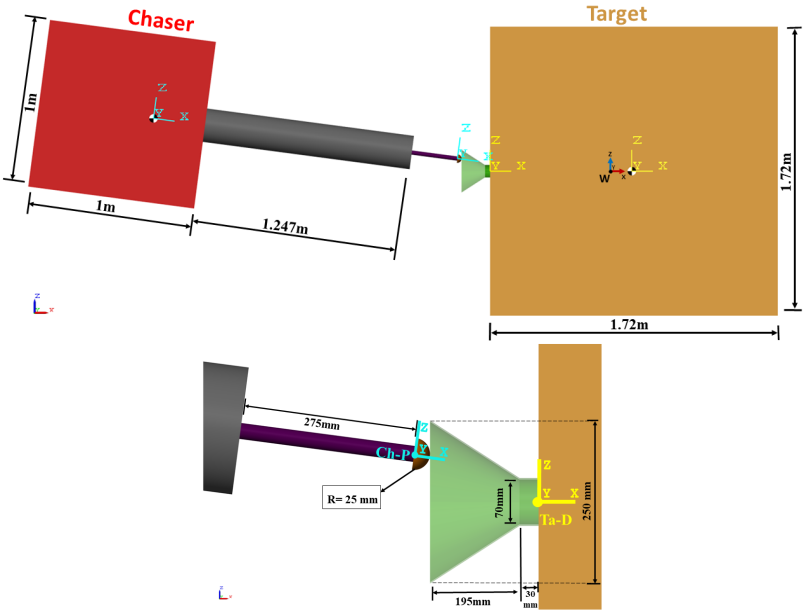

Figure 6.16: Geometrical properties of the spacecraft (Chaser and Target) in this case-study. Figure from [Bondoky et al., 2018]

(see Eq. 4.28), the materials and radii were required. The material of the probe-tip (half-sphere) was assumed to be Polyimide ($\nu_1 = 0.35$, $E_1 = 4 \cdot 10^9$ Nm^{-2}), while the material of the drogue of the Target was assumed to be Aluminum ($\nu_2 = 0.34$, $E_2 = 69 \cdot 10^9$ Nm^{-2}). Meaning, the modeled contact scenario was between a Polyimide half-sphere (probe-tip) and an Aluminum plane (surface inside the cone-shaped drogue), so that the combined Young's modulus $E^* = 4.3068 \cdot 10^9$ Nm^{-2}. As the radius of the half-sphere was 25 mm and radius of plane was considered infinite, the combined radius was $R^* = 25$ mm. Finally, the coefficient of restitution c_r was set to 0.8. For such materials, the stiction friction coefficient (μ_0) equals 0.35, while the sliding friction coefficient (μ_1) is 0.25. Furthermore, the Stribeck velocity (v_S) equals 0.015 m/s.

C) ***Initial Parameters***:
For simplification purposes, the simulation and results were focused on the 2D motion plane XZ-plane, although the model was capable of simulating and analyzing the system in 3D motion. Initializing parameters are presented in Table 6.9. Moreover, the simulation used SimMechanics toolbox in Simulink®and used the (ODE45) Dormand-Prince solver with a variable time-step and a maximum time-step size of 5µs.

Table 6.9: Initial parameters of spacecraft docking simulation. Table from [Bondoky et al., 2018]

	Chaser	**Target**
Position (w.r.t W-frame) [m]	based on varying parameters	$[0.0855\ 0\ 0]^T$
Orientation (w.r.t. W-frame) [deg]	based on varying parameters	$[0\ 0\ 0]^T$
Velocity [m/s]	$[0.1\ 0\ 0]^T$ (represented in the "Ch-P" frame coordinates)	$[0\ 0\ 0]^T$
Angular Velocity	$[0\ 0\ 0]^T$	$[0\ 0\ 0]^T$
Acceleration (linear and angular)	$[0\ 0\ 0]^T$	$[0\ 0\ 0]^T$

D) ***Varying key-parameters***:
In order to find the worst-case docking scenario, the key-parameters that affected the docking were varied. In addition to the key-parameters considered in this case-study, normally, the relative velocity is an important factor for docking scenarios as well, however, it was selected in this study

to be set constant at 0.1m/s for simplification. This value was generally considered as the upper boundary for various previous docking missions. Accordingly, the considered key-parameters (as seen in Fig. 6.17) were varied within the following range:

a) Relative attitude: [-10° to 10°] with an incremental value of 2.5°.

b) Relative translation: [-100mm to 100mm] with an incremental value of 25mm.

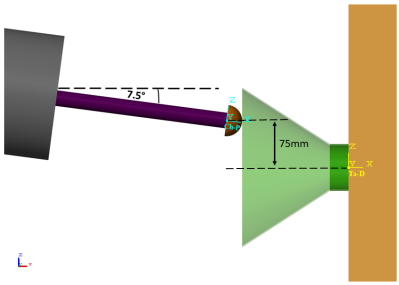

Figure 6.17: Docking scenario key-parameters illustration. Figure from [Bondoky et al., 2018]

6.5.1.2 Successful Docking Criteria

In the original design of the docking mechanism of this case-study there were different latches that act as a locking mechanism, once the probe-tip reaches a certain distance inside the docking cylinder. For simplification purposes of the modeling, only the cone and the cylinder were modeled, without the latches. Therefore, in this simulation the docking was considered successful, once the probe-tip touched the inner-wall (Frame Ta-D) of the Target after passing through the docking cylinder.

6.5.1.3 Case-Study Results

In this section, the results of the docking case-study are presented. Firstly, the identified worst-case docking scenario is presented. Secondly, the dynamic results of the S/C during the docking simulation of the identified worst-case scenario are presented, such that the displacement, the velocity, the forces, the torques, as well as the energy analysis of the whole multibody system are presented.

A) **Worst-Case Scenario Definition**
Worst-case docking scenario can also be defined as the boundary docking scenario, which is important to be identified for each mission beforehand. If the properties (in particular the key parameters) of the real docking scenario in space are not within the range of the successful modeled docking scenarios properties, then the real docking is expected to fail.

In order to find the worst-case docking scenario, the docking simulation was repeated many times and each time one of the key-parameters defined above in Section 6.5.1.1 was changed within the defined range. After testing the full range defined for the key-parameters, two mirrored worst-case docking scenarios were found, as follows:

a) A relative attitude of 7.5° (around Y-axis) and a relative displacement of 75 mm (along Z-axis) between both spacecraft.

b) A relative attitude of -7.5° (around Y-axis) and a relative displacement of -75 mm (along Z-axis) between both spacecraft.

The simulation showed that for the considered S/C, if the relative displacement becomes less than 75 mm (or more than -75 mm), the range of the successful relative-attitude angles increases. Of course, the identified values were dependent on the shape of the docking mechanism and its geometry.

A visualization of the studied successful/failed docking scenarios is depicted in Fig. 6.18, such that each line-segment represents one docking scenario and its docking-probe's pose, while the color and the line type (solid or dashed) represent the state of the docking scenario; green-solid represents successful, red-dashed represents failure.

B) **Dynamic Results**

i. **Displacement, Velocity, Force and Torques**:
In Fig. 6.19, the dynamic results of each S/C are shown for analysis. Linear and angular displacement (see Fig. 6.19a) of each S/C were important to be analyzed and taken into consideration, especially if the docking scenario should be verified using a HIL simulation. The estimated displacements in the results provided an indication concerning the workspace of a potential robotic hardware for the HIL simulation. Likewise for the linear and angular velocity in Fig. 6.19b. Moreover, the forces and torques (see Fig. 6.19c) applied on each S/C during the docking process provided an indication

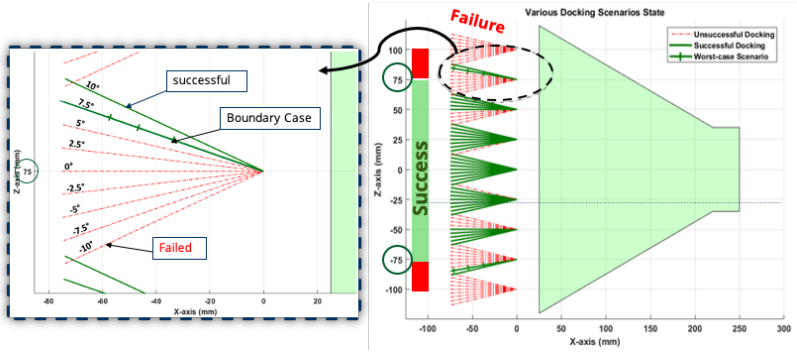

Figure 6.18: Two (mirrored) worst-case scenarios have been defined, after carrying out the docking simulation, using different values of the key-parameters. The successful and failed docking scenarios are depicted in this figure.

about the required force/torque capabilities of a potential robotic hardware.

ii. **Energy**:
In Fig. 6.20, the energy analysis of the whole multibody model is presented. The mechanical energy of the system throughout the whole simulation is depicted in Fig. 6.20a. It is composed of the Kinetic Energy (KE) of the Chaser and Target, as well as the Potential Energy (PE) stored during contact, due to the elastic component of the contact model. On the contrary, the total dissipated energy of the whole system throughout the docking simulation is depicted in Fig. 6.20b. The energy dissipation was mainly due to the friction between both bodies and the dissipation due to impact forces which is due to the damping component of the contact model.

In order to verify the multibody model, the energy balance of the whole system was produced by adding the dissipated energy to the mechanical energy in the system. When adding both of them together, one should get a constant value (which is equal to the initial energy of the system before any impacts) during the whole simulation. In such a case, one can verify that energy is correctly modeled in the system. In Fig. 6.20c, the energy balance of the whole simulation is depicted.

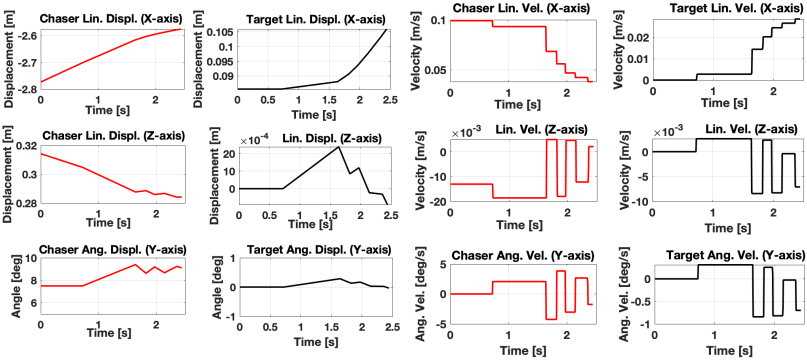

(a) Linear and angular displacement.

(b) Linear and angular velocity.

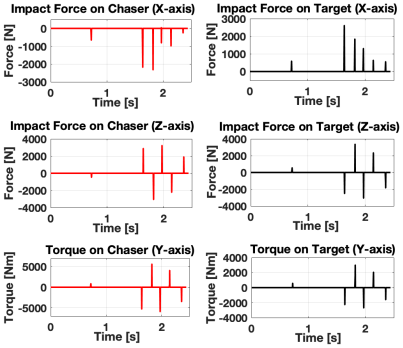

(c) Forces and Torque.

Figure 6.19: Dynamics Analysis Results of the Chaser and Target throughout the Docking.

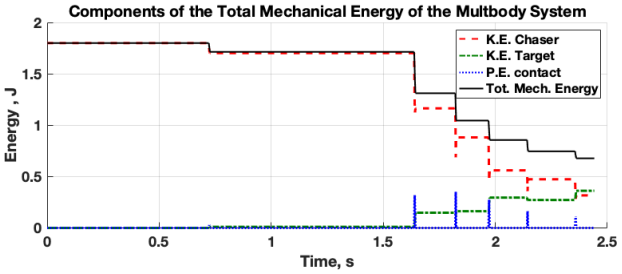

(a) Mechanical energy components.

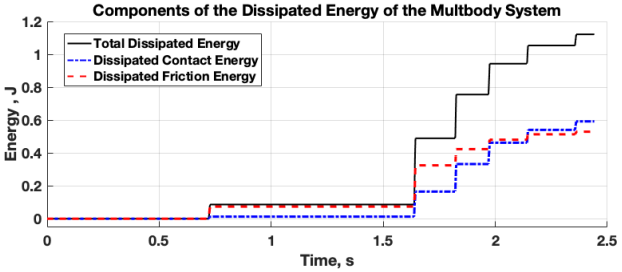

(b) Dissipated energy components.

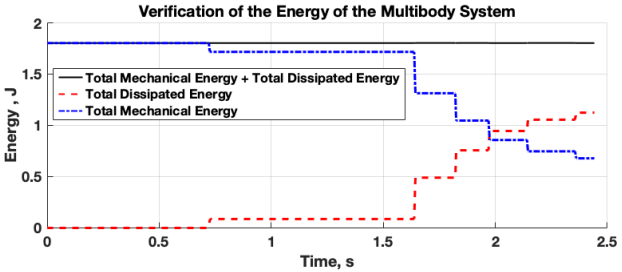

(c) Energy balance of the multibody system.

Figure 6.20: Energy analysis results of the Chaser and Target throughout the docking simulation.

6.5.2 HIL Model Simulation

In this section, a simulation of a docking scenario is presented, which is simulated using the "Docking Model" and "HIL Model" introduced in Section 6.3 and 6.4, respectively. Both models were implemented and ran in the same Simulink® model, which allowed both models to run simultaneously under the same simulation conditions (e.g., solver, time-step, etc.). Moreover, the Simulink® model exported the results of each model, as well as the errors (differences between models) to Matlab® for analysis. In addition, this Simulink® model made use of the SimMechanics toolbox to visualize the docking scenario in both models. This Simulink® model was also used for the the "6DOF HIL Testbed Framework Parametric Study" presented in Chapter 7.

The goal of this simulation is to demonstrate the main capabilities of the "HIL Model" and its concept (introduced in Section 6.4.2). In particular, how the HIL equipment affects the fidelity of the HIL docking simulation in comparison to the software docking simulation ("Docking Model"). Therefore, the main goal here is not to check if the docking scenario would be successful or not (like in the previous case-study in Section 6.5.1), but rather to compare and analyze how different the docking scenario would be when it is carried out using the "HIL Model" simulation, compared to the "Docking Model". Accordingly, the objectives of this simulation are:

- Demonstrate the capability of the HIL modeling concept introduced and implemented above, which promotes it as a practical tool for industry.
- Simulate and analyze a selected docking scenario using the docking "HIL Model" versus the "Docking Model".
- Identify the effect of the HIL equipment dynamics on the docking HIL simulation, by comparing the results of the "HIL Model" versus the "Docking Model".
- Identify the fidelity assessment criteria of the docking HIL testbed.

In the following subsections, the simulation properties are firstly described. Secondly, the simulation conditions and the successful docking criteria are explained. Thirdly, the results of the simulation are presented and discussed. Finally, in Section 6.6, the conclusions drawn from the modeling and simulation presented in this chapter are presented.

6.5.2.1 Simulation Properties

A) **Spacecraft**:
The physical properties of the Chaser and Target S/C are summarized in Table 6.2 and 6.4, respectively. In addition, the geometrical properties of the S/C are presented in Fig. 6.7.

B) **Contact Dynamics**
The contact dynamics properties of this simulation were similar to the one introduced before in the docking simulation of the case-study in Section 6.5.1.1.

C) **HIL equipment**
Each hardware model was parameterized with mainly two parameters (total-delay D and resolution R), which were the same for each of the six components of each hardware.

i. 6DOF Robotic Hardware:
$D_{rob} = 1$ (ms)
$R_{rob} = 10^{-6}$ (m, rad)

ii. Force/Torque Sensor:
$D_f = 0.1$ (ms)
$R_f = 1$ (N, Nm)

D) **Docking Scenario**
This simulation and its results were focused on the 2D motion plane XZ-plane for simplification purposes (like in the case-study in Section 6.5.1.1), although both models ("HIL Model" and "Docking Model") are capable of simulating and analyzing the system in 3D motion.

When it came to selecting the docking scenario, the identified (boundary) worst case-scenario from the case-study (Section 6.5.1.1) was initially selected, in order to test for the worst-case. However, it was observed that due to the modeled HIL equipment, the "Docking Model" successfully docked while the "HIL Model" failed, which led to two totally different incomparable trajectories.

Since the objective of this simulation was to focus on the comparison between the "HIL Model" and the "Docking Model" rather than focusing on successfulness of the docking, a docking scenario was required where the trajectories of both models (from the beginning till the end of the simulation) were not very distinct from each other.

Accordingly, the following docking scenario was selected; initial relative-displacement 7.5mm, initial relative-orientation $-7.5°$ (see Fig. 6.21)

and initial relative-linear-velocity of 0.1m/s in x-direction of probe-tip frame. In fact, this docking scenario is a failed scenario for both models, however, the trajectory of both models are more comparable to each other than the other tested scenarios. Therefore, the introduced failed docking scenario was selected for the simulation.

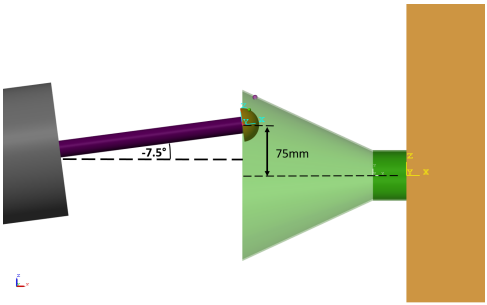

Figure 6.21: Visualization of the selected docking scenario for the ("HIL Model" vs "Docking Model") simulation.

E) **Initial Parameters**
For the initialization of the model, the relative-pose (displacement and orientation) and relative-velocity between the Chaser and Target were some of the main dynamic attributes required for each scenario. Specifically, the pose and velocity of the probe-tip w.r.t. the drogue-tip. Therefore, the initial dynamic attributes of the COM of each S/C were automatically calculated (in an initialization Matlab® script), based on the required relative-pose and relative-velocity of probe-tip $\{F_3\}$ w.r.t drogue-base $\{F_4\}$. As a result, the initial parameters of the considered docking scenario are presented in Table 6.10.

F) **Solver and Time-step**
This simulation ran using the Runge-Kutta solver (ODE45) with a variable time-step, a maximum time-step of 10^{-4} s, absolute tolerance of 10^{-7} and relative tolerance of 10^{-4}. The justification for such selections are explained in Section 7.3.2.

6.5.2.2 Conditions and Docking Criteria

The successful docking criteria were the same as the one introduced in the "Docking Model" (Section 6.5.1.1), where docking is considered successful

Table 6.10: Physical parameters of simulated spacecraft

	Chaser	**Target**
Position (w.r.t W-frame) [m]	[-1.8168 0 -0.1642] ^{T}	[1.0927 0 0]^T
Euler angles [deg]	[0 -7.5 0]	[0 0 0]^T
Velocity (w.r.t. body-fixed COM frame) [m/s]	[0.1 0 0]^T	[0 0 0] ^{T}
Angular Velocity	[0 0 0] ^{T}	[0 0 0] ^{T}
Acceleration (linear and angular)	[0 0 0] ^{T}	[0 0 0] ^{T}

as soon as the probe-tip touches the inner wall of the docking cylinder. The simulation of ("HIL Model" or "Docking Model") stopped either when the docking was successful or when the probe-tip became outside of the drogue.

6.5.2.3 Results

In this section, the simulation results of the selected docking scenario are presented. Firstly, a visualization of the docking trajectory of each of the "HIL Model" and the "Docking Model" is shown. Afterwards, the docking S/C dynamic results of the "Docking Model" versus the "HIL Model", along with the error (difference between both models) are presented. Based on the analysis of the results, the S/C dynamic results are presented again but focusing only on the "first impact". Finally, the energy analysis of both models of the considered docking scenario are presented.

A) **Docking Trajectory**
Figure 6.22 shows the trajectory of the probe-tip w.r.t. the drogue throughout the docking simulation. The figure shows that the only common impact (out of the 8-9 impacts) between the "Docking Model" and the "HIL Model" was the first impact.

B) **Dynamics Attributes**
Figure 6.23 depicts the three main dynamic attributes that were observed during the docking simulation. In order to simplify the comparison between both considered models, the analysis was focused on the magnitude of the selected attributes. These three attributes were

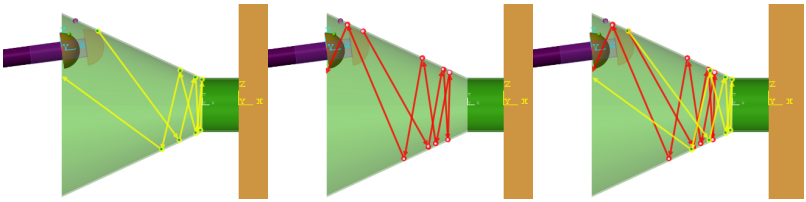

(a) Docking Model **(b)** HIL model **(c)** Both Models

Figure 6.22: Trajectory of relative-displacement of Probe-tip w.r.t. Target's Drogue of both (Docking and HIL) models

the same main quality control factors considered in the "Generic HIL Testbed Framework Analysis Tool" (as explained in Section 3.3), which are:

i. Contact force.

ii. Penetration-depth (normal relative-displacement).

iii. Penetration-velocity (normal relative-velocity).

The graphs of each of these selected attributes can be seen in Fig. 6.23. In each graph, the "Docking Model" and the "HIL Model", as well as the error (difference between both models) are depicted.

It is observed in the relative-displacement (upper graph in Fig. 6.23) that after the first impact, each of the two models ("HIL Model" and "Docking Model") starts to behave totally different compared to each other.

Moreover, it is noticed that the impact forces (middle graph) of the "HIL Model" are more stiff compared to the "Docking Model", such that the second impact force of "HIL Model" is greater than that of "Docking Model" and the same applies for the following impacts.

Based on the results in Fig. 6.23, it is observed that the second impact in the "HIL Model" takes place earlier than in the "Docking Model", which is explained by looking at the relative-velocity (bottom graph). The graph shows that the relative-velocity after the first-impact in the "HIL Model" is faster than in the "Docking Model". Hence, the second-impact of the "HIL Model" is earlier than in the "Docking Model".

Therefore, it was noticed that not only after each impact the "HIL Model" became more intense (higher force, higher penetration-depth

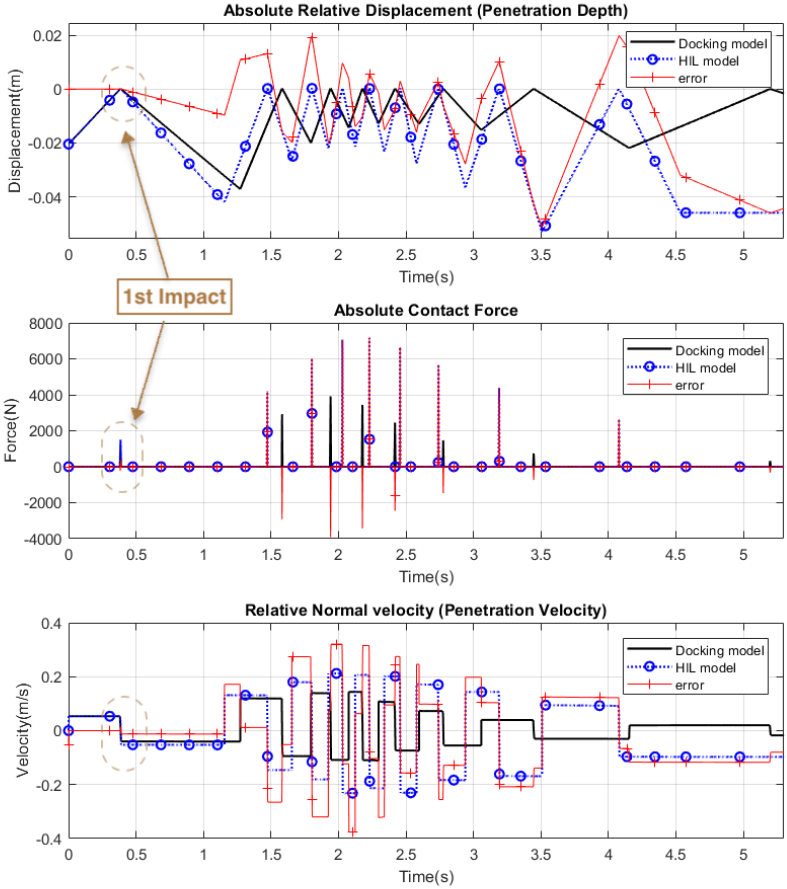

Figure 6.23: Dynamics attributes for the considered docking scenario of the "HIL Model" vs "Docking Model" and the error (difference between both models). (Top graph) Relative displacement between S/C throughout docking. Impact starts as soon as the relative displacement is more than or equal to zero. Positive relative displacement means that bodies are in contact, while negative means they are separated. (Middle graph) Magnitude of the normal contact force. (Bottom graph) Relative normal velocity.

and higher relative velocity), but also both models started to behave totally different, which was mainly due to the modeled dynamics of the HIL equipment introduced in the "HIL Model". This has made it very challenging to find a common property for comparison and analysis of a certain docking scenario simulation using both the "HIL Model" and the "Docking Model", except for the first impact which was the single common aspect between both models and it is discussed next.

C) **First-Impact Analysis**
The "first impact" was the single common aspect between both models, such that the docking simulation of both models before the first impact took place were (almost) identical. Therefore, in Fig. 6.24 the three main attributes are presented and analyzed again but with the focus on the first impact only.

The errors in the impact arose due to the dynamics (time-delays, as well as the resolution) introduced in the hardware models (i.e., robotic hardware model and F/T sensor model) of the "HIL Model". The time-delay effect can be observed in the three graphs of Fig. 6.24, where the "HIL Model" (dashed-blue) is delayed compared to the "Docking Model" (solid black).

In the "Docking Model", during an impact, the continuous contact force (applied on each of the impacting bodies) was updated at each time-step of the simulation, based on the penetration-depth and the penetration-velocity values from the *"S/C dynamics"*. (See Fig. 2.1 and 6.1). This contact force was then applied to the multibody dynamics at the next time-step, which accordingly updated the position and velocity. As a result, the penetration-depth and the penetration-velocity were updated, therefore contact force was updated. Obviously, the contact force was held constant for the time duration of each time-step until it was updated in the next time-step.

On the contrary in the "HIL Model", due to the time-delays implemented in the hardware models, the contact force was held constant for a longer time-period (i.e., as long as the implemented time-delay of the hardware model), which was longer than the time-step and the "Docking Model". In this case, the *"S/C dynamics"* perceived it in a way that a constant external contact force was acting on the bodies for a longer time-duration, until the duration of hardware time-delay was over, afterwards the contact force was updated.

Therefore, as seen in Fig. 6.24, an impact in the "HIL Model" shows to

have errors (i.e., higher penetration-depth, velocity and contact force) in comparison to the "Docking Model".

D) **Energy**

In this section the energy analysis of the whole multibody model are presented.

Firstly, in Fig. 6.25 the mechanical energy and its components of the whole multibody system of each model are depicted. Mechanical energy is composed of the Kinetic Energy (KE) of the Chaser and Target, as well as the Potential Energy (PE) stored during contact, due to the elastic component of the contact model. All graphs of the "Docking Model" showed to be physically reasonable (i.e., KE reduced after each impact).
On the other hand, the "HIL Model" appeared to be unrealistic, due to the fact that the KE did not decrease as it should. The reason for that was the introduced dynamics (e.g., delays) in the modeled hardware. Due to the modeled time-delay in the "HIL Model", the multibody dynamics model perceived the delayed-constant-force as a large impulse. Accordingly, the force and the relative-velocity between the bodies (in the "HIL Model") became much larger after each impact than they should have been (as in the "Docking Model"). Since KE energy is directly dependent on the velocity, the perceived higher relative-velocity leads to higher KE. Hence, KE errors occurred.

Secondly, in Fig. 6.26, the energy balance (bottom graph), total dissipated energy (middle graph) and mechanical energy (upper graph) of the whole system are depicted. Physically speaking, the energy is mainly dissipated due to the friction between both bodies, as well as the impact force (where energy is dissipated by being converted into other forms of energy, e.g., heat, vibration). Likewise in the simulation, energy was dissipated due to friction and impact (due to the damping component of the contact model). It is observed in the dissipation energy graph (middle graph in Fig. 6.26) that the "Docking Model" appears to behave as expected, (i.e., some energy is lost after each impact, which is a proportion of the total initial energy of the system).
On the contrary, the "HIL Model" shows a very unrealistic physical behavior, where the dissipated energy (after many impacts) becomes larger than the initial total energy of the system, at the beginning of the simulation. This error occurred due to the introduced dynamics of the hardware model (i.e., delays).

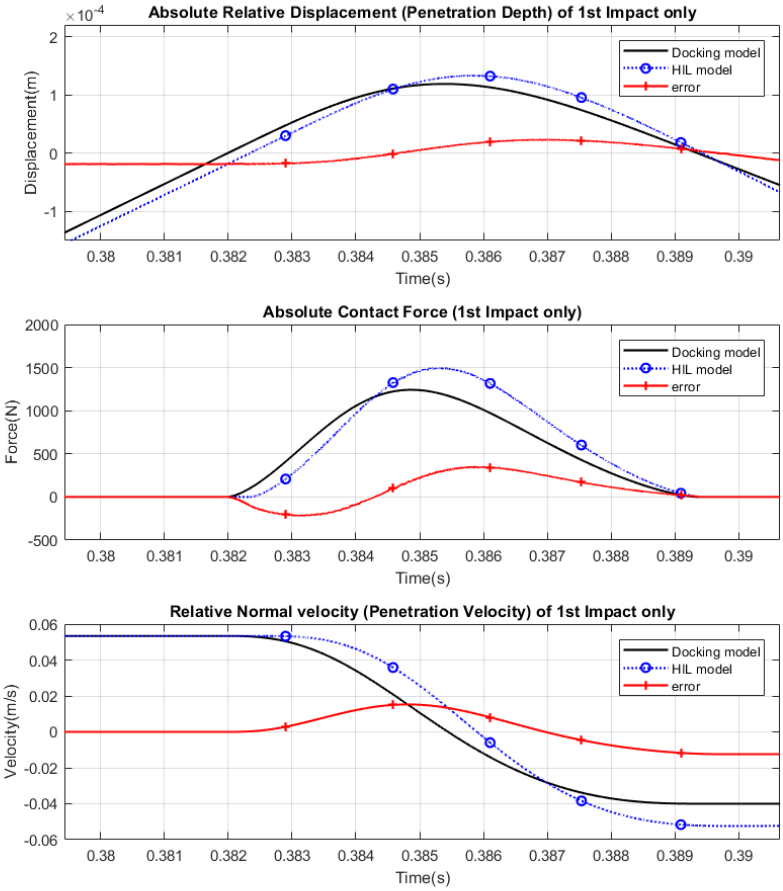

Figure 6.24: Dynamics attributes of only the first impact only of the simulated docking scenario of the "HIL Model" vs the "Docking Model" and the error (difference between both models). (Top) Relative displacement between S/C throughout docking. Impact starts as soon as the relative-displacement is more than or equal to zero. The positive relative displacement indicates that the bodies are in collision, while the negative means they are separated. (Middle) Magnitude of the normal contact force. (Bottom) Relative normal velocity.

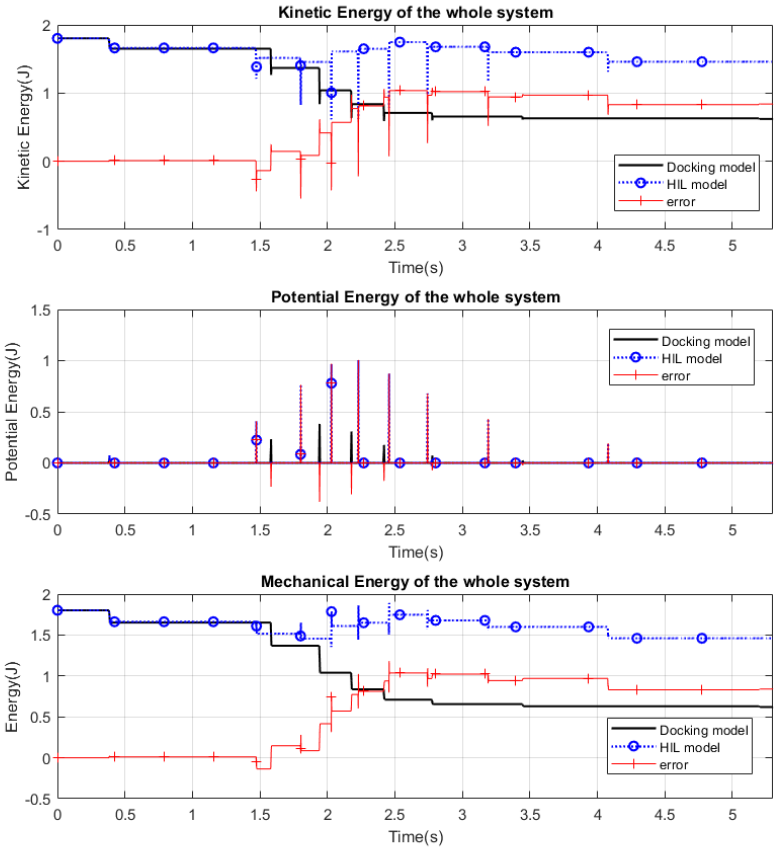

Figure 6.25: Mechanical Energy (Bottom) and its components (kinetic energy (Top) and potential energy (Middle) of the multibody system during docking simulation

One valid reason why this dissipated-energy error took place is that the dissipation-energy depends on the damping component of the contact model, which is dependent on the relative-velocity before and after impact [Kraft, 2016]. By observing the relative-velocity in the "HIL Model", it is noticed that relative-velocity after-impact is higher than relative-velocity before-impact. This error occurred after each impact and it started to accumulate during the simulation. Accordingly, one observes the dissipation energy error in the "HIL Model".

Finally, to verify the multibody model, the energy balance of the whole system was analyzed (see bottom graph of Fig. 6.26). The energy balance is the summation of the dissipated and the mechanical energy in the system, which ideally should always be a constant value during the simulation and equal to the initial energy of the system. The energy balance of the "Docking Model" is shown to be constant through the whole simulation, which is a validation of the accuracy the multibody model. On the other hand, in the "HIL Model" (because of the accumulated kinetic and dissipated energy errors discussed before), it appears that the energy balance (i.e., mechanical energy plus dissipation energy) of the system increases (at least) two times more than the initial energy at the beginning of the simulation.
Obviously, that was not physically reasonable, however this simulation showed a representation of how the docking HIL simulation would react, which provided an estimation of its HIL fidelity. In addition, these "HIL Model" results would be used as reference for the future real 6DOF docking HIL simulation.

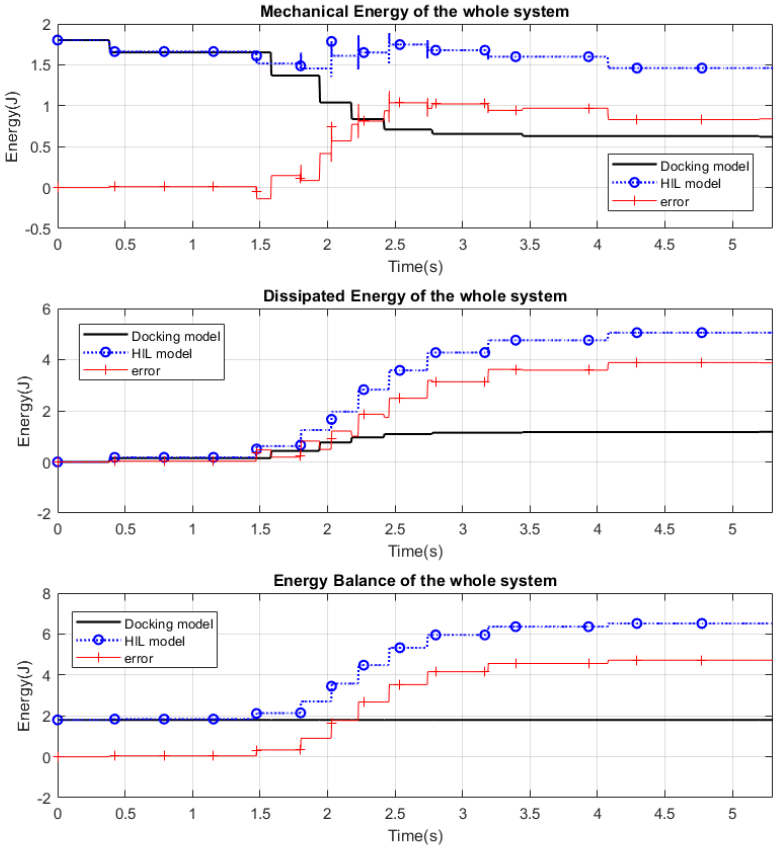

Figure 6.26: Energy balance of the whole system during the simulation is used to verify a multibody system. Energy balance (Bottom) is the summation of the mechanical energy (Top) and the dissipated Energy (Middle) in the whole system

6.6 Conclusions

The following conclusions are drawn from the work introduced in this chapter:

1. "Docking Model" can simulate, visualize and verify docking scenarios.

2. "Docking Model" can be used to estimate the failed and successful docking scenario's properties of the two docking S/C (by varying the docking scenarios key-parameters; pose and velocity). This provides an insight to the engineers of the docking missions concerning the scenarios that must be excluded to assure a successful docking. This promotes the "Docking Model" as a practical tool for the industry.

3. A model of the docking HIL simulation testbed was built, which simulated the effect of the HIL equipment on the docking simulation. The "HIL Model" gave an insight about the fidelity of the considered HIL simulation testbed. Moreover, the "HIL Model" results acted as a reference for the real docking HIL simulation to be built.

4. Based on the simulations in this chapter, the "first impact" was considered the single common qualitative aspect in the docking simulation of the "HIL Model" versus the "Docking Model", because it was observed that the errors (differences between "HIL Model" and "Docking Model") increased and accumulated after each impact, which led to two incomparable trajectories. Therefore, the fidelity analysis for such a system (e.g., 6DOF HIL analysis in the following chapter) shall be focused on what happens exactly during a single impact and how and why errors occur, rather than focusing on the whole docking scenario.

Chapter 7

6DOF HIL Testbed Framework Parametric Study

In this chapter, a 6DOF HIL generic parametric study is carried out using the "Generic HIL Testbed Framework Analysis Tool" (presented in Chapter 3), which is one of the main contributions of this work. This parametric study is focused on the considered 6DOF docking system and its HIL testbed model.
In this chapter, the concept of the the generic parametric study and the considered parameters are briefly introduced, afterwards the results and the conclusions of the study are presented and discussed.
The goal of this chapter is to carry out a systematic investigation of the considered HIL system and analyze it. This helps to identify the preliminary requirements for the 6DOF HIL testbed. In addition, by investigating the considered scenario and analyzing the results generated through this tool, one would understand the capabilities and the functionality of the "Generic HIL Testbed Framework Analysis Tool".

7.1 Introduction

7.1.1 Overview

In the third step of the work-flow, the investigations of the HIL testbed framework were expanded from 1DOF to a 6DOF. This 6DOF framework included the full range of motion of the spacecraft dynamics in space, as well as the effects of the HIL equipment's dynamics on the HIL simulation.

The results of this study assisted to identify the key-parameters, which are required to be taken into consideration when designing a HIL docking testbed. A key-parameter is a parameter in a design-space which has a high sensitivity to the metrics under evaluation. This study could be seen as a sensitivity analysis. With this study one could also identify the dynamic requirements of the HIL instruments, so that the figure-of-merits of each

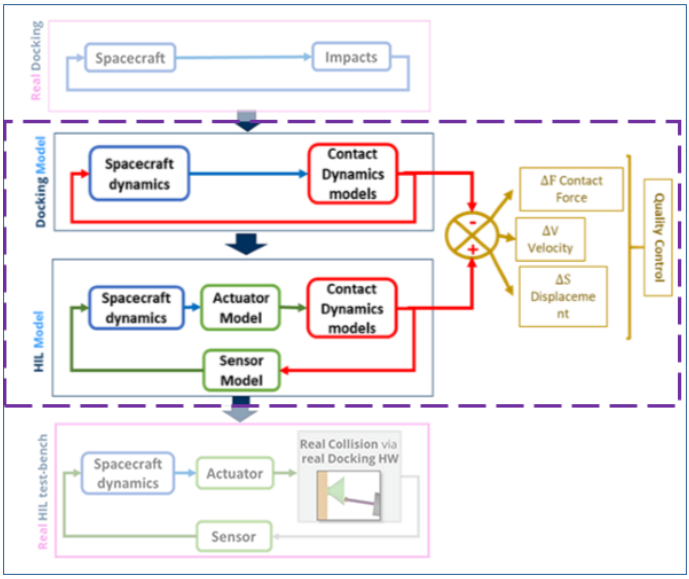

Figure 7.1: In this chapter, the performance analysis on the HIL testbed model is carried out using the "Generic HIL Testbed Framework Analysis Tool". Analysis of the "HIL Model" versus the physical "Docking Model" was carried out and HIL errors were estimated.

hardware can be identified, according to the desired framework.

This study was built in a generic way such that it would be easily utilized to identify any HIL testbed design frame, so that one could estimate and predict the testbed fidelity. Accordingly, a system engineer could make a justified decision whether a testbed should be implemented or not.

7.1.2 Objectives and Study Questions

Like the 1DOF parametric study, the objectives of this parametric study were formalized in a form of questions, which were required to be answered through this study. These study questions are:

1. Which are the key-design-parameters from the "HIL design-space" that have the most influence on the HIL errors?

2. Which are the key-parameters in the other design-spaces that influence the HIL errors?

3. What are the predicted errors percentage of the HIL simulation, when the key-parameters of the design-spaces are varied?

4. Are there critical values of the selected key-parameters, which should be taken into consideration when designing a HIL testbed for the system under consideration?

7.2 Methodology

To find the answer of the study questions above, the "Generic HIL Testbed Framework Analysis Tool" was used to systematically vary the parameters of each of the considered design-spaces. It allowed to re-run the simulation in a systematic way, each time one of the considered parameters within the defined range was changed, in order to study the whole range. Moreover, it calculated the HIL errors for each scenario. Accordingly, one could investigate the different scenarios considered to determine how the HIL errors change, when each of the parameters change. This parametric study could be seen as a sensitivity analysis as well.

The numerical range of each of the parameters has been selected, after consideration with the adequate realistic values in real life. The range of robotic-hardware motion resolution and the robotic-hardware total-delay have been selected, after doing a market survey of the available hardware. Likewise for the force/torque sensor. Likewise for the other design-spaces.

In the same way as in the 1DOF parametric study in Section 5.4, three design-spaces were considered in this study: HIL, Spacecraft, Contact Dynamics. Fig. 3.1 illustrates the available design-spaces and their parameters. Moreover, Fig. 3.2 depicts all the parameter in a clearer form.

In this study, it was practical to firstly start by investigating which of the parameters of the "HIL design-space" was more influential, as the HIL equipment would clearly have a high impact on the docking simulation. Afterwards, the other design-spaces were considered.

7.2.1 First-Impact Analysis

In this study, only the first impact of the 6DOF docking simulation were analyzed, due to the following reasons:

1. The first impact was the only common aspect between the "HIL Model" and the "Docking Model" that could be compared and analyzed in a qualitative manner. After the first impact, the HIL and Docking models reacted in a very different way. After the first impact they were seen as two totally independent scenarios. (See Section 6.5.2.1-C for details). Therefore, fidelity analysis was only carried out on the first impact.

2. One of the parametric-study's goals is to investigate a wider range of the design parameters, to see their effect on the HIL fidelity. Therefore, analyzing the first impact only allowed the expansion to the full range of the considered parameters in the parametric study.

7.2.2 HIL Fidelity Attributes

Different attributes were utilized to define quality control. The HIL errors (described in details in Chapter 3.3) were calculated based on the values of these attributes (from the "HIL Model" and the "Docking Model"). These attributes are the following:

1. Normal contact force
2. Normal relative-displacement (penetration depth)
3. Normal relative-velocity (penetration velocity)
4. Multibody system energy:
    a) Total energy balance
    b) Mechanical energy:

i. Kinetic energy

ii. Potential energy

7.3 Simulation

7.3.1 Simulation Properties

All the parameters considered in the parametric study were assigned specific constant values as noted below, unless explicitly defined elsewhere. Meaning, each parameter of each design-space was assigned a range of values. The simulation was repeated multiple times and each time a new value from the defined range was assigned to the parameter. Therefore, as a rule in this study, unless parameters of a certain design-space are explicitly defined, the default simulation parameters are assigned as follows:
Relative-pose vector = $[x\ y\ z\ \phi\ \theta\ \psi]' = [0\ 0\ 0.075\ 0\ -7.5\ 0]'$ (m, deg),
Relative-velocity vector = [0.1 0 0 0 0 0]' (m/s, deg/s),
Chaser-mass = 360 kg, Target-mass = 760 kg,
Probe-tip Material = Polyimide, Drogue Material = Aluminum,
Coefficient of restitution = 0.8 and Contact Model= Flores et al.

7.3.2 ODE Solver

There are many factors that are taken into consideration when a solver and a time-step are to be selected, such as, accuracy, stability of the system, simulation time and effort, etc. One possible approach to select a solver and a time-step for such complex non-linear system is the testing of several solvers and time-steps and comparing their results to the reference results in order to assess the quality of these solvers.

Firstly, one has to identify the reference results, which was not trivial for the considered system, as it was a complex non-linear system. A possible method to identify the reference results is using the trapezoidal implicit solver (ode23t), which is considered to be accurate but has a long simulation computational time. Due to the long simulation computational time of the ode23t solver, it could not be used as the main solver for this parametric study. However, it was useful to identify the reference results, because short simulation computational time was not the main requirement for the reference results, but accuracy.

Therefore, to identify the reference results, the system was simulated using Simulink®, Matlab®2015b) with the trapezoidal implicit solver (ode23t),

with a variable time-step and a maximum time-step set at 10^{-4} s, which is the best value that the computer could execute.

After several testing and comparison of the results of the different solvers to the reference results, the Runge-Kutta ODE solver (ode45) was selected for this study with a variable time-step, a maximum time-step of 10^{-4} s, an absolute-tolerance of 10^{-7} and a relative-tolerance of 10^{-4}.

7.4 Discussion and Results

7.4.1 HIL Design-space

In the HIL design-space (see Section 3.2 for details), four parameters were included and were varied systematically within the following range:

1. Robotic-hardware total-delay (D_{rob})
   $[0.5, 1-10$ (step of 1), $20-100$ (step of 10)] (ms)
2. Robotic-hardware displacement resolution (R_{rob})
   $[0.1, 1, 5, 10, 50, 100, 500, 1000] \times 10^{-6}$ (m),(deg)
3. Force/Torque sensor total-delay (D_f)
   $[10, 100, 500, 1000]$ (µs)
4. Force/Torque sensor resolution (R_f)
   $[0.1, 1, 10]$ (N),(Nm)

In order to study the results in more detail, the simulation has been repeated over each of the values within the full range of the considered parameters. In particular, for dynamics of the robotic-hardware (total-delay D_{rob}, resolution R_{rob}), the simulation has been repeated to test them all w.r.t. each other. Meaning, for each value of total-delay (D_{rob}), the simulation has been re-run each time with a new value of (R_{rob}) until the full range of (R_{rob}) was considered. This assisted not only to identify which parameters were more sensitive than others, but also at what range they were sensitive and when.

In the following sections, the results of the parametric study are presented and discussed in detail.

7.4.1.1 Robotic-Hardware Resolution (R_{rob})

Figure 7.2 depicts the HIL errors due to the various robotic-hardware parameters: R_{rob} (along the x-axis) and D_{rob} (represented in the legend). The

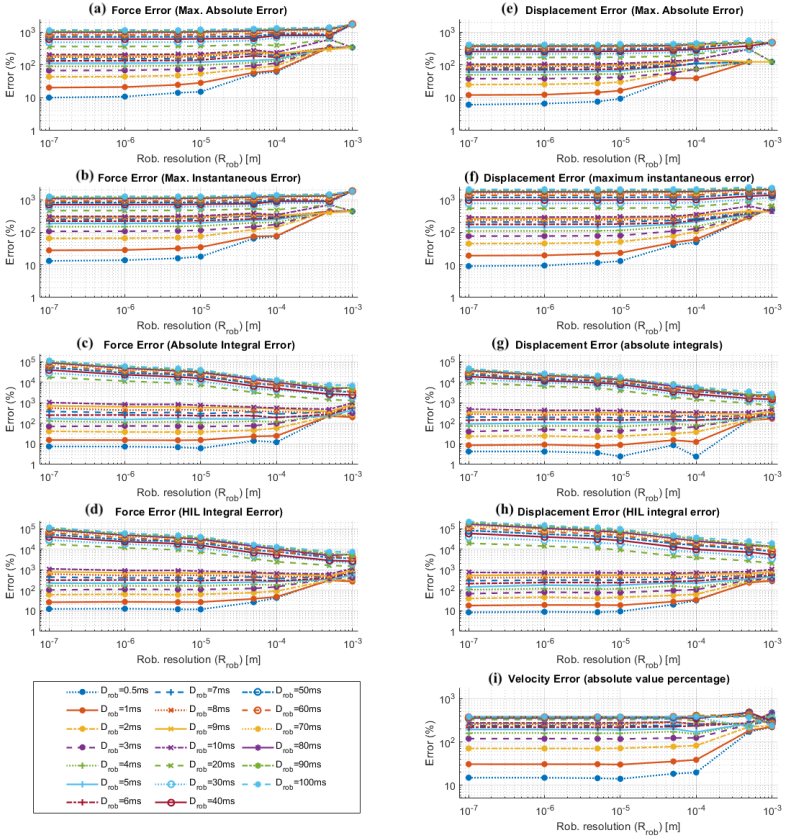

Figure 7.2: Effect of varying robotic-hardware resolution (R_{rob}), at various total-delay (D_{rob}), on HIL errors

goal here is to analyze how the robotic-hardware parameters affect the HIL errors.

In order to analyze the errors, only the "non-integral errors" are firstly presented and analyzed, then the "integral errors" are followed. Afterwards, the "energy errors" graphs are presented. Finally, the main conclusions are presented. For a detailed explanation of the errors, see Section 3.3.

Observations

1. **Non-integral Errors**:
   (Max. Absolute (Fig. 7.2a, 7.2e), Max. Instantaneous (Fig 7.2b, 7.2f))

   a) when ($R_{rob} < 10^{-4}$m) and ($D_{rob} > 4$ms):
   It is observed in this range that the HIL errors are not notably affected, as R_{rob} changes along the x-axis within the range: $[10^{-7} - 10^{-4}]$ (m). While they are significantly affected as D_{rob} changes withing the range: $[4 - 100]$ (ms). As a result, one can conclude that R_{rob} is not influential in this range, while D_{rob} is more influential.

   b) when ($R_{rob} < 10^{-4}$m) and ($D_{rob} < 4$ms):
   It is observed in this range that HIL errors are still significantly affected, as D_{rob} changes within the range: $[4 - 100]$ (ms). However, unlike before, the HIL errors are notably affected as R_{rob} changes along the x-axis within the range: $[10^{-7} - 10^{-4}]$ (m).
   As a result, one can conclude that in a docking system, there may be a *"trade-off point"* between the dominance of two parameters on the HIL errors, where both parameters shall be considered influential.
   For this system, both parameters (D_{rob}, R_{rob}) were influential at the identified *"trade-off point"*, i.e., when ($R_{rob} < 10^{-4}m$) and ($D_{rob} < 4ms$).

   c) when ($R_{rob} > 10^{-4}$m):
   It is observed in this range that HIL errors are significantly affected, as R_{rob} and D_{rob} vary within the defined range. However, while studying the scenarios of ($R_{rob} > 10^{-4}$ m), it was observed that the contact dynamics graphs (i.e., penetration-depth) appear to be totally distorted.
   One reasonable explanation is that the R_{rob} was greater than or equal to the maximum penetration-depth (in the "Docking

Model") in the first-impact (between 0.1mm and 0.2mm). As a result, the modeled hardware did not simulate motion well and HIL simulation was not reliable anymore.
Accordingly, it is concluded that the R_{rob} should be 10 times smaller (i.e., better) than the expected maximum penetration-depth in the "Docking Model", otherwise the simulation is not valid.

2. **Integral Errors:**
(Absolute Integral (Fig. 7.2c, 7.2g), HIL Integral (Fig. 7.2d, 7.2h))

   Surprisingly, it is observed that the HIL errors decrease (i.e., improve), as the R_{rob} increases (i.e., worsen), when D_{rob}>10ms.
   One possible explanation for this is that quantization was used to model the robot's resolution (refer to Section 6.4.2). When larger resolution values were modeled (i.e., worse performance), the curve shape became more distorted, due to the quantization. Accordingly, the total area-under-the-curve of the quantized signal was smaller compared to the original signal, which was then perceived as a smaller HIL error.

3. **Energy Errors**:
   The HIL energy errors may be useful for further analysis of HIL docking system. They are depicted in Fig. 7.3 as an example, but without analysis.

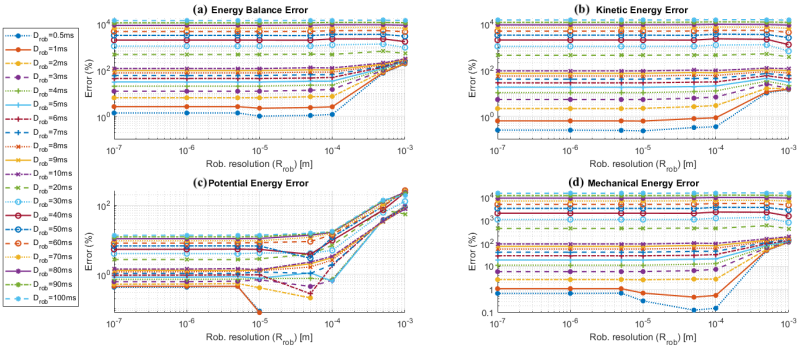

Figure 7.3: Effect of varying robotic-hardware resolution (R_{rob}) at various total-delay (D_{rob}), on the HIL errors

Conclusion

- Robotic-hardware total-delay (D_{rob}) is a more influential key-parameter than the resolution (R_{rob}).
- For this system, if the total-delay of the robotic-hardware is less than 4 ms ($D_{rob} < 4$ ms), its resolution (and the *trade-off point*) must be considered as a key-parameter as well.
- Robotic-hardware resolution (R_{rob}) should be 10 times smaller than max. penetration depth. Hence, in the considered model (R_{rob}) should be 10 times smaller than 0.1 mm (i.e., $R_{rob} <= 0.01$ mm)
- Generally, it is important to identify if there is a "*trade-off point*" in each case-study, so that the HIL testbed requirements are accordingly set.

7.4.1.2 Robotic-hardware Total-delay (D_{rob})

In order to analyze the previous HIL errors observations deeply, the same data is presented in Fig. 7.4, however this time the D_{rob} is on the x-axis, while R_{rob} is represented in the legend. These graphs provide deeper insights and confirmation to the analyses of the previous section.

Observations

1. **Non-integral Errors**:
   (Max. Absolute (Fig. 7.4a, 7.4e) and Max. Instantaneous (Fig 7.4b, 7.4f))
   a) When ($R_{rob} < 10^{-4}$ m):
      It is observed that the HIL errors are directly proportional to the D_{rob} (for all values). In addition, by observing how HIL errors change (for each R_{rob} value) as D_{rob} increases along the X-axis (i.e., slope), it is noticed that the positive slope is steeper compared to Fig. 7.2. Accordingly, this confirmed that the D_{rob} is more influential than R_{rob}.
   b) When ($R_{rob} < 10^{-4}$ m) and ($D_{rob} < 4$ ms):
      One can notice that the behavior of the HIL error curves slightly changes before and after the $D_{rob} = 4$ ms point. The R_{rob} starts to slightly affect the HIL errors, only when $D_{rob} < 4$ ms. This highlighted the *"trade-off point"* discussed in the above section.

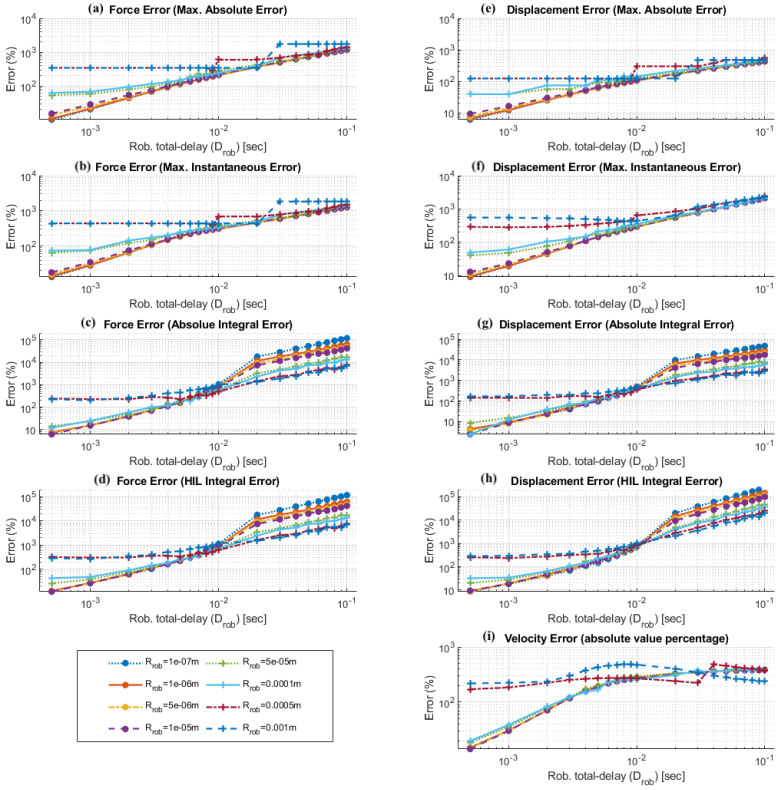

Figure 7.4: Effect of varying robotic-hardware total-delay (D_{rob}) at various resolution (R_{rob}), on the HIL errors

Hence, both parameters (D_{rob}, R_{rob}) are required to be taken into consideration, if the HIL framework lies within this range.

c) When ($R_{rob} > 10^{-4}$ m):
It is observed that HIL errors are much larger when $R_{rob} > 0.1$ mm and they remain constant (for a certain range) and independent of D_{rob} value. Only when D_{rob} value is worse, the HIL errors start to change. This confirms what was presented in the previous section that R_{rob} should be 10 times less than max. penetration-depth (i.e., in this case $\approx$ 0.1 mm), otherwise simulation is not reliable. The same proposed explanation (in the previous section) applies here as well.

2. **Integral Errors:**
(Absolute Integral (Fig. 7.4c, 7.4g) and HIL Integral (Fig. 7.4d, 7.4h))

The same surprising observation that was discussed in the previous section (i.e., integral errors improves, when R_{rob} is worsened), can also be seen in Fig. 7.4, when $D_{rob} > 10$ ms. The same explanation applies.

3. **Energy Errors:**
Fig. 7.5 depicts the energy HIL errors again, but in a different format.

Conclusion
By analyzing the same data but in a different form, the same observations and conclusions of the previous section are confirmed.

7.4.1.3 Force/Torque Sensor Total-delay (D_f)

Figure 7.6 shows that D_f is not affecting the HIL errors at all, for all the considered values of the (D_{rob}) and at R_{rob} of $1\mu m$. Hence, this concludes that F/T sensor total-delay within the considered range is not a key-parameter.

7.4.1.4 Force/Torque Sensor Resolution (R_f)

Figure 7.7 shows that R_f is not affecting the HIL errors at all either, for all the considered values of the (D_{rob}) and at R_{rob} of $1\mu m$. Hence, this concludes that F/T sensor resolution within the considered range is not a key-parameter.

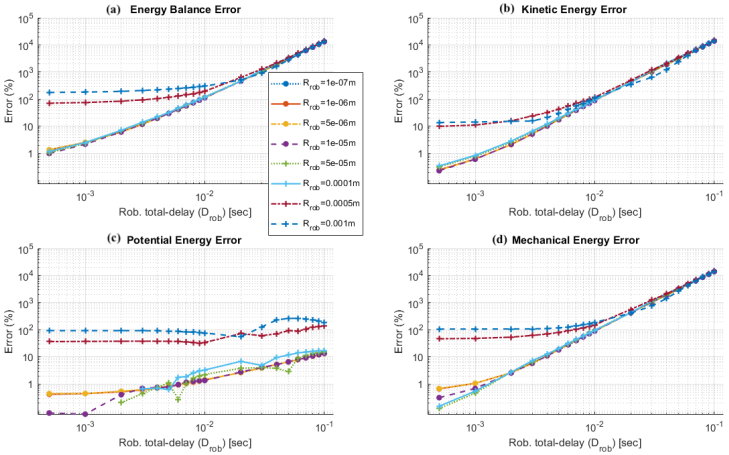

Figure 7.5: Effect of varying robotic-hardware total-delay (D_{rob}) at various resolution (R_{rob}), on the HIL energy errors

7.4.1.5 Summary

Based on the investigation and the parametric study on the HIL design-space of the considered system, the following conclusions are drawn (which answer some of the study questions presented in Section 7.1.2):

1. The robotic-hardware parameters are more influential than the parameters of the Force/Torque sensor.

2. Based on the observations from the considered range of robotic-hardware parameters (see Section 7.4.1.1 and 7.4.1.2) and the Force/Torque sensor parameters (see Section 7.4.1.4 and 7.4.1.3), it is concluded that the robotic-hardware total-delay parameter (D_{rob}) is the most influential key-parameter in the HIL design-space.

3. If the total-delay of the robotic-hardware is less than 4 ms (i.e., $D_{rob} <$ 4ms), the robotic-hardware resolution (and the trade-off point) must be considered as an influential "key-parameter" as well.

4. The robotic-hardware resolution (R_{rob}) should be 10 times smaller than max. penetration depth. Hence, in the considered model (R_{rob}) should be 10 times smaller than 0.1mm (i.e., $R_{rob} <= 0.01$mm)

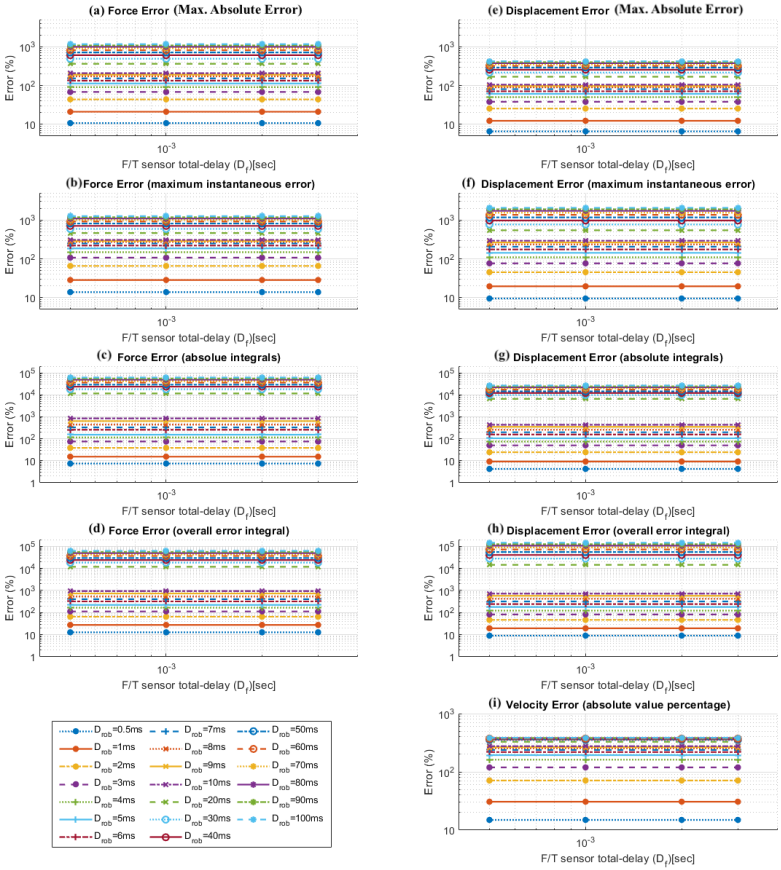

Figure 7.6: Effect of varying Force/Torque total-delay (D_f) at various robotic-hardware total-delay (D_{rob}), on the HIL errors

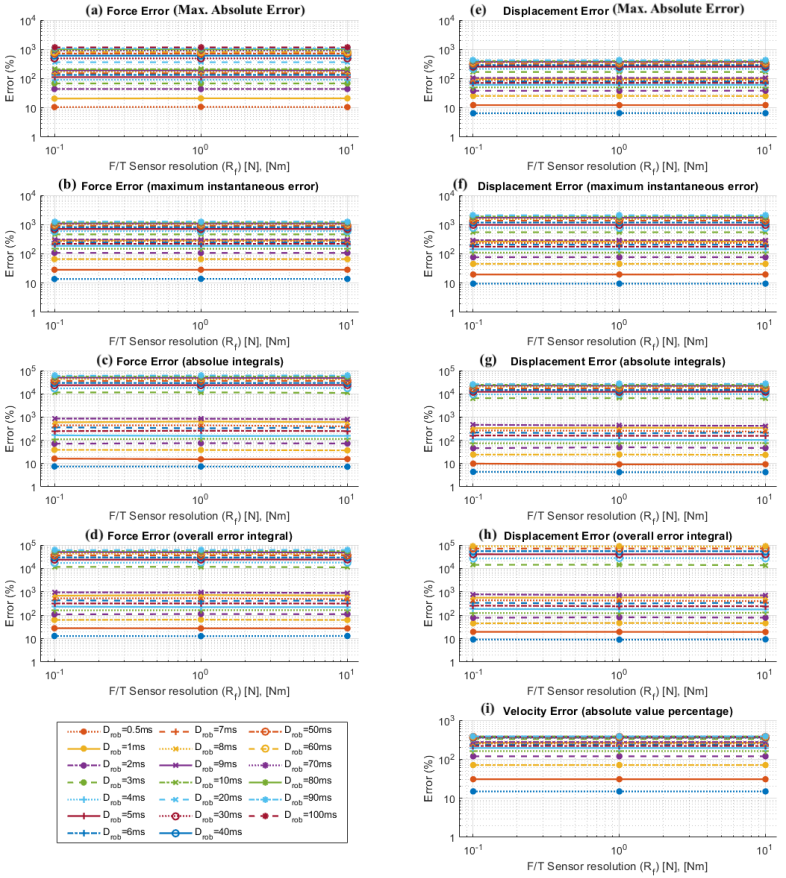

Figure 7.7: Effect of varying Force/Torque resolution (R_f) at various robotic-hardware total-delay (D_{rob}), on the HIL errors

7.4.2 Spacecraft Design-space

Two parameters in this design-space are considered: the initial relative velocity and the masses. Both parameters were varied systematically against each of the values of the robotic-hardware total-delay considered range. The robotic-hardware total-delay is the only parameter that was selected to be tested against the parameters of this design-space, because it showed that it has the most significant effect on the HIL fidelity.

The objective here is to see how the performance and the fidelity of the HIL testbed are affected by the parameters of the spacecraft design-space. The results of this test are very interesting and useful, as they are relevant to the real-life applications.

7.4.2.1 Masses

The number of the micro, or mini S/C (e.g., cubesats mass is $\approx$ 10 kg), or small S/C (i.e., 100-1000 kg) is increasing in space. The need for such satellites to dock together, perhaps autonomously, would also increase. Therefore, it is important to know how the masses of the docking S/C affect the fidelity of docking HIL simulation. Accordingly, the masses of the spacecraft (Chaser and Target) are varied within the following range, respectively: [10-10, 35-35, 35-70, 50-100, 175-375 and 360-770] (kg).

The medium or large spacecraft (1-100 ton or more, such as ISS), could be tested using this tool as well.

Previously, in the 1DOF parametric study (see Section 5.4), it was concluded that:

1. The ratio between the masses of the S/C is not an important factor on the HIL docking fidelity, rather the equivalent mass of both spacecraft.

2. The smaller the masses of the docking S/C, the more challenging the HIL simulation becomes. The reason is that the contact duration during impacts of small spacecraft requires a robotic-hardware with a fast response to simulate the motion properly. Hence, the required robotic-hardware figure-of-merits become challenging.

Observations

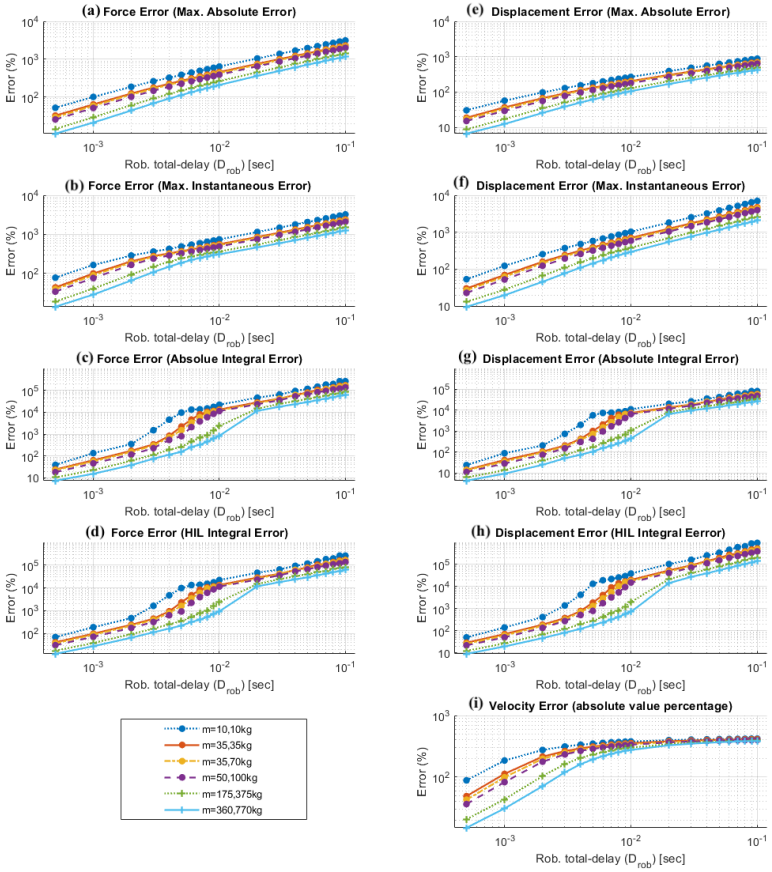

Figure 7.8: Effect of varying impacting body-masses, at various robotic-hardware total-delay (D_{rob}), on HIL errors

1. Figure 7.8 confirms what was observed in the 1DOF parametric study that the smaller the equivalent-mass, the higher the errors. The explanation for it was that the larger the mass, the faster the reaction of the bodies, i.e., the shorter the contact duration (impact duration). Therefore, due to the delays from the HIL equipment, the shorter the contact duration, the higher the errors, see Fig. 7.9a.

2. It is also observed that the equivalent mass of the docking S/C affects the max. impact force, as well as the max. penetration depth, as seen in Fig. 7.9b. Moreover, the velocity after impact (after separation) is also affected by the equivalent mass, such that the smaller the equivalent mass, the worse the velocity error, as seen in Fig. 7.9c. This is mainly due to the same conclusion above that the faster the impact, the worse the fidelity of the HIL simulation.

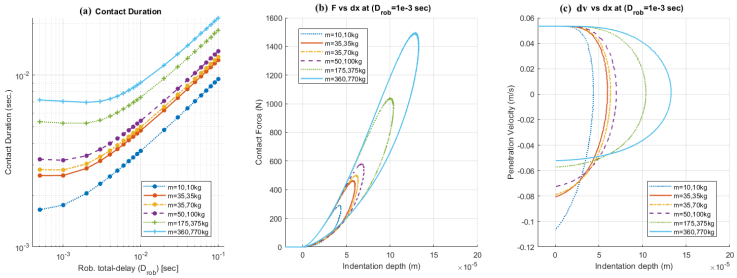

Figure 7.9: Contact dynamics analysis of various impacting body-masses at robotic-hardware total-delay ($D_{rob} = 1$ms). Graph (a) shows the duration where bodies where in contact. Graph (b) shows the hysteresis-diagram of force versus penetration-depth. Graph (c) shows the velocity before and after impact.

Conclusions

- The results from the 6DOF mass variation versus the robotic-hardware total-delay (D_{rob}) confirmed the same conclusions (about mass variation) that were drawn in the 1DOF parametric study.

- Masses of Spacecraft (in particular, the equivalent-mass of both S/C) is one of the significant key-parameters for the HIL simulation.

7.4.2.2 Velocity

Docking velocity is one of the most important factors that influence the docking success. Usually, docking takes place with relative velocities less than 0.1m/s. Therefore, it would be interesting to see the effect of the relative velocity on the HIL fidelity. Accordingly, the initial relative-velocity is varied within [0.05 - 0.15] (m/s) in the Chaser's body-fixed frame, in order to widen the testing range. Important to mention is that the initial relative-velocity is not the same as the penetration-velocity. Penetration-velocity is the rate of change of normal-distance between the two surfaces colliding with each other.

Observations

The results in Fig. 7.10 show that indeed the initial relative-velocity is directly proportional to the HIL errors, as it was proved in the 1DOF parametric study. However, it is obvious from the results below that varying the impact velocity is not significant on the HIL errors.

Nevertheless, the initial impact-velocity plays an important role on the max. impact force, as well as the max. penetration depth, see Fig. 7.11.

Conclusions

Initial impact velocity is not a significant key-parameter for the HIL fidelity. However, it is important to be taken into consideration as it affects the max. impact forces and max. penetration dept.

7.4.3 Contact Dynamics Design-space

7.4.3.1 Material

Out of the three parameters in this design-space (i.e., material, coefficient-of-restitution, contact model), only the material was varied as it is most relevant to real-life docking scenarios. The materials were varied in parametric study against the various considered robotic-hardware total-delay values. The objective here is to see how the material affects the HIL fidelity, as well as to check if the material of the impacting body is dependent on its mass or not. Meaning, would it make a difference if the material of the Chaser's (360kg) probe-tip and the Target's (760kg) drogue were aluminum and polyimide, respectively or vice versa?

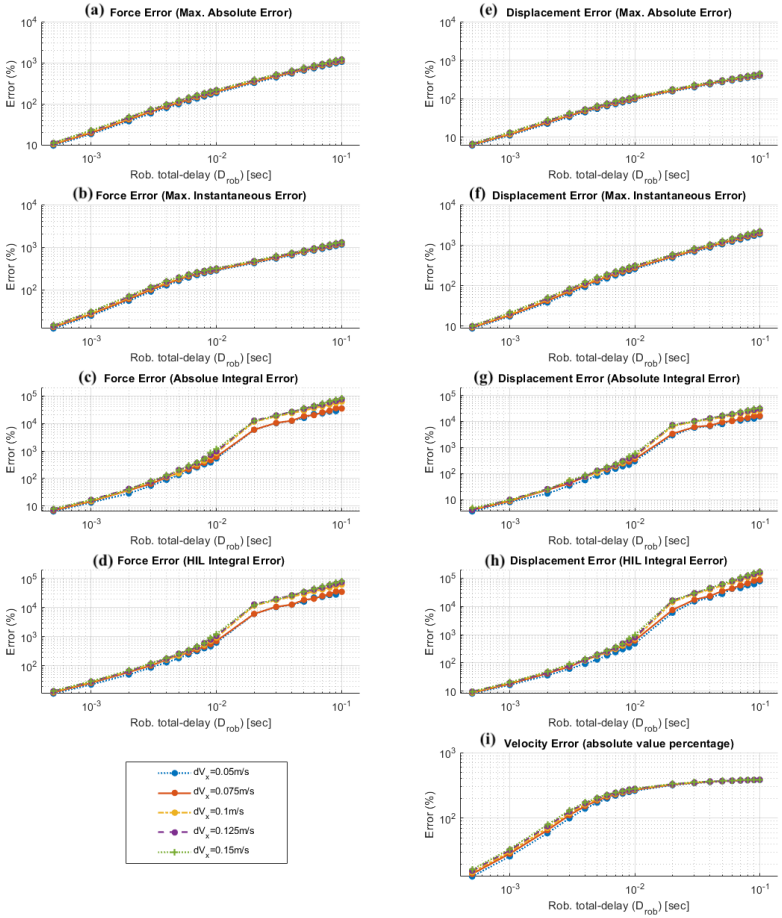

Figure 7.10: Effect of varying initial impact velocity at various robotic-hardware total-delay (D_{rob}) on HIL errors

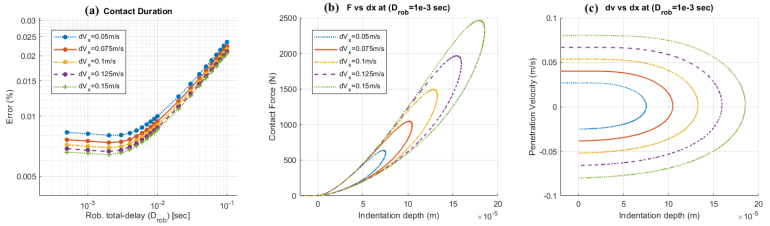

Figure 7.11: Contact dynamics analysis of various varying initial impact velocity at robotic-hardware total-delay ($D_{rob} = 1$ ms). Graph (a) shows the duration where bodies where in contact. Graph (b) shows the hysteresis-diagram of force versus penetration-depth. Graph (c) shows the velocity before and after impact.

Two main material variations were considered in this test; Aluminum (Alu) and Polyimide (Poly).

Observations

1. The results in Fig. 7.12 show that the material type indeed affects the HIL fidelity. The stiffer the impacting materials, the higher the HIL error. This has also been previously proven in the 1DOF parametric study.

2. It is interesting to see that the material combination of the two impacting spacecraft is independent of their masses. This is proved in Fig. 7.12 and 7.13 that the two cases (Alu-Poly and Poly-Alu) are exactly the same, even-though the Chaser and Target have different masses.

3. Figure 7.12a shows that the stiffer the material, the shorter the contact-duration; hence the higher the error. The hysteresis graph in Fig. 7.13b depicts this more clearly; in case of (Alu-Alu) the max. impact force becomes much higher, compared to the other two scenarios. Likewise, the stiffer the material, the less the max. penetration depth becomes.

Conclusion

The material of the impacting parts of the docking mechanism affects the HIL fidelity. Therefore, material is considered as one of the important key-parameters for the HIL simulation of the considered system.

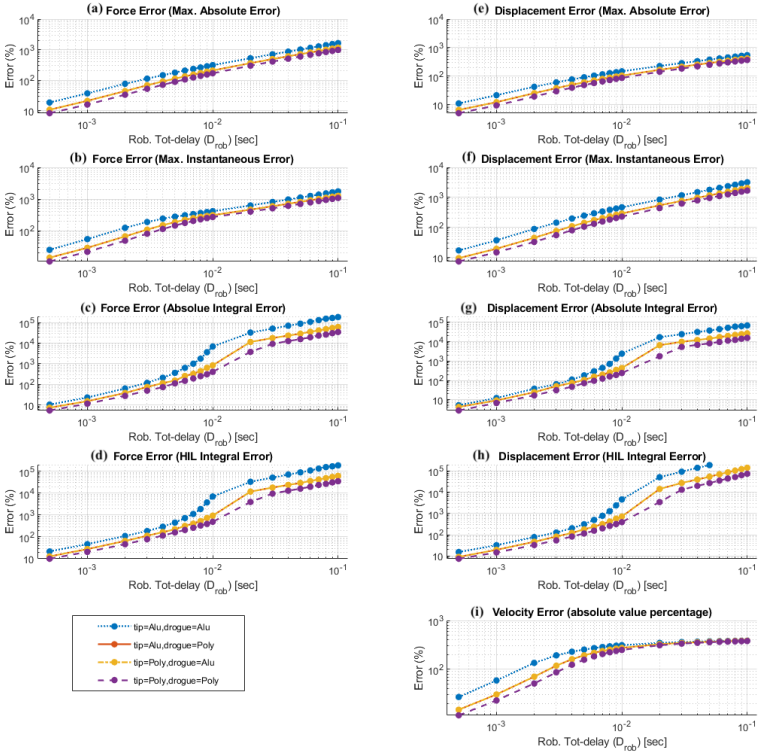

Figure 7.12: Effect of varying the material at various robotic-hardware total-delay D_{rob}, on the HIL errors

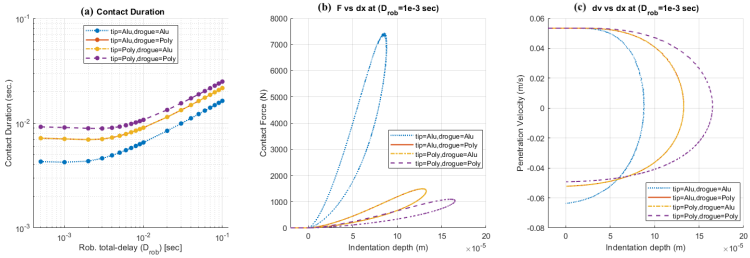

Figure 7.13: Contact dynamics analysis of various impacting body-material at robotic-hardware total-delay ($D_{rob} = 1$ ms). Graph (a) shows the duration where bodies where in contact. Graph (b) shows the hysteresis-diagram of force versus penetration-depth. Graph (c) shows the velocity before and after impact.

7.5 Conclusion

In this chapter, a parametric study was carried out using the "Generic HIL Testbed Framework Analysis Tool" (presented in Chapter 3) in order to investigate the 6DOF "Docking Model" and the "HIL Model" (which includes HIL equipment models). In this study, all the available design-spaces and their defined parameters were investigated. Accordingly, the key-parameters were identified. Moreover, the errors of various scenarios have been estimated.

The parametric-study and fidelity-analysis were based on the first impact only, as it is the only common aspect between the "HIL Model" and the "Docking Model" that can be compared and analyzed in a qualitative manner.

The summary and the conclusions of this study (based on the considered docking system and its HIL testbed model) are as follows:

1. The parametric study on the HIL design-space parameters showed that the robotic-hardware total-delay (D_{rob}) was the most influential parameter out of the four parameters in the HIL design-space. In addition, the robotic-hardware resolution (R_{rob}) did affect the HIL errors and it must be considered too. (This is especially clear in the considered model, when the ($D_{rob} < 4$ms)). Therefore, it is important to take into consideration both parameters while investigating the HIL testbed design-space. **This answers the first study question.**

2. The parametric study on the spacecraft design-space showed that out

of the two considered parameters (masses, initial impact velocity), only the spacecraft masses was significant, while the initial impact-velocity did not significantly affect the HIL results. Furthermore, the parametric study on the contact dynamics design-space showed that the material is a key-parameter. **This answers the second study question**.

3. In addition, multiple different scenarios have been simulated which allowed to analyze how the HIL simulation errors change, as the influential parameters are varied. **This answers the third study question.**

4. Moreover, the parametric study showed that the robotic-hardware resolution (R_{rob}) should be 10 times smaller than the expected max. penetration depth. Hence, in the considered model, the R_{rob} should be 10 times smaller than 0.1 mm (i.e., $R_{rob} <= 0.01$ mm) **This answers the fourth study question**.

As a result, it was concluded that it is very challenging to realize a 6DOF HIL simulation for the whole docking scenario (i.e., not only first impact) without compliance, due to the challenging robotic-hardware requirements (i.e., figure-of-merits).
In order to expand and realize a 6DOF non-compliant docking HIL simulation to the whole scenario, one should study the sources of the errors in an impact, in order to predict them and compensate for them in the "HIL Model". This way, errors accumulation shall be relatively compensated, hence; both models ("Docking Model" and "HIL Model") shall have a comparable whole docking trajectory. This is considered as future work.

Chapter 8

HIL Simulation Experiment for Contact Dynamics Validation

In this chapter, the experimental results of the 1DOF HIL simulation (two-specimen impact) tests are presented. These results serve as a significant contribution to the contact dynamics research. The one-of-a-kind testbed was designed and built specifically for the validation of the contact dynamics of the docking model in this work. Therefore, in addition to the results presented in this chapter, a detailed explanation of the testbed, its equipment are presented, including how the testbed was set up and validated. The objectives of this chapter are as follows:

1. Present and explain in detail the unique 1DOF HIL testbed, its model, as well as the whole setup of the HIL real-time simulation.
2. Identify the model of the controlled-piezoactuator and the force-sensor, in order to be implemented in the *Simulated HIL*.
3. Present the effectiveness for using the "Generic HIL Testbed Framework Analysis Tool" to define the accepted and rejected simulation scenarios, based on the testbed capabilities.
4. Present the experimental results of the (contact dynamics) HIL simulation, by testing the impacts of various materials, velocities, as well as masses.
5. Provide the results of the contact dynamics HIL simulation of various scenarios, as a contribution to the contact dynamics research.

The structure of this chapter is as follows: firstly, the HIL simulation experiment is introduced in Section 8.1, where the motivation behind the experiment, the experiment overview and the objectives are presented. Secondly, in Section 8.2, the HIL testbed is introduced in detail, as well as its equipment, implementation and validation. In that section, the estimated models of the actual piezoactuator and the force-sensor are presented, which were inserted in the *Simulated HIL* model (refer to Fig. 2.3). Thirdly, in

Section 8.3, it is explained how the HIL simulation was carried-out and its properties. Fourthly, in Section 8.4.1, the results of one of the scenarios is presented in detail, while the results of all the other test scenarios are presented in Appendix C. Finally, the summary and the conclusion of this chapter are presented in Section 8.5.

8.1 Introduction

HIL simulation is a real-time simulation, which consists of a software part and a hardware part. The software part consists of a model of the physical system (or at least part of it) and is carried out on the real-time processor. The hardware part executes the real physical process and contains the interface with the real-time processor to receive output signals from the real-time processor and send the measured values to the real-time processor. Compared to a full computer simulation, a HIL simulation increases the realism of the experiment, because of using the actual hardware.

8.1.1 Motivation for Experiment

One of the main motivation aspects to build and run this experiment was the lack of the validation of contact dynamics model considered (Flores model [Flores et al., 2011]), under the required test-criteria (i.e., impact velocity, material, masses). Thus, the need arose to build a 1DOF HIL testbed to test and validate the contact dynamics model implemented in the docking model of this work. In addition, this 1DOF HIL testbed acted as a simpler lower-cost precursor to the 6DOF HIL simulator. Moreover, it allowed to demonstrate the feasibility and the principle-of-operation performance of the HIL simulation.

The experimental results of this HIL testbed serve as a significant contribution to the contact dynamics research. Although several contact dynamics experiments have been already carried out before to validate contact models, this testbed outperformed many of them for various of reasons:

1. Many researchers made use of gravitational acceleration for contact dynamics testing, e.g., free-fall impacts [Zhang and Sharf, 2009]. Although these tests were easy and efficient, they would be very challenging for the testing of slow-impacts (i.e., 0.01 - 0.1 m/s), due to the challenge of the exact positioning of the specimen in the required position at the beginning of the simulation, in order to achieve the

required speed at impact. In the considered 1DOF HIL test, such low-velocity impacts were conducted much easier.

2. Another test was carried out using quasi-static testing (using a linear ball-screw actuator), due to the complexity of finding a fast enough actuator to realize the real-impact scenario [Boos and McPhee, 2011]. This however totally ignored the damping component of any contact-model. In the considered HIL testbed, this has been taken care of due to the use of piezoactuator, which has high acceleration capabilities.
3. Another test used a robotic arm to simulate the impact via HIL simulation [Gonthier, 2007]. However, the robotic arm's stiffness and delay introduce limitations for the proper testing of contact dynamics models, which requires fast precise micro-meter resolution motion capability, as well as high force-blocking. This has been overcome in the introduced HIL testbed by using a 1DOF piezoactuator, which has a fast precise motion with micro-meter resolution and a high force-blocking capability.
4. Moreover, in the presented HIL test, the masses and velocities of the impacting bodies could simply be modified on the computer models, which allowed the testing of different scenarios easily. In addition, this testbed allowed to test impacts of various materials with each other.

8.1.2 Experiment Overview

Based on the validation concept introduced in Section 2.3 and Fig. 2.3, a brief introduction about how the experiment was set up is presented, to provide an overview of the system. As mentioned before, the HIL simulation is a real-time simulation that has a software part and a hardware part.

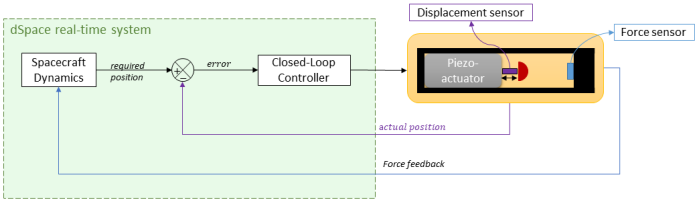

Figure 8.1: Simplified Block-diagram of Testbed

The real-time system "dSpace DS1103" was used as the real-time sim-

ulator processor. The HIL simulation environment included the following hardware: a piezoelectric actuator, a force sensor and a displacement sensor (i.e., eddy-current differential-sensor), as seen in Fig. 8.1. The software contained the 1DOF two rigid-spacecraft dynamics model, as well as the closed-loop control algorithm designed for the positioning of the piezoactuator.

The piezoactuator emulated the relative-distance (between the two spacecraft), which was calculated by the *"Spacecraft Dynamics"* model. Once the piezoactuator impacted the specimen fixed to the force sensor, the real contact force (measured by the force sensor) was fed-back as an input signal to the *"Spacecraft Dynamic"* model in the real-time dSpace system. Accordingly, the position of each spacecraft was updated and thus the new relative-displacement was sent to the actuator to be emulated.

Each experiment provided all required data that can be used to validate any contact model, which includes penetration-depth (from the measured displacement of the piezoactuator), penetration-velocity (from the derivative of the displacement-data by experiment-time) and impact-force (from the force sensor). By comparing the HIL experimental data (*Real HIL*) to the results of the *Simulated HIL* (refer to Fig. 2.3), the errors and the fidelity were calculated and the results were utilized for the contact-model validation.

8.1.3 Experiment Objectives

The objectives of this 1DOF HIL simulation experiment are as follows:

1. Pave the way for the design and implementation of the 6DOF HIL testbed, using a simpler lower-cost simulator.

2. Demonstrate the feasibility and principle-of-operation performance of the HIL simulation.

3. Proof of the validation concept (refer to Section 2.3), which states that the 1DOF HIL simulation is sufficient to validate the utilized contact dynamics model.

4. Present very significant experimental results, as a contribution for the contact dynamics research.

8.2 HIL Testbed Setup

8.2.1 Overview

The actual setup of the whole experiment (including all equipment, amplifiers, etc.) is shown in Fig. 8.2a. A close-up view of the testbed and sensors is depicted in Fig. 8.2b and 8.2c. The aluminum frame contained the piezoactuator, the eddy-current differential-sensor (which measures externally the displacement of the piezoactuator) and the force sensor, which measures the impact force during impact. Moreover, two different specimen were included: a solid-flat-cylinder and a half-sphere (which represents the probe-tip of the docking mechanism), see Fig. 8.2c. Each of the specimen shapes were available in various materials for various tests, which can be seen in Fig. 8.2b.

(a) Testbed overview

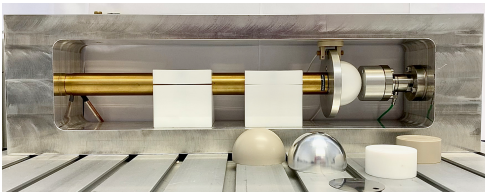

(b) Realized Testbed

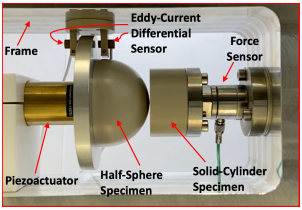

(c) CloseUp View

Figure 8.2: HIL Testbed

In order to see the physical connection between all the devices and the relation between each other, a schematic diagram of the configuration of the whole testbed is depicted in Fig. 8.3.

One required step was to build a closed-loop controller for the piezoactua-

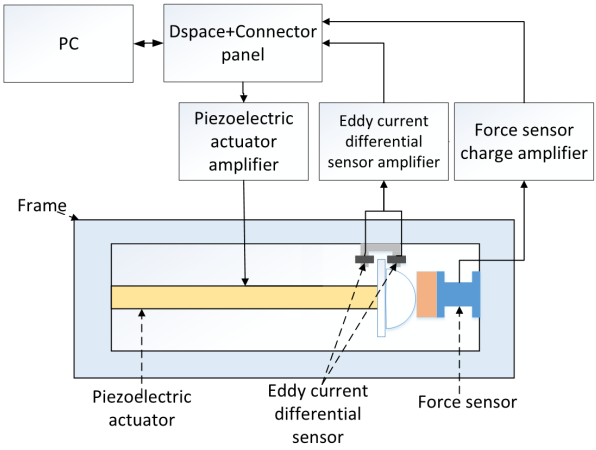

Figure 8.3: Testbed Schematic Diagram. Adapted from [Lei, 2019]

tor, which required to have the feedback of the actual position. Accordingly, the eddy-current differential-sensor was used to provide the displacement feedback. The eddy-current sensor was a better solution than the piezoactuator's built-in strain-gauge, because eddy-current sensor measured the actual external displacement of the probe-tip adapter (part 4 in Fig. 8.5). A block-diagram of the whole system is depicted in Fig. 8.4.

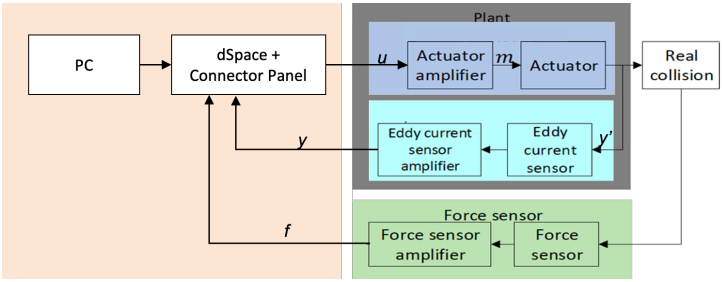

Figure 8.4: Testbed Block-diagram

8.2.2 Mechanical Design

This experiment dealt with high impact forces and displacement measurements of micrometers, therefore the mechanical frame which held all the equipment together was required to be very rigid to avoid any bending during an impact, which could affect the results. Accordingly, the material of all the parts that were directly part of the impact (i.e., frame, force-sensor flange, solid-shims) were of a higher stiffness than the specimen of the experiment. This way, any deformations during an impact would take place in the less stiff materials (i.e., specimen). The material and description of all the parts of the testbed are summarized in Fig. 8.5 and Tab. 8.2. Three different material-pairing were used for the specimen: Aluminum (AL6060), PEEK and Teflon (PTFE), as seen in Fig. 8.2b. The properties of the chosen materials are presented in Tab. 8.1.

Table 8.1: Properties of the considered materials

Material	Aluminum (AL6060)	PEEK	Teflon
Type	EN AW-2007 T4 (AlCuMgPbT4)	Ketron® 1000 PEEK	TEFLON PTFE
Young's modulus (E_i) [GPa]	71	4.34	0.45
Poisson's ratio (ν_i)	0.33	0.4	0.42

Moreover, the accuracy of the manufacturing was quite accurate with very small tolerances, as the experiment dealt with micro-meters. In order to adjust the air-gap between the half-sphere (probe-tip) and the solid-cylinder specimen, steel solid-shims of various thicknesses were manufactured and were used to adjust the air-gap as required.

8.2.3 Equipment

8.2.3.1 HIL Real-Time Simulator

The HIL real-time simulation ran on the DS1103 real-time platform, which is produced by dSpace. The DS1103 has been specially designed for the development of multivariable high-speed digital controllers and real-time

Table 8.2: Description and material of testbed components.

Number	Description	Material
1	Metal Frame	Aluminum (AL7075)
2	Piezoactuator	–
3	Actuator Support	Teflon (PTFE)
4	Adapter (actuator, specimen)	Aluminum (AL7075)
5	Specimen (half-sphere)	AL6060/PTFE/PEEK
6	Specimen (solid-cylinder)	AL6060/PTFE/PEEK
7	Solid-shims	Stainless-steel
8	Force-Sensor Flange	Steel
9	Force Sensor	–
10	Adapter (Eddy-current sensor, Frame)	PEEK
11	Eddy-current differential Sensor	–

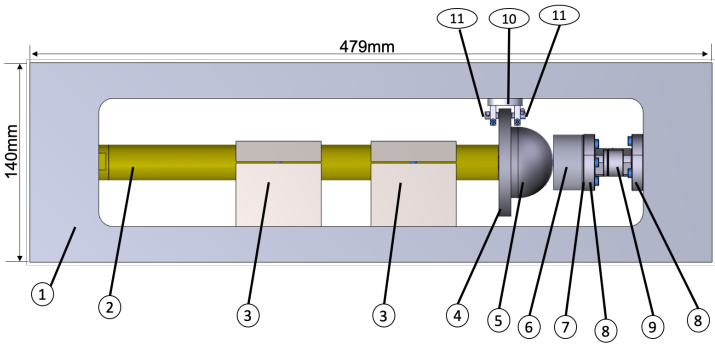

Figure 8.5: Testbed Design (See Tab. 8.2 for components' description and material)

simulations in various fields, see Fig. 8.6a. It is a complete real-time control system based on a PowerPC processor. [dSpace, 2016]

(a) DS1103 Processor

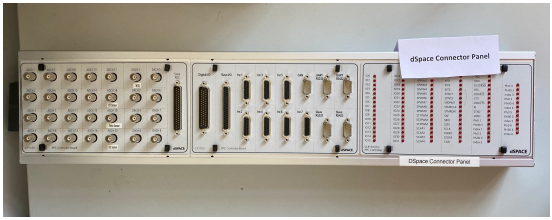

(b) Connector Panel CLP1103

Figure 8.6: HIL Real-time Simulator

The CLP 1103 connector LED panel (Fig. 8.6b) served as an interface between the DS1103 and all the other external devices (i.e., piezoactuator, the eddy-current differential-sensor and the force-sensor). The input/output signals to/from the DS1103 passed through the CLP1103 connector panel. The connector panel contains 28 BNC connectors; 20 Analogue-to-Digital (AD) connectors (ADCH1-ADCH20) and 8 Digital-to-Analogue (DA) connectors (DACH1-DACH8). The input/output voltage ranges from -10V to +10V.

8.2.3.2 Piezoelectric Actuator

Actuator

Nowadays, piezoelectric actuators are widely used in micro/nano meter scale manipulation and positioning. They have the capability to couple mechanical and electrical properties to each other and can respond to mechanical loads and electrical signals in a very short time. Piezoactuator allows (with low energy) to generate a high blocking force and to keep a steady position [Muhammad et al., 2015]. Its working principle is the reciprocal of the piezoelectric effect, which means piezoelectric actuator converts electrical signal to mechanical behavior (physical displacement).

Due to the challenging required figure-of-merits of the desired actuator (see Section 5.5.2), it was not possible to find an off-the-shelf solution. Therefore, a custom made piezoactuator was specifically built for this experiment by PiezosystemJena. It is a voltage steered actuator made of several

Figure 8.7: (left) Piezoelectric Actuator. (Right) High-voltage switching amplifier

piezostacks and it has a stroke of $300\mu m$. Its operating voltage range is between -200 and $+1000V$, its resonance-frequency is 2kHz, its stiffness is 20 N/μm and its max. blocking force is 8kN. [Piezosystemjena, 2019]

High-voltage Amplifier

The piezoelectric actuator amplifier RCV 1000/7 is a high voltage analog switching amplifier designed by PiezosystemJena, see Fig. 8.7. It is specially designed for the use of piezoelectric actuators or other capacitive loads with at least 2 µF capacitance. It has a maximal output voltage of $1000V$ and a maximal output current of $7A$. This amplifier is very suitable for dynamic operation [Piezosystemjena, 2016]. The D-SUB 5W1 connector "OUT" on the device was connected directly to drive the custom-made piezoactuator utilized in this experiment, with an output voltage that ranged from 0 to +1000V. The BNC connector "MOD" received the reference desired-position signal from the dSpace system. The "MON" connector is a scaled amplifier's output ("OUT") by a factor of 0.01, i.e., "MON" outputs voltage between 0 and 10.

8.2.3.3 Eddy-Current Differential-Sensor

The eddy-current differential-sensor (Kaman KD-5100-004A) measured the actuator's external displacement by measuring the displacement of the aluminum adapter fixed to actuator's moving-part (i.e., part 4 in Fig. 8.5). It

has a very high measuring accuracy; up to nano-meters [Kaman Precision Products, 2015]. Two matched sensor coils were positioned relative to the target (i.e., the adapter), on both sides of the target, see Fig. 8.8. When the target moved away from one sensor-coil, it moved the exact equal distance toward the other one.
The sensor coils were powered by an AC current and they generated an electro-magnetic field, which caused a magnetic coupling between the conductive target (Aluminum AL7075) and the sensor coils.

The principle-of-operation is the impedance variation caused by eddy-currents induced in the conductive-target located within the measuring-range of each sensor. When the target is electrically centered between the two sensor coils, the system's output-voltage is zero. When the target starts to move, the impedance between the sensors is no longer equal. This impedance imbalance is detected by the bridge circuit inside the voltage regulator and presented as a linear analog signal proportional to the target position. [Kaman Precision Products, 2015]

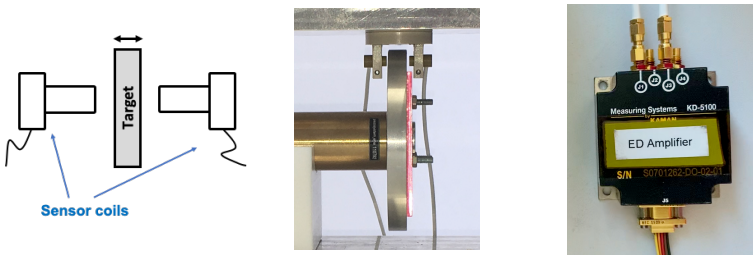

Figure 8.8: Eddy-current differential-sensor consists of two coils, which measured the displacement of the target placed between them. (Left) Diagram of sensor setting. (Middle) actual mounting of eddy-current sensor. (Right) Kaman Amplifier KD-5100

8.2.3.4 Force-Sensor

The 1DOF force-sensor "9323AA" by "Kistler" was utilized in this experiment, see Fig. 8.9. It has a measuring range of 0 - 10 kN and a resolution of 0.01N [Kistler Group, 2018]. The sensor's principle-of-operation is the piezoelectric effect. Meaning, the force-sensor converts the mechanical displacement (due to an external force) to an electrical signal. It is the

inverse process of the piezoelectric actuator. When a force is applied to the force-sensor, the sensor generates an electrical-charge, which is measured and amplified by the charge amplifier "Kistler, Type 5015" [Kistler Group, 2013]. This amplifier converts the measured charge into force and outputs the value as an analog signal (which was connected to the dSpace) and is then displayed on the LCD display of the amplifier as well.

Figure 8.9: (Left) "Kistler" Force Sensor "9323AA" and the amplifier 5015 (Right)

8.2.4 Real HIL Testbed Model

In this section, the identified model of the HIL testbed is presented, which was then inserted in "HIL Model" in the *Simulated HIL* as in Fig. 2.3. Likewise for the force-sensor. Before modeling the real HIL testbed, the experiment was calibrated and the closed-loop displacement controller was designed beforehand, so that the real HIL testbed model would include the whole controlled-actuator-system and the force-sensor. The calibration of the piezoactuator and the implementation of the closed-loop displacement controller are presented in Appendix A.

Concept

In order to predict the results of the *Real HIL* scenarios and to estimate the errors using the *Simulated HIL* (refer to Fig. 2.3), it was required to find the approximate model of each of the equipment and their noises, in order to substitute the actuator-model and the force-sensor-model in the "HIL Model", in the *Simulated HIL*. For illustration, Fig. 8.10 depicts both the

"Real HIL Testbed" in comparison to the "HIL Model", where the approximate models are implemented.

In this section the approximate transfer-function of each of the controlled-actuator-system (controller, piezoactuator and amplifier, eddy-current sensor and its amplifier), its noise model, as well as the force sensor system and its noise model are presented.

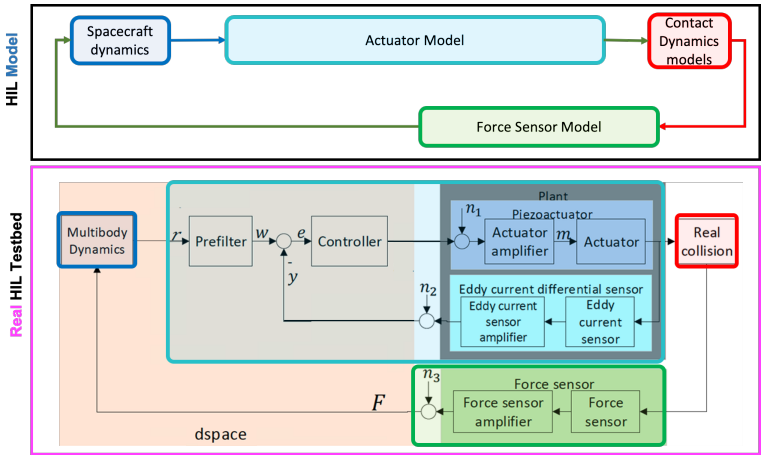

Figure 8.10: Comparison of block-diagrams of "Real HIL Testbed" and "HIL Model" for illustration. (refer to Fig. 2.3). Parts of the figure adapted from [Lei, 2019].

The following abbreviated notations are used for simplification:

$$\{d,w\} = 1 + 2d\frac{s}{w} + \frac{s^2}{w^2} \tag{8.1}$$

8.2.4.1 Controlled-Actuator-System

A. Transfer-Function ($T_{act}(s)$)
The frequency-response of the closed-loop system (see Fig. 8.11 for more details) was taken into consideration, to identify the approximate transfer-function of the controlled-actuator-system. Accordingly, the system was approximated as a 2nd order system (as seen in Fig. 8.11),

as follows:

$$T_{act}(s) = \frac{1}{\{d,w\}} = \frac{1}{\{0.8,3000\}} \tag{8.2}$$

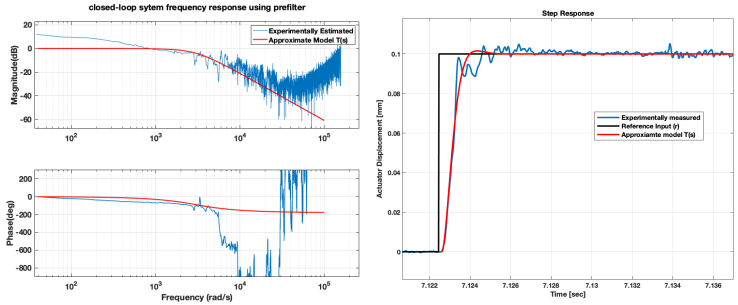

(a) Frequency response

(b) Step response

Figure 8.11: Comparison of experimental closed-loop system, versus approximate model $T_{act}(s)$. Figure adapted from [Lei, 2019]

B. Noise model (η_2)

The noise of each equipment in this experiment was modeled as a colored noise in Simulink® (see Fig. 8.12) [Janschek, 2012]. As the noise of the controlled-actuator system was mainly from the actual-displacement-feedback by the eddy-current sensor, accordingly, the transfer-function of the sensor was required to be identified, as well as the standard deviation of its noise measurement.

The sensor's datasheet [Kaman Precision Products, 2015] states that the sensor amplifier is a standard 2nd order Butterworth configuration. Therefore, PT2 element was used to simulate the dynamics of the eddy-current sensor system. Accordingly, the damping constant d_e in the PT2 was 0.707. The -3dB point is at ≈23kHz [Kaman Precision Products, 2015]. Thus, the transfer-function of eddy-current sensor was as follows:

$$T_e(s) = \frac{K_e}{\{d_e, w_e\}} = \frac{1}{\{0.707, (2 \cdot \pi \cdot 23000)\}} \tag{8.3}$$

Moreover, the standard deviation was estimated using experimental measurements to be $\sigma_d = 0.73\mu m$. Power Spectral Density (PSD) was

$S_n = 1.0428 \cdot 10^{-11}$ mm^2/Hz. Thus, the "Random-number" block properties were set as follows: mean = 0, seed = 0, sampling time, $T_s = \frac{1}{100}\frac{2\pi}{w} = 4.3478 \cdot 10^{-7}$ sec. Variance: $\sigma^2 = \frac{S_n}{T_s} = 2.3985 \cdot 10^{-5}$ mm^2

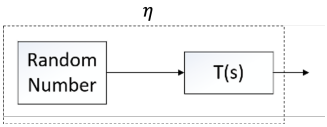

Figure 8.12: Simulink® Model for the colored noise generation

8.2.4.2 Force Sensor

A. Transfer-Function ($T_f(s)$)
Likewise, the force sensor transfer-function was derived based on the information provided in its data sheet [Kistler Group, 2013], [Kistler Group, 2018], which states that the sensor amplifier is approximated as a 2nd order Butterworth filter. The resonant-frequency of the force sensor is much larger (74.5kHz) than the amplifier (the cut-off frequency at -3dB is 1kHz, was set manually in the settings of the amplifier). Therefore, PT2 element was used to simulate the dynamics of the force-sensor system. Accordingly, the damping constant d_f in the PT2 was 0.707. The -3dB point is at ≈1kHz [Kaman Precision Products, 2015]. Thus, the transfer-function of force sensor system was as follows:

$$T_f(s) = \frac{K_w}{\{d_f, w_f\}} = \frac{1}{\{0.707, (2 \cdot \pi \cdot 1000)\}} \tag{8.4}$$

B. Noise Model (η_3)
The same transfer-function defined above in Eq. 8.4 was used for the noise model. In addition, the standard deviation was estimated experimentally to be $\sigma_d = 1.5N$. Power Spectral Density (PSD) was $S_n = 0.001$ N^2/Hz. Thus, the "Random-number" block properties were set as follows: mean = 0.6 (experimentally measured bias error of 0.6N), seed = 0, sampling time, $T_s = \frac{1}{100}\frac{2\pi}{w} = 1 \cdot 10^{-5}$ sec. Variance: $\sigma^2 = \frac{S_n}{T_s} = 100$ N^2

8.3 HIL Contact Dynamics Simulation

In this section, firstly the detailed description of the contact dynamics HIL test scenario is presented in Section 8.3.1, including the description of the implemented Simulink® model, as well as the simulation properties. Afterwards, in Section 8.3.2, the various potential scenarios are presented. Then, in Section 8.3.3, the criteria upon which a scenario was qualified to be simulated using the testbed or not, is presented. Finally the properties of all the qualified scenarios are presented in Section 8.3.4.

It is important for the reader to understand well the concept presented in Section 2.3 before reading the following subsections. The "*Spacecraft Dynamics*" in Fig. 2.3 was called "*Multibody dynamics*" in this HIL test.

8.3.1 HIL Test Description

The "*multibody dynamics*" block (shown in Fig. 8.14) is exactly the same as the one introduced in Section 4.4.1. It models the dynamics of two rigid-bodies (i.e., Body1 is a sphere and Body2 is a cube) in 1DOF and calculates the relative-displacement and relative-velocity between both bodies at each time-step, due to any external forces acting on them.
For the considered test, the two rigid-bodies (in the "*multibody dynamics*" model) moved towards each other until an impact took place and then they rebounded due to the impact-force that acted on each one of them. The considered HIL simulation test emulated the relative-motion using the piezoactuator and measured the real impact-force using the force-sensor. The initialization parameters that were varied in each scenario are masses and initial relative-velocity, while the constant parameters are initial displacement of each body and initial acceleration (set to zero).

For a proper realization of HIL contact dynamics simulation, it was important to make sure that the "penetration-depth" and the "air-gap" lied within the limited range-of-motion of the piezoactuator, i.e., $300\mu m$, (the air-gap corresponds to a real physical air-gap in the testbed for each scenario). An air-gap was required to be considered in order to allow the piezoactuator to accelerate to reach the desired impact-velocity. Therefore, in (each scenario of) the HIL test, only a section of the relative-displacement x from the "*multibody dynamics*" was considered and it was called, "simulated displacement" r, see Fig. 8.13 for illustration. The "simulated displacement" consists of an "air-gap" (before the real physical impact takes place) and a "penetration-depth" (during an impact).

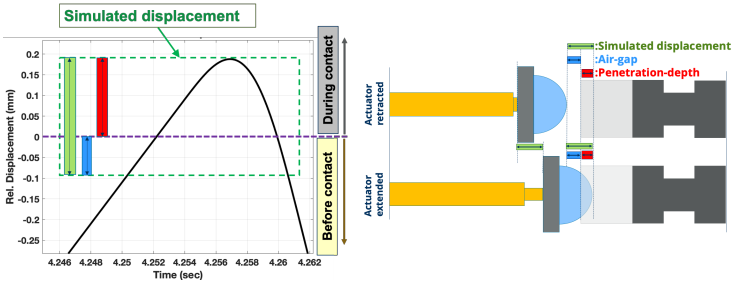

Figure 8.13: Illustration to visualize "simulated displacement", "penetration-depth" and "air-gap". Left figure illustrates the "simulated-displacement" section on the relative-displacement curve of the *"multibody dynamics"*. Right figure depicts how the actuator realizes the "simulated-displacement".

Simulink® Model

The Simulink® model of the HIL test (running on dSpace system) was built according to the above description which is illustrated in Fig. 8.14. The block "*simulated displacement filter*" was added to include only data that lies within the accepted range. Moreover, saturation blocks were added to protect the equipment by making sure that the allowed values were within the acceptable range as follows: *Saturation1* = [0 - 0.239], *Saturation2* = [0 - 1].

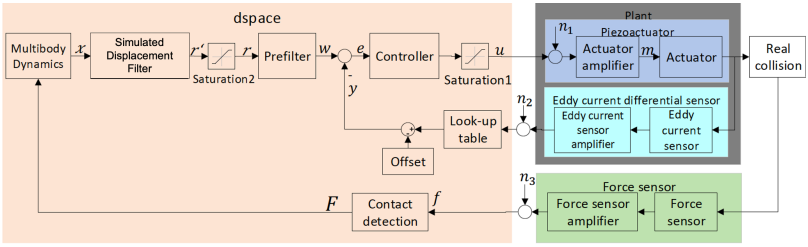

Figure 8.14: HIL test scenario block-diagram. Figure adapted from [Lei, 2019]

In addition, "*Contact Detection*" and "*Offset*" were added to avoid errors that occurred due to sensor noises. These errors could affect the simulation quality and reliability, if they were not dealt with. Ideally, the force-sensor should output $0N$ when no contact takes place, however, due to the sensor noise of (+/- 15N), it tricked the "*multibody dynamics*" that there was a contact; hence simulation was disrupted. Therefore, a "*contact detection*" block was added to the raw output signal of the force sensor, such that if the measured-force (f) was less than or equal to $22N$, it was ignored.
Likewise when the actuator was at rest at zero position (no extension), the noises that arose from the eddy-current sensor also fluctuated with a $+/-9\mu m$. Therefore, an "*Offset*" was introduced to the zero position of the actuator. In most cases, the offset was $20\mu m$, but it was varied depending on each scenario.

Simulation Properties
The simulation was carried out using Matlab® 2015b and Simulink®. After thorough testing and analysis (using the real HIL equipment as well), the Fixed-Step Solver ODE4 (Runge-Kutta) was selected, with a fixed time-step of 13.333 μsec (i.e, sampling-frequency of 75kHz) for the *Simulated HIL* and real-time *Real HIL*.

8.3.2 *Simulated HIL* Simulation

Before running the real HIL test, a simulation of the "simulated HIL" took place using the contact model under investigation (Flores model [Flores et al., 2011]). The *Simulated HIL* was updated with the approximate models of the closed-loop HIL system in Section 8.2.4. The objectives of simulating various scenarios using *Simulated HIL* are: to estimate the results of each scenario, to identify (based on estimated results) which scenarios are technically qualified to be simulated by the *Real HIL* and to estimate the (predicted) HIL errors.
The *"Contact Dynamics"* subsystem was initialized with the same initialization in Section 5.3.1, except for the parameters specifically defined below.

Various scenarios were simulated in a systematic order by varying one of the parameters at each simulation using the "Generic HIL Testbed Framework Analysis Tool". Accordingly, 72 scenarios were simulated (for each COR value) and the results of each scenario, as well as the HIL errors are estimated. The whole range of each of the following parameters has been considered in the simulations:

1. *Velocity (m/s):* [0.05, 0.075, 0.1]
2. *Material:* PEEK-PEEK, PEEK-Alu, PEEK-Teflon, Alu-Alu, Alu-Teflon, Teflon-Teflon
3. *Masses (kg):* [35-35, 35-70, 50-50, 50-100]
4. *Coefficient-of-Restitution (COR):* [0.8, 0.9]

For the selection of the scenarios, mainly all scenarios with COR = 0.8 were focused on, while for the analysis later on, the scenarios with both COR values (0.8 and 0.9) were considered.

8.3.3 Qualification Criteria

In order to protect the expensive HIL equipment from any hazardous accidents during the HIL impact test, a theoretical actuator safety-check was required to be passed for all qualified scenarios. Actuator manufacturer "PiezosystemJena" (also [Piezomechanik GmbH, 2020]) states that the maximum blocking force capability of the piezoactuator is inversely proportional to how much the actuator is extended. Meaning, when the considered piezoactuator is at rest, it can withstand up to 8kN. However, the more the piezoactuator extends, the less the blocking force becomes. Therefore, the used theoretical safety-check estimated the capability of the actuator to withstand the predicted external force from the "simulated HIL", with respect to the expected extension. The theoretical actuator safety-check was formulated as follows: (the equation is introduced by [Piezomechanik GmbH, 2020]):

$$x_{test} \cdot \frac{F_{act}}{F_{act} - F_{test}} < x_{act} \tag{8.5}$$

such that F_{act}, x_{act} is the max. force and max. stroke in the data-sheet of the actuator, respectively. x_{test} is the predicted max. extension of the actuator in a scenario. F_{test} is the predicted max. force in a scenario. If the left-hand-side of the equation is indeed smaller than the right-hand-side, then the safety-check is passed.

Accordingly, only 23 scenarios (out of 72) have passed the safety-check. Moreover, based on the preliminary HIL testing of various scenarios, an empirical safety-factor of (20%) was defined, which reduced the number of possible HIL scenarios to 12 (out of 23) scenarios.

8.3.4 Qualified Test Scenarios

Based on the simulated scenarios using the *Simulated HIL*, as well as the qualification criteria , 12 scenarios passed the qualification criteria and were indeed simulated using the *Real HIL* simulation. (See scenarios properties in Tab. 8.3). Such that V_i is the initial impact velocity. Airgap is the actual air-gap between probe-tip and specimen (see Fig. 8.13) and offset represents the zero position of the piezoactuator (see Fig. 8.14).

Table 8.3: Scenarios that were carried out employing the *Real HIL* simulation

Scenario	Material		Mass (kg)		V_i	Airgap	Offset	Temp.
Number	body 1	body 2	body 1	body 2	[m/s]	[µm]	[µm]	[°C]
1	Alu	PEEK	35	35	0.05	43	20	23.1
2	Alu	PEEK	35	35	0.075	14	10	22
3	Alu	PEEK	35	70	0.05	43	20	23.3
4	Alu	PEEK	50	50	0.05	48	20	23
5	Alu	PEEK	50	100	0.05	48	20	22.6
6	PEEK	PEEK	35	35	0.05	50	20	23
7	PEEK	PEEK	35	35	0.075	9	15	22.6
8	PEEK	PEEK	35	70	0.05	9	20	22.6
9	PEEK	PEEK	50	50	0.05	9	20	22.2
10	PEEK	PEEK	50	100	0.05	9	20	22
11	Alu	PTFE	35	35	0.05	5	10	22.4
12	PEEK	PTFE	35	35	0.05	41	10	21.7

8.4 Results

8.4.1 Experimental HIL Simulation Results

Experimental results of the HIL contact dynamics simulation are presented and discussed in the following subsections. The results of only one of the twelve qualified scenarios are presented in this section, which include contact-dynamic results, predicted and actual error percentages and observations from the results. The results of the other scenarios are presented in Appendix C.

8.4.1.1 Selected Scenario Properties

The results of the HIL scenario number four (see Tab. 8.3) is presented below. This scenario is distinguished because of its properties: a) it has

the lowest initial impact velocity of considered range (0.05 m/sec), b) its material pairing (Aluminum-PEEK) is the same as the real docking S/C docking under consideration, c) the two bodies have the same mass, 50kg. The airgap for this scenario is $48\mu m$ and the piezoactuator has a zero offset of $20\mu m$ (refer to Section 8.3.1). The "HIL Model" presented here used a COR value of 0.9 and the rest of the properties were the exactly the same as the realized experimental scenario.

8.4.1.2 HIL Contact-Dynamic Results

As mentioned before, the three main quality-control parameters that were considered for contact dynamics analysis in this work are: force, penetration-depth and penetration-velocity, which were all considered with respect to time. Moreover, the hysteresis diagram of the penetration-depth versus the contact force is useful to visualize the energy differences in an impact. Therefore, the behavior of all of these parameters of the considered scenario are presented in Fig. 8.15.

In each graph in Fig. 8.15, three models are shown; "HIL experiment", "HIL Model" and "Docking Model". In reference to Fig. 2.3, "HIL experiment" are the actual results from the physical impact using the *Real HIL* Testbed, while "HIL model" is the predicted results using the model of the HIL testbed (built in Section 8.2.4) and the contact model. The "Docking Model" presents the simulation of the impact using the contact model and multibody dynamics only, i.e., no hardware (actual or model) are included. The "HIL experiment" model shown is the smoothed data of the raw data.

Observations

From the graphs in Fig. 8.15, it is observed that the behavior of the predicted results from the "HIL model" are relatively close to the "HIL experiment" results, but not exactly the same.

In order to analyze the force and penetration-depth graphs, the "max. absolute" and "integral absolute" differences were taken into consideration (errors are explained in Section 3.3). "Max. Absolute" considers the difference between the peak value of two models (e.g., "HIL experiment" model and the predicted results from "HIL model"). While "Integral absolute" considers the difference between the area-under-the-curve of both models,

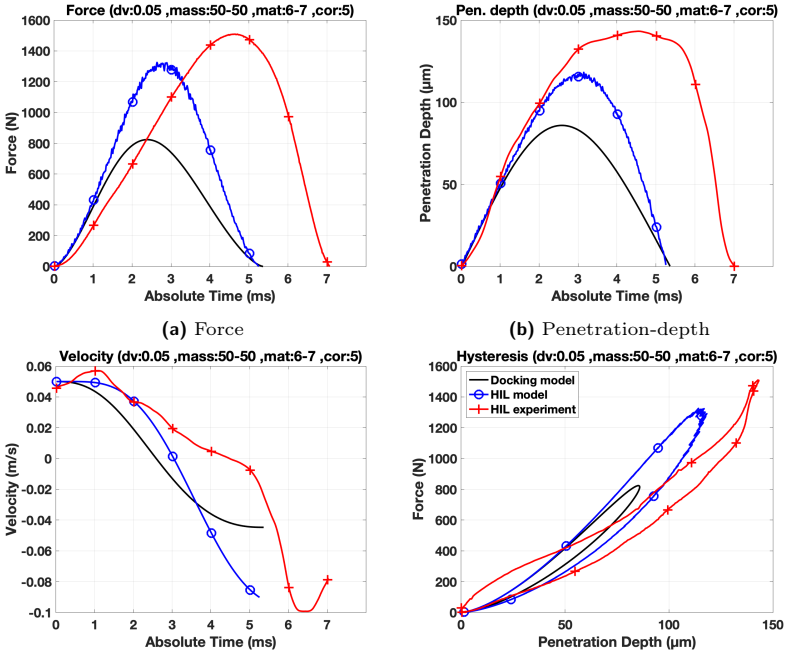

(a) Force **(b)** Penetration-depth

(c) Velocity **(d)** Hysteresis

Figure 8.15: Results of the HIL contact dynamics simulation of the fourth scenario (refer to Tab. 8.3), which present the behavior of the different models: HIL experiment vs. HIL model vs. Docking model

which takes into consideration the time duration of impact as well.

The force and the penetration-depth graphs (Fig. 8.15a, 8.15b respectively) show that even-though the "max. absolute" differences between "HIL experiment" and "HIL model" are not exactly the same, they are relatively close. On the contrary, the "integral absolute" differences appear to be relatively large, mainly because the impact in the experimental test takes a longer span of time than predicted.

Moreover, the hysteresis diagram (Fig. 8.15d) representing the penetration-depth versus the contact force, shows that the "HIL Model" and "HIL experiment" are not exactly the same, nevertheless they are relatively similar, i.e, peaks on each axis are relatively close.

In order to study the relative-velocity graph of any scenario, the velocity before and after impact were observed and compared to the predicted model. Ideally, in an elastic collision, the velocity-after-impact is the same as the velocity-before-impact. Therefore, to calculate errors between models the focus was on the COR parameter and the difference in velocity-after-impact, since the velocity-before-impact was the same for all models of the same scenario. Based on that, it is observed in the relative-velocity graph of this scenario in Fig. 8.15c in the relative-velocity graph that the velocity-after-impact of the "HIL experiment" is relatively close to the predicted "HIL model".

8.4.1.3 Errors and Fidelity Results

In this section, the errors analysis of the considered scenario is presented in Tab. 8.4. The definition and the explanation of the "Max. Absolute" and "Integral Absolute" errors have been presented before in Section 3.3.

The concept of testing and validation of contact dynamics model in this work (presented in Section 2.3) was to show the differences between *Simulated HIL* and *Real HIL*. Therefore, for the considered scenario, all of these results were summarized in Tab. 8.4. The following abbreviations of errors and fidelity in the table were used:

- "Simulated HIL Error" (E_{md}): is the difference between the "HIL model" (m) and the "Docking model" (d); $E_{md} = m - d$. In percentage, it is as follows: $E_{md}(\%) = \frac{m-d}{d} \cdot 100$.

- "Real HIL Error" (E_{hd}): is the difference between the "HIL test" (h) and the "Docking model" (d); $E_{hd} = h - d$. In percentage, it is as follows: $E_{hd}(\%) = \frac{h-d}{d} \cdot 100$
- Fidelity (ζ): is the percentage of how equivalent is the simulated HIL to the Real HIL, as follows: $\zeta = \frac{E_{md}}{E_{hd}} \cdot 100$
- "HIL Contact Error" (E_{hm}): is the error between the real impact in the "HIL test" (h) versus the simulated impact (using contact model) in the "HIL model" (m); $E_{hm} = h - m$. In percentage, it is as follows: $E_{hm}(\%) = \frac{h-m}{m} \cdot 100$

Observations

As discussed before, the "max. absolute" differences between the modeled and the experimental results were rather relatively close to each other. The "integral absolute" differences were rather large, due to the longer impact time of the experimental tests.

In Tab. 8.4, it is observed that the absolute "Real HIL errors" (E_{hd}) of the force and the penetration-depth (82.85% and 77.76%, respectively) are slightly larger than the desired relative-error (i.e., $\approx$ 20% higher than the desired 60%), upon which the preliminary actuator's figure-of-merits were defined in Section 5.5.2. On the other hand, the integral errors are much larger.

The "max. absolute" results of the force measurements in Tab. 8.4a shows that the fidelity of the contact model is 73% (in case of COR 0.9). Meaning, the contact model predicted the max. force of impact with exactness of 73% of the experimental HIL impact. While, the fidelity of the "integral absolute" differences was 35.73%.

The "max. absolute" results of the penetration-depth measurements in Tab. 8.4b shows that the fidelity of the contact model is 56.4% (in case of COR 0.9). While, the fidelity of the "integral absolute" differences is 24%.

There were two ways to analyze velocity results (both are representing the same data): first, to focus on the final-velocity only, second is to focus on COR parameter, which is the ratio between velocity-after-impact to velocity-before-impact. The expected COR in each scenario are presented in grey in Tab. 8.4c, while the resultant COR of each model are represented in dark

Table 8.4: Results of the HIL contact dynamics simulation of the fourth scenario (refer to Tab. 8.3), which demonstrate the errors of the *Simulated HIL* and the *Real HIL* (HIL vs ideal), the difference between both of them and the fidelity.

(a) Force

Real HIL Test No.	Material		Mass (kg)		V_i (m/s)	COR	Force													
							max. force [N]			Error (max. absolute)							Error (Integral absolute)			
							Docking model (d)	HIL model (m)	HIL test (h)	E_md		E_hd		Fidelity	E_hm		E_md	E_hd	Fidelity	E_hm
	b1	b2	b1	b2			value	value	value	value [N]	%	value [N]	%	%	value [N]	%	%	%	%	%
4	Alu	PEEK	50	50	0.05	0.8	796.06	1320.50	1506.37	524.44	65.88	710.30	89.23	73.83	185.87	14.08	48.56	167.01	29.07	79.74
4	Alu	PEEK	50	50	0.05	0.9	823.81	1325.62	1506.37	501.80	60.91	682.55	82.85	73.52	180.75	13.64	54.36	152.15	35.73	63.35

(b) Penetration-depth

Real HIL Test No.	Material		Mass (kg)		V_i (m/s)	COR	Penetration Depth													
							max. penetration [um]			Error (max. absolute)							Error (Integral absolute)			
							d	m	h	E_md		E_hd		Fidelity	E_hm		E_md	E_hd	Fidelity	E_hm
	b1	b2	b1	b2			value	value	value	value [µm]	%	value [µm]	%	%	value [µm]	%	%	%	%	%
4	Alu	PEEK	50	50	0.05	0.8	81.87	112.39	143.24	30.52	37.28	61.37	74.96	49.74	30.85	27.45	27.68	146.32	18.92	92.91
4	Alu	PEEK	50	50	0.05	0.9	85.90	118.24	143.24	32.34	37.65	57.35	66.76	56.40	25.01	21.15	32.78	138.36	23.69	79.51

(c) Velocity After Impact

Real HIL Test No.	Material		Mass (kg)		V_i (m/s)	COR	Final Velocity										COR		
							Velocity after-impact			Error (absolute)									
							d	m	h	E_md		E_hd		Fidelity	E_hm		d	m	h
	b1	b2	b1	b2			value [m/s]	value [m/s]	value [m/s]	value [m/s]	%	value [m/s]	%	%	value [m/s]	%			
4	Alu	PEEK	50	50	0.05	0.8	-0.039	-0.083	-0.059	-0.043	110.07	-0.019	49.12	224.09	0.024	-29.01	0.79	1.66	1.40
4	Alu	PEEK	50	50	0.05	0.9	-0.045	-0.096	-0.059	-0.052	115.49	-0.014	31.54	366.14	0.038	-38.96	0.89	1.93	1.40

blue in the last columns. Accordingly, one observes that the resultant COR of the "HIL experiment" impact is closer to the "Docking model", than the "HIL model". As the fidelity was calculated based on the error differences, one could notice that the fidelity percentage was really high and it was misleading. Therefore, for velocities, it was better to compare the resultant COR values for analysis.

8.4.2 General Testbed Results

The general results of this 1DOF HIL simulation experiment are as follows:

1. The presented 1DOF HIL testbed was an attractive option as a simpler lower-cost precursor to a 6DOF HIL simulator. In fact, it paved the way for the design and implementation of the 6DOF HIL testbed.
2. It allowed to demonstrate the feasibility and principle-of-operation performance of the HIL simulation.
3. Most importantly, it showed to be sufficient to validate the contact dynamics model implemented in the docking simulations. (refer to Section 2.3).
4. It presented very significant experimental results, as a contribution for the contact dynamics research.

8.5 Summary and Conclusion

- In this chapter, the 1DOF HIL testbed simulation is presented in detail. The testbed was uniquely designed and built for the contact dynamics testing and validation, based on the validation concept presented in Section 2.3. In the presented description, it is explained how the testbed was built, modeled and then implemented in the *Simulated HIL*. Within the testbed setup, a closed-loop displacement controller was designed and validated, which is presented in Appendix A

- The "Generic HIL Testbed Framework Analysis Tool" showed to be very useful to simulate various scenarios systematically (based on varying each of the parameters considered from each design-space). Accordingly, 144 scenarios were simulated, which predicted the HIL results and errors. After introducing a qualification criteria to protect the HIL equipment, 12 scenarios were qualified and were tested using the HIL Simulation testbed.

- The analysis of one of the scenarios (scenario number four in Tab. 8.3) was presented in detail. It showed that based on the validation concept and the HIL testbed set up, the Flores contact-dynamic model [Flores et al., 2011] under investigation predicted the max. absolute values with acceptable accuracy, with a fidelity percentage of 73% for force and 56% for penetration-depth. On the other hand, the "integral absolute" error appear to be relatively large, mainly because the impact in the experimental test took a longer span of time than it was predicted. As a result, for the integral errors, the contact-model showed a fidelity of 35.7% and 23.7% for force and penetration-depth, respectively.

- Based on the HIL results, it is concluded that the Flores contact model could be utilized for the considered system, to provide preliminary results. For more reliable results, it is recommended to take into consideration the identified HIL errors within the docking modeling. Moreover, it is concluded that more research and investigations are required, in order to find other contact dynamics models, or to design a new one, which models the real-life impacts at the considered low-impact velocities and materials. In addition, it is recommended to utilize the presented 1DOF HIL testbed and the existing experimental results in the designing process of a new contact model. Hence, a new contact model would be based on the experimental results. Furthermore, this 1DOF HIL testbed provides a very useful tool for contact dynamics research, as it allows to test and validate various contact dynamics scenarios. Hence, contact models can be validated.

Chapter 9

Conclusion

The scope of this dissertation was focused on carrying out a systematic investigation of the technically possible HIL docking contact dynamics simulation performances. This included carrying out a performance analysis of a 1DOF and 6DOF spacecraft docking. In addition, a HIL testing and a validation of a docking contact dynamics was carried out using a uniquely designed 1DOF HIL testbed.

Within this work, the following was achieved:

1. Built a generic tool for carrying out a systematic investigation for exploration of the available design-spaces.
2. Carried out a research and a critical analysis of non-linear contact dynamics models.
3. Built a model of a 1DOF HIL docking testbed, which allowed to identify the required figure-of-merits of the desired hardware.
4. Built a generic 6DOF spacecraft docking model, which was utilized to carry out a performance analysis of various 6DOF spacecraft docking scenarios.
5. Built a model of a 6DOF docking HIL testbed, which was used to study and to identify the preliminary requirements for a 6DOF docking HIL testbed.
6. Designed and built a 1DOF HIL simulation testbed, which was used for an experimental testing and validation of contact dynamics.

In the next sections, the summary of the results of this work, main conclusions and the future work are presented.

9.1 Generic HIL Testbed Framework Analysis Tool

In this work, a "Generic HIL Testbed Framework Analysis Tool" was built to carry out a performance analysis and fidelity estimation of any HIL testbed

(presented in Chapter 3). This tool carries out a systematic investigation of the technically possible HIL docking contact dynamics simulation performances. It was very usefully utilized in this work to identify the key-design-parameters of the 1DOF and 6DOF HIL testbeds, by exploring the available design-spaces in the design-framework of the 1DOF and 6DOF HIL testbeds. Accordingly, the figure-of-merits of HIL instruments were identified according to the required design-framework.

In addition, it was employed to identify the qualified scenarios that were carried out using the HIL simulation experiment.

9.2 Analysis and Performance Evaluation of Contact Dynamics

After carrying out an extensive contact dynamics research and analysis (including a detailed parametric study) on the available contact dynamics models, it is concluded in Chapter 4 that the "Flores" non-linear contact dynamic model [Flores et al., 2011] is the most representative contact model for the considered docking system.

9.3 Investigation and Analysis of 1DOF HIL System.

In Chapter 5, a 1DOF docking HIL simulation model was introduced in detail and studied. Based on the simulation results, it is concluded that the dynamics of the hardware used in the HIL simulation indeed affect the 1DOF "docking system". Accordingly, the HIL errors were identified and calculated.

Using the "Generic HIL Testbed Framework Analysis Tool", a detailed parametric study of the available design-spaces and their parameters were carried out. Accordingly, it is concluded that the actuator time-delay D_{act} is the key-parameter of the HIL design-space and is the main key-parameter for the considered HIL design process. Therefore, it was used to identify figure-of-merits of the required actuator.

According to the results of the various actuator's total-delay simulations, the required figure-of-merits of the actuator was defined and is presented in Section 5.5.2.

9.4 Investigation and Analysis of 6DOF HIL System.

In Chapter 6 the "Docking Model" which was built in a generic way, is presented. It is capable of simulating, visualizing and verifying docking scenarios. Accordingly, it was used to estimate the properties of the failed and the successful docking scenarios of a case-study. This model (and its concept) promotes itself as a practical tool for the industry, as it can predict the properties of the successful and failed docking scenarios of a docking mission.

A model of the 6DOF docking HIL simulation testbed was built. It simulated the effect of the HIL equipment on the docking simulation and provided an insight into the fidelity of the considered HIL simulation testbed. The results act as a reference for the future real docking HIL simulation.

It is concluded that the "first impact" in the 6DOF docking simulation is very important, as it was the single common qualitative aspect between the "HIL Model" and the "Docking Model". Therefore, the fidelity analysis for such a system, should be focused on what happens exactly during the first impact (i.e., why and how do errors occur?) rather than focusing on the whole docking scenario. Accordingly, the followed parametric study in Chapter 7 was focused on the first impact only.

In Chapter 7, a parametric study was carried out (using the "Generic HIL Testbed Framework Analysis Tool") on the 6DOF testbed's HIL design-space. It showed that the robotic-hardware total-delay (D_{rob}) is the most influential parameter out of the four parameters in the HIL design-space. In addition, the robotic-hardware resolution (R_{rob}) affects the HIL errors and it must to be considered too. (This was especially clear in the considered system, when the ($D_{rob} < 4ms$).) Therefore, one has to take into consideration both parameters (D_{rob}, R_{rob}) while investigating this HIL testbed design-space.

Moreover, the results showed that the considered robotic-hardware resolution (R_{rob}) should be 10 times smaller than the expected max. penetration depth. Hence, in the considered model, the (R_{rob}) should be 10 times smaller than 0.1mm (i.e., $R_{rob} <= 0.01$mm).

The parametric study on the 6DOF testbed's spacecraft design-space showed that the spacecraft masses are important. In addition, the initial impact velocity does not affect significantly the HIL results. On the other hand, the material is considered also as a key-parameter.

As a result, it is concluded that it is very challenging to realize a 6DOF HIL simulation for the whole docking scenario (i.e., not only first impact) without compliance, due to the challenging robotic-hardware requirements.

In order to expand and realize a 6DOF non-compliant docking HIL simulation to the whole scenario, one should study the errors' sources in an impact, in order to predict them, and compensate for them in the "HIL Model". This way, errors accumulation shall be relatively compensated, hence both models ("Docking Model" and "HIL Model") shall have a comparable whole docking trajectory. This is considered as future work.

9.5 Experimental 1DOF HIL Simulation Testbed

In Chapter 8, the 1DOF HIL simulation testbed is presented in detail. It was uniquely designed and built for the contact dynamics testing and validation, based on the validation concept presented in Section 2.3.

Using the "Generic HIL Testbed Framework Analysis Tool", various scenarios were systematically simulated using the *Simulated HIL* (refer to Section 2.3). Accordingly, 144 scenarios were simulated and they predicted the HIL results and errors. After introducing a qualification criteria to protect the HIL equipment, 12 scenarios were qualified and were tested using the HIL Simulation testbed.

The analysis of one of the scenarios (Scenario 4) showed that based on validation concept and the HIL testbed set up, the Flores contact-dynamic model [Flores et al., 2011] under investigation predicted in this scenario the max. absolute values with acceptable accuracy, with a fidelity percentage of 73% for force, and 56% for penetration-depth. On the other hand, the "integral absolute" differences appeared to be relatively large, mainly because the impact in the experimental test took a longer span of time than predicted. As a result, the contact model showed for this scenario a fidelity of 35.7% and 23.7% for force and penetration-depth, respectively.

Based on the HIL results, it is concluded that the Flores contact model could be utilized for the considered system, to provide preliminary results. For more reliable results, it is recommended to take into consideration the identified HIL errors within the docking modeling. Moreover, it is concluded that more research and investigations are required, in order to find other

contact dynamics models, or to design a new one, which models the real-life impacts at the considered low-impact velocities and materials.

In addition, it is recommended to utilize the presented 1DOF HIL testbed and the existing experimental results in the designing process of a new contact model. Hence, a new contact model would be based on the experimental results.

Furthermore, this 1DOF HIL testbed provides a very useful tool for contact dynamics research, as it allows to test and validate various contact dynamics scenarios. Hence, contact models can be validated.

9.6 Future Work

In order to expand and realize a 6DOF non-compliant docking HIL simulation to a whole docking scenario (i.e., not only first impact), one should study the errors' sources in the single impact, in order to predict the errors and compensate for them in the "HIL Model", so that both models ("Docking Model" and "HIL Model") have a comparable whole docking trajectory.

More contact dynamics models should be tested and validated using the presented 1DOF HIL testbed, to identify more representative contact models than the one utilized in this work.

More contact dynamics scenarios (i.e., various materials, various impact velocities, various masses, etc.) should be tested and validated using the presented 1DOF HIL testbed, to provide more experimental results for the advancement of the contact dynamics research.

Contact dynamics research should be carried out, to propose a new contact model that takes into consideration the experimental impact results from the HIL tests.

References

Amirouche, Farid (May 2007). *Fundamentals of Multibody Dynamics: Theory and Applications*. en. Springer Science & Business Media (cit. on p. 76).

Ariane Group (2017). *400N Bipropellant Apogee Motors* (cit. on p. 2).

Bell, Robert, John Collins, James Wertz, and L. Jane Hansen (Sept. 2003). "Hardware-in-the Loop Tests of an Autonomous GN&C System for On-orbit Servicing". en. In: American Institute of Aeronautics and Astronautics (cit. on p. 6).

Boge, T., T. Wimmer, O. Ma, and M. Zebenay (2010). "Epos-a robotics-based hardware-in-the-loop simulator for simulating satellite rvd operations". In: *10th International symposium on artificial intelligence, robotics and automation in space, Sapporo, Japan* (cit. on pp. 3, 5).

Boge, Toralf, Heike Benninghoff, Melak Zebenay, and Florian Rems (Sept. 2012). "Using Robots for Advanced Rendezvous and Docking Simulation". In: (cit. on pp. 3, 5).

Bondoky, Karim (2015). "On-Orbit Servicing Satellite Docking Mechanism Modeling and Simulation". eng. MA thesis (cit. on pp. 91, 100).

Bondoky, Karim, Klaus Janschek, Andreas Rathke, and Sebastian Schwarz (Sept. 2017a). "Analysis of Hardware-in-the-Loop setup without artificial compliance for docking contact dynamics of satellites". en. In: American Institute of Aeronautics and Astronautics (cit. on pp. 44, 45, 47, 51, 53).

Bondoky, Karim, Klaus Janschek, Andreas Rathke, and Sebastian Schwarz (Mar. 2017b). "Analysis of small satellite docking contact dynamics for Hardware-in-the-Loop Testing". In: *Fachtagung Mechatronik 2017: Dresden (09.03.-10.03.2017)*. VDI Mechatronik - Dresden, Germany, pp. 117–122 (cit. on p. 53).

Bondoky, Karim, Klaus Janschek, Andreas Rathke, and Sebastian Schwarz (Sept. 2018). "Analysis and Modeling of 6DOF Docking without Compliance Using Nonlinear Contact Dynamics". en. In: *2018 AIAA SPACE and Astronautics Forum and Exposition*. Orlando, FL: American Institute of Aeronautics and Astronautics (cit. on pp. 103–106).

Boos, Michael and John McPhee (Jan. 2011). "Volumetric Contact Dynamics Models and Experimental Validation of Normal Forces for Simple Geometries". In: pp. 275–284 (cit. on p. 151).

dSpace (2016). *DS1103 Hardware Installation and Configuration*. en (cit. on p. 157).

Flores, Paulo, Margarida Machado, Miguel T. Silva, and Jorge M. Martins (Mar. 2011). "On the continuous contact force models for soft materials in multibody dynamics". en. In: *Multibody System Dynamics* 25.3, pp. 357–375 (cit. on pp. 41, 53, 98, 150, 166, 175, 178, 180).

Flores-Abad, Angel, Ou Ma, Khanh Pham, and Steve Ulrich (July 2014). "A review of space robotics technologies for on-orbit servicing". en. In: *Progress in Aerospace Sciences* 68, pp. 1–26 (cit. on p. 1).

Fossen, Thor I. and Ola-Erik Fjellstad (Jan. 1995). "Nonlinear modelling of marine vehicles in 6 degrees of freedom". In: *Mathematical Modelling of Systems* 1.1, pp. 17–27 (cit. on p. 80).

Geenhuizen, J. A. van (2008). "Friction compensation for the printer system". MA thesis. Dept. Mech. Eng., Eindhoven Univ. Technol., Eindhoven, The Netherlands (cit. on p. 98).

Goldsmith, Werner (1960). "Impact: The Physical Theory and Behaviour of Colliding Solids". In: *London: Edward Arnold Ltd* (cit. on pp. 33–35, 39).

Gonthier, Yves (2007). "Contact dynamics modelling for robotic task simulation". PhD Thesis. University of Waterloo (cit. on pp. 30, 39, 151).

Gonthier, Yves, John McPhee, Christian Lange, and Jean-Claude Piedbœuf (2004). "A novel contact model based on volumetric information". In: *Multibody System Dynamics* 11, pp. 209–233 (cit. on p. 31).

Guess, Trent M., Ganesh Thiagarajan, Mohammad Kia, and Meenakshi Mishra (2010). "A subject specific multibody model of the knee with menisci". In: *Medical Engineering and Physics* 32.5, pp. 505–515 (cit. on p. 37).

Hall, Drew P., B. Mark Slone, and Patrick A. Tobbe (May 2006). "Modeling and testing of docking and berthing mechanisms". In: ed. by Pejmun Motaghedi, p. 62210D (cit. on p. 3).

Han, Junwei, Qitao Huang, and Tongli Chang (2008). "Research on space docking hil simulation system based on stewart 6-dof motion system". In: *Proceedings of the JFPS International Symposium on Fluid Power*. Vol. 2008. The Japan Fluid Power System Society, pp. 213–218 (cit. on pp. 3, 6).

Hardt, Michael, Carlos Mas, A. Ayuso, Daniel Cocho, Luis Mollinedo, Oscar Gracia, and Peter Urmston (2011). "Validation of space vehicle docking with the international berthing & docking mechanism and a kuka robot". In: *Proc. 14th Eur. Space Mech. Tribol. Symp.* Pp. 113–120 (cit. on pp. 3, 7).

Herbert, R. G. and D. C. McWhannell (1977). "Shape and frequency composition of pulses from an impact pair". In: *Journal of Engineering for Industry* 99.3, pp. 513–518 (cit. on pp. 34, 37).

Hertz, Heinrich Rudolf (1882). "Uber die Beruhrung fester elastischer Korper und Uber die Harte". In: *Verhandlung des Vereins zur Beforderung des GewerbefleiBes, Berlin*, p. 449 (cit. on p. 34).

Hunt, K. H. and F. R. E. Crossley (1975). "Coefficient of restitution interpreted as damping in vibroimpact". In: *Journal of applied mechanics* 42.2, pp. 440–445 (cit. on pp. 35–37).

Janschek, Klaus (2012). *Mechatronic Systems Design: Methods, Models, Concepts*. en. Berlin Heidelberg: Springer-Verlag (cit. on pp. 162, IV, V, XI).

Kaman Precision Products (2015). *KD-5100 Differential Measuring System User's Manual* (cit. on pp. 159, 162, 163).

Kistler Group (2013). *Instruction Manual Charge Meter Type 5015A* (cit. on pp. 160, 163).

Kistler Group (2018). *Instruction Manual. Press Force Sensor Type 9323AA, 9323A, 9333A, 9343A, 9363A, 9383A, 9393A* (cit. on pp. 159, 163).

Kraft, Matthias (Mar. 2016). "Modeling, Analysis and Comparison of Various Nonlinear Contact Dynamics Models for a Multibody System". English. Studienarbeit. Technische Universität Dresden (cit. on pp. 31, 121).

Lankarani, H. M. and P. E. Nikravesh (1990). "A contact force model with hysteresis damping for impact analysis of multibody systems". In: *Journal of mechanical design* 112.3, pp. 369–376 (cit. on p. 38).

Lankarani, Hamid M. and Parviz E. Nikravesh (1994). "Continuous contact force models for impact analysis in multibody systems". In: *Nonlinear Dynamics* 5.2, pp. 193–207 (cit. on p. 39).

Lee, Ting W. and A. C. Wang (Sept. 1983). "On The Dynamics of Intermittent-Motion Mechanisms. Part 1: Dynamic Model and Response". en. In: *Journal of Mechanisms, Transmissions, and Automation in Design* 105.3. Publisher: American Society of Mechanical Engineers Digital Collection, pp. 534–540 (cit. on p. 38).

Lei, Zhou (Nov. 2019). "Setup and Implementation of a Hardware-In-The-Loop (HIL) Simulation Testbed for the Validation of Docking Contact Dynamics". English. Studienarbeit. Technische Universität Dresden (cit. on pp. 154, 161, 162, 165, I, III, V–XIV, XVI, XVII, XIX).

Ma, Ou, Angel Flores-Abad, and Toralf Boge (Dec. 2012). "Use of industrial robots for hardware-in-the-loop simulation of satellite rendezvous and docking". en. In: *Acta Astronautica* 81.1, pp. 335–347 (cit. on pp. 3, 5).

Machado, Margarida, Pedro Moreira, Paulo Flores, and Hamid M. Lankarani (July 2012). "Compliant contact force models in multibody dynamics: Evolution of the Hertz contact theory". en. In: *Mechanism and Machine Theory* 53, pp. 99–121 (cit. on p. 41).

Micro-Epsilon Messtechnik GmbH (2008). *Instruction Manual optoNCDT 2300* (cit. on pp. II, III).

Muhammad, Bashir Bala, Md. Habibur Rahman, and Mohd Ridzuan bin Ahmad (May 2015). "Modelling and simulation of piezoelectric actuator for vibration control". In: *2015 10th Asian Control Conference (ASCC)*, pp. 1–6 (cit. on pp. 157, IV).

Pereira, Cândida M., Jorge A. Ambrósio, and Amílcar L. Ramalho (2010). "A methodology for the generation of planar models for multibody chain drives". In: *Multibody system dynamics* 24.3, pp. 303–324 (cit. on p. 39).

Piedboeuf, J.-C., J. De Carufel, Farhad Aghili, and Erick Dupuis (1999). "Task verification facility for the Canadian special purpose dextrous manipulator". In: *Robotics and Automation, 1999. Proceedings. 1999 IEEE International Conference on*. Vol. 2. IEEE, pp. 1077–1083 (cit. on p. 3).

Piezomechanik GmbH (2020). *First Steps towards Piezoaction* (cit. on p. 167).

Piezosystemjena (2016). *instruction manual switching amplifier RCV 1000/7*. en (cit. on p. 158).

Piezosystemjena (2019). *Datasheet. PSt 1000/16/300 VS25 – customized Piezocomposite Actuator - series PStVS with preload* (cit. on p. 158).

Ploen, Scott R., Fred Y. Hadaegh, and Daniel P. Scharf (2004). "Rigid body equations of motion for modeling and control of spacecraft formations-part 1: Absolute equations of motion". In: (cit. on p. 80).

Schilling, Robert J. (1996). *Fundamentals of Robotics: Analysis and Control*. 1st. Simon & Schuster Trade (cit. on p. 87).

Schwartz, Jana L., Mason A. Peck, and Christopher D. Hall (July 2003). "Historical Review of Air-Bearing Spacecraft Simulators". en. In: *Journal of Guidance, Control, and Dynamics* 26.4, pp. 513–522 (cit. on p. 3).

Wang, Qian, Feng Gao, Chenkun Qi, Jinxin Sun, and Minglun Yang (2017). "Hardware-in-the-loop Simulation of Space Docking Device Using 6-DOF Parallel Robot". en. In: ACM Press, pp. 1–6 (cit. on p. 6).

Wasfy, Tamer M. and Ahmed K. Noor (Nov. 2003). "Computational strategies for flexible multibody systems". In: *Applied Mechanics Reviews* 56.6, pp. 553–613 (cit. on p. 39).

Wertz, James R. and Robert Bell (2003). "Autonomous rendezvous and docking technologies: status and prospects". In: *Space Systems Technology and Operations*. Vol. 5088. International Society for Optics and Photonics, pp. 20–31 (cit. on p. 1).

Witkin, Andrew and David Baraff (1997). "Physically Based Modeling: Principles and Practice: Differential Equation Basics". In: *Course Note A SIGGRAPH* 97 (cit. on p. 80).

Wohllebe, Daniel (Oct. 2017). "Multibody Modeling and Analysis of a Docking Process for a HIL Test". English. Diplomarbeit. Technische Universität Dresden (cit. on pp. 76, 78, 91).

Zebenay, Melak (2014). "Development of a robotics-based satellites docking simulator." English. OCLC: 905870812. PhD thesis. S.l.: [s.n.] (cit. on p. 5).

Zebenay, Melak, Toralf Boge, Rainer Krenn, and Daniel Choukroun (2015). "Analytical and experimental stability investigation of a hardware-in-the-loop satellite docking simulator". In: *Proceedings of the Institution of Mechanical Engineers, Part G: Journal of Aerospace Engineering* 229.4, pp. 666–681 (cit. on pp. 3, 5, 35).

Zhang, Yuning and Inna Sharf (2009). "Validation of Nonlinear Viscoelastic Contact Force Models for Low Speed Impact". en. In: *Journal of Applied Mechanics* 76.5, p. 051002 (cit. on p. 150).

Zipfel, Peter H. (Jan. 2007). *Modeling and Simulation of Aerospace Vehicle Dynamics, Second Edition*. en. Reston ,VA: American Institute of Aeronautics and Astronautics (cit. on p. 80).

Appendix

Appendix A

Displacement Closed Loop Controller Design

This section describes the implementation of the testbed. Firstly, it is explained in Section A.1 how the displacement sensor was calibrated. Secondly, it is presented in Section A.2 how the plant was modeled (i.e., identify the Transfer Function (T.F.) of the plant). Thirdly, in Section A.3, based on the identified plant T.F. a displacement closed-loop controller that was designed, is presented.

Most of the ideas and the concepts in this section were developed and implemented by my supervised student "Zhou Lei" during his student-research-project ("Studienarbeit") [Lei, 2019].

A.1 Calibration

As this experiment was dealing with micro-meters, accurate calibration of eddy-current differential sensor was required. The laser-sensor "optoNCDT ILD 2300" by "Micro-Epsilon Messtechnik GmbH" was used (See Fig. A.1a). The laser sensor operates according to the principle of optical triangulation. It emits a laser beam on the target, which is reflected to the receiver positioned at a certain angle to the optical axis of the laser beam inside the laser sensor. An overview of the calibration setup is shown in Fig. A.1.

The calibration process was automated, so that it could be repeated multiple times to get the average measurements and to calibrate the sensor with the highest possible resolution. In a Simulink® model, a stair signal was used to drive the piezoactuator (see Fig. A.2a). This stair signal increased until it reached the maximum drive voltage of the actuator, then it decreased. The stair signal had a 5V step for 5 seconds in up-stage and a -5V step for 5 seconds in down-stage. This 5 seconds period was the time duration for each step in the stair signal, which guaranteed that the actuator reaches its steady state.

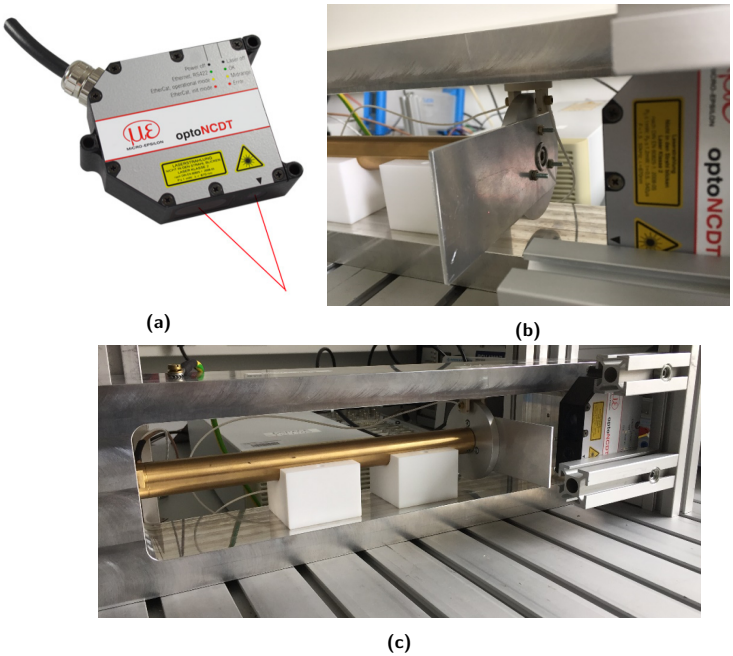

Figure A.1: Sensor Calibration Setup. (a) Lase sensor "optoNCDT ILD 2300" Image from: [Micro-Epsilon Messtechnik GmbH, 2008] (b) Close-up of the calibration setup illustrates the laser sensor while measuring the motion of actuator (projected laser-beam can be shown on the an extended thick metal-piece fixed to actuator's moving part) (c) Overview of the calibration setup

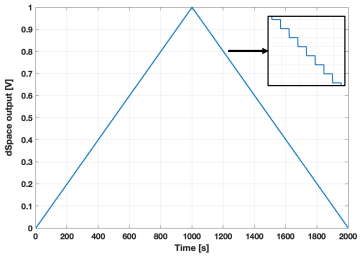

(a) Stair Signal used for calibration.

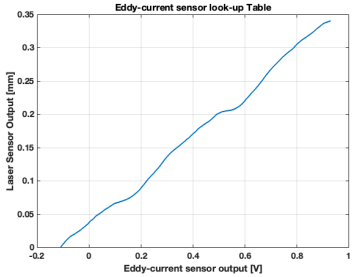

(b) Produced Look-up Table of Eddy-current sensor and Actual Displacement.

Figure A.2: Method and Result of Sensor Calibration. Figure adapted from [Lei, 2019]

During the calibration process, the eddy-current sensor, as well as the laser-sensor measured the displacement of the piezoactuator at the same time. Accordingly, a look-up table of the eddy-current measurements and the actual displacement (measured by laser-sensor) was built, see Fig. A.2b. The calibration results in Fig. A.2b describe the relationship between the eddy-current differential-sensor output voltage in volts and the actuator displacement in mm. These results were the average taken from five different measurements.

According to Eq. A.1 [Micro-Epsilon Messtechnik GmbH, 2008], the laser-sensor output voltage is converted to displacement, using the following equation:

$$d_{ls} = V_{ls} \cdot 10 \cdot \frac{L_{max} - L_{min}}{V_{max} - V_{min}} \tag{A.1}$$

where d_{ls} is the displacement in mm, V_{ls} is the laser sensor output voltage, L_{max} and L_{min} are the maximum and minimum distance that the laser can detect respectively. V_{max} is the sensor maximal output voltage, when the distance between the laser sensor and the measured object is equal to L_{max}, while V_{min} is the minimum output voltage when the distance is equal toL_{min}. The laser sensor attributes for this calibration process are summarized in Table A.1.

Table A.1: Laser-sensor Settings

Measuring rate	30 kHz
Output Voltage range ([V_{min}-V_{max}])	[-10V - +10V]
Detection range ([L_{min}-L_{max}])	[22.5mm - 23mm]

A.2 Plant Model

The goal in this section is to build a mathematical model of the plant (i.e., find the transfer function of the plant), see Fig. A.3. The resulted model was used in the next Section A.3 to design a closed-loop displacement controller for the piezoactuator.

Various methods are suggested to model such a system, such as:

1. Physical-based modeling, where the model is built based on material and structure parameters, e.g., piezoelectric force-constants, Young's modulus, dielectric constants, etc.
2. "Modeling by experiment", such that the model is determined by input-output data from the experiment. [Muhammad et al., 2015], [Janschek, 2012].
3. "System Identification Toolbox" in Simulink®, Matlab®, to identify the considered system.

In this testbed, the necessary parameters for building the piezoelectric actuator model were not known and it was not convenient to measure those parameters experimentally. Therefore, the second method was used to identify the piezoactuator and plant model and was validated using the Simulink® toolbox (third method).

A.2.1 Method Description

A colored-noise signal was used as an input-signal to the experiment, in order to identify the plant model. The block diagram depicting the plant model identification is shown in Fig. A.3. Such that u is the dSpace-output signal to the piezoactuator-amplifier. m is the piezoactuator-amplifier output's signal to the piezoactuator. y' is the actual physical displacement of the piezoactuator. y is the piezoactuator displacement measured by the eddy-current sensor.

Using this method, firstly, the transfer-function of various parts of the plant were identified independently. Afterwards, the transfer-function of

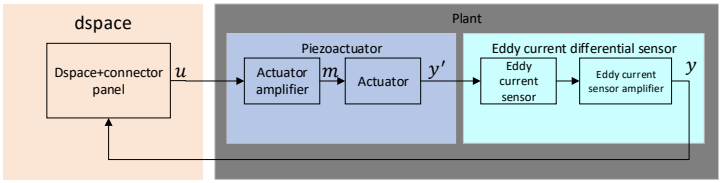

Figure A.3: Block-diagram for the plant model identification. [Lei, 2019]

the whole system was identified. The following steps were followed for frequency response and transfer function identification:

i) **Piezoactuator-amplifier**: using signal u and m, the frequency response of the piezoactuator-amplifier is estimated.

ii) **Piezoactuator and Eddy-current sensor**: using signal m and y, the frequency response of the actuator together with the eddy-current sensor is estimated.

iii) **Whole Plant**: using signal u and y the frequency response of the whole plant is identified.

The following abbreviated notations were used for simplification:

$$[w] = 1 + \frac{s}{w} \tag{A.2}$$

$$\{d,w\} = 1 + 2d\frac{s}{w} + \frac{s^2}{w^2} \tag{A.3}$$

$$\{w\} = 1 + \frac{s^2}{w^2} \tag{A.4}$$

The frequency-response $G(jw)$ of the system under inspection was estimated using Eq. A.5. The detailed derivation procedure of Eq. A.5 can be found in [Janschek, 2012]

$$G\left(jw\right) = \frac{S_{uy}\left(jw\right)}{S_{uu}\left(jw\right)} \tag{A.5}$$

where u is the input-signal of the researched object, y is the output-signal. And S_{uy} is the cross spectral density, (see Eq. A.6) and S_{uu} is the power

spectral density (see Eq. A.7) and are as follows:

$$S_{uy}(jw) = \int_{-\infty}^{\infty} r_{uy}(\tau) e^{-jw\tau} d\tau \tag{A.6}$$

$$S_{uu}(jw) = \int_{-\infty}^{\infty} r_{uu}(\tau) e^{-jw\tau} d\tau \tag{A.7}$$

such that $r_{uy}(\tau)$ is the cross-correlation of the signals $y(t)$ and $u(t)$, $r_{uu}(\tau)$ is the auto-correlation of the signal $u(t)$.

A.2.2 Transfer Function (T.F.) Estimation

First, piezoactuator-amplifier only, then piezoactuator with the eddy-current system and finally the T.F. of the whole system.

i) **Piezoactuator-amplifier only** (using signal u & m)

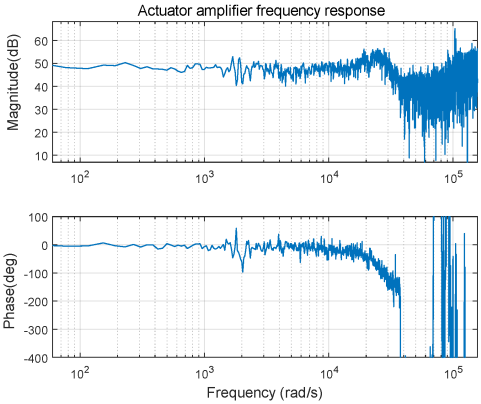

Figure A.4: Frequency response of the piezoactuator-amplifier [Lei, 2019]

The frequency-response of the piezoactuator-amplifier is shown in Fig. A.4. It shows that the piezoactuator-amplifier is a 2nd order system, because in this bode-diagram there is a resonant peak at the frequency

approximately $26000 rad/s$ and the phase at the same frequency has a -180° shift. Thus, the transfer function of the piezoactuator-amplifier can be defined as Eq. A.8. Accordingly, the parameters K_1, d_1 and w_1 can be easily determined based on the frequency-response of the piezoactuator-amplifier.

$$G_1(s) = \frac{M(s)}{U(s)} = \frac{K_1}{\{d_1, w_1\}} \tag{A.8}$$

where $M(s)$ is the Laplace-transformation of the signal m. $U(s)$ is the Laplace-transformation of the signal u. w_1 is the resonant-frequency of the piezoactuator-amplifier, d_1 is the damping constant, K_1 is the gain.

ii) **Piezoactuator and Eddy-current sensor** (using signal m & y)

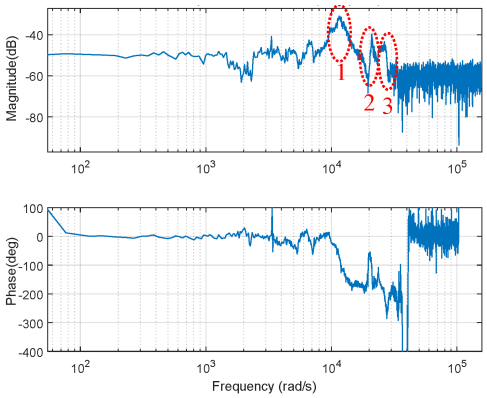

Figure A.5: Frequency response of the piezoactuator and eddy-current system (sensor & amplifier). Figure adapted from[Lei, 2019]

The frequency-response of the piezoactuator and the eddy-current system (sensor and amplifier) is shown in Fig. A.5. Three red-dashed circles are added to highlight important attributes. The first circle marks the first resonant peak (w_{p1}), the second circle marks the first eigenmode (w_{z1} and w_{p2}), the third circle marks the second eigenmode (w_{p3} and w_{z2}). In order to calculate the damping constants, the dominant characteristics (three peaks and two valleys, marked in Fig. A.5)

were considered.
Moreover, it is observed in the phase diagram that there is a -180 degrees shift at the first dominant resonant frequency, while the phase at the first eigenmode has firstly a positive jump and then has a negative jump (i.e., phase increases when there is a zero and decreases when there is a pole). Also, the phase at the second eigenmode has firstly a negative jump and then has a positive jump. Therefore, the transfer function of the piezoactuator and the eddy-current system is defined as Eq. A.9.

$$G_2^{'}(s) = \frac{Y(s)}{M(s)} = \frac{K_2}{\{d_{p1},w_{p1}\}} \frac{\{d_{z1},w_{z1}\}}{\{d_{p2},w_{p2}\}} \frac{\{d_{z2},w_{z2}\}}{\{d_{p3},w_{p3}\}} \tag{A.9}$$

where $Y(s)$ is the Laplace-transformation of the signal y, K_2 is the gain, w_{p1}, w_{p2}, w_{p3} is the first, second and third resonant frequency, respectively. In addition, w_{z1}, w_{z2} is the first and second anti-resonant frequency, respectively. While, d_{p1}, d_{p2}, d_{p3}, d_{z1} and d_{z2} are the damping constants at frequency w_{p1}, w_{p2}, w_{p3}, w_{z1} and w_{z2} respectively.

From the bode diagram (Fig. A.5) of the piezoactuator and the eddy-current system, the following parameters were known: w_{p1}, w_{p2}, w_{p3}, w_{z1}, w_{z2}, the magnitudes g_{p1}, g_{p2}, g_{p3}, g_{z1}, g_{z2} at w_{p1}, w_{p2}, w_{p3}, w_{z1}, w_{z2}, respectively, as well as the magnitude g_{dc} for DC signal. In order to identify the damping constants d_{p1}, d_{p2}, d_{p3}, d_{z1} and d_{z2}, a smart method was developed by [Lei, 2019] and is presented in detail in the Appendix B.
Using the developed method (see Appendix B), the required damping constants were identified, (for the following case: $w_{p1} = 10700$, $w_{p2} = 21700$, $w_{p3} = 26960$, $w_{z1} = 19750$, $w_{z2} = 28990$, $g_{p1} = -33$, $g_{p2} = -44$, $g_{p3} = -45$, $g_{z1} = -60$, $g_{z2} = -60$), as follows: $d_{z1}^2 = 0.0035, d_{z2}^2 = 0.0124, d_{p1}^2 = 0.0047, d_{p2}^2 = 0.0006656, d_{p3}^2 = 0.0004326$

To simplify the model of the considered system, the third red-dashed-circle in Fig. A.5 was ignored, such that only the first two resonant frequencies (w_{p1}, w_{p2}), as well as the first anti-resonant frequency (w_{z1}) were considered. Accordingly, the simplified model (in contrast to Eq.

A.9) appears as follows:

$$G_2(s) = \frac{K_2}{\{d_{p1},w_{p1}\}} \frac{\{d_{z1},w_{z1}\}}{\{d_{p2},w_{p2}\}} \tag{A.10}$$

$$= \frac{9.195 \cdot 10^{26} s^2 + 1.145 \cdot 10^{30} s + 3.587 \cdot 10^{35}}{1.888 \cdot 10^{21} s^4 + 4.51 \cdot 10^{24} s^3 + 1.093 \cdot 10^{30} s^2 + 1.134 \cdot 10^{38}}$$

iii) **Whole Plant** (using signal u & y)
By combining both models (Eq. A.8, A.10) together, the transfer-function of the whole plant is as follows:

$$\begin{aligned} G(s) = \frac{Y(s)}{U(s)} &= \frac{M(s)}{U(s)} \cdot \frac{Y(s)}{M(s)} \\ &= G_1(s) \cdot G_2(s) \\ &= \frac{K_1}{\{d_1,w_1\}} \cdot \frac{K_2}{\{d_{p1},w_{p1}\}} \frac{\{d_{z1},w_{z1}\}}{\{d_{p2},w_{p2}\}} \end{aligned} \tag{A.11}$$

After substituting all the required parameters, the transfer-function of the plant is as follows:

$$\begin{aligned} G(s) =& G_1(s) \cdot G_2(s) \\ =& \left(\frac{1.758 \cdot 10^{15}}{2600 s^2 + 3.802 \cdot 10^8 s + 1.758 \cdot 10^{13}}\right) \cdot \\ & \left(\frac{9.195 \cdot 10^{26} s^2 + 1.145 \cdot 10^{30} s + 3.587 \cdot 10^{35}}{1.888 \cdot 10^{21} s^4 + 4.51 \cdot 10^{24} s^3 + 1.093 \cdot 10^{30} s^2 + 1.134 \cdot 10^{38}}\right) \end{aligned} \tag{A.12}$$

In order to validate the mathematical model G(s) (developed by Zhou Lei [Lei, 2019]), the plant model was also identified using the "System Identification Toolbox" in Simulink®, Matlab®. The comparison of the frequency response of the different methods incorporated, as well as the raw experimental frequency response, is shown in Fig. A.6. From the figure, it is observed that the model estimated by the Matlab® toolbox has two resonant peaks, but it does not estimate the zero, while Lei's model shows the two resonant peaks, as well as the zero and accordingly Zhou validated his model.

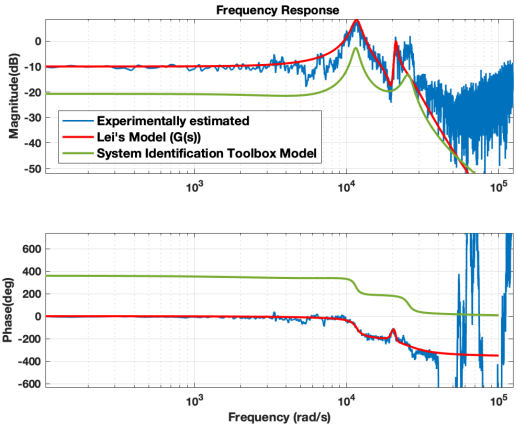

Figure A.6: Frequency response of the different methods (experimentally estimated, mathematical modeling by "Zhou Lei" [Lei, 2019], "System Identification Toolbox") used to model the system plant.

A.3 Controller Design (Closed-Loop)

In this section, the closed-loop controller is presented, which was designed by [Lei, 2019] to control the piezoactuator displacement, using the eddy-current sensor as the feedback. The controller was firstly designed based on the model of plant $G(s)$ (See Eq. A.12 and Fig. A.7). Afterwards, the controller was improved based on the real plant.
The control block-diagram is depicted in Fig. A.7, such that r is reference input, w is the filtered reference input (after the prefilter $F(s)$), e is control error, u is controller output, y is controlled variable (i.e., displacement of actuator measured by eddy-current sensor) and η_1, η_2 are noises.

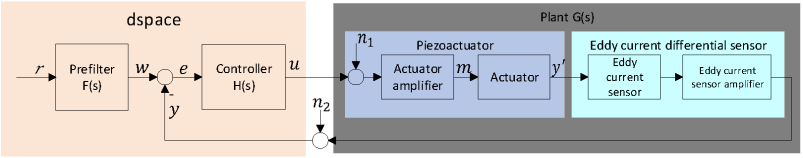

Figure A.7: Controller Block-diagram [Lei, 2019]

A.3.1 Method Description

A structure of two Design-Degrees-Of-Freedom (DDOF) was taken into consideration. Firstly, a closed-loop controller was designed to make the plant robustly stable. Afterwards, a prefilter was designed to improve the controller's response based on the closed control-loop. [Janschek, 2012]

The following transfer-functions are defined for the design-process (refer to Fig. A.7):
Open-loop transfer-function $L(s)$:

$$L(s) = H(s)G(s) \tag{A.13}$$

Complementary sensitivity:

$$T(s) = \frac{L(s)}{1 + L(s)} \tag{A.14}$$

Reference-input transfer function:

$$T_w(s) = \frac{Y(s)}{W(s)} = \frac{L(s)}{1 + L(s)} = T(s) \tag{A.15}$$

$$T_r(s) = \frac{Y(s)}{R(s)} = \frac{F(s)L(s)}{1 + L(s)} = F(s)T(s) \tag{A.16}$$

such that $T(s)$ is the closed-loop transfer function. $W(s)$ is the Laplace-transformation of the signal w. $R(s)$ is the Laplace-transformation of the signal r.

A.3.2 PID Closed-Loop Controller

To simplify the system's stability analysis, [Lei, 2019] used Nichols diagram for the controller design. Figure A.8a shows Nichols diagram with a P controller, where P is unit gain. It shows that it has a bad robust stability and it requires a PID controller to provide a positive phase shift, to improve system stability. Accordingly, a PID controller was designed, which provided the positive shift (as in Fig A.8b) and hence improved the system stability. After several attempts, the PID controller $H(s)$ was selected as in Eq. A.17. A bode diagram of the PID and its effect on the system is shown in Fig. A.9.

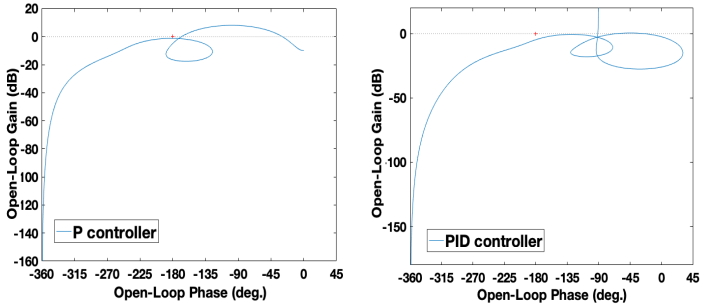

(a) open-loop, P controller **(b)** open-loop, PID controller

Figure A.8: Nichols diagrams. Figure adapted from [Lei, 2019]

$$H(s) = K_{PID}\frac{\{d_N, w_N\}}{s\,[w_D]} = 2700\frac{\{0.1{,}6500\}}{s\,[35000]} \tag{A.17}$$

A.3.3 Prefilter Design

The step response y_w of the closed-loop system with the PID controller (based on the modeled plant $G(s)$) shown in Figure A.9c, confirms that the system is stable, however, the transient performance required improvement. Thus, the second DDOF, prefilter $F(s)$, was necessary to improve the transient behavior. Accordingly, the prefilter was firstly designed based on the model of the plant $G(s)$ and presented in Eq. A.18. Afterwards, it was verified and updated w.r.t. the real plant (i.e., not the model) and presented in Eq. A.19.

A. **Model-based Design**

After several attempts and tests, the prefilter was designed (see Eq. A.18), based on the model of the plant $G(s)$.

From the bode diagram $T_w(jw)$ (see Fig. A.9b), one observes a dip in the magnitude at frequency of 6500 rad/s. Therefore, an anti-notch filter $\frac{\{d_{N1}, w_0\}}{\{d_{D1}, w_0\}}$ was used to compensate for that dip. Moreover, the magnitudes at the first and second resonant-frequency were required to be reduced, therefore, two notch filters $\frac{\{d_{N2}, w_{p1}\}}{\{d_{D2}, w_{p1}\}}$ and $\frac{\{d_{N3}, w_{p2}\}}{\{d_{D3}, w_{p2}\}}$ were used

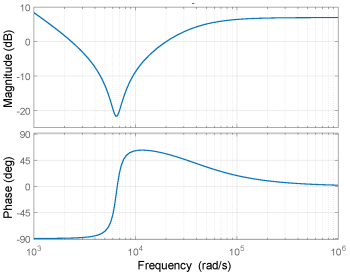

(a) Bode diagram of PID $H(s)$ only

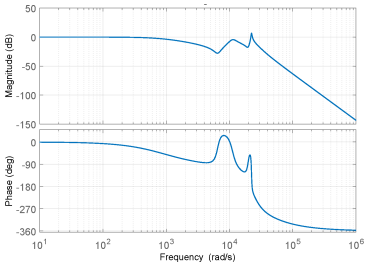

(b) Bode diagram of $T_w(jw)$

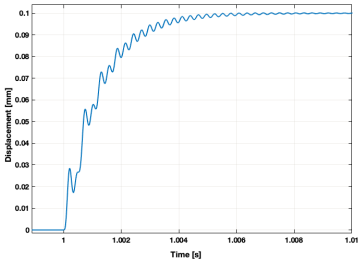

(c) Step response y_w for the reference input w

Figure A.9: Analysis of PID (without prefilter). Figure adapted from [Lei, 2019]

for the prefilter.

Using only the previous components of the prefilter showed that the settling time was too long and it required to be improved. (See Fig. A.10). Therefore, a lead term $\frac{[w_N]}{[w_D]}$ was added, in order to keep the closed-loop frequency response as flat as possible over the widest possible frequency band.

$$\begin{aligned} F(s) &= \frac{[w_N]}{[w_D]} \frac{\{d_{N1}, w_0\}}{\{d_{D1}, w_0\}} \frac{\{d_{N2}, w_{p1}\}}{\{d_{D2}, w_{p1}\}} \frac{\{d_{N3}, w_{p2}\}}{\{d_{D3}, w_{p2}\}} \\ &= \frac{[880]}{[8000]} \frac{\{1{,}6500\}}{\{0.1{,}6500\}} \frac{\{0.1{,}11660\}}{\{1{,}11660\}} \frac{\{0.07{,}21200\}}{\{2{,}21200\}} \end{aligned} \tag{A.18}$$

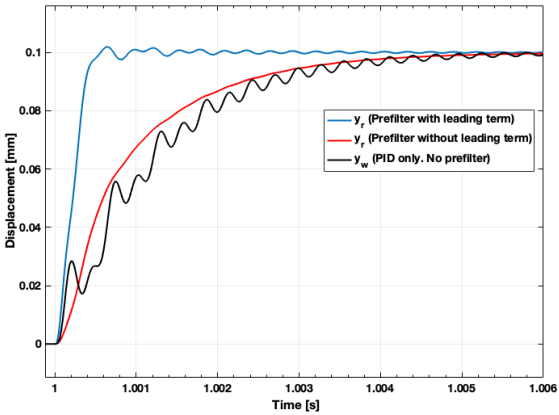

Figure A.10: Step-response of PID only, versus the different prefilters designed. Figure adapted from [Lei, 2019]

B. **Optimization/Validation**
The frequency response $T_{y/w}(jw)$ of the closed-loop system using the real plant was experimentally measured and shown in Fig. A.11a. Such that the reference input w was fed to the the PID controller $H(s)$, which drove the piezoactuator, while the feedback output y was the actual displacement measured by the eddy-current sensor. (see Fig. A.7).

In the bode diagram in Fig. A.11a, one observes a dip in the magnitude at a frequency of ~$6000 rad/s$, which is clearly caused by the PID controller (refer to Fig. A.9b). To compensate for the behavior at this frequency and other frequencies, the prefilter was updated once again. After multiple attempts, the prefilter equation was selected in Eq. A.19, as follows:

$$F(s) = \frac{[1200]}{[4500]} \frac{\{1.8{,}5700\}}{\{0.1{,}5700\}} \frac{\{0.05{,}10700\}}{\{1{,}10700\}} \frac{\{0.1{,}21700\}}{\{1{,}21700\}} \frac{1}{\{2{,}14000\}} \tag{A.19}$$

- The anti-notch filter $\frac{\{1.8,5700\}}{\{0.1,5700\}}$ was used to compensate the dip in magnitude of the frequency response $T_{y/w}(jw)$ caused by the PID controller.
- The notch filters $\frac{\{0.05,10700\}}{\{1,10700\}}$ and $\frac{\{0.1,21700\}}{\{1,21700\}}$ were used to reduce the magnitude at the first and the second peak.
- The second order low-pass filter $\frac{1}{\{2,14000\}}$ was used to reduce unmodeled high-frequency peaks.
- The lead item $\frac{[1200]}{[4500]}$ was used to keep the frequency response of the output y to the external reference input r as flat as possible over the widest possible frequency band.

Finally, the frequency response $T_{y/r}(jw)$ of the closed-loop system including real plant, prefilter and PID controller was experimentally estimated and showed to be satisfactory. (Fig. A.11b).

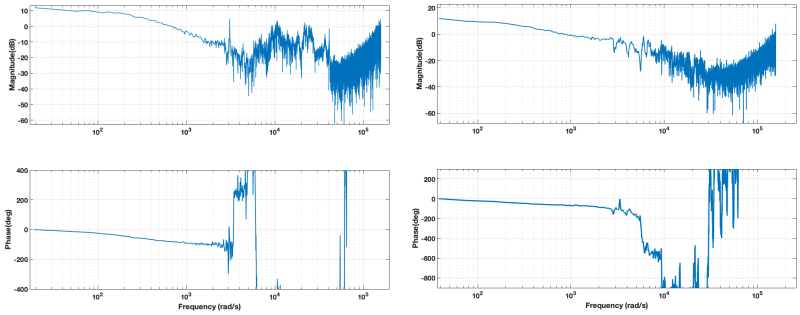

(a) $T_{y/w}(jw)$ (without prefilter) **(b)** $T_{y/r}(jw)$ (with prefilter)

Figure A.11: Experimentally Estimated Frequency Response of Closed-Loop System. Figure adapted from [Lei, 2019]

A.4 Controller Validation and Results

In this section, the designed controller (PID with Prefilter) was tested with the real testbed (instead of the model), to show the accuracy of the controlled actuator and its fast response. Firstly, the controlled displacement of the piezoactuator is presented. Afterwards, the step-response of the piezoactuator with the controller is presented.

i. **Hysteresis Curve**
Figure A.12, shows the difference between the piezoactuator motion with controller and without controller. The realized displacement by the piezoactuator is on the Y-axis (measured by the eddy-current sensor), while the reference input (required displacement) is on the X-axis. Accordingly, using the designed controller, the hysteresis effect was completely compensated for and steady-state error was canceled.

ii. **Step-Response of Piezoactuator**
In Fig. A.13, three different step-responses of 0.1mm to the piezoactuator were presented: open-loop, PID controller only and PID controller with Prefilter. Using the PID controller with prefilter improved the transient response significantly and reduced the settling time as required.

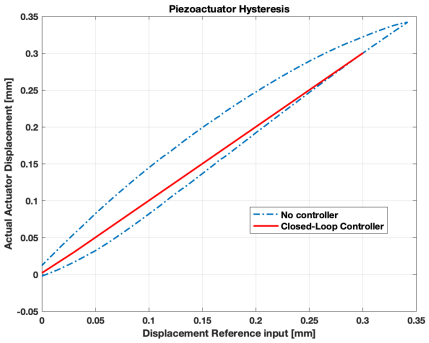

Figure A.12: Piezoactuator Displacement. Hysteresis (no controller) versus compensated displacement (with controller). Figure adapted from [Lei, 2019]

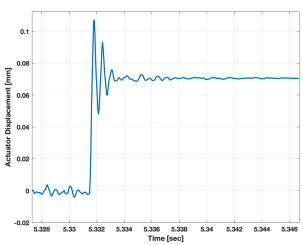

(a) Open-loop

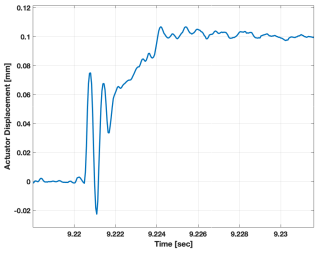

(b) PID controller only

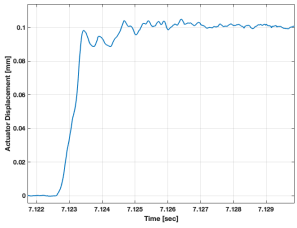

(c) PID with prefilter

Figure A.13: Step-response of $0.1mm$ of Piezoactuator. Figure adapted from [Lei, 2019]

Appendix B

Damping Constants Identification

In this appendix, the method that was developed by my supervised student "Zhou Lei" in order to find the damping constants of a model is presented. The following is quoted from [Lei, 2019]:
" From the bode diagram (see Fig. A.5) of the piezoelectric actuator & the eddy current sensor, these parameters are known: w_{p1}, w_{p2}, w_{p13}, w_{z1}, w_{z2}, *the magnitude* g_{p1} *at* w_{p1}, *the magnitude* g_{p2} *at* w_{p2}, *the magnitude* g_{p3} *at* w_{p3}, *the magnitude* g_{z1} *at* w_{z1}, *the magnitude* g_{z2} *at* w_{z2} *and the magnitude* g_{dc} *for DC signal. In order to find out the damping constants* d_{p1}, d_{p12}, d_{p3}, d_{z1} *and* d_{z2} *, the following method is applied:*

$$G_2^{'}(s) = \frac{K_2}{1+2d_{p1}\frac{s}{w_{p1}}+\frac{s^2}{w_{p1}^2}} \frac{1+2d_{z1}\frac{s}{w_{z1}}+\frac{s^2}{w_{z1}^2}}{1+2d_{p2}\frac{s}{w_{p2}}+\frac{s^2}{w_{p2}^2}} \frac{1+2d_{z2}\frac{s}{w_{z2}}+\frac{s^2}{w_{z2}^2}}{1+2d_{p3}\frac{s}{w_{p3}}+\frac{s^2}{w_{p3}^2}} \tag{B.1}$$

Substituting $j0$ *(DC signal, the frequency is 0) for* s *in Eq.B.1 to calculate* K_2*,*

$$g_{dc} = 20 * log_{10}|G_2^{'}(j0)| = 20 * log_{10}K_2 \tag{B.2}$$

Placing K_2 *in Eq.B.2 to left and organizing the equation,*

$$K_2 = 10^{\frac{g_{dc}}{20}} = 10^{\frac{50}{20}} = 316 \tag{B.3}$$

Substituting jw_{p1} *for* s *in Eq.B.1,*

$$g_{p1} = 20 * log_{10}|G_2^{'}(jw_{p1})|$$
$$|G_2^{'}(jw_{p1})| = 10^{\frac{g_{p1}}{20}} \tag{B.4}$$

$$|G_2^{'}(jw_{p1})| = \tag{B.5}$$
$$\frac{K_2}{2d_{p1}} \frac{\sqrt{(1-(\frac{w_{p1}}{w_{z1}})^2)^2 + (2d_{z1}\frac{w_{p1}}{w_{z1}})^2}}{\sqrt{(1-(\frac{w_{p1}}{w_{p2}})^2)^2 + (2d_{p2}\frac{w_{p1}}{w_{p2}})^2}} \frac{\sqrt{(1-(\frac{w_{p1}}{w_{z2}})^2)^2 + (2d_{z2}\frac{w_{p1}}{w_{z2}})^2}}{\sqrt{(1-(\frac{w_{p1}}{w_{p3}})^2)^2 + (2d_{p3}\frac{w_{p1}}{w_{p3}})^2}}$$

From Eq.B.4 and Eq.B.5, the following equation is derived,

$$10^{\frac{g_{p1}}{20}} = \tag{B.6}$$
$$\frac{K_2}{2d_{p1}} \frac{\sqrt{(1-(\frac{w_{p1}}{w_{z1}})^2)^2 + (2d_{z1}\frac{w_{p1}}{w_{z1}})^2}}{\sqrt{(1-(\frac{w_{p1}}{w_{p2}})^2)^2 + (2d_{p2}\frac{w_{p1}}{w_{p2}})^2}} \frac{\sqrt{(1-(\frac{w_{p1}}{w_{z2}})^2)^2 + (2d_{z2}\frac{w_{p1}}{w_{z2}})^2}}{\sqrt{(1-(\frac{w_{p1}}{w_{p3}})^2)^2 + (2d_{p3}\frac{w_{p1}}{w_{p3}})^2}}$$

In Eq.B.6 moving $\frac{K_2}{2}$ *to left and squaring on both sides,*

$$(\frac{2}{K_2}10^{\frac{g_{p1}}{20}})^2 = \tag{B.7}$$
$$\frac{1}{d_{p1}^2} \frac{(1-(\frac{w_{p1}}{w_{z1}})^2)^2 + (2d_{p1}\frac{w_{p1}}{w_{p2}})^2}{(1-(\frac{w_{p1}}{w_{p2}})^2)^2 + (2d_{p2}\frac{w_{p1}}{w_{p2}})^2} \frac{(1-(\frac{w_{p1}}{w_{z2}})^2)^2 + (2d_{z2}\frac{w_{p1}}{w_{z2}})^2}{(1-(\frac{w_{p1}}{w_{p3}})^2)^2 + (2d_{p3}\frac{w_{p1}}{w_{p3}})^2}$$

In following, a_1 *is used to represent* $(\frac{w_{p1}}{w_{z1}})^2$*,* A_1 *represents* $(1-(\frac{w_{p1}}{w_{z1}})^2)^2$*,* b_1 *represents* $(\frac{w_{p1}}{w_{z2}})^2$*,* B_1 *represents* $(1-(\frac{w_{p1}}{w_{z2}})^2)^2$*,* c_1 *represents* $(\frac{w_{p1}}{w_{p2}})^2$*,* C_1 *represents* $(1-(\frac{w_{p1}}{w_{p2}})^2)^2$*,* d_1 *represents* $(\frac{w_{p1}}{w_{p3}})^2$*,* D_1 *represents* $(1-(\frac{w_{p1}}{w_{p3}})^2)^2$*,* k_1 *represents* $(\frac{2}{K_2}10^{\frac{g_{p1}}{20}})^2$*. Simplifying Eq.B.7 by using* a_1*,* A_1*,* b_1*,* B_1*,* c_1*,* C_1*,* d_1*,* D_1*, and* k_1*,*

$$k_1 = \frac{1}{d_{p1}^2} \frac{A_1 + 4d_{z1}^2 a_1}{C_1 + 4d_{p2}^2 c_1} \frac{B_1 + 4d_{z2}^2 b_1}{D_1 + 4d_{p3}^2 d_1} \tag{B.8}$$

Moving the denominator in Eq.B.8 to left,

$$k_1 d_{p1}^2 (C_1 + 4d_{p2}^2 c_1)(D_1 + 4d_{p3}^2 d_1) = (A_1 + 4d_{z1}^2 a_1)(B_1 + 4d_{z2}^2 b_1) \tag{B.9}$$

Developing Eq.B.9,

$$k_1 d_{p1}^2 (C_1 D_1 + 4c_1 D_1 d_{p2}^2 + 4C_1 d_1 d_{p3}^2 + 16 c_1 d_1 d_{p2}^2 d_{p3}^2) = \tag{B.10}$$
$$(A_1 B_1 + 4a_1 B_1 d_{z1}^2 + 4A_1 b_1 d_{z2}^2 + 16 a_1 b_1 d_{z1}^2 d_{z2}^2)$$

Ignoring terms in Eq.B.10 which have fourth power or higher power,because they have less effect.

$$4a_1B_1d_{z1}^2 + 4A_1b_1d_{z2}^2 - k_1C_1D_1d_{p1}^2 = -A_1B_1 \tag{B.11}$$

Similar procedures for w_{p2}, w_{p3}, w_{z1}, w_{z2} give

$$4a_2B_2d_{z1}^2 + 4A_2b_2d_{z2}^2 - k_2C_2D_2d_{p2}^2 = -A_2B_2 \tag{B.12}$$

$$4a_3B_3d_{z1}^2 + 4A_3b_3d_{z2}^2 - k_3C_3D_3d_{p3}^2 = -A_3B_3 \tag{B.13}$$

$$A_4d_{z1}^2 - 4k_4b_4C_4D_4d_{p1}^2 - 4k_4B_4c_4D_4d_{p2}^2 - 4k_4B_4C_4d_4d_{p3}^2 = k_4B_4C_4D_4 \tag{B.14}$$

$$A_5d_{z2}^2 - 4k_5b_5C_5D_5d_{p1}^2 - 4k_5B_5c_5D_5d_{p2}^2 - 4k_5B_5C_5d_5d_{p3}^2 = k_5B_5C_5D_5 \tag{B.15}$$

Forming Eqs.B.11 − B.15 in matrix,

$$\begin{pmatrix} 4a_1B_1 & 4A_1b_1 & -k_1C_1D_1 & 0 & 0 \\ 4a_2B_2 & 4A_2b_2 & 0 & -k_2C_2D_2 & 0 \\ 4a_3B_3 & 4A_3b_3 & 0 & 0 & -k_3C_3D_3 \\ A_4 & 0 & -4k_4b_4C_4D_4 & -4k_4B_4c_4D_4 & -4k_4B_4C_4d_4 \\ 0 & A_5 & -4k_5b_5C_5D_5 & -4k_5B_5c_5D_5 & -4k_5B_5C_5d_5 \end{pmatrix} \cdot \tag{B.16}$$

$$\begin{pmatrix} d_{z1}^2 \\ d_{z2}^2 \\ d_{p1}^2 \\ d_{p2}^2 \\ d_{p3}^2 \end{pmatrix} = \begin{pmatrix} -A_1B_1 \\ -A_2B_2 \\ -A_3B_3 \\ k_4B_4C_4D_4 \\ k_5B_5C_5D_5 \end{pmatrix}$$

Organizing Eq.B.16,

$$\begin{pmatrix} d_{z1}^2 \\ d_{z2}^2 \\ d_{p1}^2 \\ d_{p2}^2 \\ d_{p3}^2 \end{pmatrix} = \tag{B.17}$$

$$\begin{pmatrix} 4a_1B_1 & 4A_1b_1 & -k_1C_1D_1 & 0 & 0 \\ 4a_2B_2 & 4A_2b_2 & 0 & -k_2C_2D_2 & 0 \\ 4a_3B_3 & 4A_3b_3 & 0 & 0 & -k_3C_3D_3 \\ A_4 & 0 & -4k_4b_4C_4D_4 & -4k_4B_4c_4D_4 & -4k_4B_4C_4d_4 \\ 0 & A_5 & -4k_5b_5C_5D_5 & -4k_5B_5c_5D_5 & -4k_5B_5C_5d_5 \end{pmatrix}^{-1} \cdot$$

$$\begin{pmatrix} -A_1B_1 \\ -A_2B_2 \\ -A_3B_3 \\ k_4B_4C_4D_4 \\ k_5B_5C_5D_5 \end{pmatrix}$$

After substituting 10700 for w_{p1}, 21700 for w_{p2}, 26960 for w_{p3}, 19750 for w_{z1}, 28990 for w_{z2}, -33 for g_{p1}, -44 for g_{p2}, -45 for g_{p3}, -60 for g_{z1}, -60 for g_{z2}, the numerical value of the damping constants is

$$\begin{pmatrix} d_{z1}^2 \\ d_{z2}^2 \\ d_{p1}^2 \\ d_{p2}^2 \\ d_{p3}^2 \end{pmatrix} = \begin{pmatrix} 0.0035 \\ 0.0124 \\ 0.0047 \\ 0.0006656 \\ 0.0004326 \end{pmatrix}$$

Using the algorithm introduced above, these damping constants d_{p1}, d_{p12}, d_{p3}, d_{z1} and d_{z2} are calculated. "

Appendix C

Experimental HIL Simulation Results

In this appendix, the experimental results of the HIL contact dynamics simulation of all the carried out scenarios are presented. Firstly, in section C.1, the tables that summarize all the errors and fidelity of all the scenarios are presented. Afterwards, in section C.2, the HIL contact dynamics results graphs of all the scenarios are presented.

A summary of the properties of all the scenarios is presented in Tab. 8.3.

C.1 Error and Fidelity Results

The following tables present the errors of *"Simulated HIL"* and *"Real HIL"*, the difference between both of them and the fidelity.

Table C.1: Force results of HIL contact dynamics simulation of all scenarios demonstrating the errors of *"Simulated HIL"* (E_{md}) and *"Real HIL"* (E_{hd}), the differences between both of them and the fidelity.

Real HIL Test No.	Material		Mass (kg)		V_i (m/s)	COR	Force																	
							max. force [N]			Error (max. absolute)							Error (Integral absolute)							
	b1	b2	b1	b2			Docking model (d)	HIL model (m)	HIL test (h)	E_md		E_hd		Fidelity	E_hm		E_md		E_hd		Fidelity	E_hm	
							value	value	value	value [N]	%	value [N]	%	%	value [N]	%	%	%	%	%	%	%	
1	Alu	PEEK	35	35	0.05	0.8	642.70	1158.34	1258.07	515.64	80.23	615.37	95.75	83.79	99.73	8.61	59.43	184.66	32.18	78.55				
	Alu	PEEK	35	35	0.05	0.9	665.09	1145.96	1258.07	480.87	72.30	592.98	89.16	81.09	112.11	9.78	66.14	168.82	39.18	61.81				
2	Alu	PEEK	35	35	0.075	0.8	1045.46	1951.84	1887.04	906.38	86.70	841.58	80.50	107.70	-64.80	-3.32	67.31	203.00	33.16	81.09				
	Alu	PEEK	35	35	0.075	0.9	1081.91	1937.27	1887.04	855.36	79.06	805.13	74.42	106.24	-50.23	-2.59	74.21	186.14	39.87	64.24				
3	Alu	PEEK	35	70	0.05	0.8	763.78	1286.04	1437.60	522.26	68.38	673.82	88.22	77.51	151.55	11.78	50.48	167.39	30.16	77.68				
	Alu	PEEK	35	70	0.05	0.9	790.40	1298.53	1437.60	508.13	64.29	647.19	81.88	78.51	139.07	10.71	56.47	152.51	37.03	61.37				
4	Alu	PEEK	50	50	0.05	0.8	796.06	1320.50	1506.37	524.44	65.88	710.30	89.23	73.83	185.87	14.08	48.56	167.01	29.07	79.74				
	Alu	PEEK	50	50	0.05	0.9	823.81	1325.62	1506.37	501.80	60.91	682.55	82.85	73.52	180.75	13.64	54.36	152.15	35.73	63.35				
5	Alu	PEEK	50	100	0.05	0.8	946.03	1498.25	1603.03	552.22	58.37	656.99	69.45	84.05	104.77	6.99	41.35	142.89	28.94	71.83				
	Alu	PEEK	50	100	0.05	0.9	979.02	1525.68	1603.03	546.66	55.84	624.01	63.74	87.60	77.35	5.07	46.63	129.37	36.04	56.43				
6	PEEK	PEEK	35	35	0.05	0.8	499.46	795.56	879.12	296.10	59.28	379.66	76.01	77.99	83.56	10.50	41.62	134.03	31.05	65.25				
	PEEK	PEEK	35	35	0.05	0.9	516.88	810.69	879.12	293.81	56.84	362.24	70.08	81.11	68.43	8.44	47.05	121.01	38.88	50.29				
7	PEEK	PEEK	35	35	0.075	0.8	812.48	1336.67	1394.60	524.18	64.52	582.11	71.65	90.05	57.93	4.33	46.93	151.67	30.94	71.29				
	PEEK	PEEK	35	35	0.075	0.9	840.81	1340.13	1394.60	499.32	59.39	553.79	65.86	90.16	54.47	4.06	52.72	137.66	38.30	55.62				
8	PEEK	PEEK	35	70	0.05	0.8	593.57	902.47	1047.26	308.90	52.04	453.69	76.43	68.09	144.79	16.04	35.54	124.91	28.45	65.94				
	PEEK	PEEK	35	70	0.05	0.9	614.26	916.42	1047.26	302.16	49.19	433.00	70.49	69.78	130.83	14.28	40.41	112.40	35.95	51.27				
9	PEEK	PEEK	50	50	0.05	0.8	618.65	934.54	1087.52	315.89	51.06	468.87	75.79	67.37	152.98	16.37	34.25	123.04	27.84	66.14				
	PEEK	PEEK	50	50	0.05	0.9	640.22	944.59	1087.52	304.37	47.54	447.30	69.87	68.05	142.93	15.13	38.96	110.63	35.22	51.57				
10	PEEK	PEEK	50	100	0.05	0.8	735.21	1058.26	1270.28	323.05	43.94	535.07	72.78	60.37	212.02	20.04	29.34	113.57	25.83	65.13				
	PEEK	PEEK	50	100	0.05	0.9	760.84	1068.16	1270.28	307.31	40.39	509.44	66.96	60.32	202.13	18.92	33.54	101.69	32.99	51.03				
11	Alu	PTFE	35	35	0.05	0.8	267.58	348.65	575.13	81.08	30.30	307.56	114.94	26.36	226.48	64.96	18.58	80.90	22.97	52.56				
	Alu	PTFE	35	35	0.05	0.9	276.90	353.94	575.13	77.03	27.82	298.23	107.70	25.83	221.20	62.50	21.52	70.83	30.38	40.58				
12	PEEK	PTFE	35	35	0.05	0.8	257.73	334.18	495.47	76.45	29.66	237.74	92.24	32.16	161.29	48.26	17.74	66.45	26.69	41.37				
	PEEK	PTFE	35	35	0.05	0.9	266.72	338.94	495.47	72.22	27.08	228.75	85.77	31.57	156.53	46.18	20.56	57.19	35.96	30.38				

Table C.2: Penetration-depth results of HIL contact dynamics simulation of all scenarios demonstrating the errors of *"Simulated HIL"* (E_{md}) and *"Real HIL"* (E_{hd}), the differences between both of them and the fidelity.

Penetration Depth																										
Real HIL Test No.	Material		Mass (kg)		V_i (m/s)	COR	max. penetration [µm]			Error (max. absolute)									Error (Integral absolute)							
							d	m	h	E_md		E_hd		Fidelity		E_hm		E_md		E_hd		Fidelity		E_hm	
	b1	b2	b1	b2			value	value	value	value [µm]	%	value [µm]	%	%		value [µm]	%	%		%		%		%	
1	Alu	PEEK	35	35	0.05	0.8	70.99	101.20	139.29	30.21	42.56	68.30	96.22	44.23		38.09	37.64	34.15		165.36		20.65		97.80	
	Alu	PEEK	35	35	0.05	0.9	74.48	106.20	139.29	31.72	42.59	64.81	87.03	48.94		33.09	31.16	39.97		156.79		25.49		83.46	
2	Alu	PEEK	35	35	0.075	0.8	98.18	144.45	176.24	46.27	47.13	78.06	79.50	59.28		31.79	22.00	38.86		177.55		21.89		99.88	
	Alu	PEEK	35	35	0.075	0.9	103.01	150.45	176.24	47.44	46.06	73.23	71.09	64.79		25.79	17.14	44.94		168.59		26.66		85.31	
3	Alu	PEEK	35	70	0.05	0.8	79.64	109.89	143.81	30.25	37.98	64.17	80.57	47.15		33.91	30.86	28.81		156.75		18.38		99.32	
	Alu	PEEK	35	70	0.05	0.9	83.56	115.39	143.81	31.84	38.10	60.25	72.11	52.84		28.41	24.62	34.08		148.45		22.96		85.30	
4	Alu	PEEK	50	50	0.05	0.8	81.87	112.39	143.24	30.52	37.28	61.37	74.96	49.74		30.85	27.45	27.68		146.32		18.92		92.91	
	Alu	PEEK	50	50	0.05	0.9	85.90	118.24	143.24	32.34	37.65	57.35	66.76	56.40		25.01	21.15	32.78		138.36		23.69		79.51	
5	Alu	PEEK	50	100	0.05	0.8	91.86	123.24	151.12	31.38	34.16	59.26	64.52	52.96		27.88	22.62	23.46		130.74		17.95		86.89	
	Alu	PEEK	50	100	0.05	0.9	96.37	128.71	151.12	32.34	33.55	54.75	56.81	59.07		22.41	17.41	28.06		123.29		22.76		74.36	
6	PEEK	PEEK	35	35	0.05	0.8	91.34	122.24	183.64	30.90	33.82	92.30	101.04	33.47		61.40	50.23	23.59		154.19		15.30		105.67	
	PEEK	PEEK	35	35	0.05	0.9	95.83	128.24	183.64	32.41	33.81	87.81	91.62	36.91		55.40	43.20	28.32		145.98		19.40		91.70	
7	PEEK	PEEK	35	35	0.075	0.8	126.34	170.94	211.12	44.60	35.30	84.78	67.11	52.61		40.18	23.51	26.71		129.88		20.56		81.43	
	PEEK	PEEK	35	35	0.075	0.9	132.55	180.16	211.12	47.61	35.92	78.57	59.28	60.60		30.96	17.18	31.76		122.46		25.94		68.83	
8	PEEK	PEEK	35	70	0.05	0.8	102.48	132.71	176.41	30.23	29.49	73.92	72.13	40.89		43.70	32.93	19.99		111.87		17.87		76.57	
	PEEK	PEEK	35	70	0.05	0.9	107.52	139.50	176.41	31.99	29.75	68.89	64.07	46.43		36.90	26.45	24.23		105.02		23.07		65.04	
9	PEEK	PEEK	50	50	0.05	0.8	105.35	135.71	176.58	30.36	28.82	71.23	67.61	42.62		40.87	30.12	19.24		103.80		18.53		70.92	
	PEEK	PEEK	50	50	0.05	0.9	110.53	141.50	176.58	30.98	28.03	66.05	59.76	46.90		35.07	24.79	23.33		97.22		24.00		59.91	
10	PEEK	PEEK	50	100	0.05	0.8	118.20	148.48	190.30	30.29	25.62	72.10	61.00	42.01		41.81	28.16	16.35		92.99		17.58		65.88	
	PEEK	PEEK	50	100	0.05	0.9	124.01	154.98	190.30	30.97	24.97	66.29	53.46	46.72		35.32	22.79	19.99		86.76		23.04		55.64	
11	Alu	PTFE	35	35	0.05	0.8	170.50	200.42	197.70	29.92	17.55	27.20	15.95	110.00		-2.72	-1.36	10.09		1.42		713.25		-7.88	
	Alu	PTFE	35	35	0.05	0.9	178.88	211.42	197.70	32.54	18.19	18.82	10.52	172.92		-13.72	-6.49	12.60		-1.86		-677.53		-12.85	
12	PEEK	PTFE	35	35	0.05	0.8	177.01	207.42	230.18	30.41	17.18	53.16	30.03	57.19		22.76	10.97	9.60		8.28		115.97		-1.21	
	PEEK	PTFE	35	35	0.05	0.9	185.72	217.42	230.18	31.70	17.07	44.46	23.94	71.31		12.76	5.87	12.03		4.78		251.50		-6.47	

Table C.3: Velocity-after-impact results of HIL contact dynamics simulation of all scenarios demonstrating the errors of *"Simulated HIL"* (E_{md}) and *"Real HIL"* (E_{hd}), the differences between both of them and the fidelity.

Real HIL Test No.	Material		Mass (kg)		V_i (m/s)	COR	Final Velocity												COR		
							Velocity after-impact			Error (absolute)											
							d	m	h	E_md		E_hd		Fidelity	E_hm		d	m	h
	b1	b2	b1	b2			value [m/s]	value [m/s]	value [m/s]	value [m/s]	%	value [m/s]	%	%	value [m/s]	%			
1	Alu	PEEK	35	35	0.05	0.8	-0.039	-0.093	-0.050	-0.053	134.81	-0.011	27.76	485.70	0.042	-45.59	0.79	1.85	1.31
	Alu	PEEK	35	35	0.05	0.9	-0.045	-0.107	-0.050	-0.063	140.29	-0.006	12.70	1105.06	0.057	-53.10	0.89	2.15	1.31
2	Alu	PEEK	35	35	0.075	0.8	-0.059	-0.149	-0.009	-0.090	152.10	0.050	-85.07	-178.80	0.140	-94.08	0.79	1.99	0.29
	Alu	PEEK	35	35	0.075	0.9	-0.067	-0.172	-0.009	-0.105	157.26	0.058	-86.83	-181.12	0.164	-94.88	0.89	2.30	0.29
3	Alu	PEEK	35	70	0.05	0.8	-0.039	-0.085	-0.053	-0.045	114.49	-0.013	33.18	345.06	0.032	-37.91	0.79	1.69	1.35
	Alu	PEEK	35	70	0.05	0.9	-0.045	-0.098	-0.053	-0.054	119.94	-0.008	17.48	686.17	0.046	-46.59	0.89	1.97	1.35
4	Alu	PEEK	50	50	0.05	0.8	-0.039	-0.083	-0.059	-0.043	110.07	-0.019	49.12	224.09	0.024	-29.01	0.79	1.66	1.40
	Alu	PEEK	50	50	0.05	0.9	-0.045	-0.096	-0.059	-0.052	115.49	-0.014	31.54	366.14	0.038	-38.96	0.89	1.93	1.40
5	Alu	PEEK	50	100	0.05	0.8	-0.039	-0.076	-0.058	-0.037	93.86	-0.018	46.92	200.05	0.019	-24.21	0.79	1.53	1.38
	Alu	PEEK	50	100	0.05	0.9	-0.045	-0.089	-0.058	-0.044	99.17	-0.013	29.60	335.05	0.031	-34.93	0.89	1.78	1.38
6	PEEK	PEEK	35	35	0.05	0.8	-0.039	-0.077	-0.086	-0.037	94.55	-0.047	118.49	79.80	-0.009	12.31	0.79	1.53	1.84
	PEEK	PEEK	35	35	0.05	0.9	-0.045	-0.089	-0.086	-0.045	99.99	-0.041	92.74	107.83	0.003	-3.63	0.89	1.79	1.84
7	PEEK	PEEK	35	35	0.075	0.8	-0.059	-0.122	-0.002	-0.063	105.92	0.058	-97.39	-108.76	0.120	-98.73	0.79	1.62	0.06
	PEEK	PEEK	35	35	0.075	0.9	-0.067	-0.142	-0.002	-0.075	111.41	0.065	-97.70	-114.04	0.140	-98.91	0.89	1.89	0.06
8	PEEK	PEEK	35	70	0.05	0.8	-0.039	-0.071	-0.011	-0.032	80.73	0.029	-72.57	-111.25	0.060	-84.82	0.79	1.43	0.48
	PEEK	PEEK	35	70	0.05	0.9	-0.045	-0.083	-0.011	-0.038	85.86	0.034	-75.80	-113.27	0.072	-86.98	0.89	1.66	0.48
9	PEEK	PEEK	50	50	0.05	0.8	-0.039	-0.070	-0.012	-0.031	77.81	0.027	-69.02	-112.73	0.058	-82.58	0.79	1.40	0.56
	PEEK	PEEK	50	50	0.05	0.9	-0.045	-0.082	-0.012	-0.037	82.83	0.032	-72.67	-113.98	0.070	-85.05	0.89	1.63	0.56
10	PEEK	PEEK	50	100	0.05	0.8	-0.039	-0.066	-0.012	-0.026	66.57	0.028	-70.08	-94.98	0.054	-82.04	0.79	1.31	0.53
	PEEK	PEEK	50	100	0.05	0.9	-0.045	-0.077	-0.012	-0.032	71.24	0.033	-73.61	-96.79	0.065	-84.59	0.89	1.53	0.53
11	Alu	PTFE	35	35	0.05	0.8	-0.039	-0.056	-0.001	-0.016	41.40	0.039	-98.42	-42.07	0.055	-98.88	0.79	1.11	0.04
	Alu	PTFE	35	35	0.05	0.9	-0.045	-0.065	-0.001	-0.020	45.24	0.044	-98.60	-45.88	0.064	-99.04	0.89	1.30	0.04
12	PEEK	PTFE	35	35	0.05	0.8	-0.039	-0.055	-0.060	-0.016	39.50	-0.020	51.25	77.07	-0.005	8.42	0.79	1.10	1.49
	PEEK	PTFE	35	35	0.05	0.9	-0.045	-0.064	-0.060	-0.019	43.03	-0.015	33.42	128.75	0.004	-6.72	0.89	1.28	1.49

Table C.4: Contact duration results of HIL contact dynamics simulation of all scenarios demonstrating the errors of *"Simulated HIL"* (E_{md}) and *"Real HIL"* (E_{hd}), the differences between both of them and the fidelity.

Real HIL Test No.	Material		Mass (kg)		V_i (m/s)	COR	Contact duration (seconds)									
							time (s)						Error			
	b1	b2	b1	b2			d	m	hil (Force)	hil (pen. Depth)	E_md	E_hd	E_hm
							sec.	sec.	sec.	sec.	sec.	sec.	sec.
1	Alu	PEEK	35	35	0.05	0.8	4.71	4.49	6.33	6.29	-0.21	1.58	1.79
	Alu	PEEK	35	35	0.05	0.9	4.63	4.60	6.33	6.29	-0.03	1.66	1.69
2	Alu	PEEK	35	35	0.075	0.8	4.35	4.20	7.65	7.66	-0.15	3.31	3.46
	Alu	PEEK	35	35	0.075	0.9	4.27	4.32	7.65	7.66	0.05	3.39	3.34
3	Alu	PEEK	35	70	0.05	0.8	5.28	5.03	7.02	7.03	-0.25	1.75	2.01
	Alu	PEEK	35	70	0.05	0.9	5.20	5.12	7.02	7.03	-0.08	1.83	1.91
4	Alu	PEEK	50	50	0.05	0.8	5.44	5.17	7.11	7.01	-0.27	1.57	1.83
	Alu	PEEK	50	50	0.05	0.9	5.35	5.24	7.11	7.01	-0.11	1.66	1.77
5	Alu	PEEK	50	100	0.05	0.8	6.09	5.77	7.91	7.82	-0.32	1.73	2.05
	Alu	PEEK	50	100	0.05	0.9	6.00	5.85	7.91	7.82	-0.15	1.82	1.97
6	PEEK	PEEK	35	35	0.05	0.8	6.07	5.76	7.42	7.42	-0.31	1.35	1.66
	PEEK	PEEK	35	35	0.05	0.9	5.96	5.83	7.42	7.42	-0.13	1.46	1.59
7	PEEK	PEEK	35	35	0.075	0.8	5.59	5.31	8.45	9.62	-0.28	4.03	4.31
	PEEK	PEEK	35	35	0.075	0.9	5.49	5.41	8.45	9.62	-0.08	4.12	4.20
8	PEEK	PEEK	35	70	0.05	0.8	6.80	6.41	8.86	8.88	-0.39	2.08	2.47
	PEEK	PEEK	35	70	0.05	0.9	6.69	6.52	8.86	8.88	-0.17	2.19	2.36
9	PEEK	PEEK	50	50	0.05	0.8	7.00	6.61	9.16	8.95	-0.39	1.95	2.34
	PEEK	PEEK	50	50	0.05	0.9	6.88	6.68	9.16	8.95	-0.20	2.07	2.27
10	PEEK	PEEK	50	100	0.05	0.8	7.85	7.43	10.02	9.76	-0.43	1.91	2.34
	PEEK	PEEK	50	100	0.05	0.9	7.72	7.48	10.02	9.76	-0.24	2.04	2.28
11	Alu	PTFE	35	35	0.05	0.8	11.32	10.81	8.69	9.50	-0.51	-1.82	-1.31
	Alu	PTFE	35	35	0.05	0.9	11.13	10.77	8.69	9.50	-0.36	-1.63	-1.27
12	PEEK	PTFE	35	35	0.05	0.8	11.76	11.21	9.33	9.62	-0.55	-2.14	-1.59
	PEEK	PTFE	35	35	0.05	0.9	11.56	11.21	9.33	9.62	-0.35	-1.94	-1.59

C.2 HIL Contact-Dyanmics Results

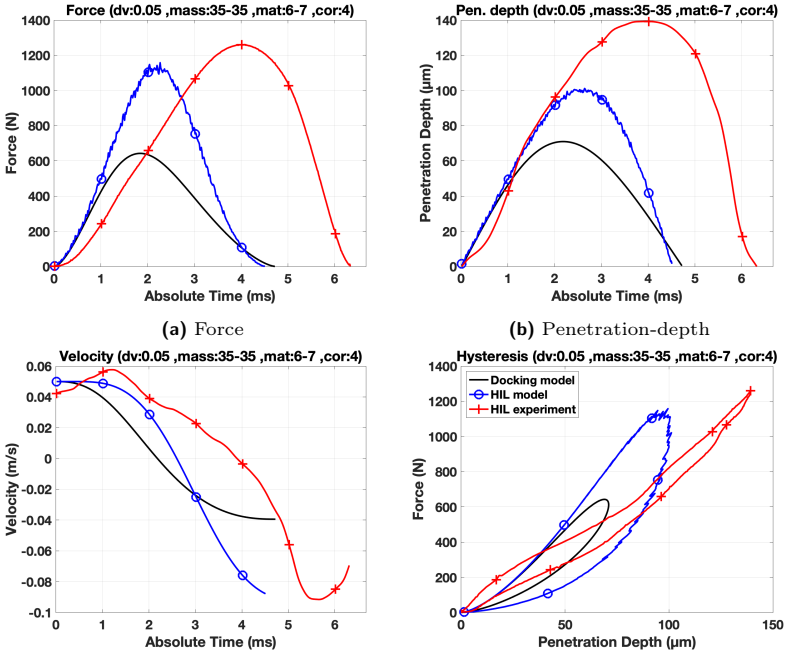

(a) Force **(b)** Penetration-depth

(c) Velocity **(d)** Hysteresis

Figure C.1: Results of Scenario 1 (COR = 0.8): Alu-PEEK, Mass=35-35 kg, V_i=0.05 [m/s]

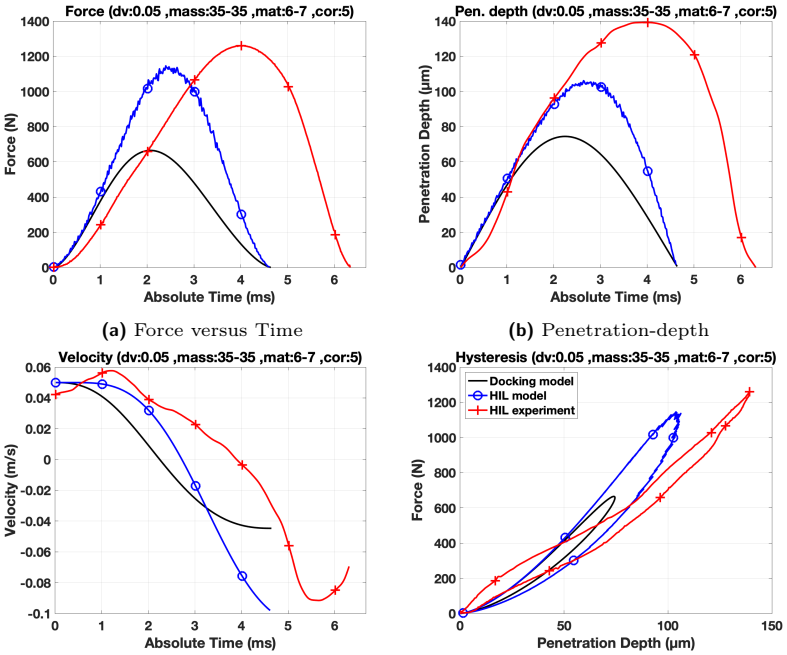

(a) Force versus Time

(b) Penetration-depth

(c) Velocity

(d) Hysteresis

Figure C.2: Results of Scenario 1 (COR = 0.9): Alu-PEEK, Mass=35-35 kg, V_i=0.05 [m/s]

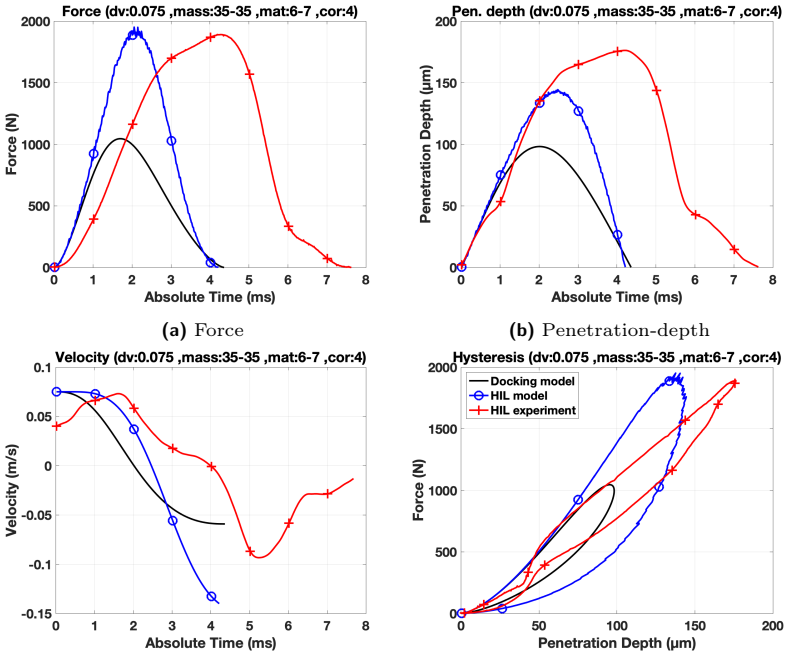

(a) Force **(b)** Penetration-depth

(c) Velocity **(d)** Hysteresis

Figure C.3: Results of Scenario 2 (COR = 0.8): Alu-PEEK, Mass=35-35 kg, V_i=0.075 [m/s]

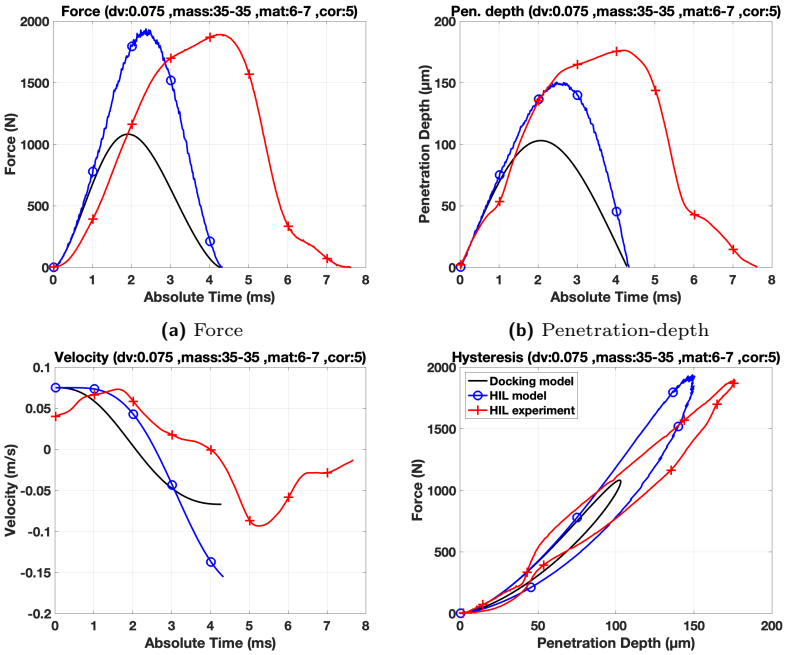

(a) Force **(b)** Penetration-depth

(c) Velocity **(d)** Hysteresis

Figure C.4: Results of Scenario 2 (COR=0.9): Alu-PEEK, Mass=35-35 kg, V_i=0.075 [m/s]

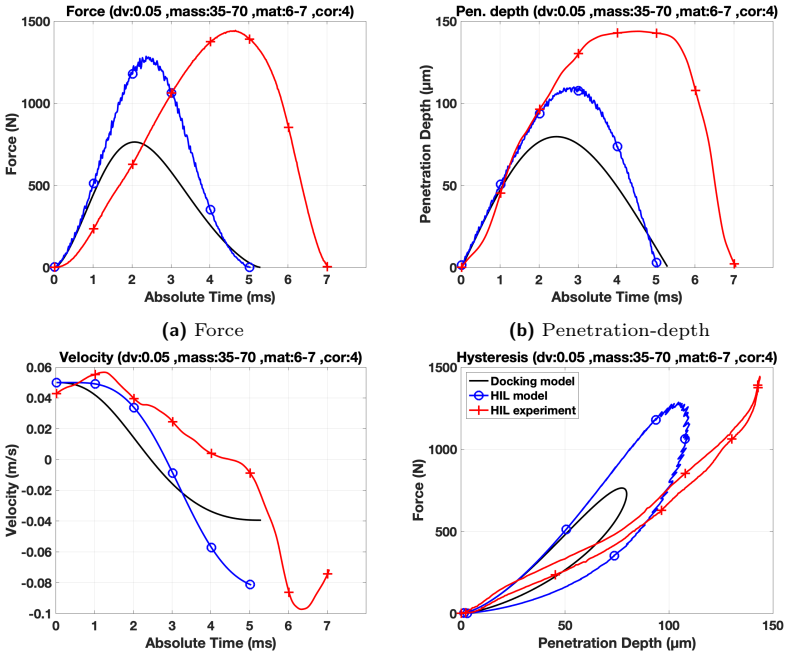

(a) Force **(b)** Penetration-depth

(c) Velocity **(d)** Hysteresis

Figure C.5: Results of Scenario 3 (COR=0.8): Alu-PEEK, Mass=35-70 kg, V_i=0.05 [m/s]

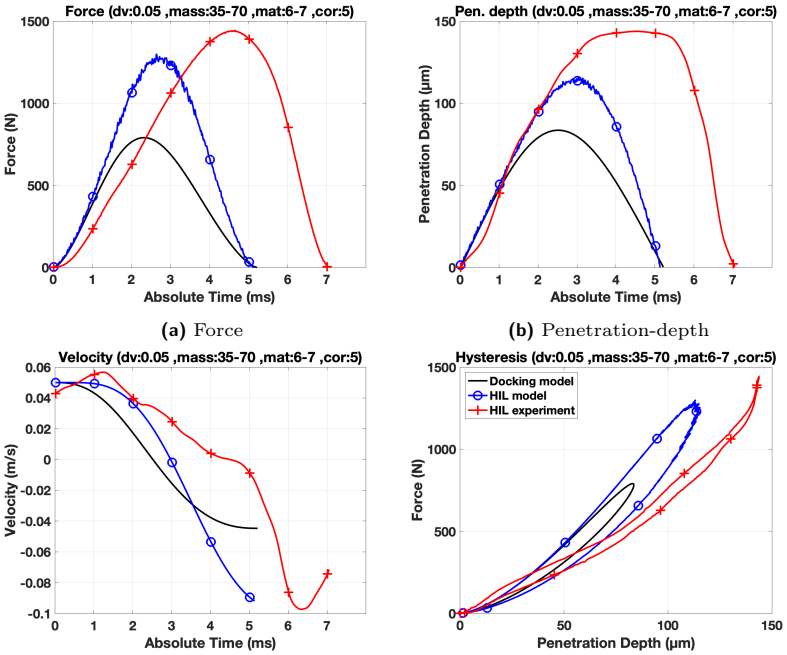

(a) Force **(b)** Penetration-depth

(c) Velocity **(d)** Hysteresis

Figure C.6: Results of Scenario 3 (COR=0.9): Alu-PEEK, Mass=35-70 [kg], V_i=0.05 [m/s]

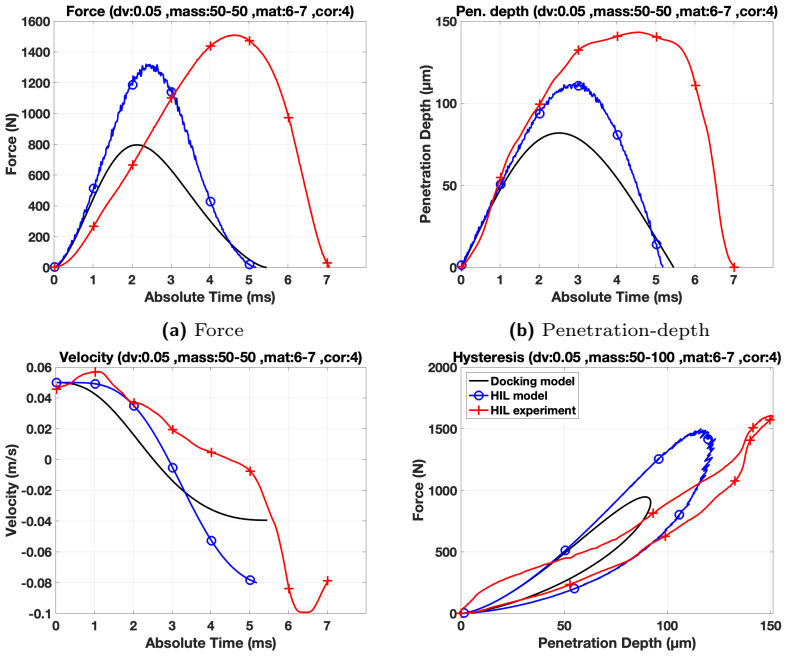

(a) Force **(b)** Penetration-depth

(c) Velocity **(d)** Hysteresis

Figure C.7: Results of Scenario 4 (COR= 0.8): Alu-PEEK, Mass=50-50 kg, V_i=0.05 [m/s]

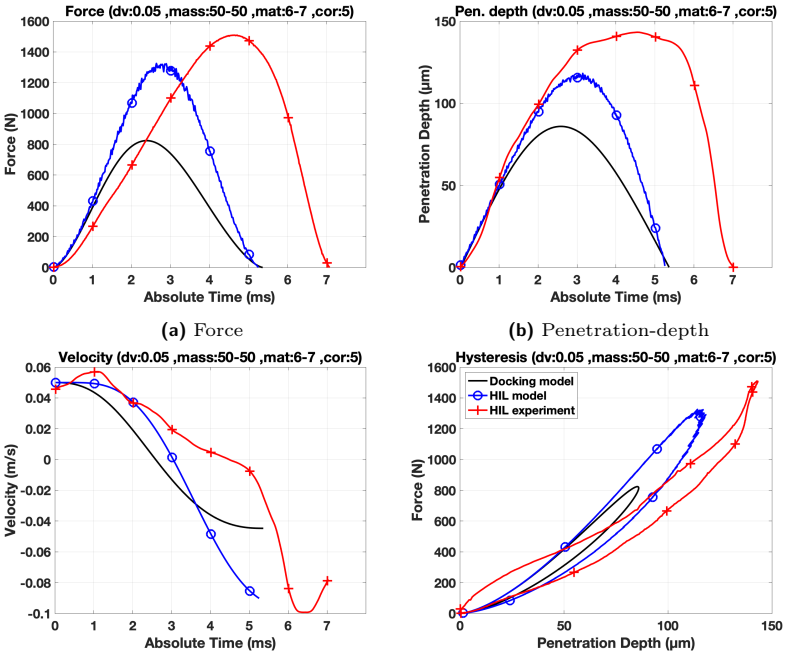

(a) Force **(b)** Penetration-depth

(c) Velocity **(d)** Hysteresis

Figure C.8: Results of Scenario 4 (COR= 0.9): Alu-PEEK, Mass=50-50 kg, V_i=0.05 [m/s]

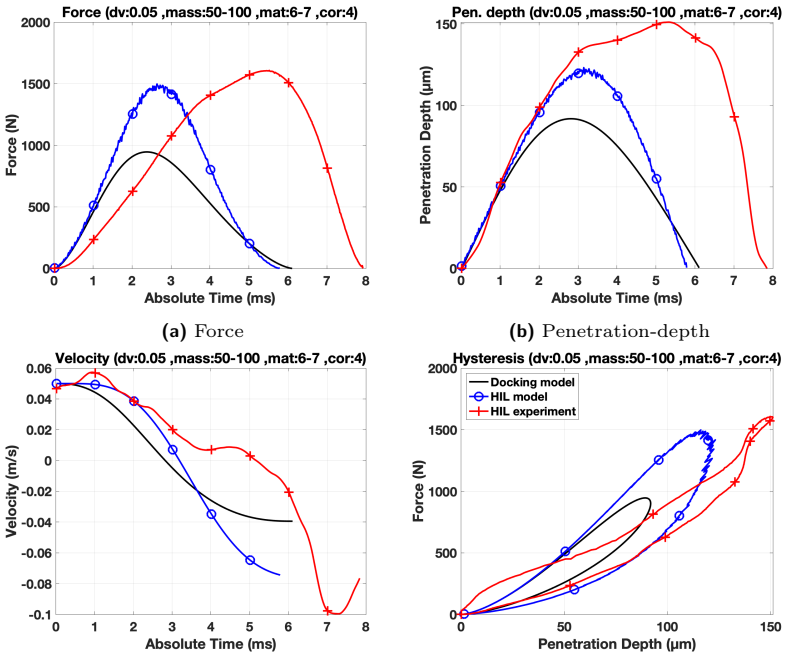

(a) Force **(b)** Penetration-depth

(c) Velocity **(d)** Hysteresis

Figure C.9: Results of Scenario 5 (COR=0.8): Alu-PEEK, Mass=50-100 kg, V_i=0.05 [m/s]

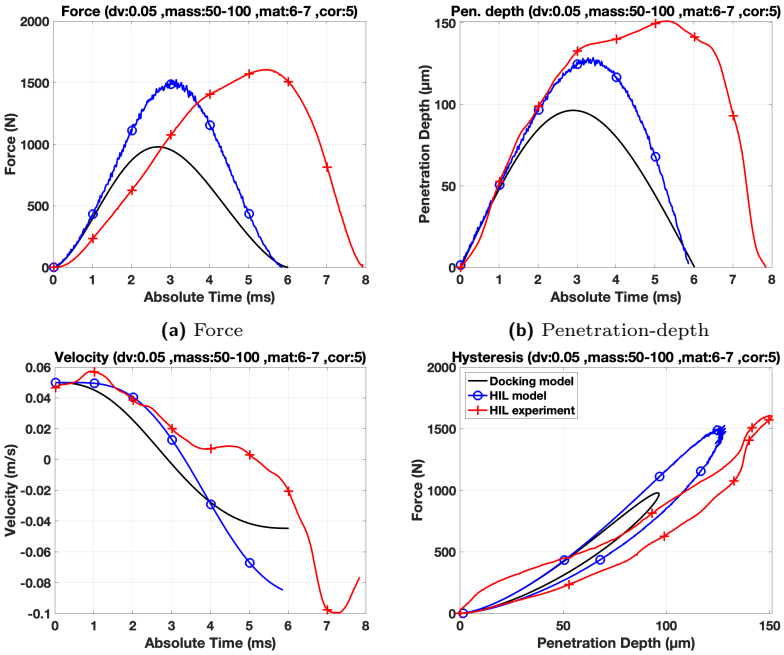

(a) Force **(b)** Penetration-depth

(c) Velocity **(d)** Hysteresis

Figure C.10: Results of Scenario 5 (COR=0.9): Alu-PEEK, Mass=50-100 [kg], V_i=0.05 [m/s]

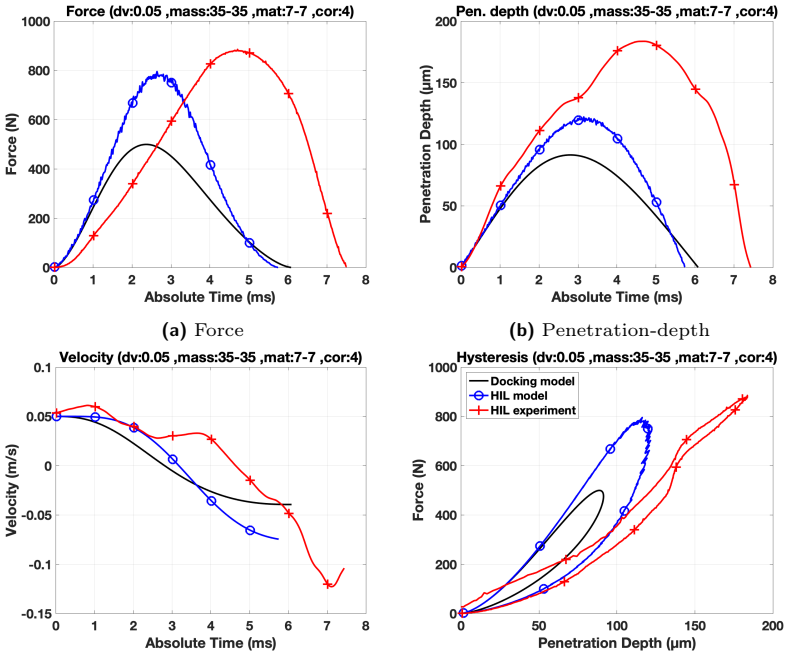

(a) Force **(b)** Penetration-depth

(c) Velocity **(d)** Hysteresis

Figure C.11: Results of Scenario 6 (COR=0.8): PEEK-PEEK, Mass=35-35 kg, V_i=0.05 [m/s]

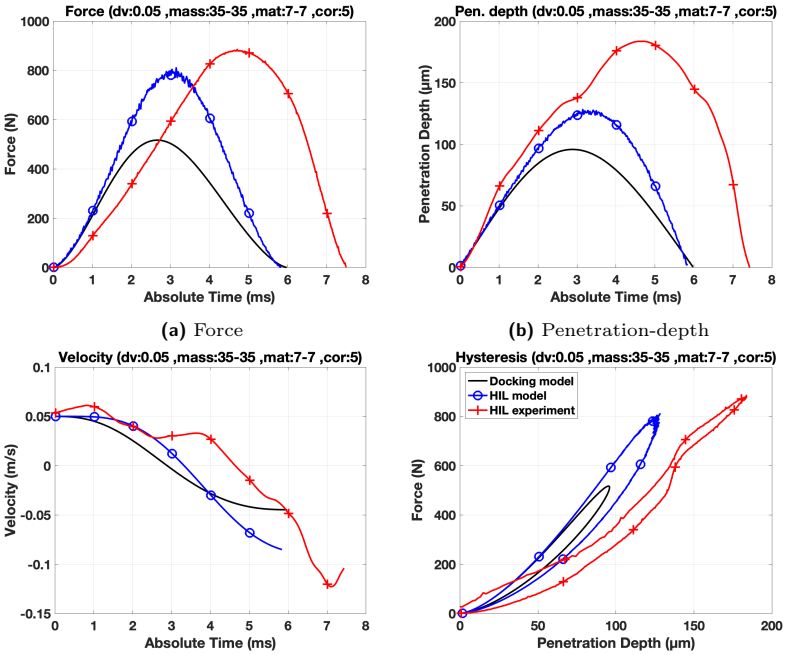

(a) Force **(b)** Penetration-depth

(c) Velocity **(d)** Hysteresis

Figure C.12: Results of Scenario 6 (COR=0.9): PEEK-PEEK, Mass=35-35 [kg], V_i=0.05 [m/s]

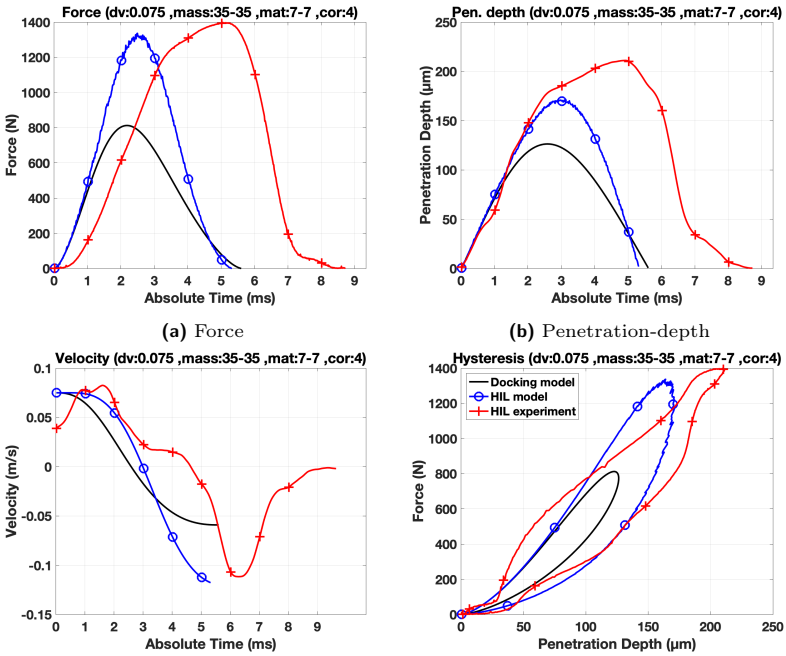

(a) Force **(b)** Penetration-depth

(c) Velocity **(d)** Hysteresis

Figure C.13: Results of Scenario 7 (COR = 0.8): PEEK-PEEK, Mass=35-35 kg, V_i=0.075 [m/s]

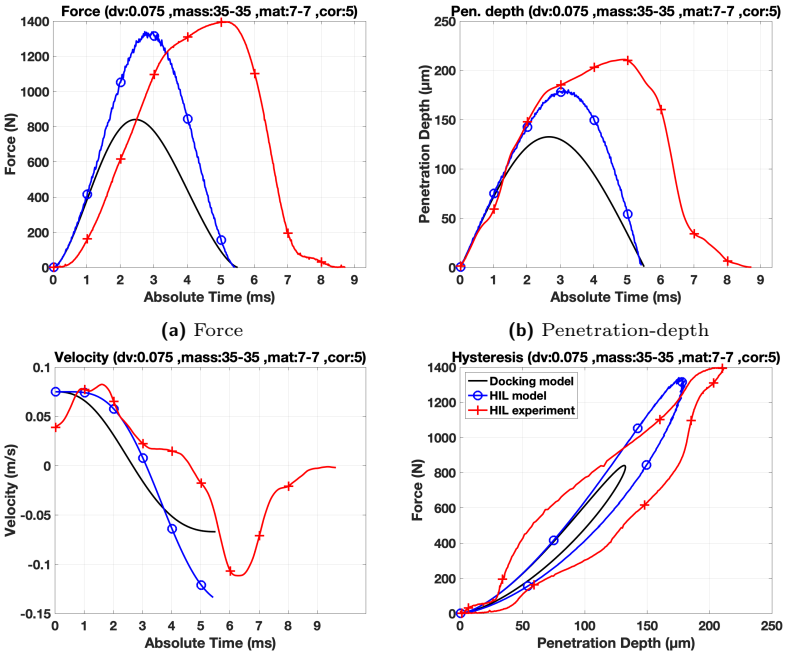

(a) Force **(b)** Penetration-depth

(c) Velocity **(d)** Hysteresis

Figure C.14: Results of Scenario 7 (COR=0.9): PEEK-PEEK, Mass=35-35 kg, V_i=0.075 [m/s]

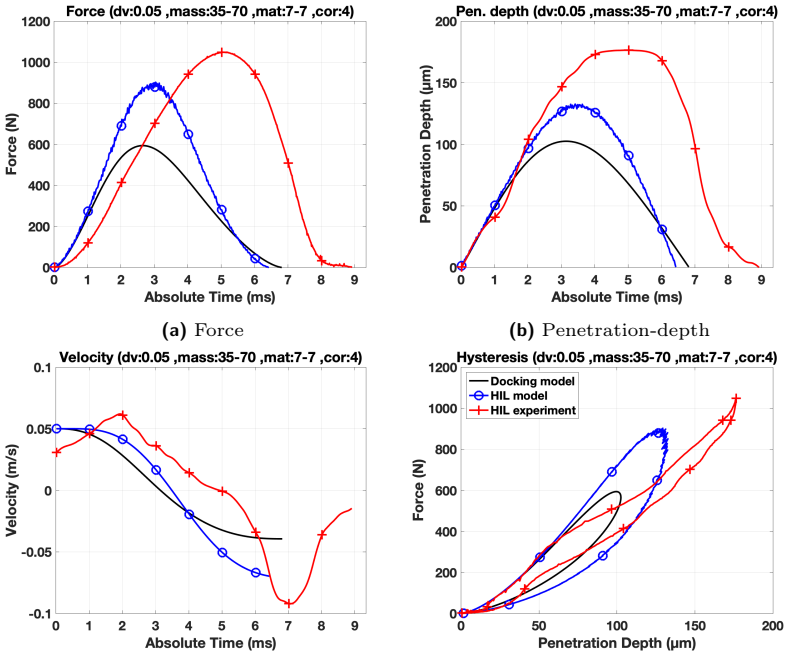

(a) Force **(b)** Penetration-depth

(c) Velocity **(d)** Hysteresis

Figure C.15: Results of Scenario 8 (COR=0.8): PEEK-PEEK, Mass=35-70 kg, V_i=0.05 [m/s]

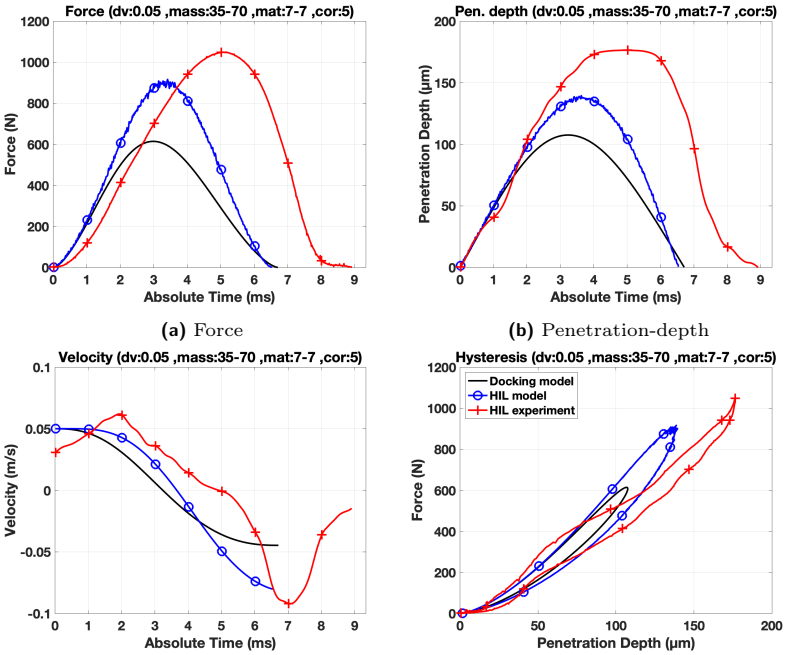

(a) Force **(b)** Penetration-depth

(c) Velocity **(d)** Hysteresis

Figure C.16: Results of Scenario 8 (COR=0.9): PEEK-PEEK, Mass=35-70 [kg], V_i=0.05 [m/s]

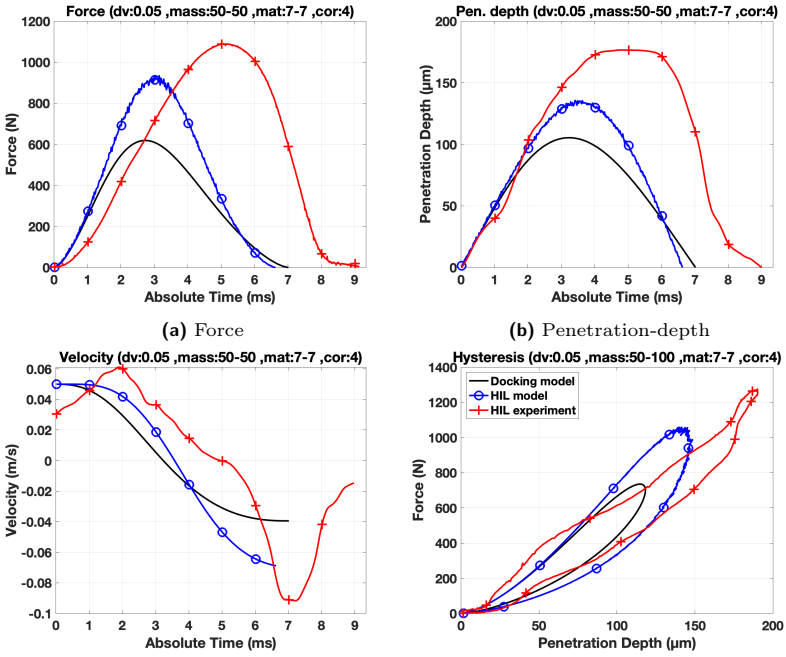

(a) Force **(b)** Penetration-depth

(c) Velocity **(d)** Hysteresis

Figure C.17: Results of Scenario 9 (COR= 0.8): PEEK-PEEK, Mass=50-50 kg, V_i=0.05 [m/s]

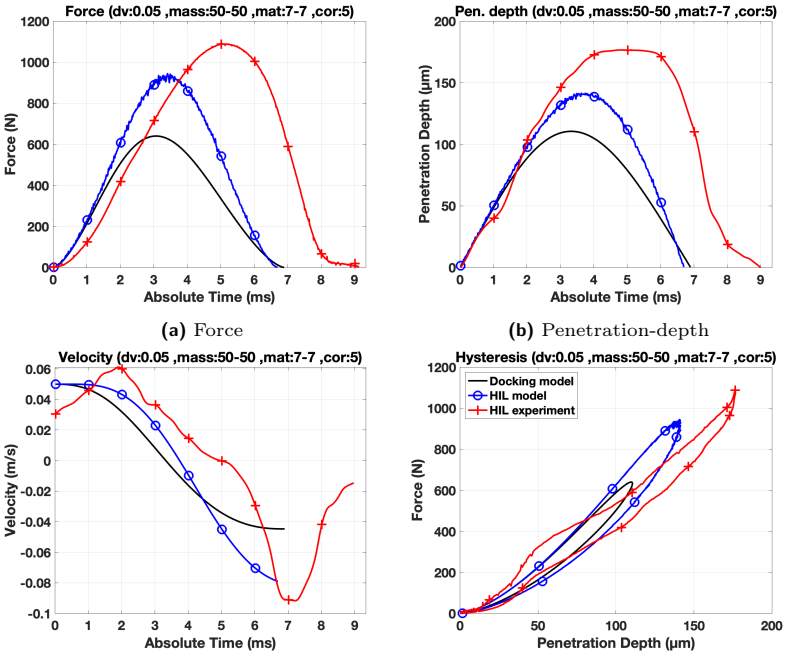

(a) Force **(b)** Penetration-depth

(c) Velocity **(d)** Hysteresis

Figure C.18: Results of Scenario 9 (COR= 0.9): PEEK-PEEK, Mass=50-50 kg, V_i=0.05 [m/s]

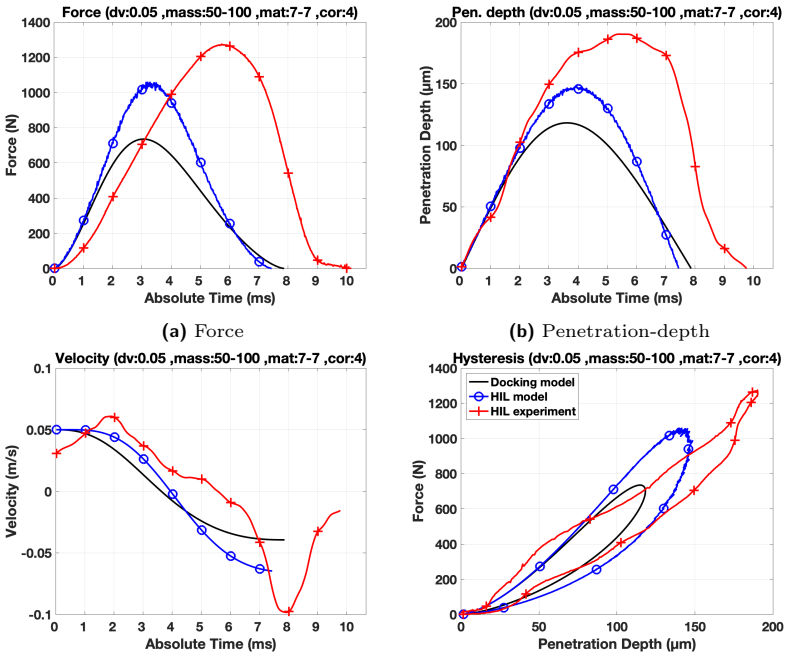

(a) Force **(b)** Penetration-depth

(c) Velocity **(d)** Hysteresis

Figure C.19: Results of Scenario 10 (COR=0.8): PEEK-PEEK, Mass=50-100 kg, V_i=0.05 [m/s]

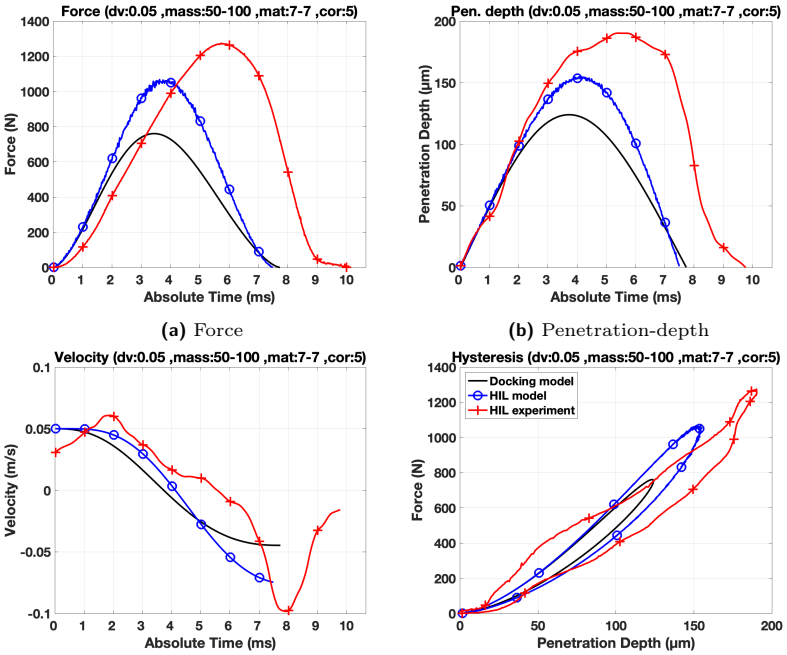

(a) Force **(b)** Penetration-depth

(c) Velocity **(d)** Hysteresis

Figure C.20: Results of Scenario 10 (COR=0.9): PEEK-PEEK, Mass=50-100 [kg], V_i=0.05 [m/s]

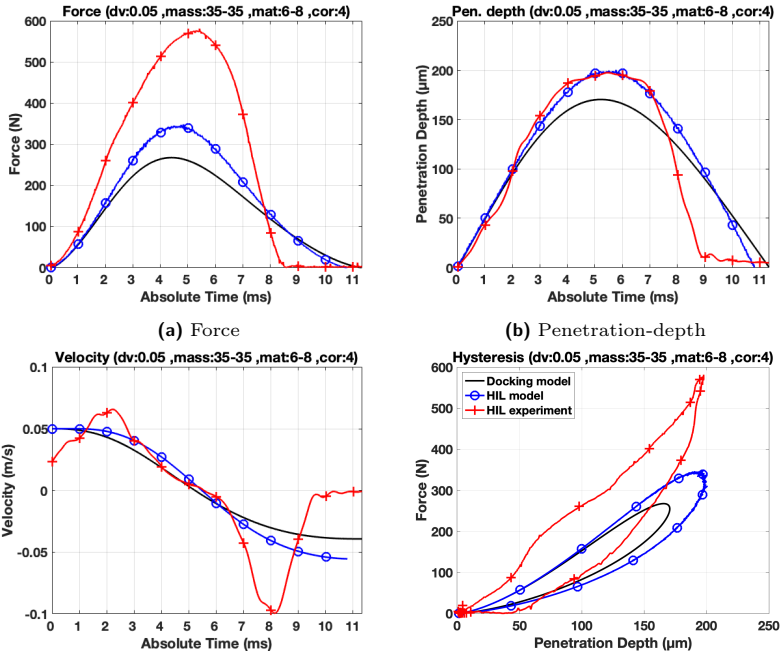

(a) Force **(b)** Penetration-depth

(c) Velocity **(d)** Hysteresis

Figure C.21: Results of Scenario 11 (COR=0.8): Alu-PTFE, Mass=35-35 kg, V_i=0.05 [m/s]

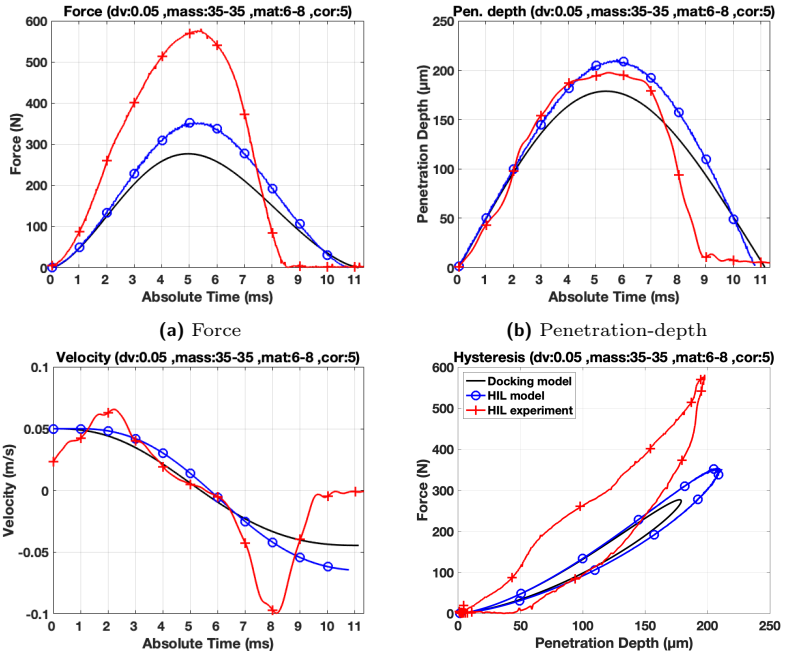

(a) Force **(b)** Penetration-depth

(c) Velocity **(d)** Hysteresis

Figure C.22: Results of Scenario 11 (COR=0.9): Alu-PTFE, Mass=35-35 [kg], V_i=0.05 [m/s]

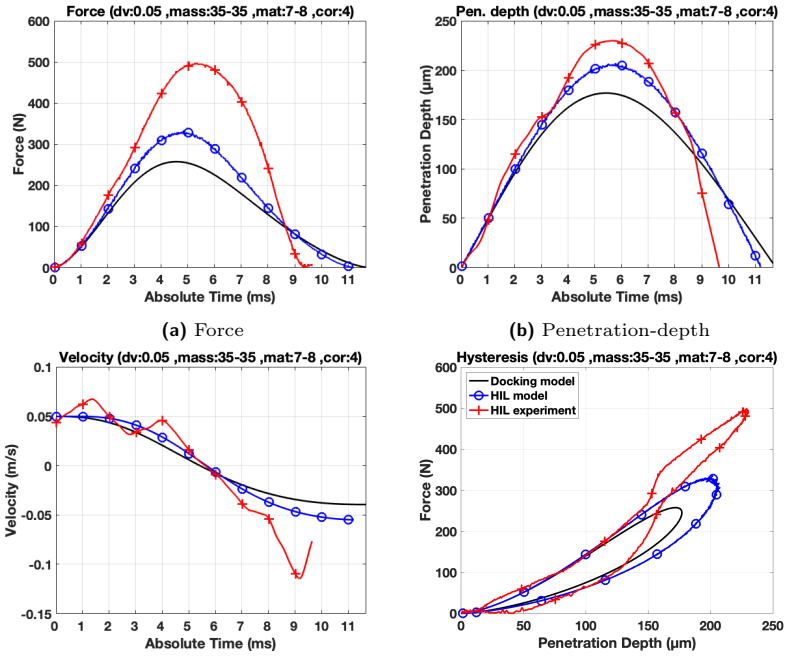

(a) Force **(b)** Penetration-depth

(c) Velocity **(d)** Hysteresis

Figure C.23: Results of Scenario 12 (COR=0.8): PEEK-PTFE, Mass=35-35 kg, V_i=0.05 [m/s]

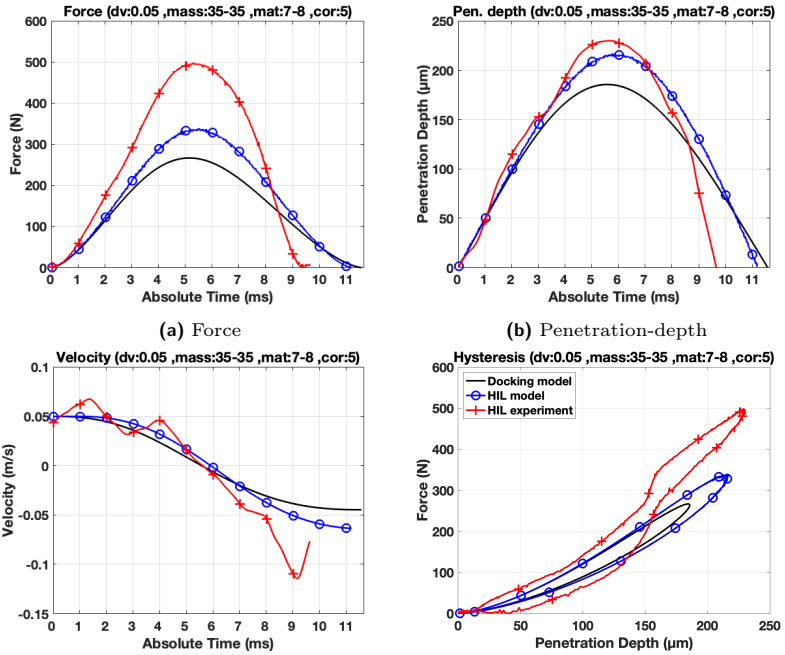

(a) Force **(b)** Penetration-depth

(c) Velocity **(d)** Hysteresis

Figure C.24: Results of Scenario 12 (COR=0.9): PEEK-PTFE, Mass=35-35 [kg], V_i=0.05 [m/s]